The Impact of Isoprene Emissions on Air Quality in China

A thesis submitted to the School of Environmental Science at the University of East Anglia in partial fulfilment of the requirements for the degree of Doctor of Philosophy

Yanhui Liu

September 2019

Abstract

Isoprene, primarily emitted by vegetation, is considered to be the most important biogenic volatile organic compound in the troposphere due to its strong rate of emission and high ozone (O_3) formation potential. In model simulations, the impact of isoprene on the O_3 distribution is highly affected by the chemical mechanism used, including the treatment of isoprene nitrates (INs) and their impact on NO_X recycling. However, most of the chemical schemes included in the chemistry transport model have a rather simple representation of isoprene chemistry with intermediates lumped, which may not be able to reproduce the nonlinear chemistry of isoprene very well.

This study aims to understand the detailed isoprene chemistry and its impact under various NO_X-VOCs regimes in China using the WRF-Chem model. To do so, a more explicit isoprene chemical mechanism (M4) is developed and implemented into WRF-Chem, and its simulations are validated with the field observations in Beijing as part of the APHH-Beijing programme.

The modelled diel patterns of INs agree well with the observations suggesting that the key chemical processes are captured reasonably well, although there are discrepancies in absolute concentrations. Compared to the simpler chemical mechanism (MOZART-4), the reaction between RO_2 and HO_2 and other RO_2 are more competitive in M4 resulting in a slower NO_X recycling and lower NO_X concentrations over China, which then impact the O_3 distribution ($\pm 4\%$).

In very high NO_X environments, 25% reduction of NO_X emissions is simulated to result in up to 20% (10 ppb on average) O_3 enhancement, which is due to the increased O_3 production owing to reduced loss of HO_2 and reduced O_3 titration by NO. If isoprene emission increases in these areas, the photochemical pollution can become even more severe. Hence, different O_3 control measures need to be designed according to the local NO_X-VOCs regimes.

Acknowledgements

Firstly of all, I would like to thank my supervisory team: Claire Reeves, Steve Dorling and Graham Mills. You have always been very helpful, supportive and generous with your time. It was your valuable suggestions and insightful comments that have been helping me think critically and scientifically.

Special thanks to my parents, Fangzhen Chen and Mengde Liu. You have always been encouraging and caring during my study. Also, you supported me financially for the past four years, which is a big sacrifice for me. I could not finish this thesis without your kind support. I love you.

I would like to thank Alba Badia Moragas, Johana Leidy Romero Alvarez, Tabish Ansari, Scott Archer-Nicholls, Douglas Lowe and Gordon McFiggans for your help when I had errors in running the model. It is really nice to have a group to share WRF-Chem knowledge and codes. I acknowledge Jim Cross and the staff of High Performance Computing (HPC) in UEA for helping me set up and run the model on the HPC platform, especially when shifting from the GRACE to HPC. Thanks to Maria Zamyatina for sharing useful paper, code and chemical knowledge with me. I would also like to acknowledge James Lee, James Hopkins, Simone Kotthaus, Lisa Whalley, Joe Acton, Lekan Popoola, Pingqing Fu and their colleagues for kindly share their measurements with me, and Oliver Wild, Qiang Zhang, Ruili Wu for providing the up-to-date emission inventory.

Thanks to Chata Isabel Seguro, Elise Droste, Karina Adcock, Gianfranco Anastasi, Fazrin Mohd Hanif, Geoffrey Lee, David Buchanan, Seth Thomas, Ruth Payn and Reuben Gilbertson for sharing the not only the office but laugh and tears with me. Our office is the best! I want to thank Beatrice Heighton, Sammi Lai and Dominic Rodrigues for being great flatmates and friends. Finally, thank my best friends, Qiaochu Zhao, Zanist Hama-Aziz, Yuanxin Tian, Mingxin Qu, Yanxin Wang, Weici Zhong, Shuang Tong, Longji Deng and Rui Meng for your care and support.

Contents

List of Figures

List of Tables

1

Introduction

Isoprene, as a reactive hydrocarbon emitted primarily by vegetation, plays an important role in the tropospheric ozone (O_3) formation. However, recent studies show that the formation of isoprene nitrates (INs) in its oxidation can change the O_3 distribution by temporarily terminating the local O_3 production and encouraging the O_3 formation downwind. However, INs are hard to be measured and identified. As a result, the INs chemistry, as well as its contribution to the O_3 formation is poorly understood.

INs were identified and measured in Beijing for the first time by our group during the field campaigns as part of the joint UK-China air pollution research programme. This study is embedded in this programme, and aims to improve the understanding of isoprene and INs chemistry and assess their impact under different emission scenarios and ambient air conditions, using China as the study area. In this document, I present and discuss the results from the model simulations and the comparison of the campaign measurements.

In the first chapter here, I introduce the chemical background, the uncertainties in the isoprene chemistry, and the current air quality status in China. The structure of this thesis is mentioned in the end.

Section 1.1 introduces the tropospheric O_3 related chemistry as well as the current understanding of isoprene chemistry. Isoprene chemistry is complicated and involved in many important chemical systems. Three major pathways of isoprene oxidation are discussed in detail here. The current understanding of the INs formation and the uncertainties in their chemistry are also included in this section.

Section 1.2 describes the air pollution issue in China, as well as the measures taken by the Chinese government to improve air quality in recent decades. Key pollutants and their trend are discussed. This chapter will provide the reader with a basic idea of the air pollution evolution in China.

The last section of this chapter gives an overview of this document. The objectives and the thesis structure are listed here.

1.1 Overview of tropospheric chemistry

1.1.1 Tropospheric O_3 formation

O_3 is one of the most important pollutants in the troposphere. Ground-level O_3 at high concentrations poses a great threat to human health as it increases the risk of respiratory disease, and is also detrimental to crops and other vegetation (McKee, 1993). Tropospheric O_3 is also the third most important greenhouse gas (Stocker et al., 2013). It has a lifetime of about 22 days, which means the impact of O_3 is not limited to the local area but can be regional (Stevenson et al., 2006).

As a secondary pollutant, O_3 is mainly produced photochemically, which involves the three significant chemical systems: HO_X chemistry (hydroxyl radical (OH) and hydroperoxy radical (HO_2)), NO_X (nitric oxide (NO) and nitrogen dioxide (NO_2)) chemistry and the organic chemistry. Therefore, these three basic tropospheric chemical systems are introduce here.

Almost all the O_3 is formed by the photochemical reaction below,

$$O_2 + O(^3P) + M \longrightarrow O_3 + M \tag{1.1.1}$$

where the $O(^3P)$ is atomic oxygen and M is a third body that is involved in the energy exchange of the reaction. M usually is N_2 and O_2 in the atmosphere (Jacob, 1999).

$O(^3P)$ is mainly produced by the photolysis of O_3.

$$O_3 + h\nu \longrightarrow O(^1D) + O_2 \tag{1.1.2}$$

$$O(^1D) + M \longrightarrow O(^3P) + M \tag{1.1.3}$$

It is noticeable that no net O_3 is produced in the cycle of reaction 1.1.1, reaction 1.1.2 and reaction 1.1.3, as the formation of $O(^3P)$ destroys O_3 molecule.

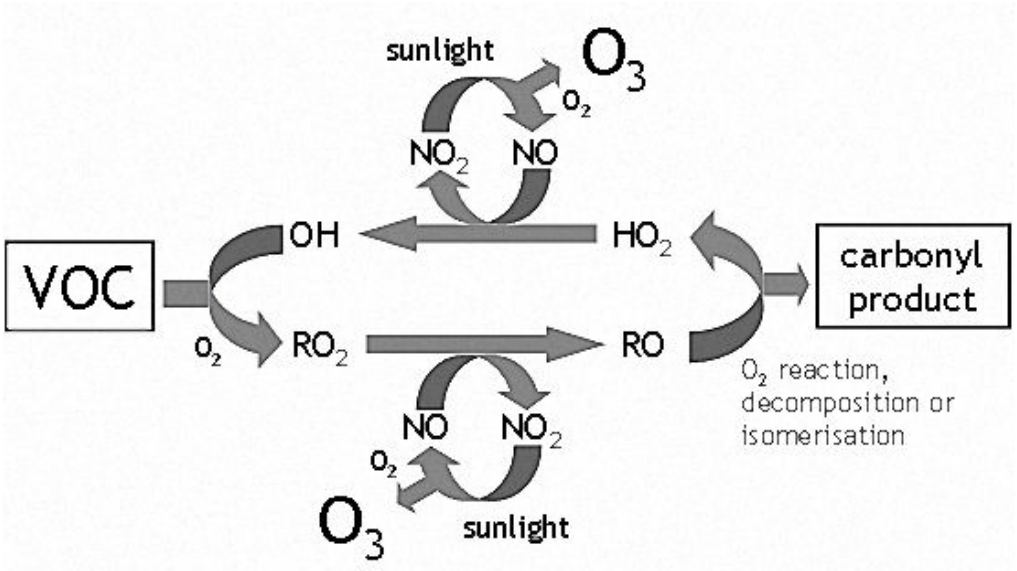

Figure 1.1.1: Schematic representation of the chemistry of VOCs and NO_X in the troposphere (*source: http://mcm.leeds.ac.uk/MCMv3.2/project.htt*).

Another source of $O(^3P)$ in the troposphere is from NO_2 photolysis.

$$NO_2 + h\nu \longrightarrow O(^3P) + NO \tag{1.1.4}$$

The majority of NO_2 is formed through the oxidation of NO, and in the troposphere the O_3-NO reaction is the dominant pathway of this process.

$$NO + O_3 \longrightarrow NO_2 + O_2 \tag{1.1.5}$$

Similar to above, in the reaction 1.1.1, reaction 1.1.4 and reaction 1.1.5 cycle, the net production of O_3 is still zero. In other words, net O_3 can be formed when the oxidation reaction of NO to NO_2 occurs by other oxidants, namely peroxy radicals, which are the products of CO and hydrocarbon oxidations.

A very large number of volatile organic compounds (VOCs) exist in the troposphere, and their oxidation products are often involved in the NO_X cycle.

Fig. 1.1.3 illustrated the photochemical formation of O_3 in the presence of VOCs and NO_X. VOC react with OH, with break of the C–H, C=C or C≡C bond forming a radical referred as R. Preoxy radical (RO_2) is rapidly formed with the reaction between R and O_2.

$$R + O_2 \longrightarrow RO_2 \tag{1.1.6}$$

RO_2 reacts with NO forming NO_2 and an alkoxy radical, RO.

$$RO_2 + NO \longrightarrow RO + NO_2 \tag{1.1.7}$$

In this way, NO_2 is converted from NO with no consumption of O_3, and the subsequent photolysis leads to the net formation of O_3 (reaction 1.1.1 and reaction 1.1.4).

$$RO \longrightarrow \text{carbonyl products} + HO_2 \tag{1.1.8}$$

$$HO_2 + NO \longrightarrow OH + NO_2 \tag{1.1.9}$$

This is not the end of the story. During the degradation of the RO, with the presence of O_2, a hydroperoxy radical (HO_2) can be produced as a byproduct, which can also convert NO to NO_2. Some of the carbonyl products react similarly to their parent hydrocarbons, forming peroxyl radicals during its decomposition. Hence, in the troposphere, O_3 is produced efficiently via the oxidation of VOCs in the presence of NO_X, which acts as a catalyst.

The sink of NO_2 (reaction 1.1.10) leads to a reduction of O_3 formation.

$$OH + NO_2 + M \longrightarrow HNO_3 + M \tag{1.1.10}$$

1.1.2 Impact of NO_X and VOCs concentrations on O_3 formation

The previous section introduced the mechanism of the tropospheric O_3 formation, which is via the oxidation of VOCs in the presence of NO_X. The O_3 production control seems straightforward: by restricting the VOC or NO_X emissions as they are the precursors of O_3. However, O_3 formation is not always reduced when NO_X or VOC concentration is lower. The reactions between VOC and NO_X are complex, have multiple branches and the dominant reactions can vary responding to the different ambient air compositions.

In the very low NO_X environment ($NO_X \leq 100$ ppt), RO_2 are produced normally via reaction 1.1.6 and reaction 1.1.8. However, due to lack of NO, the reaction rate of reaction 1.1.7 and reaction 1.1.9 become low, as a result, more preoxy radical can react with O_3 leading to destruction of O_3.

$$RO_2 + O_3 \longrightarrow RO + 2\,O_2 \tag{1.1.11}$$

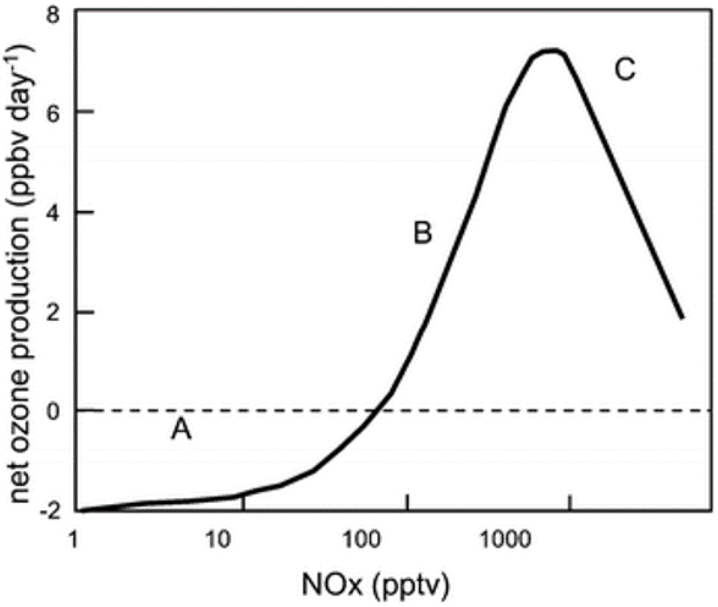

Figure 1.1.2: The dependence of the net O_3 production (or destruction) rate on the NO_X concentration (Hewitt and Jackson, 2009).

$$HO_2 + O_3 \longrightarrow OH + 2\,O_2 \tag{1.1.12}$$

In contrast, if the NO_X mixing ratio is very high ($NO_X \geq 10$ ppb), significant amount of NO_2 can be formed rapidly through the O_3 titration (reaction 1.1.5) making reaction 1.1.10 more competitive. The formation of nitric acid (HNO_3) is not reversible due to its high deposition velocity, which means O_3 is removed from the atmosphere permanently via this process. Hence, in this regime, O_3 production rate is lower with the enhanced NO_X in the atmosphere.

Fig. 1.1.2 shows the dependence of the net O_3 production rate change on the NO_X concentration from a numerical model. The region A represents the very low NO_X condition, where the negative O_3 production rate is due to reaction 1.1.11 and reaction 1.1.12. In the B region, sufficient amount of RO_2 exits in the atmosphere and O_3 production is constrained by the concentration of NO_X, so called NO_X limited regime. The net O_3 production rate is highly sensitive to the NO_X mixing ratio until the NO_X concentration reaches the region C. In this region, the abundant NO_X titrates and removes O_3 via reaction 1.1.5 and reaction 1.1.10. However, in region C if an addtional source of VOCs is included, the enhancement of RO_2 can encourage O_3 production and shift this regime to regime B. In other words, the net O_3 production rate in this region is limited by VOCs.

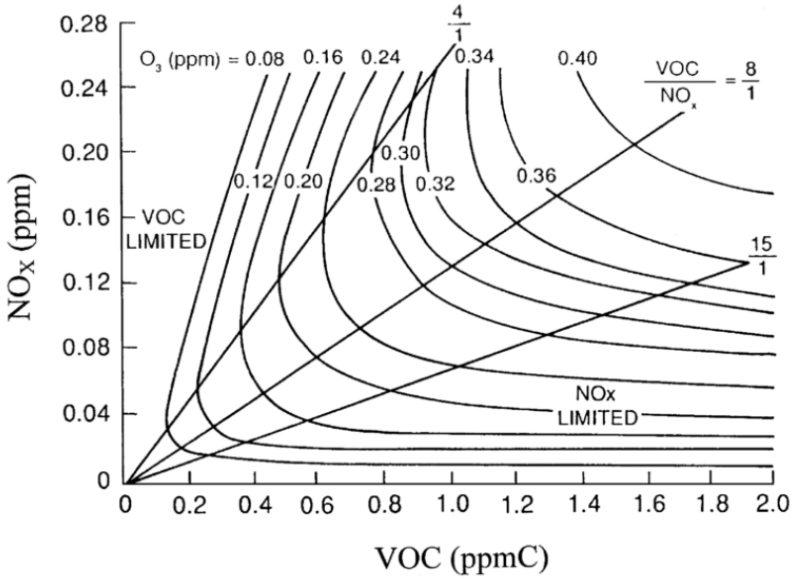

Figure 1.1.3: Diagram of ozone isopleths, showing the maximum O_3 concentration in various conditions. The x-axis and y-axis are the initial mixing ratios of VOC and NO_X in the model and the straight lines represent different VOC to NO_X ratios (Jenkin and Clemitshaw, 2000).

The NO_X limited and VOCs limited regimes are not defined by the concentration of NO_X or VOCs, but the ratio between the two. Fig. 1.1.3 illustrates the O_3 concentration in relation to different NO_X and VOC concentrations. The O_3 isopleths in the figure are generated by box modelling which calculates the maximum O_3 mixing ratios change over time with various NO_X and VOC initial mixing ratios. This method is called empirical kinetic modelling approach (EKMA) (Dodge, 1977). The curves are the modelled O_3-isopleths and the straight lines represent different VOC to NO_X ratios.

This figure shows the O_3 concentration in different regimes. If the VOC to NO_X ratio is ≥ 15, the O_3 mixing ratio is very sensitive to the NO_X concentration, which means it is the NO_X limited condition (the region B in Fig. 1.1.2). This condition usually occurs in rural areas where abundant of RO_2 are formed but lack of NO_X to react with.

The condition where the VOC to NO_X ratio is ≤ 4 is the VOC-limited regime (region C in Fig. 1.1.2). The O_3 mixing ratio drops with increasing NO_X concentration, which suggests that O_3 is destroyed at a higher speed than its production. This environment occurs in the regions close to the anthropogenic source, such as urban areas.

When the VOC to NO_X ratio is between 4 to 15, O_3 concentration increases with the enhanced VOC and NO_X mixing ratios. O_3 is produced efficiently in this regime since sufficient VOC and NO_X are presence in the atmosphere to react. The equivalent region in Fig. 1.1.2 of this regime is near the peak of O_3 production area in between of the region B and C. It is worth mentioning that with more VOC presence, the curve of Fig. 1.1.2 can be different. The peak O_3 production rate is expect to be larger and appear in higher NO_X concentrations if the VOCs concentration is larger.

To conclude, the O_3 formation rate is not a linear function of VOC or NO_X concentration, but it is related to the ratio of the two.

1.1.3 Isoprene and its emissions

Isoprene (2-methyl-1,3-butdiene, C_5H_8, formula $CH_2=C(CH_3)-CH=CH_2$, Fig. 1.1.4) is the most important biogenic VOC (BVOC) in the troposphere due to its high reactivity and abundant emission.

As illustrated in the Fig. 1.1.4, though there are 5 carbons atoms in isoprene, the main chain is composed with 4 of them (labelled 1 to 4), and the second carbon always has 4 bonds linking to the carbon atoms. The order of the carbon atoms in the chain is important in naming the isoprene derived isomers, which have the same compositions but different structures. The naming method is explained in the section 1.1.5, where the IN isomers are introduced.

With high reactivity, once be emitted in the atmosphere, isoprene rapidly oxidised by the oxidants, leading to a short lifetime (less than one hour during daytime in summer) (Perring et al., 2009). Hence, the impact of isoprene itself is considered to be regional. However, during its oxidation some relatively longer lived nitrates and other secondary products such as methyl vinyl ketone (MVK) and methacrolein (MCAR) can be formed, which may be involved in the O_3 formation downwind.

The range of global natural emission of isoprene is 410 TgC per year to 600 TgC per year, and constitutes approximately 40% of the total global non-methane volatile organic compound (NMVOC) emissions in terms of mass

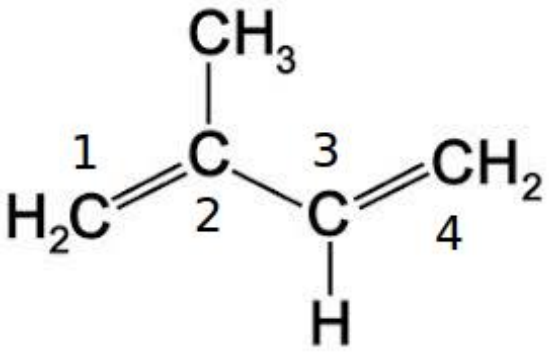

Figure 1.1.4: Structure of isoprene.

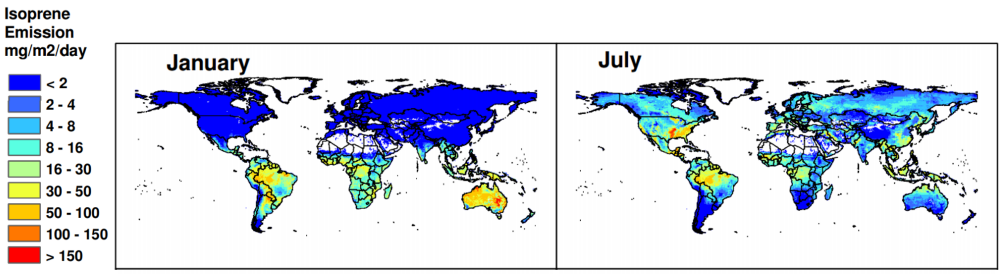

Figure 1.1.5: Monthly average isoprene emission rates estimated with MEGAN for 2003 (Guenther et al., 2006).

(Stocker et al., 2013; Guenther et al., 2006).

As a BVOC, isoprene is primarily emitted by vegetation, especially broadleaved trees. Temperature, intensity of sunlight and the plant function type are the main factors affecting its emission. As a result, isoprene emission shows a strong diurnal and seasonal cycle. Fig. 1.1.5 shows the monthly average global emission rate map of isoprene using the simulation from the Model of Emissions of Gases and Aerosols from Nature (MEGAN). Globally, isoprene is mainly emitted in the southern hemisphere (SH) tropics during northern hemisphere (NH) winter. However, still significant amount isoprene is released in mid-latitudes of NH in NH summer. In July, isoprene emission in the south and north-east of China can reach 2 to 4 mg $\cdot$ m^{-2} $\cdot$ h^{-1} (Archibald et al., 2010).

Due to large geographical differences in China, the density and predominant vegetation changes from region to region. As a result, the potential isoprene emissions vary over large scales in China. According to a light-temperature model simulation, Beijing, Tianjing, and Shanghai contribute only 0.22% to the total isoprene emission in China. By contrast, the emissions of the forest in the

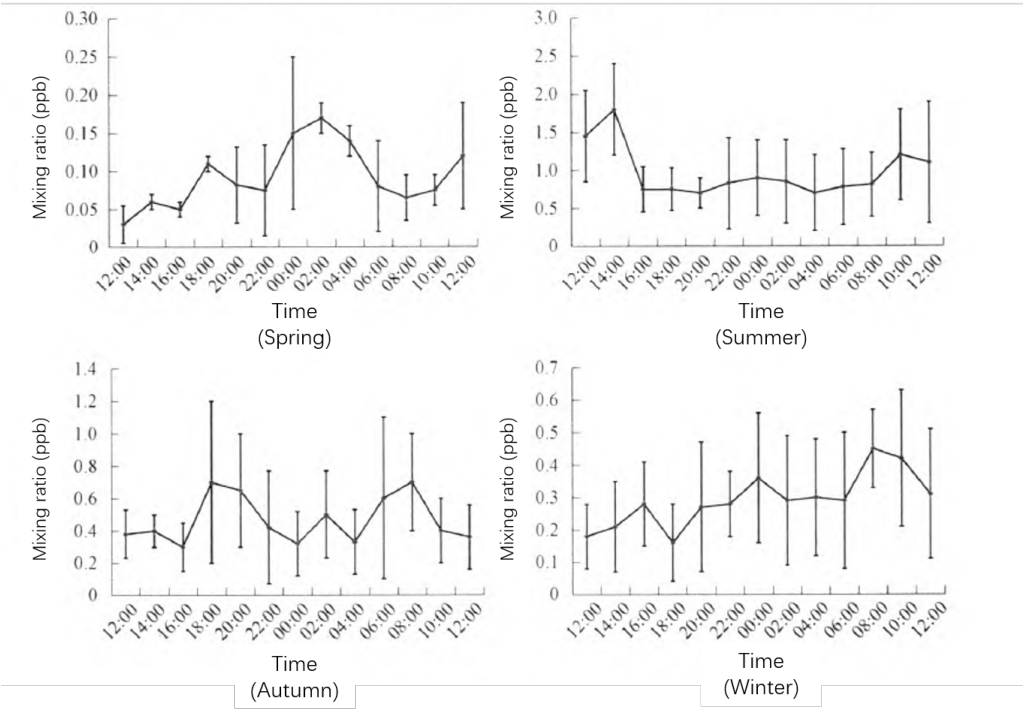

Figure 1.1.6: Diel cycle of monthly averaged mixing ratios of isoprene in Beijing (Li et al., 2013).

SE and NE of China contribute 22% and 11% respectively to the total isoprene emission (Zhang et al., 2003).

The isoprene emission rates vary with different plant species. Broad-leaved trees are the main sources of isoprene emission, especially chinar, which has a high emission rate of 139 $\pm$ 42 $\mu g \cdot g^{-1} \cdot h^{-1}$, followed by poplar trees with an emission rate of 105.8 $\pm$ 16.1 $\mu g \cdot g^{-1} \cdot h^{-1}$ (Wang et al., 2010). However, this emission rate is not a fixed value. As mentioned above, it is also affected by temperature and intensity of sunlight. Assuming the intensity of sunlight remains constant, vegetation emits more isoprene with the increasing temperature and reaches the peak value at around 40 ^{o}C (Wang et al., 2003). Intensive sunlight will encourage the emission of isoprene.

Strong correlation between isoprene and CO emissions were founded in many countries, which indicates the anthropogenic sources of isoprene (Duan et al., 2013; Borbon et al., 2001). Larger emissions of isoprene were recorded in areas close to traffic rather than regions with denser vegetation in winter Beijing, which indicated a considerable contribution of human activities to isoprene emissions (Duan et al., 2013).

Fig. 1.1.6 shows the seasonal averaged isoprene mixing ratio diel pattern in Beijing. Peak isoprene mixing ratio appears in summer (up to 1.7 ppb), followed by autumn (up to 0.8 ppb). The diurnal pattern varies differently in the four seasons. In spring, maximum isoprene concentration is shown at night (1 a.m.), which is likely to be associated with the flow control of the trucks. In Beijing, heavy turcks are not allowed to enter the central city (inner 5th ring road region) during the day. As a result, these heavy diesel vehicles are travelling to Beijing at around midnight. This peak of isoprene concentration has been observed over the whole year, though it is less obvious in the other three seasons due to higher daytime emissions. In summer, isoprene concentration increases in the morning with the increasing temperature and radiation intensity and reaches a peak at 12.00 - 14.00, which agrees with the previous discussion of biogenic isoprene emissions. This pattern is not obvious in the other three seasons. Isoprene mixing ratio represents the balance of its emission and its oxidation, so the low value of isoprene at noontime in spring, autumn and winter can be the result of that the photochemical reactions dominate over the emission. In autumn and winter, high isoprene were seen in the morning (8.00 - 10.00) and afternoon (15.00 - 17.00) when sunlight is present but not strong enough to dirve fast photochemistry.

1.1.4 Isoprene oxidation chemistry

The oxidation of isoprene can be initiated by several oxidants in the atmosphere, such as OH, O_3 and the nitrate radical (NO_3) (Archibald et al., 2010; Fan and Zhang, 2004). The OH-isoprene pathway dominates daytime oxidation of isoprene, while during the night isoprene mainly reacts with NO_3. Compared to OH oxidation, the reaction rate of O_3 with isoprene is not very fast. However, this pathway is important in this study since O_3 participants in the chemistry as a reactant.

OH-isoprene reactions Isoprene oxidation by OH is similar to VOC-OH reactions. Isoprene can be oxidised to hydroxy radicals (ISOPR). The reaction rate constant of this reaction is 1.0×10^{-10} cm^3 $mol^{-1}s^{-1}$, which has been measured experimentally and calculated theoretically (Lee et al., 2014; Fan and Zhang, 2004).

Depending on which double carbon bond is destroyed, four ISOPR isomers (ISOA, ISOB, ISOC and ISOD, Fig. 1.1.7) can be formed. As mentioned in section 1.1.3, there are four carbons on the main carbon chain of isoprene, and carbon 2

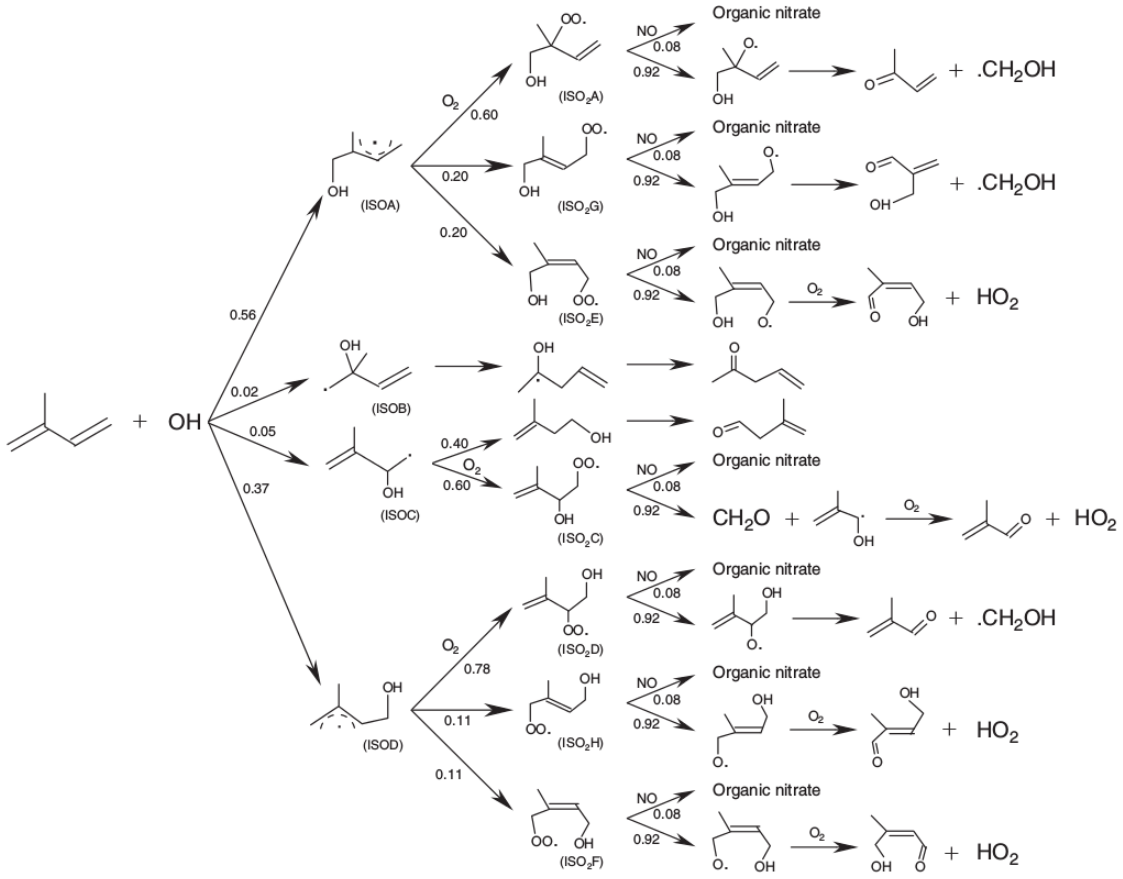

Figure 1.1.7: Schematic of the OH initiated reaction pathways of isoprene (Fan and Zhang, 2004).

is connected with carbon 5. These five carbons are referred as C1 to C5 in the following text. For ISOA and ISOD, double bonds between C1 and C2, and C3 and C4 are both broken forming a new double bond between C2 and C3. Hence, the OH can attach to either C1 (ISOA) or C4 (ISOD). The ISOB is formed when the double bond between C1 and C2 is broken and OH attaches to C1. If OH is captured by C4 breaking the C3 to C4 double bond, ISOC is produced. The branching ratio of ISOA : ISOB : ISOC : ISOD is measured to be 0.56 : 0.02: 0.05 : 0.37 (Fan and Zhang, 2004).

$$C_5H_8 + OH \longrightarrow 0.56\,\mathrm{ISOA} + 0.02\,\mathrm{ISOB} + 0.05\,\mathrm{ISOC} + 0.37\,\mathrm{ISOD} \qquad (1.1.13)$$

The ISOPR isomers react rapidly with molecular oxygen forming 6 peroxy radicals (ISOPO2) isomers, which are (1,2)-ISOPO2, (4,3)-ISOPO2, E-(1,4)-ISOPO2, Z-(1,4)-ISOPO2, E-(4,1)-ISOPO2 and Z-(4,1)-ISOPO2. E and Z are referred to trans- and cis- isomers with same functional groups at the same positions but different configurations (Fan and Zhang, 2004; Lockwood

et al., 2010). Wennberg et al. (2018) recommended the ratio between these ISOPO2 are 0.479, 0.259, 0.102, 0.049, 0.048, and 0.063 follow the order above.

The subsequent reaction of ISOPO2 with NO leads to the formation of hydroxy alkoxy radicals (ISOPO) and NO_2, or hydroxy isoprene nitrates (hy-INs).

$$\mathrm{ISOPO_2 + NO \longrightarrow (1-\alpha)\ NO_2 + (1-\alpha)\ ISOPO} \tag{1.1.14}$$

$$\mathrm{ISOPO_2 + NO \longrightarrow \alpha\ \ hy{-}IN} \tag{1.1.15}$$

where α is the yield of hy-IN.

Six hy-IN isomers can be formed from the according ISOPO2. NO_X is temporarily tied into the nitrate functional group when hy-IN is formed. As a result, less NO is converted to NO_2 leading to a reduction of O_3 formation. If hy-IN is removed from the atmosphere via deposition or involved in the heterogeneous chemistry forming aerosol, NO_X concentration is reduced permanently. The photolysis of hy-IN releases NO_2 back to the air (reaction 1.1.16), which continues the NO_X cycle. However, compared to isoprene, hy-IN is relatively long-lived with the lifetime of hours to days, which means it can be transported to area far from the source region. That is to say, NO_X can be released to the remote regions with low NO_X changing the O_3 production there.

$$\mathrm{hy{-}IN + h\nu \longrightarrow ISOPO + NO_2} \tag{1.1.16}$$

NO_3-isoprene reactions The night-time isoprene oxidation is a different story from the daytime chemistry. The NO_3-isoprene reaction dominates the isoprene oxidation after sunset due to the sharp decrease of OH mixing ratio and the enhanced NO_3 concentration.

Instead of reaction 1.1.13, isoprene is oxidised to nitrooxyalkyl peroxy radicals (ISOPNO3) by NO_3.

$$\mathrm{ISOP + NO_3 \longrightarrow ISOPNO_3} \tag{1.1.17}$$

Aldehydic isoprene nitrate (al-IN) is formed as the product of reaction between ISOPNO3 and NO (Fan and Zhang, 2004; Saunders et al., 2003).

$$\mathrm{ISOPNO_3 + NO \longrightarrow al{-}IN + NO_2 + HO_2} \tag{1.1.18}$$

The night-time isoprene mixing ratio is significantly lower than the daytime, however the al-IN formed via isopene-NO_3 pathway contributes to about 50% of the total isoprene nitrate (Kuhlmann et al., 2004; Horowitz et al., 2007). Similar to the hy-IN, NO_2 is a product of the photochemistry of al-IN. Al-IN can also react with OH, O_3 and NO_3 forming shorter chain nitrates.

O_3-isoprene reactions The oxidation pathway of O_3 is simpler than the two mentioned above. The overall reaction rate constant of the O_3-isoprene reaction is $1.6{\times}10^{-17}$ cm^3 $mol^{-1}s^{-1}$ (Fan and Zhang, 2004). O_3 oxidises isoprene to a shorter chain carbonyl products in this pathway. Subsequently methyl vinyl ketone (MVK) and methacrolein (MACR) are produced, with high relative branching ratio by stabilization reactions of their peroxy radicals ($MVKO_2$ and $MACRO_2$) (Lee et al., 2014). The main source of MVK and MACR is from isoprene oxidation, which makes them important trace gases in studying isoprene chemistry.

$$\begin{aligned}\mathrm{ISOP + O_3 \longrightarrow}\ & 0.33\ \ \mathrm{CH_2O_2} + 0.405\ \ \mathrm{MACRO_2} \\ & 0.23\ \ \mathrm{MVKO_2} + 0.21\ \ \mathrm{MCAR} \\ & + 0.12\ \ \mathrm{MVK} + 0.67\ \ \mathrm{CH_2O}\end{aligned} \tag{1.1.19}$$

Fig. 1.1.8 illustrates a box model simulation of the O_3 mixing ratio under various NO_X and isoprene emissions. As a reactive VOC, isoprene can be involved in the NO_X cycle producing O_3 effciently when sufficient amount of isoprene and NO_X presence in the air. Whereas when the emission is low (≤ 0.05 mg $C \cdot m^{-2} \cdot h^{-1}$), isoprene does not contribute to the O_3 concentration.

1.1.5 Isoprene nitrates and their impact

As introduced in previous section, IN is formed by the reaction between isoprene peroxy radicals and NO. Because both hy-IN and al-IN recycle NO_2 during the photochemistry, IN can be considered as the reservoir of NO_X. The subsequent chemical reaction of it, in theory, can change the O_3 distribution. This process is poorly understood by far, and one of the reason is that hy-IN

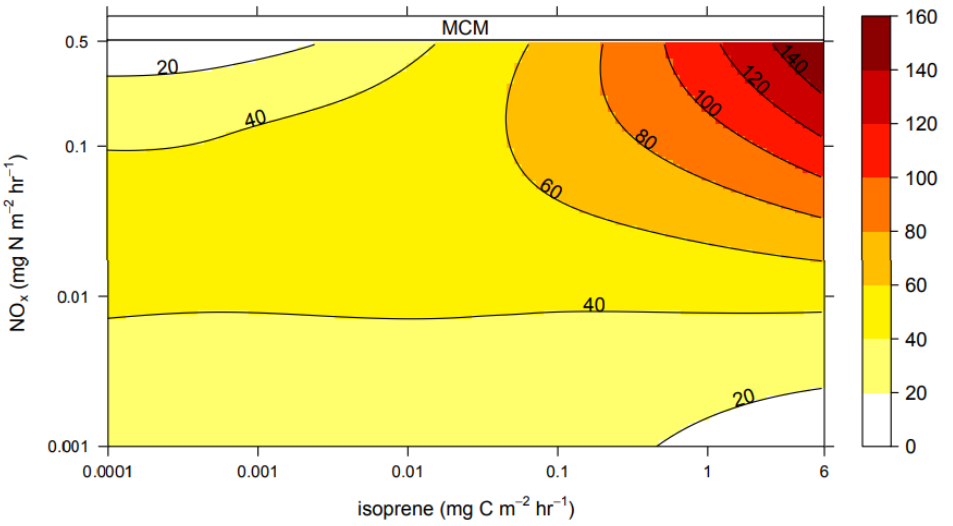

Figure 1.1.8: O_3 (ppb) isopleth plot as a function of NO_X and isoprene emissions for the Master Chemical Mechanism (MCMv3.2). This was created from a series of box model runs (Squire et al., 2015).

and al-IN are not two single species. Up to 8 different hy-IN isomers and 4 al-IN isomers can be produced in reaction 1.1.15 and reaction 1.1.18 (Lockwood et al., 2010; Rollins et al., 2009; Skov et al., 1992).

Fig. 1.1.9 and Fig. 1.1.10 show the structure of hy-INs and al-INs. The abbreviations of hy-INs A to H are E-(4,1)-IN, Z-(4,1)-IN, E-(1,4)-IN, Z-(1,4)-IN, (3,4)-IN, (4,3)-IN, (2,1)-IN and (1,2)-IN. The names of the isomers depend on the position of the two functional groups. The first number in the abbreviation is the number of carbon that connected with hydroxyl group, and the second number represents the position of nitrate group. The al-IN I and J represent the E/Z-(4,1)-al-IN and E/Z-(1,4)-al-IN isomers with the same naming function.

Though the compositions are the same, IN isomers with different structures can have different yields, different lifetimes and different degradation chemical mechanisms. Due to the difficulties in measurements, detailed INs chemistry it still poorly understood.

The branching ratio and yield of different IN isomers have been studied for decades. 8 - 13% yield of total hy-INs has been reported in 1990 (Tuazon and Atkinson, 1990). Since then, estimations of INs yield ranging from 4.4 % to 14

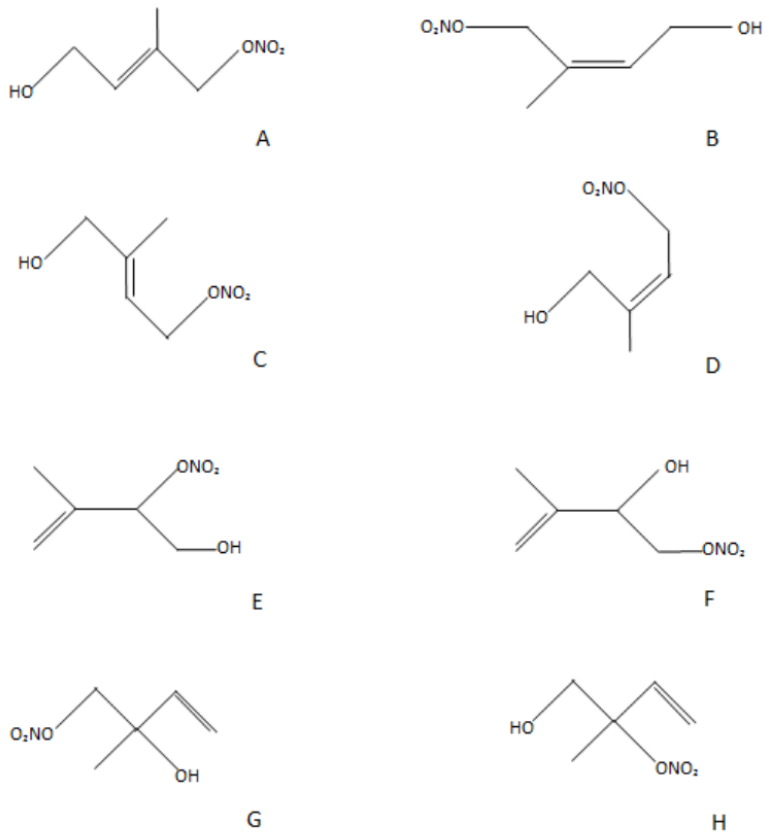

Figure 1.1.9: Chemical structures of isoprene nitrate isomers initiated by OH radicals.

Figure 1.1.10: Chemical structure of isoprene nitrate isomers initiated by reaction with NO_3.

% were published (St. Clair et al., 2015; Paulot et al., 2009; Patchen et al., 2007; Sprengnether et al., 2002; Chen et al., 1998). Apart from the big uncertainties, the branching ratio observed in most of those studies represents the yield of the total hy-INs, or even the total INs.

Fig. 1.1.11 listed the INs yields measured based on a chamber study. Yields of (1,2)-IN, Z-(1,4)-IN, E-(1,4)-IN and total al-INs were calculated as 8.5 %, 2.9

Structure	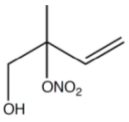	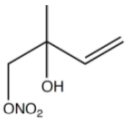	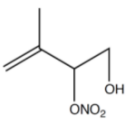	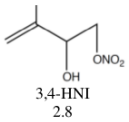
Abbreviation	1,2-HNI	2,1-HNI	4,3-HNI	3,4-HNI
Yield (%)	23.1	1.1	12.8	2.8
Structure	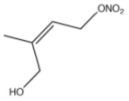	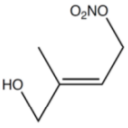	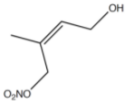	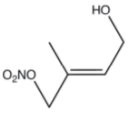
Abbreviation	(Z)-1,4-HNI	(E)-1,4-HNI	(Z)-4,1-HNI	(E)-4,1-HNI
Yield (%)	4.6	26.5	4.4	24.8

Figure 1.1.11: Yield of isoprene nitrates (Piletic et al., 2017).

%, 19.4%, and 21%, respectively (Piletic et al., 2017). This study also suggests that the yield of INs is depend on the NO_X concentration.

Based on the current knowledge of INs, researchers developed chemical mechanisms with different presentations of INs, or organic nitrates. Some modelling studies reported that isoprene chemistry differ hugely between mechanisms, resulting in uncertainties of its impact (Archibald et al., 2010; Emmerson and Evans, 2009). The different treatments of nitrates can contribute to the variability between mechanisms on their ozone production rates over a wide range of NO_X emissions (Archibald et al., 2010; Kuhlmann et al., 2004).

The ability of simulating complex chemistry makes the box model favourable for research, nevertheless, transport cannot be calculated in it. A regional transport model study in Shanghai, China suggested that the O_3 enhancement in the rural area downwind is a result of NO_X transported by the INs formed in the source region(Geng et al., 2011).

However, the contribution of INs to the NO_X recycling and O_3 concentration remain uncertain due to limited understanding of INs chemistry including its formation and degradation.

This study aims to improve the understanding of isoprene and IN chemistry and quantitatively investigate their impacts.

1.2 Overview of air quality issue in China

1.2.1 The main pollutants in China

With the rapid development of urbanization and industrialization in China, air pollution became a serious threat and is responsible for great number of cases of respiratory, cardiovascular diseases and cancers every year (Liu et al., 2018a; Zhang et al., 2017a). The key air pollutants in China are coarse and fine particulate matter (PM 10 and PM 2.5), surface O_3, NO_X, SO_2 and CO.

Among those pollutants, SO_2, CO and NO_X are emitted directly by various activities, so called primary pollutants. The source of SO_2 is mainly from coal combustion, and the dramatic increase of NO_X and CO concentrations is a result from greater fuel consumption in industry and private vehicles. PM can also be emitted directly from dust, and black and/or elemental carbon from combustion. Secondary PM, on the other hand, are formed in the atmosphere via complex chemical reactions. O_3, as a secondary pollutant, has no direct emissions but is produced from photochemical reactions involving NO_X and VOCs (mechanism introduced in section 1.1.1).

The majority of the Chinese population lives in the eastern part of China, especially in the 'BTH' (Beijing-Tianjin-Hebei) region and the Yangtze River Delta (YRD; including ShanghaiJiangsu-Zhejiang-Anhui) region. Due to the active human activities, the emissions in these regions are high, resulting in heavier pollution.

Fig 1.2.1 shows the average mass concentration of NO_2, SO_2, PM 10 and PM 2.5 across China from 2014 to 2015 (Zang et al., 2015).

High value of all four pollutants are recorded in the BTH, which suggests critical air quality in that area. The other hot spot in the NO_X distribution map is the YRD, where Shanghai locates. The desert in NW China emits great amount dust leading to the high concentration of PM 10.

Since this study focus on the isoprene chemistry and its contribution to the O_3 formation, the status of NO_X and O_3 is presented here in detail. As mentioned before, O_3 has a negative impact on both human health and corp yield. Also, due to a relatively long lifetime (about 22 days), O_3 can be transported

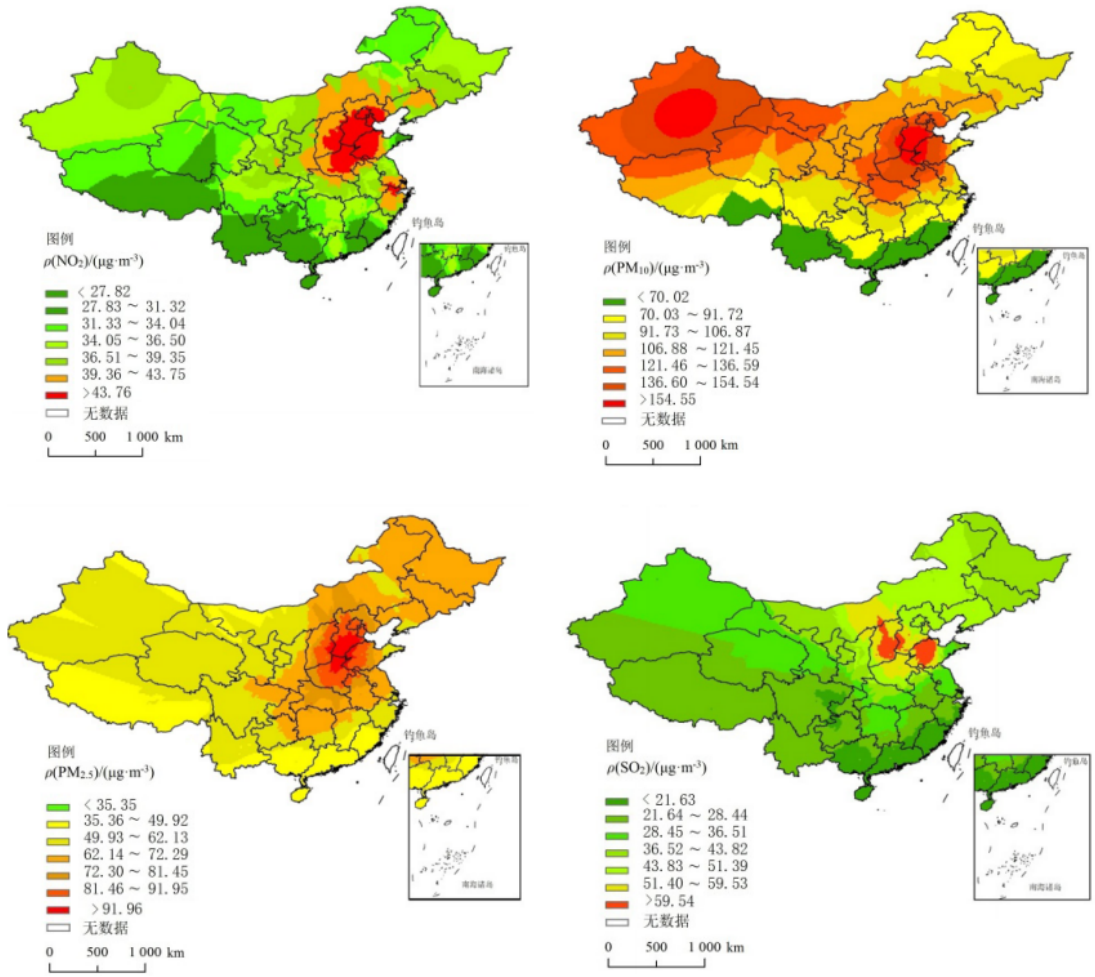

Figure 1.2.1: The special distribution of NO_2, SO_2, PM 10 and PM 2.5 in China (Zang et al., 2015).

inter-city/region having a regional impact (Stevenson et al., 2006).

There are limited observational studies on the O_3 spacial distribution across China. O_3 was not regularly monitored in Chinese cities until 2012. Even now, the coverage of O_3 monitoring station is limited to the major cities. The Ozone Monitoring Instrument (OMI) on-board on NASA's satellite can provide the surface O_3, NO_2 and SO_2 measurements from the space. However, due to the exist of O_3 layer, ground-level O_3 is calculated with large uncertainties.

High values of Maximum Daily 8-hour Average (MDA8) are recorded in BTH and YRD regions in China (Fig. 1.2.2), corresponding to the high NO_X emissions. Chengdu and Wuhan in the south of China are cities with good vegetation coverage, hence O_3 is produced efficiently in these cities. A hot spot

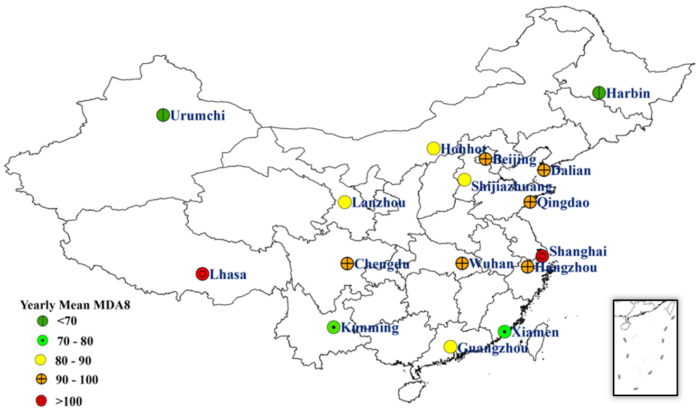

Figure 1.2.2: Average maximum daily 8 h (MDA8) O_3 (μg m^{-3}) concentrations for 16 Chinese cities from 2014 to 2016 (Gong et al., 2018).

of O_3 is found in Lhasa on the Tibet highland (Li et al., 2018a). Anthropogenic emissions in there are low, however, due to the high altitude (3000 m - 5000 m), intense solar radiation accelerates the photochemical reactions forming significant amount of O_3. Also, O_3 is transported from the stratosphere by the stratspheric intrusions (Li et al., 2018a).

In Beijing, the higher O_3 mixing ratios are observed in the comparison rural sites. The O_3 concentrations in there are 5 to 15 ppb higher than the measurements from the urban sites close to traffic junctions (WANG et al., 2014). This indicates that Beijing is in a very high NO_X environment where significant NO_X emissions depress O_3 formation. Similar results are observed in Sheyang (Liu et al., 2018b) .

Since O_3 is formed via photochemical reactions of its precursors, O_3 concentration varies significantly over seasons and different time of the day.

In Beijing, O_3 mixing ratio peaks in June with the monthly average of 38.86 ppb during the period of August 2004 to July 2005, and the lowest value was 6.23 ppb in December (An et al., 2007). Similar pattern has been observed in a different period (Dec 2012 to Nov 2013) in Beijing (Wang et al., 2014), and Shenyang (2013 to 2015) (Liu et al., 2018b). In all three studies, O_3 concentrations are positive correlated to the radiation intensities, and negative correlated to the mixing ratio of NO_X.

The diurnal pattern of O_3 in all four seasons are similar. With in a day, O_3 mixing ratios reach the peak and the minimum value in the afternoon (14.00 -

16.00) and morning (6.00 - 8.00), respectively, owing to the significant influences of photochemical production during daytime and the depletion via NO_X titration during the night ((Liu et al., 2018b; WANG et al., 2014; An et al., 2007)). NO_X levels generally displayed a pattern that is opposite to O_3.

1.2.2 Air pollution issue in China

The Ministry of Ecology and Environment (MEE) in China published the Ambient Air Quality Standard (GB-3095) (GB3095, 2012) in 2012 (Tab 1.2.1). Compared with the standard in European countries and the United States, the Chinese ambient air pollution limit is easier to meet.

However, a statistic study shows that none of the 12 monitoring sties in Beijing met the PM standards from June 2014 to May 2015 (Guo et al., 2017). O_3 concentrations exceeding the standard by 100 to 200% have been observed in China's major urban centers such as Jing-Jin-Ji, the Yangtze River delta, and the Pearl River delta Wang et al. (2017).

During 2013 to 2014, over 89 pollution days were recorded in six major cities in China (Beijing, Shijiazhuang, Xi'an, Wuhan, Shanghai and Guangzhou). There were 261 days among 301 day with valid data considered as polluted in Shijiazhuang, whereas in Beijing, it was 182 days (Hu et al., 2015). These six cities accommodates over 60 million people, so the air pollution had a huge impact.

To investigate the source and formation of urban air pollution and its impact, Chinese and the United Kingdom government established a programme: the Atmospheric Pollution and Human Health in a Developing Megacity - Beijing (APHH-China) programme. This study is embedded in the programme and the two field campaign in Beijing provided measurements for this study. The programme and campaign is introduced in section 2.2.

To improve air quality, Chinese government put great effort on reducing emissions including SO_2, NH_3 and all oxidized odd-nitrogen species (NO_Y) since 2013. By the end of 2015, the NO_Y emission is decreased by 18.6% (MEP, 2015). The PMs witness a decrease trend over most of the cities in China, especially the Beijing-Tianjin-Hebei area (BTH). However, recent national air

Standard	Unit	SO_2 hourly	NO_2 hourly	CO hourly	O_3 hourly	O_3 MDA8	PM 10 DA	PM 2.5 DA
China	ug/m^3	500	200	10000	200	160	150	75
WHO	ug/m^3		200			100	50	25
UK	ug/m^3	350	200			100	50	25
EU	ug/m^3	200				120	40	25
US	ppb		100	35000		70		

Table 1.2.1: The ambient air quality standard. MDA8 represents the maximum daily 8-hour average, and DA is the daily average.

quality monitoring report demonstrated that O_3 has overtaken PM2.5 to become the top air pollutant in summer in the major urbanized regions of China (MEP, 2015).

Silver et al. (2018) analysed the air quality monitoring data from 2015 to 2017 across the whole of China. The trends of the key pollutants are shown in Fig. 1.2.3. The concentration of the pollutants is indicated by the size of the points the left panel and the colour suggests the variation trend (blue for negative, red for positive). It is clear that O_3 shows a significant increasing trend from 2015 to 2017 in over most of China while $PM_{2.5}$ and SO_2 are decreasing. The right panel illustrates the frequency of stations against the relative trends. In 92% of the stations, the increase of annual mean O_3 MDA8 (maximun O_3 concentration in 8-hour period) exceed the median trend, which is 4.6 μg m^{-3} per year.

This increase of O_3 is likely due to the successful NO_X emission control while delayed actions in reducing VOCs emissions, which might shift the urban regions from the high-NO_X environment to the regime that O_3 is efficiently produced.

Different emission scenarios are tested in this study. In doing so, the NO_X-VOC regimes in China is better understood by analysing the change of O_3 formation. This can provide the policy maker information on efficient reduction of surface O_3.

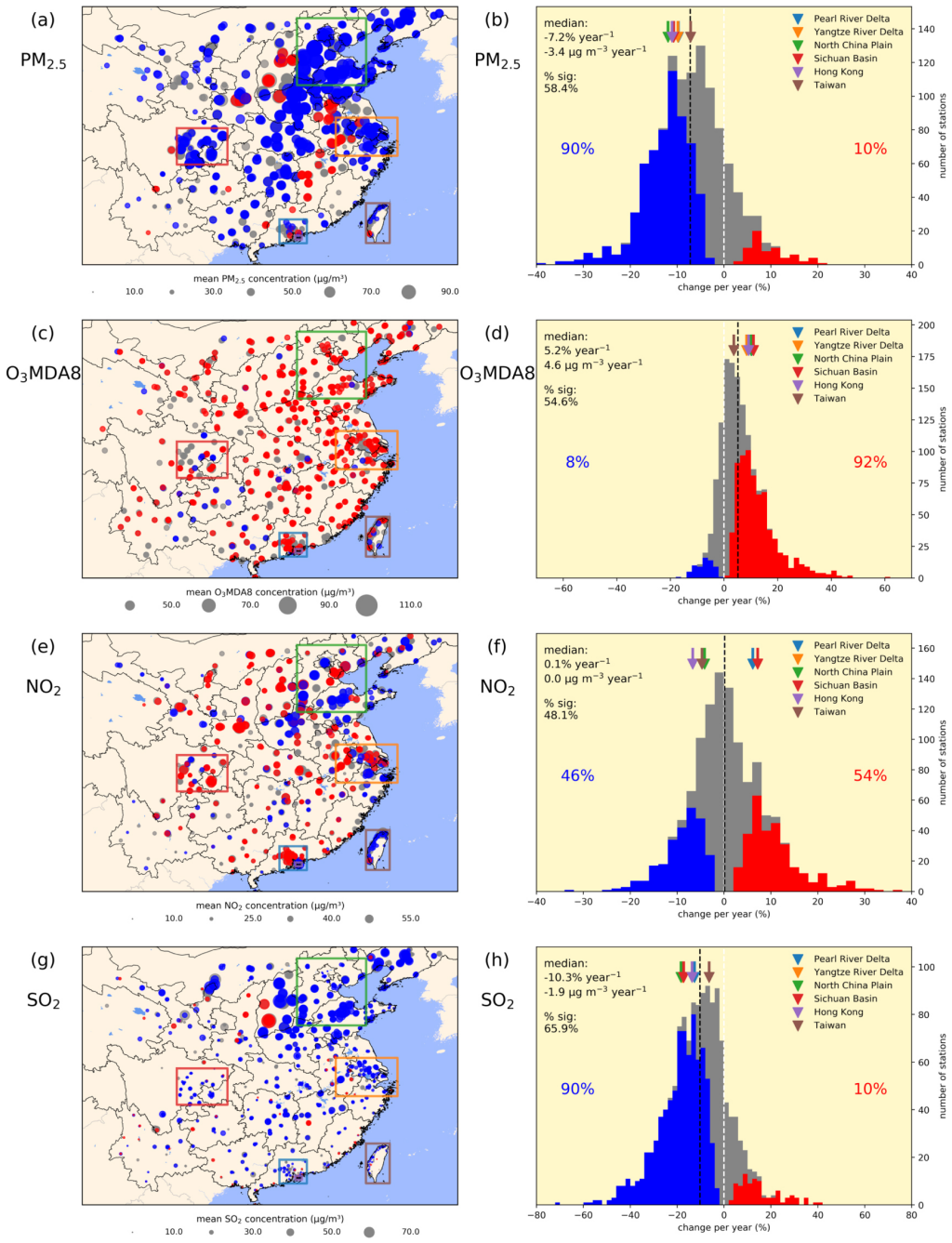

Figure 1.2.3: Concentration changes of $PM_{2.5}$ (a, b), O_3 MDA8 (c, d), NO_2 (e, f), SO_2 (g, h) across Mainland China, Hong Kong and Taiwan from 2015 to 2017. Left panels show the sign of trend (red for significant positive, blue for significant negative and grey for insignificant). The mean concentration is indicated by the size of circle. Right panels show the frequency of stations against the relative trends (Silver et al., 2018).

1.3 Overview of this thesis

1.3.1 Research aim and objectives

This thesis is an investigation of isoprene oxidation chemistry and its impact. Specifically, it aims to improve the understanding of the chemical behaviours of isoprene and INs under different NOx-VOC regimes. Also, this study aims to quantify the contribution of isoprene and INs on various tropospheric chemical systems, such as the O_3 formation, the NO_X recycling, the HO_X cycle as well as RO_2 chemistry.

To fulfill this aim, three research objectives are designed:

- **A new chemical mechanism with near explicit isoprene and IN chemistry is developed and validated with the observational data.** To reduce the computational cost, the chemical mechanisms within the chemical transport models (CTM) usually have lumped intermediates and limited reactions. These mechanisms are not adequate for studying the chemical behaviours of different IN isomers. Hence, a chemcial mechanism with more explicit and up-to-date isoprene chemistry is developed and implemented into the model. NO_X recycled by individual IN isomers can also be calculated with tagging method included in this mechanism.

- **Understand the different representations of isoprene chemistry in the model and their responses to the various NO_X-VOCs regimes.** The impact of isoprene chemistry representation is studied by comparing the simulations generated from more explicit isoprene chemical mechanism and with the original mechanism. This impact may vary in different regions of the domain, which will also be studied.

- **Quantifying the contribution of isoprene and INs to various tropospheric chemical systems is another objective of this research.** The impact of isoprene and INs can be obtained by analysing the results of different chemical treatments.

- **Study the behaviour of isoprene and INs in different NO_X and VOC regimes.** The changes of isoprene and INs chemistries under different NO_X and VOCs emission scenarios are compared. This can also

help to improve the understanding of O_3 formation mechanism, which can provide information for the O_3 control.

Structure of this thesis

This thesis is composed of 6 chapters, including one introductory chapter, one methodology chapter, three results chapters and one conclusion chapter.

- The background chemistry, overall air quality issue, the recent studies of this topic, as well as the overview of this study are included in this chapter (Chapter 1).
- Chapter 2 is named model and observations. The primary approach of this study is modelling and the fundamental tool is a modified version of the regional chemical transport model - the Weather Research and Forecasting model with coupled Chemistry (WRF-Chem). Simulations of this model are validated with the observational data. The source of the observational data, the original model system, the development of the chemical mechanism and the design of the runs are discussed in this chapter.
- By comparing the model outputs with the observational data, Chapter 3 evaluates the chemical mechanism and the model with 'base' settings. Both meteorological and chemical variables are assessed as the indicators of the ability of the model in reproducing the transport and the chemistry.
- Chapter 4 is one of the main result chapters of this study. By applying different treatments to the chemistry, this chapter evaluates the contribution of INs and isoprene chemistry to various tropospheric chemical systems including the formation of O_3 and recycling of NO_X. The differences between the two chemical mechanisms are also compared here.
- Chapter 5 includes perturbation studies with three different imaginary emission scenarios, which can provide the information for O_3 control in China.
- Chapter 6 summarises the conclusions obtained from the previous chapters and discuss the future work of this study .

2

Model and observations

In this chapter, I will introduce the modelling system, chemical mechanisms and the field measurements used in this study. This study is embedded within a joint UK/Chinese directed programme on Atmospheric Pollution and Human Health in a Chinese Megacity (APHH-China), and our team is involved in two parts: measure the individual isoprene nitrate (IN) isomers in the field, and develop and validate the chemical model to interpret the chemical fate of isoprene in China. This study focuses on modelling the chemical behaviour of isoprene and its impact and the INs was not measured by me but one of my supervisors, Graham Mills. However, to gain a better understanding of the observed data, I was involved in both field campaigns and helped with the system set-up and sample collection.

Under the APHH China programme, two field campaigns were conducted in Beijing measuring both meteorological parameters and air composition, including INs. In the campaigns, a number of individual INs have been measured in Beijing for the first time. This unique dataset, along with the observational data from other research groups in the campaign, provide valuable information on the behaviour of isoprene in different weather/emission conditions. Section 2.2 gives an overview of the APHH programme, the two field campaigns, and the data collected.

This study aims to understand the role of isoprene in secondary pollutant formation via its complex oxidation pathways. In this investigation, I modelled the atmospheric chemical and physical processes of East China with different chemical mechanisms, treatments and emission scenarios. The model adopted in this study is the Weather Research and Forecasting model coupled with Chemistry (WRF-Chem). WRF-Chem is a complex online model involving several modules. Section 2.3, section 2.4, and section 2.5 describe the model from three perspectives.

In section 2.3, the whole WRF-Chem system as a general modelling utility is introduced. However, because the default configuration of the model was not adequate for the research purpose, changes were made. Details of the model set-up and amendments to the chemical mechanism for this study are explained in section 2.4 and section 2.5, respectively. These two sections are useful to the reader, as they discuss the unique designs used to test the research questions in this study.

Section 2.6 describes the properties of runs designed in this study to interpret the isoprene chemistry and test its impact under different imaginary scenarios.

2.1 Overview of the APHH programme

2.1.1 Introduction of APHH programme

Due to the rush to industrialisation and the massive growth in motor-traffic, air quality issues in developing countries, especially China and India. Air pollution in these two countries draws great attentions from all over the world, which is not only due to the extremely high concentrations of the pollutants during the pollution episodes but also its impact on large population locally and regionally. However, the air quality issue has not been subject to the same controls that are now applied in developed countries because of the limited understanding of emission and chemical processes.

The APHH programme was therefore established to investigate the source, chemical formation of urban air pollution, as well as its impact on human health. This programme has two separate streams that focus on megacities in China (Beijing) and India (Delhi), respectively. This investigation contributes to the APHH-China programme.

The APHH-China programme is a collaboration between the UK Natural Environment Research Council (NERC), the National Science Foundation of China (NSFC), UK Medical Research Council (MRC) and UK-China Innovation Newton Fund. More than 18 universities and institutes from both countries are involved in the programme. The programme is divided into 4

themes and 5 projects:

1. Sources and emissions of air pollutants in Beijing (AIRPOLL-Beijing)
2. An integrated study of air pollution processes in Beijing (AIRPRO)
3. Air pollution impacts on the cardiopulmonary disease in Beijing: An integrated study of exposure science, toxicogenomics and environmental epidemiology (APIC-ESTEE), and Effects of air pollution on the cardiopulmonary disease in urban and peri-urban residents in Beijing (AIRLESS)
4. Integrated assessment of the emission-health-socioeconomics nexus and air pollution mitigation solutions and interventions in Beijing (INHANCE)

The first two themes focus on the emissions and the key processes that affect atmospheric pollution in the Chinese urban environment. Whereas the third theme investigates the impact of pollution on human health and economics based on the support of the first two themes. The last theme takes data collected in the theme 1-3 into consideration to develop the air pollution solutions that are cost-effective (Shi et al., 2019).

This PhD study contributes to theme 2 (AIRPRO) of the programme by improving the understanding of the interaction of isoprene and NO_X and how this impacts O_3 formation in Beijing. Meanwhile, the two field campaigns conducted in Beijing, which collect the data for themes 1 and 2, provide comprehensive information for model validation. The details of the campaigns and the measurements used in this study are discussed in the next section.

2.1.2 The field campaigns

Two field campaigns were carried out in Beijing as part of the APHH-China programme. Both campaigns have been conducted at the same locations but in different seasons. The winter campaign was from 10th Nov to 10th Dec 2016, and the measurements in summer were taken from 15th May to 22th Jun 2017. The winter campaign was shorter than the summer campaign due to a power issue at the site at the beginning of the winter campaign.

All data used in this study were collected at the Iron Tower Branch of the Institute of Atmospheric Physics, Chinese Academy of Sciences (referred as IAP

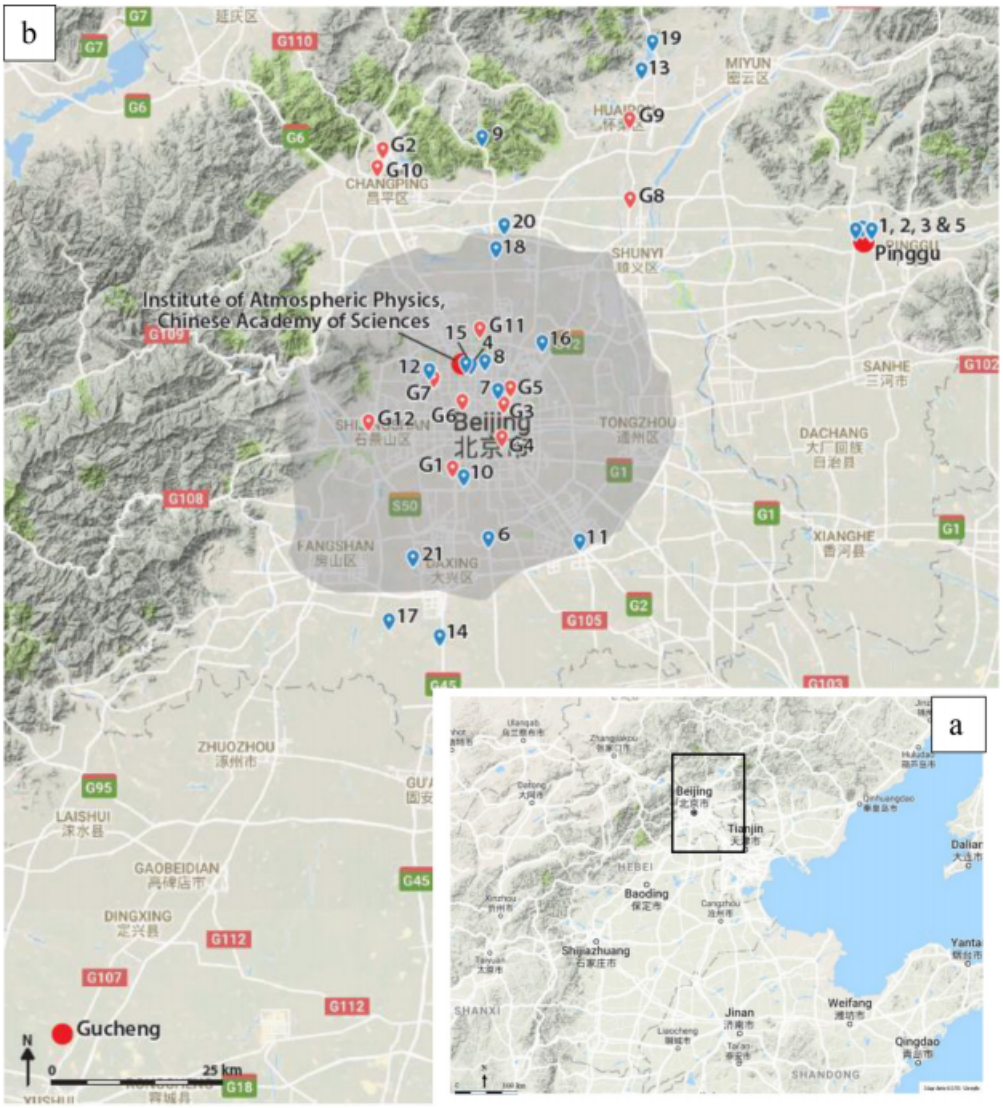

Figure 2.1.1: Study area topography of the Beijing–Tianjin–Hebei region (a) with the rectangle showing enlarged study area (b) (Shi et al., 2019). The IAP site is represented as the red dot in the middle of the map b. The red and blue symbols show the network of other measurements taken during the campaign that are not included in this study.

in the following text). The location of the IAP (39.98^o N, 116.38^o E) is indicated by the red dot in the middle of Figure 2.1.1. The IAP site is located in central Beijing in between the northern third and fourth ring roads. It is an urban site and surrounded by residential blocks with over 10 floors on average. This local feature can influence not only the emission sources and distribution but the vertical mixing at lower altitudes. The main road is approximately 100 m to the north. An overpass is about 400 m to the east of the site. The emissions from vehicles on the overpass are directly injected to the higher altitudes, which can impact the vertical distribution of the emission profile.

IAP was selected as the sampling site due to its urban location, large-capacity for taking measurements, as well as the unique 325 m meteorological tower at the site. The tower allowed measurements of vertical profiles of meteorological and chemical parameters to be made at various heights up to 320 m. The emissions of pollutants can be determined based on the flux measurements taken at 100 m platform of the tower.

Shi et al. (2019) listed the instruments deployed by the research groups during the campaigns. Researchers from eight UK institutes and six Chinese institutes were involved in the measurements at the IAP. Measurements were made for meteorological parameters, mixing ratio of gas-phase species, mass and composition of aerosols, atmospheric reactivity, and fluxes.

The observations in the campaigns provide a comprehensive record of the atmospheric characteristics in Beijing during both seasons. However, not all data have been used in this study. Section 2.2.3 introduces the observational data used in the analysis with the model outputs.

2.1.3 Campaign measurements used in this study

As introduced in the last section, a variety of data have been collected during the campaigns, and some of them are helpful in validating the model and understanding the chemical processes of particular interest to this study. These measurements are noted in Table 2.1.1 and introduced here with more details.

The meteorological data were collected by the IAP on fifteen levels of the meteorological tower (8 m, 15 m, 32 m, 47 m, 65 m, 80 m, 100 m, 120 m, 140 m, 160 m, 180 m, 200 m, 240 m, 280 m, and 320 m) as part of their routine measurements. This dataset includes key meteorological parameters, such as temperature, relative humidity, wind speed and wind direction. The planetary boundary layer height is an important parameter of vertical mixing. During the campaign, the mixing layer height is measured by the University of Reading with the ceilometer (Kotthaus and Grimmond, 2018).

Ground-level chemical tracers measured by the University of York are used in

model validation. The dataset contains mixing ratios of CO (Smith et al., 2017), NO, NO_2, O_3, gband VOCs (Hopkins et al., 2011). These species are measured with different instruments, which is shown in Table 2.1.1. OH, HO_2 and RO_2 concentrations were recorded by the University of Leeds with Fluorescence Assay by Gas Expansion (FAGE) (Whalley et al., 2010). A gas chromatography/mass spectrometry (GC-MS) based analytical system was deployed by the University of East Anglia to measure IN isomers. This GC-MS system can synthesis 5 hydroxy INs ((4,3)-IN, E/Z-(1,4)-IN and E/Z-(4,1)-IN) and 4 aldehydic INs (E/Z-(1,4)-al-IN and E/Z-(4,1)-al-IN) at the same time in the lab (Mills et al., 2016), while the (1,2)-IN can be measured with direct injection. However, E/Z-(1,4)-IN and E/Z-(4,1)-IN were not able to be identified in the campaign because there were too many nitrated compounds in the atmosphere.

The concentration of key pollutants (CO, NO, NO_2, SO_2, PM_1, $PM_{2.5}$ and PM_{10}) were recorded at six platforms of the meteorological tower (8 m, 32 m, 100 m, 160 m, 260 m, and 320 m) by the Sensor Network for Air Quality (SNAQ) boxes (Popoola et al., 2018). This dataset allows me to compare the modelled and observed vertical profiles of some gas tracers.

In addition to the concentration of the chemical tracers, the flux of CO (Gerbig et al., 1999) and NO_X (Vaughan et al., 2016) were analysed by the University of York, and the VOCs fluxes (Huang et al., 2016) were measured by Lancaster University. These flux measurements were taken at about 100 m above the ground, which can represent the emissions below.

Parameters	Category	Instruments	Institutes	Location	Reference
Wind speed; direction; T; RH	Meteorology		IAP	Tower (15 heights)	
Mixing layer height	Meteorology	Vaisala CL31 ALC ceilometer	Reading	Ground	Kotthaus and Grimmond (2018a)
C2 to C7 VOCs and oVOCs	Gases	DC-GC-FID	York	Ground	Hopkins et al. (2011)
NO	Gases	TEI 42i	York	Ground	
NO2	Gases	Teledyne CAPS	York	Ground	
O3	Gases	TEI 49i	York	Ground	
SO2	Gases	TEI 43i	York	Ground	
CO	Gases	Sensor box	York	Ground	Smith et al. (2017)
OH; HO2; RO2	Gases	FAGE	Leeds	Ground	Whalley et al. (2010)
Organic nitrates	Gases	GC-MS	East Anglia	Ground	Mills et al. (2016)
CO; NO; NO2; SO2	Gases	SNAQ boxes	Cambridge	Tower (6 heights)	Popoola et al. (2018)
NOx fluxes	Flux	Fast NOx	York	Ground	Vaughan et al. (2016)
CO fluxes	Flux	AL5002 CO analyser	York	Ground	Gerbig et al. (1999)
VOC fluxes	Flux	PTR-TOF-MS	Lancaster	Ground	Huang et al. (2016)

Table 2.1.1: The list of the campaign measurements used in this study.

2.2 Overview of WRF-Chem

The modelling system used in this study is the Weather Research and Forecasting model with coupled Chemistry (WRF-Chem system), version 3.8.1. This version was released in August 2016 by the National Center for Atmospheric Research (NCAR) and University Corporation for Atmospheric Research (UCAR), USA. WRF-Chem is a community model developed by Grell et al. (2005), and has been improved, evaluated and applied by many users and organisations all around the world (Zhang, 2010).

WRF-Chem is a 3-dimensional modelling system which can simulate major atmospheric feedbacks between meteorology, gas phase chemistry, aerosol, and radiation. As a modelling system, WRF-Chem system consists of three main components, which are 1) WRF Pre-Processing System (WPS), 2)Weather Research and Forecasting model (WRF) and 3) chemistry module. Figure 2.2.1 shows the basic structure and data flows within the model system.

WPS processes the geographical information of the selected domain and re-grids the meteorological data according to the domain configuration giving *'met files'*. These met files, along with the chemical initial conditions (IC) and boundary conditions (BC), are used by the *real* program to produce input and boundary files for the main model. The model core (*wrf.exe*) then can output simulations with provided emission information.

In this section, I provide more details on WRF-Chem modelling system, including WPS, WRF-Chem and the Kinetic Pre-Processor (KPP) components, which are the key components to modify and run the model.

2.2.1 WRF Pre-Processing System (WPS)

WPS is used to prepare the input files for the *real* program, which is designed for real-data simulations such as this study. There are three utilities (*geogrid, ungrib*, and *metgrid*) inside WPS which perform different stages of the pre-processing work with the input data and set-up conditions provided by the user.

The *geogrid* utility reads in the list of domain parameters specified by the user

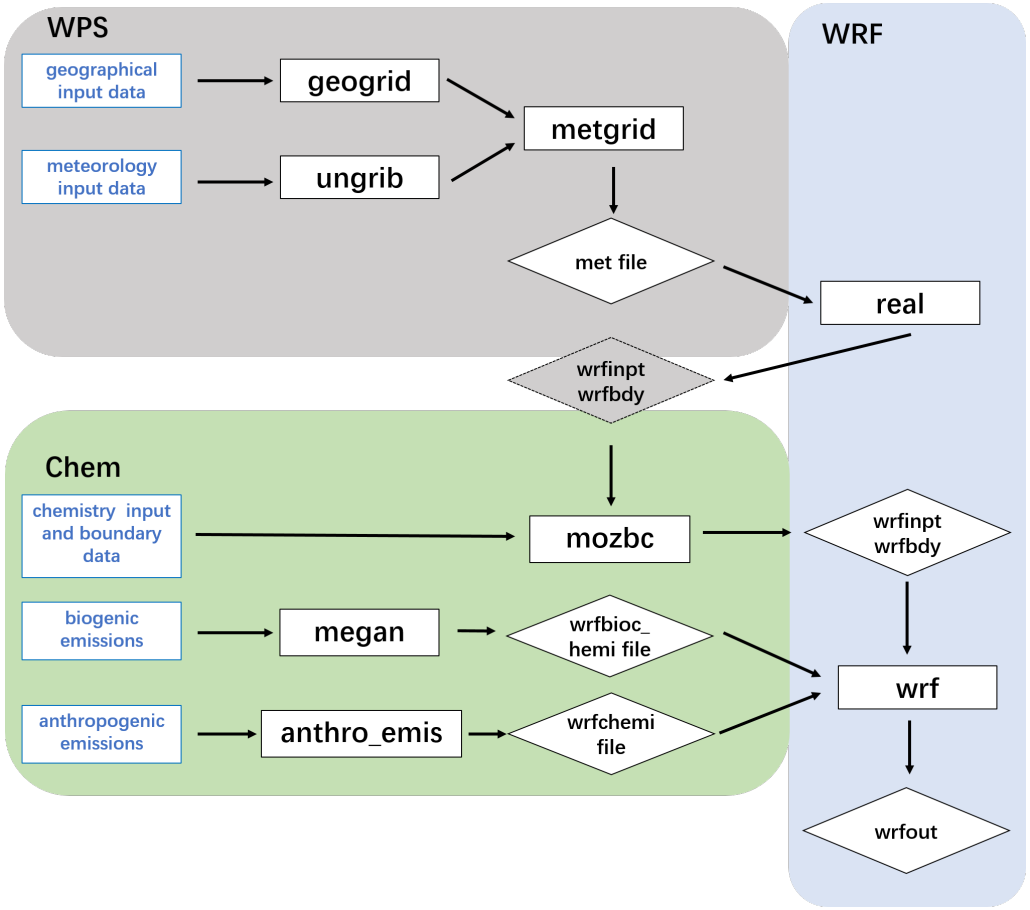

Figure 2.2.1: The flow chart of WRF-Chem modelling system. The modelling system includes three components: WPS, WRF and Chem corresponding to gray, blue and green parts in the figure. The diamond boxes are the input files/information read by WRF-Chem and the output generated by the model, whereas the black rectangular boxes represent the utilities. The data used to produce the input files are coloured in blue.

in *namelist.wps* and calculates the size of the domain and the coordinates of each grid box. This program also interpolates multiple terrestrial datasets (soil categories, annual mean deep soil temperature, land-use types, monthly vegetation fractions, monthly albedo, slope category, etc.) to the model grid. The *geo_em.d0X.nc* files are created after running this program, where X is the index of the domain.

In addition, the *real* program needs meteorological data to determine the initial and boundary meteorological conditions. These datasets used in WRF-Chem are usually generated from lower resolution global climate models. However, the output datasets of the climates models are in a compact format (GRIB files) containing a great number of variables. Hence, the *ungrib* program has been developed to 'un-grib' the files, extract meteorological fields and rewrite them

into a simple format. Since the GRIB files typically include more meteorological fields than are needed for *real*, *ungrib* selects the needed fields according to a variable table, which is called 'Vtable'. The Vtable used in this investigation is provided by the European Centre for Medium-Range Weather Forecasts (ECMWF).

The last step of the pre-processing used *metgrid* to interpolate the meteorological fields prepared by *ungrib* to the grids defined by *geogrid*, generating the *met files* that contain both meteorological and geographic information. This interpolation only occurs in the horizontal directions. The interpolation of meteorological fields to vertical levels is done by the *real* program. Since the meteorological information is time-dependent, *metgrid* also needs to read in the date ranges from the *namelist.wps* file to interpolate the meteorological data to the right period.

The WPS only processes the meteorological and geographic information needed by WRF-Chem and does not include any utilities to process the chemical situation. The IC and BC for chemistry is performed by *real* and *mozbc*.

These two utilities are introduced in the next section and the data used for meteorological and chemical IC and BC are discussed in Section 2.4.4.

2.2.2 WRF-Chem

The WRF-Chem model contains two components: the WRF model and the chemistry module.

The WRF model is an online nonhydrostatic model developed by Grell et al. (2005). The model is designed to be a flexible and advanced atmospheric simulation system that is efficient for its parallel processing platforms. In this study, the model has been run with 64 processors. WRF has two dynamical cores, which are the Advanced Research WRF (ARW) and Nonhydrostatic Mesoscale Model (NMM). The Advanced Research WRF dynamic solver is used for all simulations.

WRF works on a grid basis. Different variables are calculated within and/or at the edges of the grid box, which allows the model to produce mixing between

grids in both the horizontal and vertical dimensions. The vertical coordinate of WRF is a terrain-following hydrostatic pressure coordinate. Within the grids, Runge-Kutta 2nd and 3rd order time integration schemes, as well as the 2nd to 6th order advection schemes are applied.

The WRF model code contains an initialization program (*real.exe*), a numerical integration program (*wrf.exe*), one-way nesting program (*ndown.exe*), and a program specially for simulating tropical storm (*tc.exe*). All programs except *tc.exe* program are used in this study.

Although WRF is a complex model with thousands of lines stored in hundreds of files, all variables are defined in series of text files called registry. With the registry, users are able to control the fundamental structure of the model data efficiently. All variables in the registry are assigned with an attribute describing the dimensions, the solvers, association with WRF I/O streams, communication operations, and runtime configuration options. The changes made in the registry will automatically be passed to the locations in the source code when the model is recompiled. The registry needs to be modified to implement a chemical mechanism into the model. This is discussed in detail in the section 2.5.3.

The chemistry program provides chemical information needed for WRF to simulate a variety of chemicals. The chemistry module consists of emissions (*biogenic emissions*, *anthropogenic emissions*, *fire emissions*, etc.), chemical mechanisms (*gas-phase chemical mechanisms* and *aerosol schemes*), and chemical processors (*photolysis schemes*, *dry deposition*, *aerosol feedbacks*, etc.).

As illustrated in the flow chart (Fig. 2.2.1), the *real* utility in WRF reads in the *met files* prepared by WPS and generates the *wrfinput* and *wrfbdy* files, which have the IC and BC information of the meteorology. The *wrfinput* and *wrfbdy* files are then rewritten by the *mozbc* utility, which adds the IC and BC of the chemical species into these files. Biogenic and anthropogenic emissions are processed by the *Model of Emissions of Gases and Aerosols from Nature (MEGAN)* and the *anthro_emiss* utilities. Once all the pre-processes (generating *wrfinput*, *wrfbdy* and the emission files) are complete, outputs can be computed from the *wrf* executable. Both meteorological and chemical variables are calculated in *wrf.exe*, which is controlled by a namelist. This namelist controls the runtime, domain, physical and chemical options.

Meteorological and chemical variables are calculated with the same vertical and horizontal coordinates and the same physics parametrizations, so no interpolation is needed. The advantage of this online model is that it can simulate the interactions between the meteorology and the chemistry. Some meteorological parameters such as temperature, humidity, and mixing can perturb the concentrations of the chemicals, and the aerosol simulations also feedback on the meteorology.

2.2.3 The Kinetic Pre-Processor (KPP)

As mentioned briefly in the last section, the main body of WRF-Chem is made up of a number of hard-coded files, which make locating and modifying the files an extremely time consuming job. However, in order to understand the chemical simulations, WRF-Chem users offten wish to make changes on the mechanisms. Therefore, the Kinetic Pre-Processor (KPP) is implemented in the model for modifying the chemistry.

KPP is a program that reads in the text format of the chemical reactions and the reaction rate files and produces the code for the chemical solver in the model (Damian et al., 2002). By using KPP, users are able to modify the chemical mechanism safely and efficiently with no need to rewrite the hard-coded files in the solver.

The KPP coupled with the WRF-Chem (v 3.8.1) is the KPP Version 2.1, which processes the gas-phase chemical mechanisms. This utility is compiled automatically with the compilation of the model and generates the code for the solver according to the *registry.chem* file and the input text files. That is to say, the chemical reactions can be added in/modified easily in the addition of KPP rather than in the main WRF-Chem body. As a result, the effort for the developer to construct new mechanisms and for users to make amendments is reduced significantly . All gas-phase chemical mechanisms in WRF have a KPP version that can be edited. Also, users can develop new chemical mechanisms. In this investigation, I implemented a new chemical mechanism with KPP. The implementation work is discussed in section 2.5.3.

2.3 Model configuration in this study

The details of the model set-up used in this project is described in this section. WRF-Chem is a complex modelling utility that provides various of options for reading the emissions, calculating parameters and even running. The term 'WRF-Chem' mentioned in the previous section (section 2.3) represents the original computing utilities, which are the packages available online to all users without any parametrization. But for the rest of the document, including this section, I refer to the whole modelling system specially designed for this study as WRF-Chem. The development of this system includes elements such as domain configuration, physics and dynamic options selection, emissions, initial

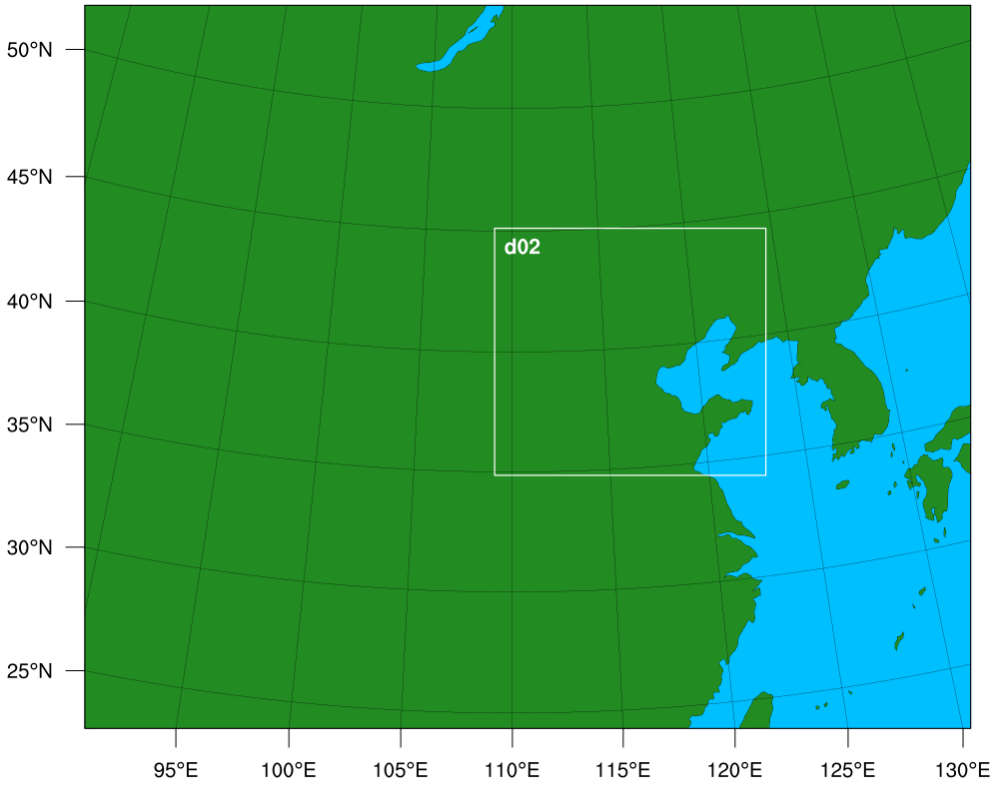

Figure 2.3.1: The map of the domains used. Domain 1 is the parent domain over east China with the 27 km resolution. Domain 2 is the nested domain over NCP with a resolution of 9 km.

and boundary conditions treatments and nesting and nudging.

2.3.1 Domain selection

The first thing in running WRF-Chem is to define the modelling area. The domain set-up in this study is suggested by Jie Li, one of our collaborators in IAP. Li and his group are experienced in simulating meteorology of east China with WRF in their research, and after comparing with different set-ups, they have been using this domain configuration continuously. Since this investigation focuses on the same area as Li's, the same domain configuration is applied. Using this domain also minimizes the variations of the underlying geographic features in results comparison.

Fig. 2.3.1 shows the two domains in this investigation. As shown in the figure,

domain 1 is the parent domain, and domain 2 is the nested domain. WRF-Chem is able to simulate nested domains, and this capability is exploited in this study. The nested domains not only have the finer spatial grids but also have higher temporal resolutions.

The outermost domain (referred as parent domain or domain 1) covers a large area of east China, as well as some regions in Russia, Japan, Kazakhstan, India and Myanmar, and the whole of Mongolia, South Korea and North Korea. The parent domain is made of 147 east-west direction boxes and 120 north-south direction boxes with a resolution of 27 km. The west of China is not included in the parent to avoid putting the Himalayas on the edge of the domain. Complicated geographic patterns at the boundaries are likely to affect the stability and performance of the model.

Domain 2 is the two nested domain which cover a section of the parent domain but with higher resolutions. The nesting ratio is 3, which means the size of grid boxes in domain 2 is 9×9 km. Domain 2 sits on the North China Plain (NCP) where the main heavy industrial parks are located. The performance of the model can often be improved by running the high-resolution nested domain, as it can capture the meteorological and chemical events on a smaller scale. One-way nesting is adopted in this study to reduce the computional cost. The detailed nesting method is discussed in the section 2.4.5.

The geographical input data were downloaded from UCAR with the resolution of 30 s and 2 min corresponding to 30-arc-second (14 km) data and 2-minute data (56 km) for the nested domain and the parent domain. Both datasets include 21 land use categories from MODIS IGBP category. As mentioned in section 2.3.1, the static geographical data are then interpolated by the *gergrid* program to the grids.

2.3.2 Physics and dynamics

WRF offers multiple physics and dynamics options that can be combined in a variety ways. The options range from the simple and efficient, to the sophisticated and more computationally expensive, and from the well-tested schemes, to newly developed schemes. The performance of the model in simulating the meteorology depends on the selection of the schemes. Since the

Table 2.3.1: The physics and dynamics schemes selected in the model.

Variable Names	Input Option	Description
mp_physics	2	microphysics: Lin et al. Scheme (1983)
ra_lw_physics	4	longwave radiation: RRTMG scheme (2008)
ra_sw_physics	2	shortwave radiation: Goddard shortwave scheme (1994)
sf_sfclay_physics	1	surface layer option: Revised MM5 Monin-Obukhov scheme
sf_surface_physics	2	land-surface option: unified Noah land-surface model
sf_urban_physics	1	urban option: Single-layer Urban Canopy Model
bl_pbl_physics	1	boundary layer option: YSU scheme (2006)
cu_physics	3	cumulus parameterization option: Grell-Freitas ensemble scheme (2013)
dif_opt	1	turbulence and mixing option: evaluates 2nd order diffusion term on coordinate surfaces
km_opt	4	horizontal Smagorinsky first order closure
w_damping	1	with vertical velocity damping

local geographic features can affect the physical and dynamical processes in the atmosphere, the performance of the same parameterization varies significantly in different regions.

However, since this study aims to understand the isoprene chemistry, it is not my primary focus to investigate the best combination of the schemes, as long as the model generates meteorological field that allow a reasonable simulation of the mixing and transport of the chemical species.

Table 2.3.1 lists schemes selected for the physics and dynamics. This combination is recommended by Jie Li, who has been working with WRF on the northern China plain for years. Similar parameterization was chosen for researches in China (Ansari et al., 2019; Wang et al., 2016; Tie et al., 2013). In Section 3.2, I assess the model's skill in reproducing the meteorological observations and found that in general, this parameterization is sufficient for the purposes of the investigation.

Radiation schemes include long and short radiation providing not only atmospheric temperature tendency profile but also surface radiative fluxes. The RRTMG longwave radiation scheme and the Goddard shortwave radiation scheme are chosen due to the better compatibility in running ARW core with Chem (Iacono et al., 2008).

The surface condition in the studying area is complex including plain urban region and mountainous rural areas. To minimize the inaccuracy associated with the surface conditions, Noah land-surface scheme and YSU boundary layer scheme are applied in this study.

2.3.3 Emissions

As suggested in the WRF-Chem flowchart (Fig. 2.2.1), the model needs to be fed with biogenic and anthropogenic emissions before running. The anthropogenic emissions are generated by the *anthro_emiss* program, while the biogenic emissions are calculated online with the *MEGAN* model coupled to WRF-Chem.

Multi-resolution Emission Inventory of China (MEIC) and Emission Database for Global Atmospheric Research (EDGAR) emission datasets are used to generate the anthropogenic emission files (*wrfchemi*) for WRF-Chem. The MEIC inventory provides the emissions for China with high resolutions (0.25^o) (Li et al., 2017). The MEIC 2013 version (Qi et al., 2017) is used in this study with the resolution of 27 km and downscaled 9 km provided by Qiang Zhang's group in Tsinghua University. Emissions from five sectiors (agriculture, industry, residential, transportation and power) are considered for all main primary pollutants including SO_2, CO, NH_3, NO_2, NO, PM2.5, PM10, and VOCs. Since MEIC contains the emissions for China only, EDGAR HTAP v2 emission inventory is select to fill the area outside China within the domain.

Biogenic emissions are calculated by the Model of Emissions of Gases and Aerosols from Nature version 2.1 (MEGAN 2), which is developed by Guenther et al. (2006). MEGAN 2 is an online model coupled with WRF-Chem that can simulate the emissions of 134 species with a fine resolution of 1 km^2. Isoprene,

monoterpenes, oxygenated compounds, sesquiterpenes, NO, NO_2, CO, SO_2 and NH_3 emissions from nature are included.

Equation 2.3.1) shows the framework of the biogenic emission calculation. Emission is calculated as the product of the emssion factor (ε), canopy factor (γ_{CE}), leaf age factor (γ_{age}), soil moisture factor (γ_{SM}) and loss and production within plant canopy (ρ).

$$Emission = \varepsilon \cdot \gamma_{CE} \cdot \gamma_{age} \cdot \gamma_{SM} \cdot \rho \tag{2.3.1}$$

The emission factor (ε) represents the emission of the species under the standard condition, and the normalized ratios (γ) are the variations of emission due to deviations from standard conditions. These factors are affected by the landuse data, weather, and atmospheric chemical composition. An input file (*wrfbiochemi* file) is generated for each domain using the *Megan_bio_emiss* utility and the landuse data. During the simulation, the *wrfbiochemi* file passes parameters for γ calculations to MEGAN 2, so it can calculate the biogenic emissions based on the meteorological field that is run by WRF at the sametime.

In this study, sensitivity tests were conducted for different isoprene emission conditions. Factors (0 and 1.5) were applied in MEGAN 2. Detailed codes are included in chapter 4 and 5.

The fire emissions were calculated from the Fire INventory from NCAR version 1 (FINN v1). This dataset offers daily emissions of trace gas and particle from open burning of biomass with a resolution of 1 km^2. The *fire_emiss* software reads in the domain information and the data from inventory generating the daily fire emission files for the model.

2.3.4 Initial and boundary conditions

Before running *wrf*, meteorological and chemical initial and boundary conditions need to be defined. The meteorological IC and BC are defined in the *wrfinput* and *wrfbdy* files generated by *real.exe* with the provided meteorological information (Fig. 2.2.1). The meteorological informations are provided by ERA-Interim reanalysis data. The ERA-Interim is a global atmospheric

reanalysis dataset with the spatial resolution of 0.75^o (∼80 km). 60 vertical levels are included in the dataset from the ground level to 0.1 hPa in the atmosphere. This dataset dates back to 1979 and has been continuously updated to present days. The frequency of ERA-Interim data is every 6 hours, offering reanalysed data at 0.00, 6.00, 12.00 and 18.00 (UTC).

Mozbc has been developed by the Atmospheric Chemistry Observations and Modeling Lab (ACOM) of NCAR, specially for processing the chemical IC and BC for all species. *Mozbc* reads in the *wrfinput* and *wrfbdy* files along with the output from the global chemical model (Model for Ozone and Related chemical Tracers version 4 (MOZART-4)), and writes the chemical information to the *wrfinput* and *wrfbdy* files.

2.3.5 Nudging and nesting

Although the boundary conditions are updated throughout the running period, the uncertainties in the meteorology accumulate with time in the simulations. There are two potential solutions to this issue: re-initialising the model, and nudging the results with the reanalysis data. Compared to simulation with no treatment, results of both approaches show better agreement with the observations and the improvements between the two treatments are similar. However, re-initialisation requires to stop the simulation for every 3 to 7 days, which is less efficient. Hence nudging is adopted in this study. The meteorological parameters are nudged with reanalysis ERA-Interim data for every 6 hours.

As introduced in the section 2.4.1, simulations of the nested domains are generated for the selected period. The nested domain runs as separate models with the necessary initial and boundary conditions provided by the parent domain. There are two method of nesting, which are 1) running the nested domain concurrently with the parent, or 2) running the nested domain with the information from the pre-generated parent simulations. The first method allows feedbacks from the nested to the parent domain, so it is called two-way nesting. Whereas, in one-way nesting (method 2), no information from the nested is read in when the simulations of the parent domain are generated.

One-way nesting is employed in this study, which is an approach that is able to fulfil the research objects with a lower computational cost. The two-way

nesting takes 20 mins to generate 1-hour outputs of both domains while the one-way nesting only needs 8 minutes. Simulations of parent and nested domains generated with the two nesting methods show very similar values in a 3-day test. Also, the nested domain does not need to cover the whole running period as the parent. Therefore the one-way nesting is more suitable for this investigation. Nested domains have been run for the selected periods (16th to 25th May, 9th to 15th June and 19th to 23rd June, 2017) due to its high computational cost (2 hour for running one day and about 45 Gb to store).

2.4 Development of the mechanism used in this study

To reduce the computational cost, isoprene nitrates are lumped in most of the tropospheric chemical mechanisms in regional CTMs. Lumping nitrates and intermediates can reproduce the atmospheric compositions with considerably lower computing cost. However, the focus of this investigation is not only on air quality modelling but also on improving the understanding of detail isoprene chemistry and its impact. Hence, a new mechanism, which includes explicit isoprene oxidation chemistry, is developed for this study.

The new mechanism is named MOZART-MIM2-MCM-MOSAIC-4bin-aq (M4) mechanism. As indicated in the name, the M4 mechanism is developed mainly based on MOZART-Mosaic-4bin-aq (MOZART-4), and Mainz Isoprene Mechanism 2 (MIM2) mechanism. To split some lumped hydroxyl INs in MIM2, some reactions are implemented from the Master Chemical Mechanism (MCM) version 3.3.1. In total, six hydroxyl INs and one aldehydic IN are added to the M4 mechanism.

The mechanisms in WRF-Chem are described in section 2.5.1, the M4 mechanism development in section 2.5.2 and modification made to implement the M4 mechanism into WRF-Chem in section 2.5.3.

2.4.1 Chemical mechanisms coupled with WRF

The chemical mechanism in WRF-Chem consists of gas phase chemical modules and aerosol modules. WRF-chem version 3.8.1 offers eight gas phase chemical mechanism options and five aerosol schemes. The selection of the two modules is not mix-and-match, for instance, MOZART and CRIMECH gas phase

mechanism only work with the Mosaic aerosol scheme.

The eight gas phase chemical mechanisms are: 1) Regional Acid Deposition Model version 2 (RADM2), 2) Regional Atmospheric Chemistry Mechanism (RACM), 3) Carbon Bond Mechanism (CB-4), 4) Carbon-Bond Mechanism version Z (CBM-Z), 5) Statewide Air Pollution Research Center (SAPRC-99), 6) Model of Ozone and Related Chemical Tracers (MOZART), 7) Nonmethane Hydrocarbons Chemistry (NMHC9), and 8) Common Representative Intermediates MECHanism (CRIMECH).

The five aerosol schemes include: 1) the Modal Aerosol Dynamics Model for Europe (MADE/SORGAM), 2) the Modal Aerosol Dynamics Model for Europe with the Volitity Basis Set aerosols (MADE/VBS), 3) the Modal Aerosol Module (MAM) coupled to the CAM5 physics, 4) the Model for Simulating Aerosol Interactions and Chemistry (MOSAIC), and 5) a bulk aerosol module from GOCART.

Table 2.4.1 gives the number of species and reactions for each mechanism, along with with the number of isoprene related reactions. The MOZART chemical mechanism is selected for various reasons.

Firstly, MOZART is a more up-to-date mechanism designed for ozone simulation purposes. One primary principle of the MOZART mechanism development is to reproduce the chemistry of ozone and its precursors (Emmons et al., 2010). This principle also agrees with the objectives of this study. Also, MOZART includes 12 essential isoprene oxidant products and 43 reactions, which gives a reasonable representation of isoprene chemistry.

Moreover, MOZART in WRF-Chem is widely used and tested, so it is unlikely to have fundamental errors. Researchers have also created and shared utilities for running this mechanism in WRF-Chem. Thanks to the effort by previous researchers, MOZART can be run smoothly and with confidence. The MOSAIC aerosol scheme is therefore selected as it is the only aerosol scheme that works with the MOZART mechanism.

Table 2.4.1: The list of gas-phase chemical mechanisms in WRF-Chem.

Mechanism	Number of reactants	Number of reactions	Number of isoprene reactions	Reference
RADM2	59	157	3	(Stockwell et al., 1990)
RACM	73	237	12	(Stockwell et al., 1997)
CB-4	55	156	10	(Gery et al., 1989)
CBMZ	56	136	10	(Zaveri and Peters, 1999)
SAPRC-99	79	235	22	(Carter, 2000)
MOZART	81	197	43	(Emmons et al., 2010)
NMHC9	60	145	21	
CRIMECH	232	638		(Jenkin et al., 2008)

2.4.2 The chemical mechanism developed for this study

As mentioned in the previous sections, the isoprene chemistry in the current WRF-Chem chemical mechanisms is not explicit enough to fulfil the research purpose of this investigation. The M4 mechanism is therefore developed and implemented into the model.

The M4 mechanism is an expansion of the MOZART gas phase chemistry coupled with MOSAIC aerosol scheme that uses 4 sectional aerosol bins and includes aqueous phase chemistry. The full mechanisms are included in the Appendix A In the gas phase, the whole isoprene chemistry is replaced by the reactions in the MIM2 mechanism. Since SOA is calculated directly from isoprene in MOSAIC, no modifications are made in the aerosol scheme.

Fig. 2.4.1 illustrates the isoprene chemistry in the MOZART mechanism. Isoprene can be oxidised in three pathways, which are initiated by OH, O_3 and NO_3. Reactions in all pathways have been replaced with the chemical processes in MIM2 and MCM. In total, 61 new species and 188 reactions has been implemented in the MOZART chemical mechanism (Appendix A). Here I

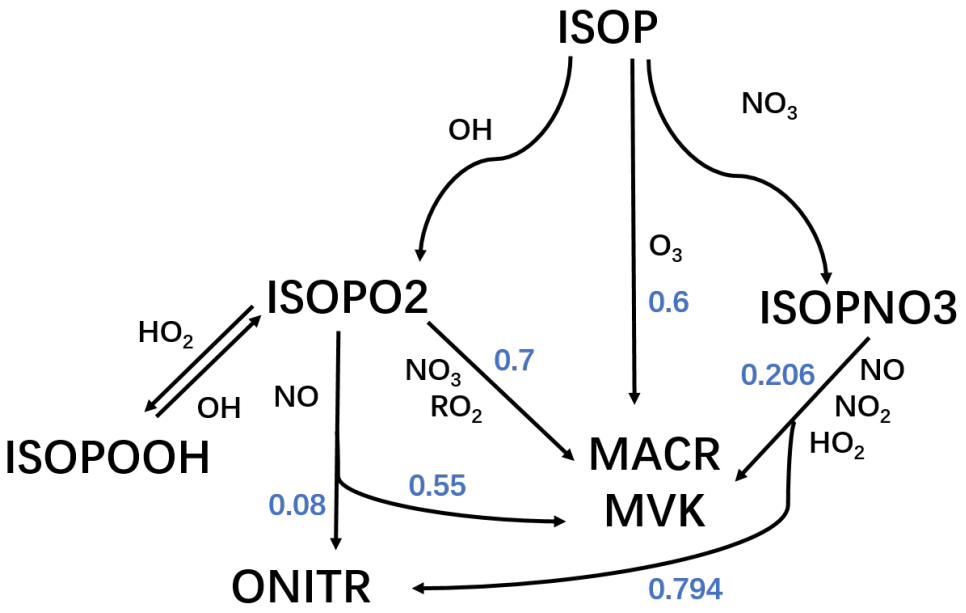

Figure 2.4.1: The isoprene chemistry in the MOZART mechanism. The branching ratios of each reaction are indicated in blue.

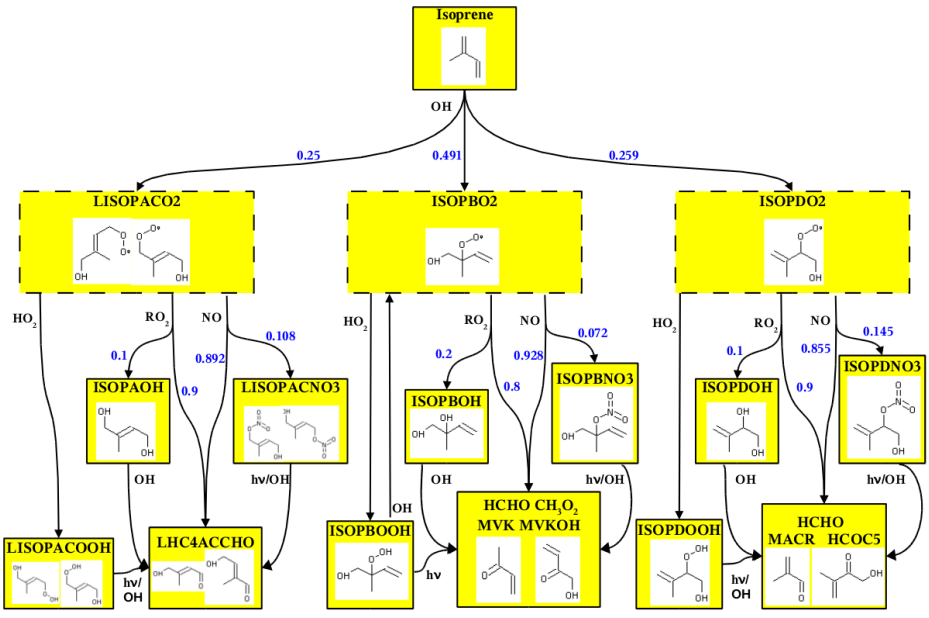

Figure 2.4.2: The OH-addition pathway in MIM2. The three short-lived peroxy radicals from isoprene are delimited by dashed lines. The branching ratios of each reaction are indicated in light blue (Taraborrelli et al., 2009).

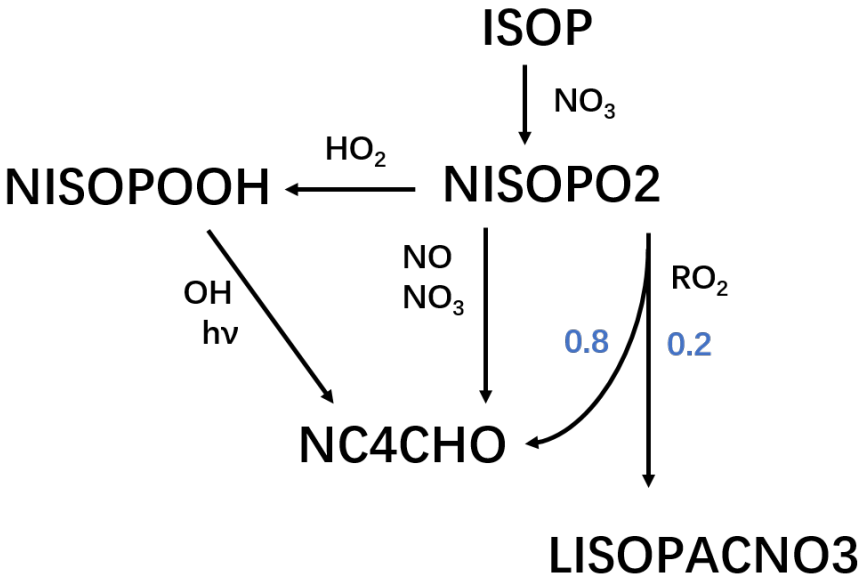

Figure 2.4.3: The NO_3-addition pathway in MIM2. The branching ratios of each reaction are indicated in light blue.

discuss the modifications made in different pathways.

In MOZART, one hydroxyl peroxy radical (ISOPO2) is formed by isoprene-OH reaction during the daytime. ISOPO2 can react with NO rapidly producing the lumped isoprene nitrate (ONITR) with a fraction of 0.08 (Fig. 2.4.1). Two other products of ISOPO2 reactions are the hydroperoxide (ISOPOOH) and the carbonyls (methacrolein (MACR) and methyl vinyl ketone (MVK)) that are the products of ISOPO2-HO_2 reactions and ISOPO2-NO_Y/RO_2 reactions. The OH-initiated chemistry in MIM2 is more complex than in MOZART (Fig. 2.4.2). MIM splits the lumped ISOPO2 into three radicals: LISOPACO2, ISOPBO2, and ISOPDO2, which are lumped E/Z-(1,4)-ISOPO2 and E/Z-(4,1)-ISOPO2 (LISOPACO2), (1,2)-ISOPO2 (ISOPBO2) and (4,3)-ISOPO2 (ISOPDO2).

Although the three peroxy radicals react with similar reactants, their reaction rates are different, as well as the structure of the products. As a result, more carbonyls, hydroperoxides, diols, and nitrates have been included. As shown in the flow diagram (Fig. 2.4.2), three isoprene nitrate isomers are formed in MIM2. The ISOPBNO3, ISOPDNO3, and LISOPACNO3 in MIM2 correspond to the (1,2)-IN, (4,3)-IN, and the lumped E/Z-(1,4)-IN and E/Z-(4,1)-IN isomers. Since this investigation aims to understand the behaviour of individual

IN isomers, the lumped LISOPACNO3 is split into ISOPAENO3, ISOPAZNO3, ISOPCENO3, and ISOPCZNO3 in the ratio of 3:12:1:7. The ratio is calculated according to the reactions in the Master Chemical Mechanism v3.3.1 (MCM). Hence, the model is able to simulate six hy-IN isomers with the M4 mechanism.

At night, NO_3 is the primary oxidant for isoprene producing another peroxy radical (ISOPNO3 in MOZART, and named NISOPO2 in MIM2, referred as ISOPNO3 in the following text). In MOZART, this peroxy radical can react with three species: NO, NO_3 and HO_2 forming an IN and carbonyls (Fig. 2.4.1). Since ISOPNO3 contains a nitrate functional group, IN is produced with significantly higher branching ratio (0.794) for all three reactions. The products of these three reactions are similar in MOZART, which is not true in MIM2 (Fig. 2.4.3). In MIM2, the aldehydic nitrate (NC4CHO) is the only product of the reactions of ISOPNO3 and NO/NO_3. Unlike MOZART mechanism, a hydroperoxide (NISOPOOH) is formed from the ISOPNO3-HO_2 reaction.

Although NISOPOOH can be converted to the nitrate by reacting with OH or photochemical processes, no NC4CHO can be formed during the night in this pathway. In addition, unlike MOZART, MIM2 also includes the reaction of ISOPNO3 with RO_2, which leads to the formation of a hydroxyl nitrate (LISOPACNO3) with a factor of 0.2. According to MCM, the composition of LISOPACNO3 produced during the night is different from the constituent of the lumped hydroxyl nitrates at daytime. Here, the night-time LISOPACNO3 consists of two hydroxyl IN isomers: ISOPCENO3 and ISOPCZNO3. The yield between the two nitrates is set at 1:7, which is the same as the ratio of OH-initiated pathway.

No isoprene nitrates are formed in the O_3 initiated pathway in both mechanisms. More intermediates are generated in ozonolysis of isoprene in MIM2, whereas in MOZART only MVK, MACR and MCO3 are the products in the O_3 reaction.

The equation file of the M4 and MOZART chemical mechanisms are attached in the Appendix A.

2.4.3 Modifications to implement the new mechanism

The M4 has been successfully implemented into WRF-Chem with Kinetic PreProcessor (KPP). Many files have been modified during the implementation, and here I discuss the edits I made in order to incorporate the new chemical mechanism.

Implementing the new mechanism included adding new species and reactions, and calculating additional photolysis and depositions rates, and specifying emissions. However, since the M4 mechanism is based on the MOZART mechanism with more explicit representation of isoprene chemistry only, all addtional species are the intermediate species from isoprene oxidation, which are relatively short-lived and have no direct emissions. As a result, no changes were made to IC and BC, or to emissions for the implementation of M4 mechanism. The modules of WRF which related to physical and dynamic simulations are have been untouched.

A mechanism is implemented into WRF-Chem with following basic steps:

- edit the **registry** to add species to the chem array structure
- create a package in **KPP** and provide input files (species file, equation file, definition file, kpp file, etc.) under the package directory
- modify the hard-coded **chemistry drivers** to call the suitable subroutines when the mechanism is selected
- recompile the model

The registry is a series of text files that define all variables involved in the WRF-Chem modelling system including the variables are or can be used in the initial, boundary, emissions, history, or restart files and the names of packages that need to be shared and called between modules within the system. Different registry files contain variables of various components of WRF-Chem. In this investigation, only chemistry-related variables were edited during the implementation. As a result, the only registry file that needed to be modified was the *registry.chem*, which is specific for defining the chemistry variables. In the following text, I refer to the *registry.chem* file as 'registry' for brevity.

The registry is divided into two parts. The first half defines all the variables related to the chemical species, and the second part has the information of

mechanism packages. The variables listed in the registry not only include the mixing ratios of the species, but also the chemical properties of them such as emissions, deposition velocities, photolysis rates, etc. Table A.1.1 lists the variables added in for each species in this investigation. Mixing ratios of all (61) species have been included in the registry, as well as photolysis rates of 33 species, and accumulated dry deposition of 33 species. Variables are added in by duplicating the pre-existing variables in each section, so the characteristics remain the same as the pre-implemented variables.

All variables for possible chemical options are defined in the registry, making a huge list. It would use significant computing resources to store all information in running the model. As a result, packages were developed with the variables assigned to them, so that only the needed variables are activated when the relevant packages are chosen. The new chemical mechanism package: *MOZART_MIM2_MCM_MOSAIC_4bin_aq* is defined in the second half of the registry with a unique number so that this chemical option can be called in the namelist.input when running WRF-Chem. All the tracers and gas-phase and aerosol species involved in the chemistry are listed under the mechanism package. The code is a duplication of the list of *MOZART_MOSAIC_4bin_aq* package with an expansion of 61 new species.

The chemical reactions of the new mechanism are implemented with KPP. As introduced in section 2.3.3, KPP is able to read in the input text files and automatically generate hard-coded files for the model, which is more efficient and accurate.
A subdirectory named *MOZART_MIM2_MCM_MOSAIC_4bin_aq* is created under the WRF/chem/KPP/mechanism directory. This folder contains multiple files that build up the main body of the MMM mechanism. The files are:

- *atoms_red* - a list of all elements on the periodic table with the atomic mass numbers assigned.
- *.def* file - the file defines all the functions and variables used in reaction rate calculation of the mechanism.
- *.eqn* file - the equation file contains gas-phase reactions, heterogeneous reactions and photolysis reaction with all the reaction coefficients.
- *.kpp* file - the file defines the properties of the output of KPP such as language, precision, solver, etc.

- *.spc* file - a list of all the species involved in the reactions including M in the third body reactions. Apart from the variational species, gases with fixed value are defined here with the number density assigned.
- *_wrfkpp.equiv* file - this file is used to map the species from KPP to WRF. Same species that are named differently in WRF-Chem and KPP (for example *HO* in WRF-Chem and *OH* in KPP) are listed in this file.

These files are the duplications of the files in the *MOZART_MOSAIC_4bin_aq* mechanism with the expansions of the species, reactions, and functions.

Under the WRF/chem/KPP/inc directory, another subdirectory which is also named *MOZART_MIM2_MCM_MOSAIC_4bin_aq* was developed. The files in this directory define the extra arguments used for computing reaction rate constants in the mechanism. For some reactions, the reaction rates depend on other variables, such as humidity and total peroxy radicals. These variables are defined here. The total peroxy radicals (RO2) is added for this study. RO2 consists of 18 peroxy radical species and is involved in 16 reactions in the model.

When simulating the chemistry in WRF-Chem, based on the option selected, the chemical driver calls a variety of the subroutines calculating all possible chemical processes, which impact the concentration of chemicals, including emissions, reactions, and depositions. Although after being defined in the registry and KPP, the mechanism is an existing option in the model, no chemistry can be simulated with this option due to lack of the links between this mechanism and the chemical driver/subroutines. Thus, edits were made in the chemical divers and modules to include the MMM mechanism. The codes that refer to the individual chemical mechanisms and variables are often hard-coded and differ between modules making the implementation hard work. Fortunately, in most cases, the subroutines and option needed by the MMM are the same as called for the *MOZART_MOSAIC_4bin_aq* mechanism. So the codes for *MOZART_MOSAIC_4bin_aq* mechanism were used as the template of the code for the new mechanism.
The MMM mechanism has been included in the following files:

- The chemistry driver (*chem_driver.F*)
- The aerosol driver (*aerosol_driver.F*)
- The cloud chemistry driver (*cloudchem_driver.F*)
- The dry deposition driver (*dry_dep_driver.F*)

- The optical driver (*optical_driver.F*)
- The wet scavenging driver (*module_wetscav_driver.F*)
- The file for calculating dry deposition (*module_dep_simple.F*)
  - Parameters related to calculating Henry's law constant are added for selected species. Data are obtained from literature (Sander, 2015).
- The emissions driver (*emissions_driver.F* and *module_bioemi_megan2.F*)
- The file for initial and boundary conditions (*chemics_init.F* and *module_input_chem_data.F*)
- The file for cumulus convection wet deposition (*module_ctrans_grell.F*)
- The file for computing aerosol optical properties (*module_optical_averaging.F*)
- The files related to the aerosol scheme (*module_mosaic_addemiss.F*, *module_mosaic_driver.F*, *module_mosaic_initmixrats.F* and *module_mosaic_wetscav.F*)
- The files related to the photolysis scheme (*photolysis_driver.F*, *module_ftuv_driver.F*, *module_ftuv_subs.F*, *module_ftuv_data.F* and *module_wave_data.F*)
  - The photolysis rates of the photolysable species are implemented in the files. The absorption cross-sections are obtained from IUPAC database.

After recompiling the model with no errors, the MMM mechanism is successfully implemented and ready to run in WRF-Chem.

2.5 Design of the runs

The previous two sections explained the set-up and changes adopted in the model. However, with different treatments of the emissions and the chemical processes, a variety of the model combinations could be tested in this study. Here, in section 2.6, I am listing the designs of the simulations applied to tackle different research questions (Table 2.5.1). All runs are nudged with the ERA-Interim reanalysis data with a frequency of 6 hours. Also, to avoid the impacts of the initial conditions, all runs are started 3 days (72 hours) before the listed periods, and the outputs of these 3 days were excluded from the analysis.

Table 2.5.1: The model runs designed for this study.

Name	Period	Domain	Mechanism	NO_x emissions	Isoprene emission
Run 1	16th May to 30th Jun	Parent	M4	full	full
Run 2	three periods	Nested	M4	full	full
Run 3	16th May to 30th Jun	Parent	MOZART	full	full
Run 4	16th May to 30th Jun	Parent	M4	full	no
Run 5	16th May to 30th Jun	Parent	M4 with no hy-INs	full	full
Run 6	16th May to 30th Jun	Parent	MOZART with no hy-INs	full	full
Run 7	16th May to 30th Jun	Parent	MOZART with no INs	full	full
ST1	16th May to 30th Jun	Parent	M4	75%	full
ST2	16th May to 30th Jun	Parent	M4	full	150%
ST3	16th May to 30th Jun	Parent	M4	75%	150%

Run 1 is the benchmark run of the study with the simulation of the parent domain for 45 days covering the summer campaign period. The new developed M4 mechanism was used in this run and there is no treatment on the emissions. Since the primary emission of isoprene is from vegetation, which is a function of temperature and radiation, the isoprene level during winter in Beijing is low (ppt level). Also, the main pollutants in the winter China are the $PM_{2.5}$ and PM_{10} and the O_3 mixing ratios are usually very low due to the high concentration of NO_X. Hence, the run for the winter campaign is not included in this study.

Run 2 is the nested with the same configuration as Run 1 (apart from the domain set-up) but for three periods, which are: 16th to 25th May, 9th to 15th June and 19th to 23rd June 2017. Most instruments were running fine during these three periods providing more comprehensive observations for model validation.

Run 3 used the same set-ups of Run 1, apart from the chemical mechanism. The original MOZART-4 mechanism was applied in this run. By comparing the difference between Run 1 and 3, the impact of the explicit isoprene chemistry is investigated. In other words, if the simulations from two different mechanisms vary largely, it indicates that more explicit treatment of nitrates is needed in the air quality modelling in China.

Run 4 is designed to quantify the contribution of isoprene chemistry to various chemical species. This run used the same configurations as Run 1 but with no isoprene emissions. Hence, the difference between Run 1 and Run 4 indicates the impact of isoprene chemistry in M4 mechanism. Where the contribution of isoprene in the MOZART-4 mechanism is calculated by subtracting simulations of Run 4 from Run 3. It is worth mentioning that the isoprene chemistry is the only difference between the two mechanisms, as a result, the two mechanisms provide exactly the same simulations when isoprene emission is turned off. This is confirmed by a 7-day test.

Runs 5, 6 and 7 are designed to quantitively study the contribution of different INs. Runs 5 was based on the configuration of Run 1 while Runs 6 and 7 were based on Run 3. As mentioned in section 1.1.4, different hy-INs isomers are formed via reactions between isoprene hydroxy peroxy radicals (ISOPO2) and NO with various branching ratios – α. The branching ratio of NO_2 and carbonyls formation through these reactions are 1-α. In Run 5 and Run 6, I set the α of all hy-INs to zero in both mechanisms, which means 100% NO is converted to NO_2 by ISOPO2. The differences between Run 1 and Run 5, Run 2 and Run 6 indicate the impact of hy-INs in the M4 and the MOZART-4 chemical mechanisms.

Based on Run 5, I also removed al-IN with the same method in the MOZART-4 chemical mechanism creating a mechanism with no INs formation at all (Run 7). The comparison between Run 6 and 7 indicates the contribution of al-IN. However, the al-IN in the M4 mechanism cannot be excluded. In M4, NC4CHO is lost through photolysis and reacting with OH, O_3 and NO_3. The products of these reactions are different from each other and the reaction rates are dependent on radiation and the concentration of the reactants that is changing during the model run. Hence, it is impossible to summarize the degradation products of NC4CHO. As a result, al-IN cannot be excluded and replaced by its

subsequent products in M4 chemical mechanism.

Sensitivity test run 1, 2 and 3 (refered as ST1, ST2 and ST3 in the following text) were based on the same configuration as Run 1. However, three imaginary NO_X and isoprene emission scenarios were tested in these runs. This perturbation study aims to understand the impact of isoprene under different potential air quality control measures across China.

3

Model assessment

3.1 Introduction

The previous chapter described the regional climate transport model – WRF-Chem, with chemical modifications made to it, is used in this study. In this and following chapters, all results shown are generated from simulations using WRF-Chem to model the air parameters and compositions in China.

Before discussing any chemical behaviour of isoprene, it is necessary to check the model performance and understand its limitations. This section shows the results of model validation. The model simulations are compared with the observational data and various components of the model are assessed including meteorology, emissions, and the chemical mechanism. Specifically, this section aims to assess the 'skill' of the model in simulating the real world and to appraise the improvement of the nested domain. Unlike run 1, which is from 16th May to 30 June and covers the entire campaign period, the nested domain is only run for 16th to 25th May, 9th to 15th June and 19th to 23rd June due to its high computational cost. These three periods are selected with more comprehensive observations, which eliminates the periods when power is cut off or has instrument failure.

Here in this section, a brief discussion of the simulations and observations used in this chapter is presented, and the output interpretation techniques are introduced. The model performance in regard to meteorology is discussed in section 3.2. Some emissions are validated with the observed flux data (section 3.3). Section 3.4 includes the discussion of the skill of the model in regard to various chemical tracers, and the overall assessment is concluded in section 3.5.

Observational data This study takes advantage of the field campaigns in the Beijing, which provided comprehensive measurements including both meteorological and chemical properties for the validation (details see section 2.2). Beside the data from the campaign site, the Chinese National Air Quality Monitoring Network record hourly ground-level measurements of 6 key pollutants in more than 1700 sites of 370 cities across China. This AQI network allows me to assess the chemical performance of the model across the domain. The China meteorological administration offers daily averaged meteorological monitoring data from 166 sites across China, which is used to validate the meteorological conditions of the whole domain. The contour map comparision in section 3.4 is generated with this dataset.

Model simulations Results from 2 runs are discussed in this chapter. Run 1, as the benchmark run of this study, is used to validate the meteorological parameters and the chemical tracers. Three nested simulations (Run 2) were set up within the period of Run 1 to test whether the model performs better with higher resolutions of meteorological conditions and emissions. To assess the modified chemical mechanism, Run 3 and Run 1 are compared with the observations. Since most of the measurements were made on the ground, the surface layer (¡ 40 m above the ground) was used for the validation if no altitude is spercified. Also, local time (UTC + 8.00) was used for all the diel variation plots in this and the following chapters.

Interpretation techniques To evaluate the performance of the model, different analytical methods are applied in this study.

The difference between the model simulation and the observation (i.e. bias) is calculated by subtracting the observed value from the model output (equation 3.1.1).

$$B_i = M_i - O_i \tag{3.1.1}$$

where M is the model simulation and O is the observation.

The mean bias (MB) (equation 3.1.2) is the average of the bias. MB provides a good indication of the mean over or under estimate of predictions.

$$MB = \frac{1}{n}\sum_{i=1}^{n}(M_i - O_i) \tag{3.1.2}$$

where n is the size of the data.

For meteorological parameters and pollutants that have values that extend over a wide range, normalised bias (NB) is used to assess the agreement. NB is computed by dividing bias by the observed concentration (equation 3.1.3).

$$NB = \frac{M_i - O_i}{O_i} \tag{3.1.3}$$

Equation 3.1.4 calculates the normalised mean gross error (NMGE). Because NMGE takes the normalised absolute error of the data, it indicates the mean error regardless of whether it is an over or underestimate.

$$NMGE = \frac{\sum_{i=1}^{n} |M_i - O_i|}{\sum_{i=1}^{n} O_i} \tag{3.1.4}$$

The root mean squared error (RMSE) is another commonly used statistic tool to assess how close the simulations are to the observations.

$$RMSE = (\frac{\sum_{i=1}^{n} (M_i - O_i)^2}{n})^{1/2} \tag{3.1.5}$$

The percentiles distribution is helpful to understand the ability of the model in capturing the dynamic range of the observations (Mathur et al., 2008). 25th and 75th percentiles are used in this chapter representing the value that 25% and 75% of the data falls below, respectively.

The standard deviation (SD) is an indicator of the extent of variability in a dataset. Lower standard deviations suggest closer distribution of the data points to the mean value. The SD of a dataset M is calculated using the equation 3.1.6.

$$SD_M = \sqrt{\frac{1}{n-1} \sum_{i=1}^{n} (M_i - \overline{M})^2} \tag{3.1.6}$$

The Pearson correlation coefficient (r) is product moment correlation coefficient, which is a measure of the extent to which two variables are linearly related. The

closer r is to 1 (or -1), the better positive (or negetive) linear correlation the two variables have. The equation 3.1.7 shows the calculation of the r value.

$$r = \frac{1}{n-1}\sum_{i=1}^{n}[(\frac{M_i - \overline{M}}{SD_M})(\frac{O_i - \overline{O}}{SD_O})] \tag{3.1.7}$$

3.2 Validation of meteorological parameters

A good representation of the meteorological processes is crucial in studying atmospheric chemistry. Meteorology can not only impact the physical mixing of the chemical tracers but directly affect the photochemical conditions, which is determined by the radiation. Previous studies suggested that meteorological conditions can be responsible for the formation of the pollution episodes in north China (Wang et al., 2018; Zhu et al., 2018).

In this section, I validate the key meteorological parameters including temperature (T), relative humidity (RH), wind speed (WS), wind direction (WD) and the planetary boundary layer height (PBLH).

3.2.1 Temperature

The temperature simulations are compared with the tower measurements at the IAP site at different vertical levels. The bottom four model levels of the parent and nested domains are selected with the heights of 2 m, approximately 60 m, approximately 145 m and approximately 257 m for the parent domain and 2 m, approximately 52 m, approximately 137 m and 248 m for the nested. Besides the surface temperature simulation, an output generated for 2 m especially, the height of the higher-level simulations needs to be calculated. The model levels are based on pressure, as a result, the model level heights can vary a little at different times. Here, I used the averaged height over the 45 days. The bottom four levels simulations of the coarse domain are paired with observations from the measuring platform at 8 m, 65 m, 140 m, and an average of 240 m and 280m accordingly. The bottom three levels of the nested domain are validated with the same observations data as for the parent, whereas measurements at 240 m are selected to compare with the nested domain simulation at approximately 248 m.

In Fig. 3.2.1, I compared the time-series of the ground-level temperature with hourly data for 44 days (17th May to 30 June). The differences between the simulations and the measurements are plotted in the lower panel. Results of the coarse domain are in blue and the nested are in red. The time-series of both domains show good agreement in the general pattern between the model and the observations with the correlation of determination of 0.86 and 0.87 and mean bias of 0.69 ^{o}C and -0.35 ^{o}C. The daily maxima of the coarse domain are

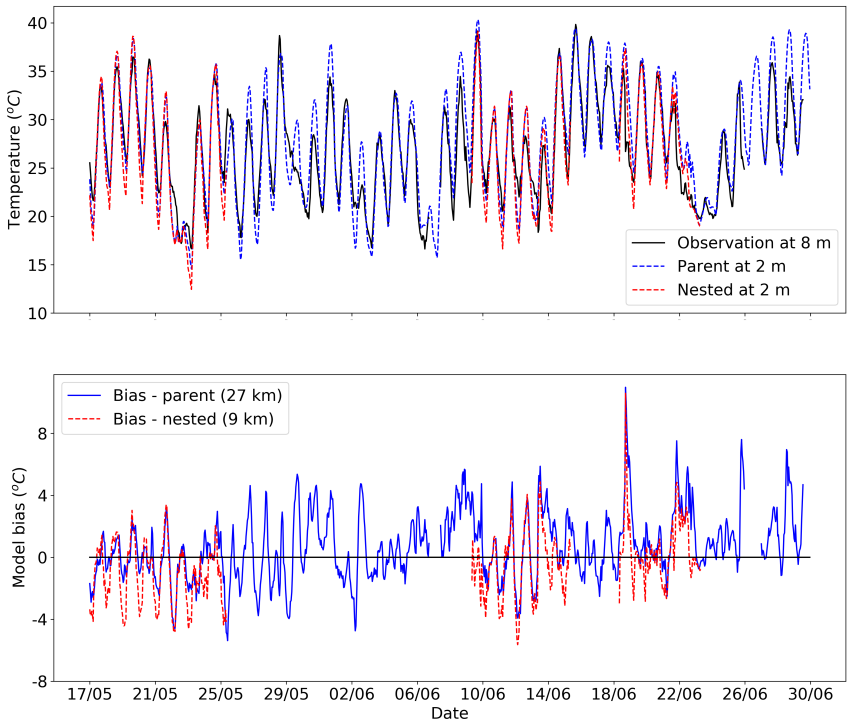

Figure 3.2.1: Time-series of the simulated (dashed) and observed (black solid) hourly surface temperature (upper panel) in Beijing, and the differences between them (lower panel). Results of the coarse domain (27 km) are in blue and red lines represent simulations of the fine domain (9 km resolution).

overestimated leading to the positive mean bias. Compared to the observations, the nested domain simulates a stronger diurnal cycle with higher daily maxima and lower daily minima, especially during the first period. The model failed to capture the detailed variation on the 30th May, 2nd, 19th and 23rd June. Given the resolution of the simulation are 27 km and 9 km, it is understandable that some local features are not reproduced.

The nested domain run shows similar results as the parent domain and some improvements are seen on the 22nd and 23rd June. However, during most of the nights, the nested domain considerably underestimates the temperature at the surface in Beijing. This might indicate that the model has difficulties in reproducing the night-time mixing in urban environments.

In Fig. 3.2.2, the averaged diel cycles with the 25th and 75th percentiles

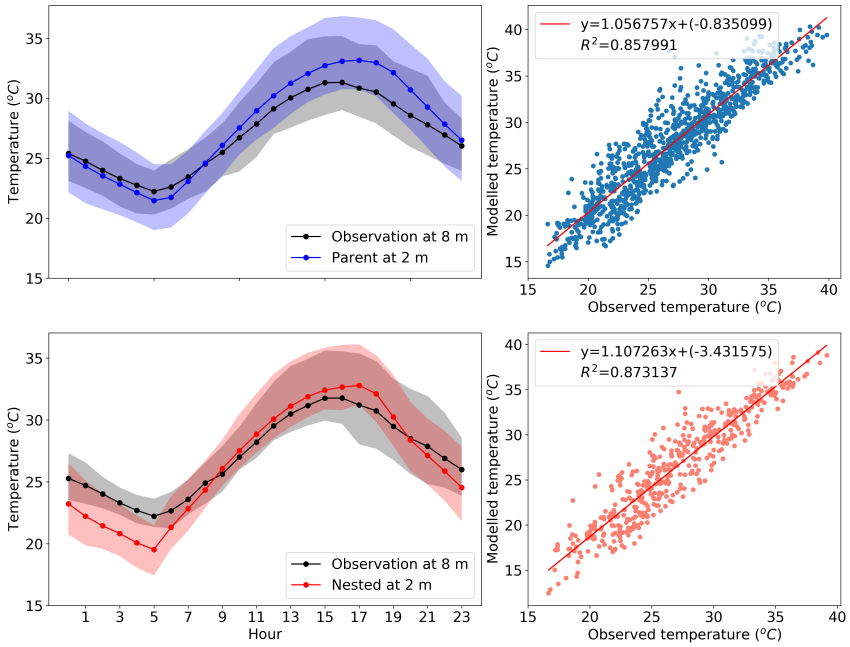

Figure 3.2.2: 45-day's averaged daily cycle of the simulated (blue and red) and observed (black) surface temperature (left panels) in Beijing, with the mean (solid line) and 25th and 75th percentiles (shaded area), and the scatter plot of the two datasets (right panels). The best least-squares linear fit is coloured in red. Regression line values and the coefficient of determination (R^2) are shown with the scatter plot. The top panels show the comparison between the parent domain and the observation, and the bottom panels are generated with data from the nested domain.

(shades) are shown in the left panels, and sactter plots of the temperatures with the best least-squares linear fits for both domains (red line) are plotted in the right.

In general, WRF-Chem predicts a similar diurnal cycle to the observations in both domains. The minimum temperature is seen in the morning at 5.00 for all three datasets, while the observed daily peak appears at 15.00 to 16.00 and simulated diel maxima appear at 17.00. This one-hour lag might be due to the uncertainties in radiation simulations and may affect the heat flux and vertical mixing.

The temperature is overestimated up to 2.6 ^{o}C in the coarse domain and 1.9 ^{o}C in the fine domain in the afternoon. In the parent domain, this difference

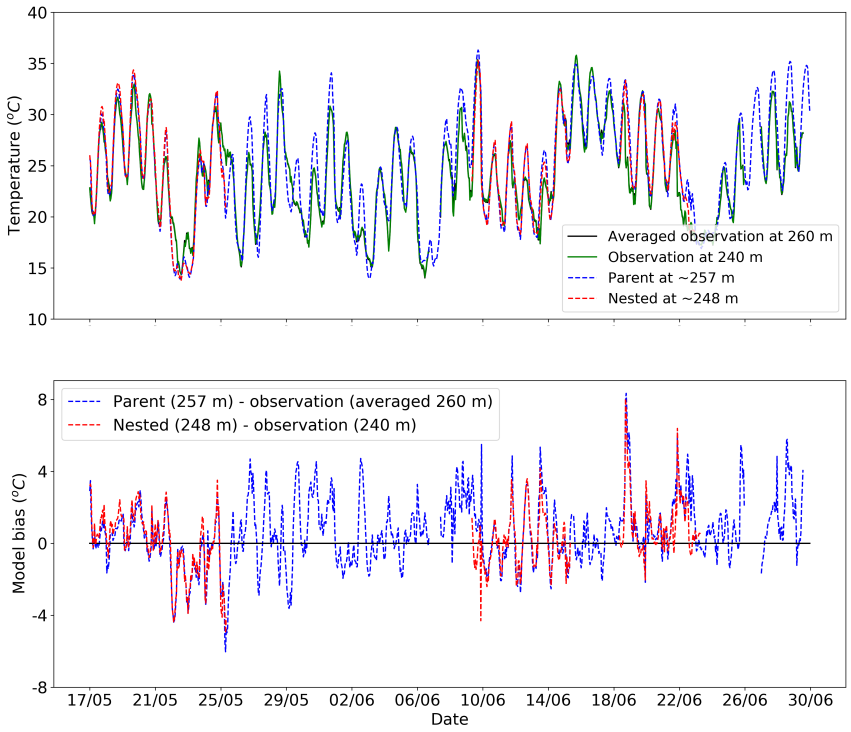

Figure 3.2.3: Same as Fig. 3.2.1, but for a different height (∼257 m).

shrinks after sunset making a better agreement of the night-time temperature simulation with the observation. However, the wider blue shaded area during night suggests a larger variation of the modelled night-time temperature than observed. As seen in the timeseries comparison, the nested domain underestimates the surface temperature during the night (from 20.00 to 8.00).

Relatively good linear correlations between measurements and model outputs are calculated with a gradient of 1.06 and R^2 of 0.86 for the parent domain and a gradient of 1.11 and R^2 of 0.87 for the nested domain.

Same comparison method is used for higher levels (Fig. 3.2.3, Fig. 3.2.4). The model simulation at about 257 m (coarse domain level 4, the blue dashed line in Fig. 3.2.3) is compared with the averaged observation of 240 m and 280 m (the black solid line in Fig. 3.2.3) and the simulation at approximate 248 m (fine domain level 4, the red dashed line in Fig. 3.2.3) is paired with the tower measurements at 240 m (the green solid line in Fig. 3.2.3).

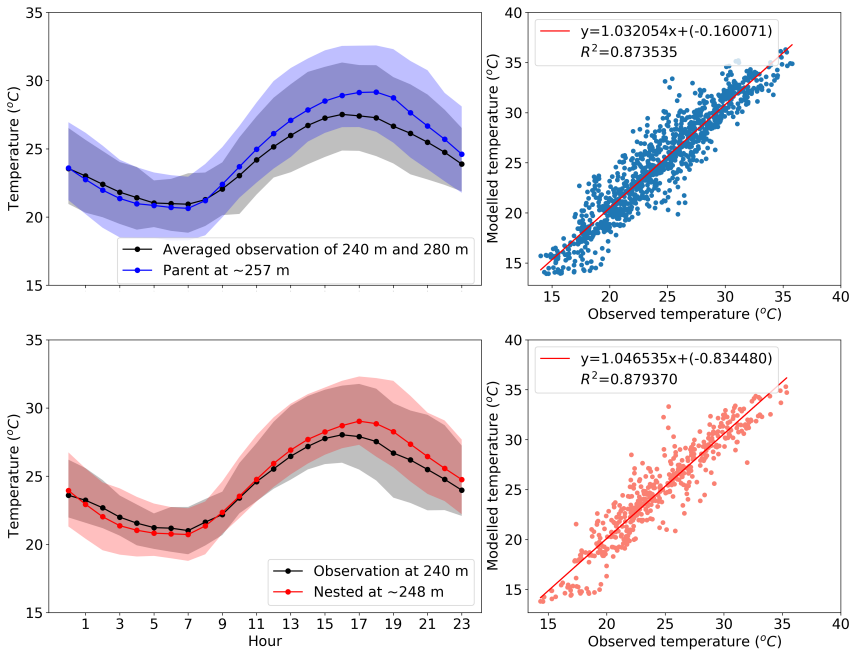

Figure 3.2.4: Same as Fig. 3.2.2, but for a different height (∼257 m).

Smaller discrepancies are shown at this altitude than at the surface (Fig. 3.2.3 and Fig. 3.2.4). This is not a surprise since the near ground temperature is going to be affected by local processes that are not resolved at 27 km or 9 km. This can be the effects of buildings and local surface characteristics like concrete or vegetation that will impact temperatures close to the land surface. Whereas at higher levels temperature represents more of a mixed regional meteorological characteristic. Hence, compared to the 2 m results, Fig. 3.2.4 also presents better agreements of the diel cycles and better correlations with the R^2 values and the gradient of the trend line closer to 1.

At this height, the nested domain run seems to slightly improve the temperature simulations during the daytime. However, some temperature drop events are still not well captured (22nd May, 19th and 23rd June). Similar results are found at around 60 m and 145 m above the ground, which are included in the Appendix B. To conclude, nesting can, to some extent, provide better temperature simulation at higher levels, however, the coarse domain appears to do a very good job simulating temperature on a scale of 27 km with a much cheaper computational cost.

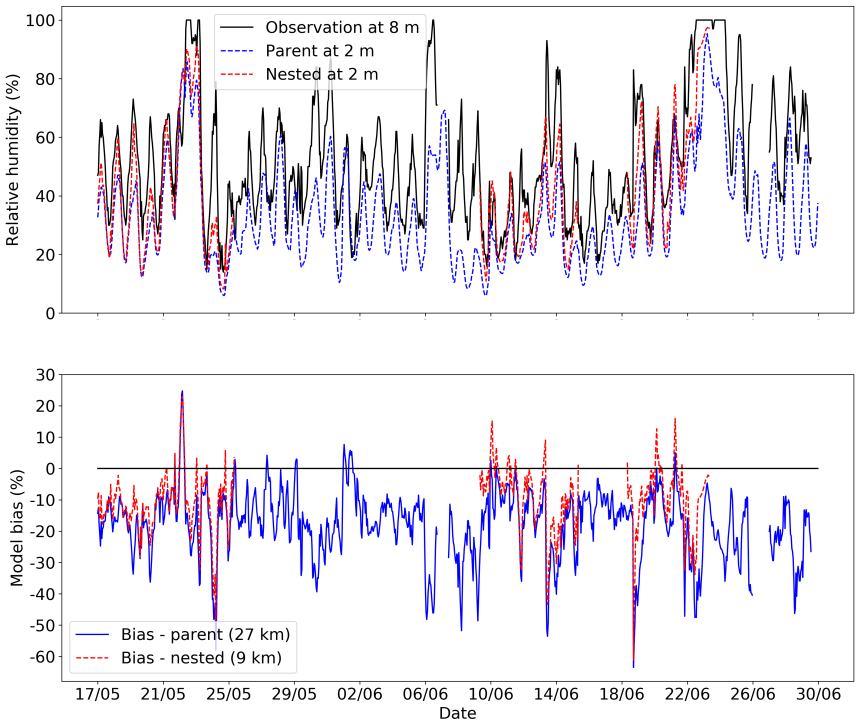

Figure 3.2.5: Same as Fig. 3.2.1, but for relative humidity.

3.2.2 Relative humidity

The simulations of relative humidity (RH) at the bottom four model layers are compared with the tower measurement using the same techniques as used for the temperature. Here I only show the results of the bottom layer and the fourth layer since similar outputs are generated at the middle two layers, which can be seen in the Appendix B.

Fig. 3.2.5 and Fig. 3.2.6 are the time-series of RH and the bias at ground-level and over 200 m. Both figures show that the model can capture the general pattern of the day-to-day variation, however, RH is systematically underestimated at these levels. Compared to Fig. 3.2.1 and Fig. 3.2.3, it is notable that the bias of RH and temperature are symmetrical, which indicates that overestimation of temperature could contribute to the low RH values. RH

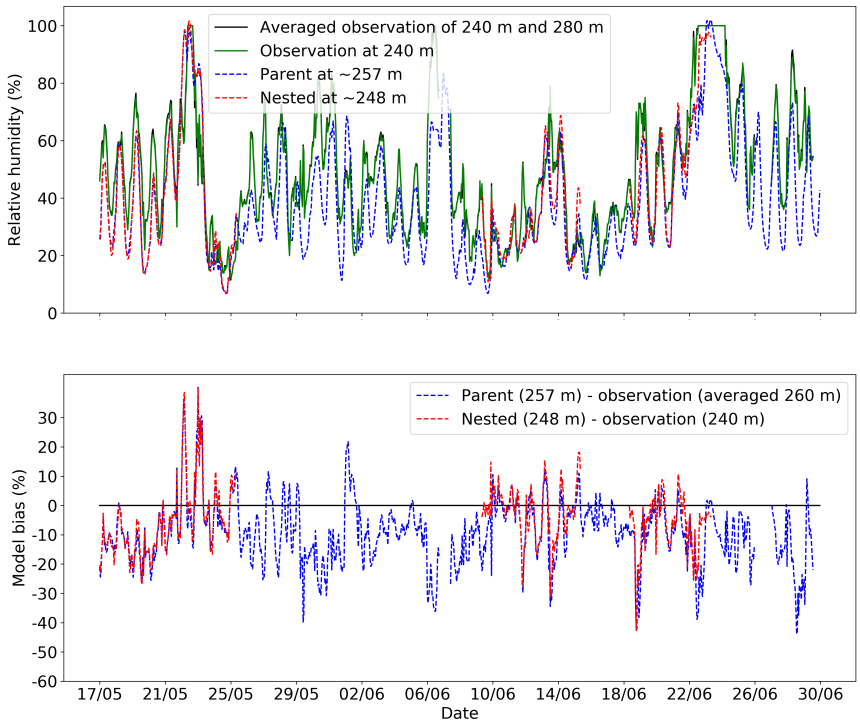

Figure 3.2.6: Same as Fig. 3.2.5, but for a different height (∼257 m).

is a measure of the amount of water vapour in the air relative to the amount that the air can hold before it becomes saturated. The saturation vapour pressure increases with higher air temperature. That is to say, with the same amount of water vapour, if the temperature is simulated too high, the RH will be too low. Therefore, the model underpredicts RH could be partly due to the temperature simulation being too high.

At 2 m, RH underestimation is approximately 20% through the day in the parent domain (clearer on Fig. 3.2.7) and can reach more than 40% on several days (24th and 31th May, 6th, 13th and 19th June). The nested simulation provides a better agreement of RH especially during the night. However, this might be partly due to the underestimation of the temperature, which may not mean more water vapour are simulated by the model. High RH values were recorded and simulated from 22nd to 24th June, which reflects a precipitation occured at that time .

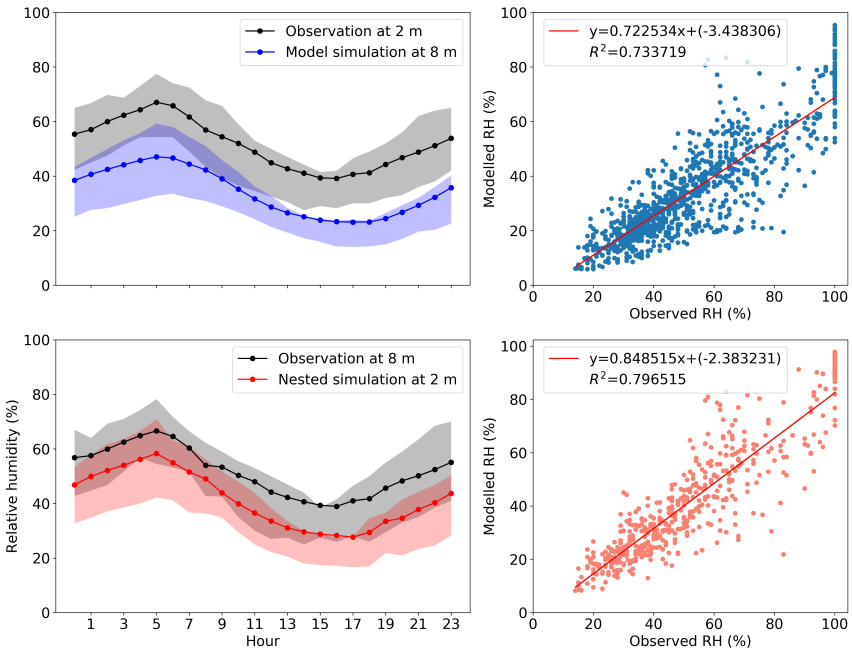

Figure 3.2.7: Same as Fig. 3.2.2, but for relative humidity.

The underestimation is of RH at around 260 m is less pronounced than the surface with smaller bias. The observations at higher altitudes are affected less by the local environments, which is expected to show better agreements with the regional model results. This is also clear on the diel cycles and scatter plots.

The diel cycle and scatter plots are shown in Fig. 3.2.7 and Fig. 3.2.8. A pronounced gap between modelled and measured RH is seen in the figures. However, the patterns of diurnal variation are reproduced by the model, even at 2 m, and reasonable R^2 are calculated at all four layers (see Appendix B). This is not a surprise as the diel cycle of temperature is well captured and RH value is related to the temperature change for the reasons discussed above.

The RH simulation at over 200 m shows a very good agreement with the observations (Fig. 3.2.8), especially during the night. The 25th and 75th percentiles of modelled RH (red and blue shades) largely overlap the measurements (grey shade) at night-time. However, RH is still underestimated in the afternoon.

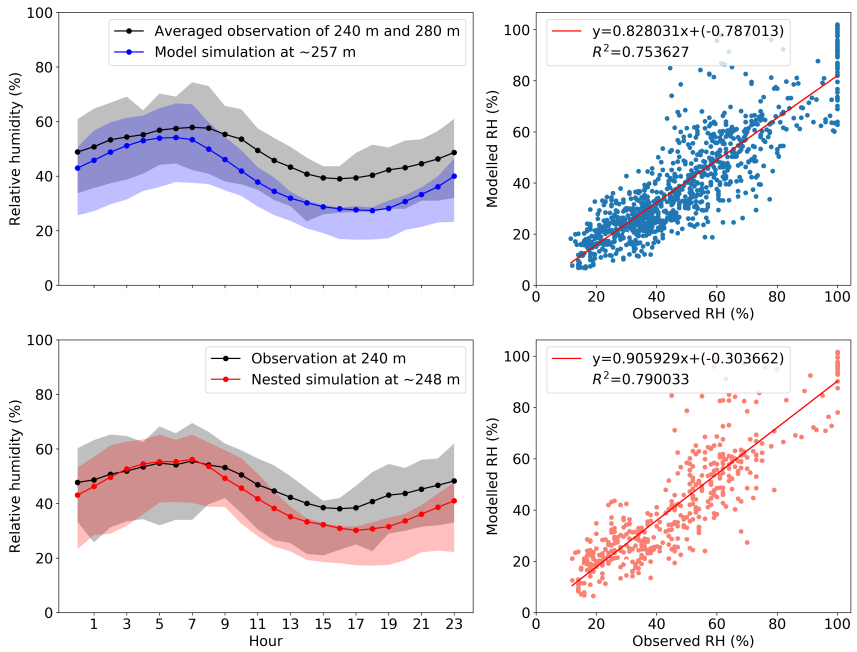

Figure 3.2.8: Same as Fig. 3.2.7, but for a different height (~257 m).

In the parent domain, maximum bias decrease from the surface to higher levels from -63 % to -44 % at around 260 m, and the NMGE reduce from 0.36 to 0.25. This is also true for the nested domain with the reduction of maximum bias by 12% and NMGE by 0.1.

3.2.3 Wind speed and direction

Wind speed (WS) and wind direction (WD) are important variables affecting the transport of air parcel. These two variables are validated against the tower measurement at IAP. Comparison of time-series and diurnal cycles at ground-level and around 260 m of the tower are shown in Fig. 3.2.9 and Fig. 3.2.10. Again, the results of the middle two levels (at around 60 m and 145 m) are included in the Appendix B.

The model significantly overestimates WS at the ground-level in both domains (Fig. 3.2.9). This is likely due to the fact that the domains with 27 km and 9 km resolutions have difficulties in reproducing the local surface characteristics such as the surface roughness and building heights that can considerably affect

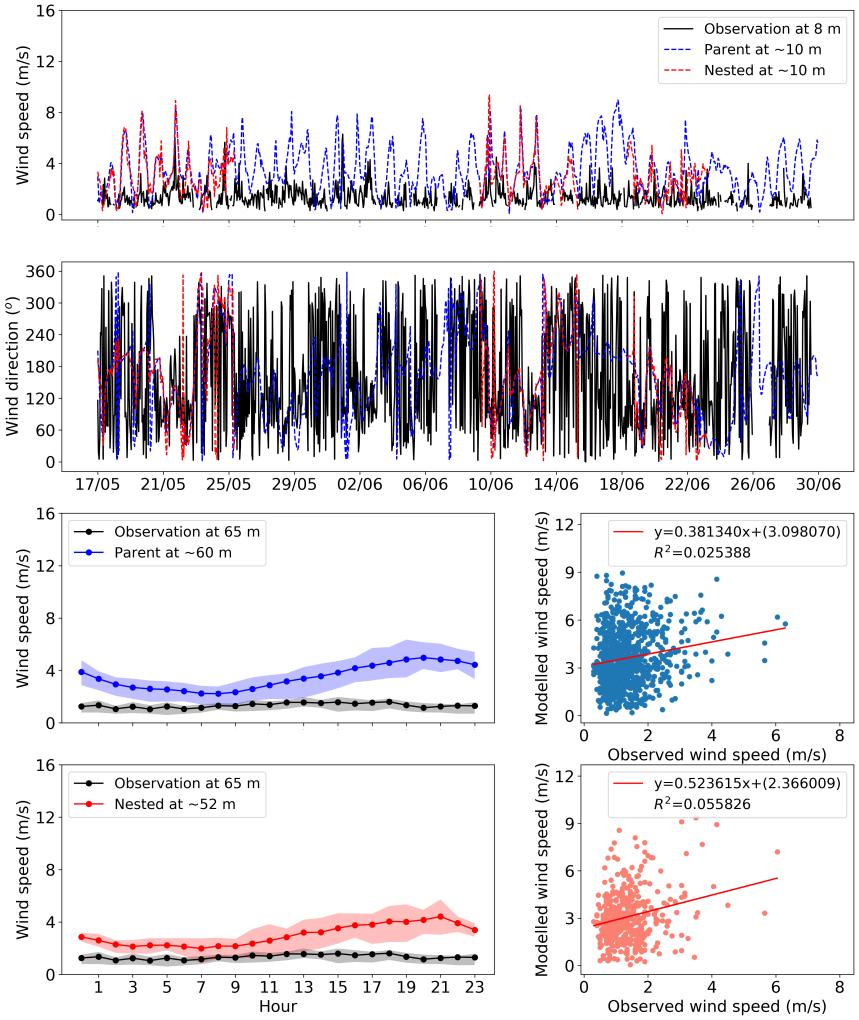

Figure 3.2.9: Comparison of the time-series (top two panels) of modelled and observed wind speed and wind direction at ∼10 m. The 45-day's averaged diel cycles of the wind speed are plotted in the bottom left panels with the 25th and 75th percentiles shaded. The scatter plots of model simulations and obserbations are shown in the lower right panels. The best least-squares linear fit is illustrated as the red line and overlayed on the scatter plots with the regression line values and the coefficient of determination (R^2). Data from the coarse domain, fine domain and the measurements are coloured in blue, red and black, respectively.

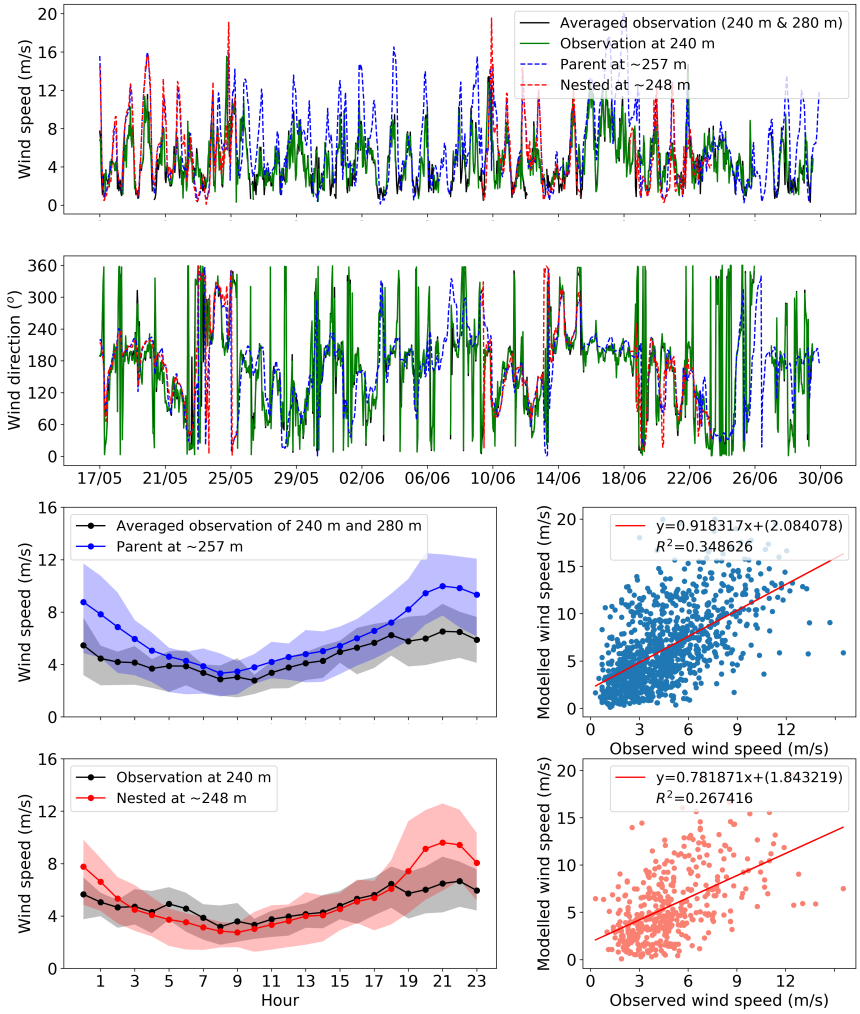

Figure 3.2.10: Same as Fig. 3.2.9, but for a different height (~257 m).

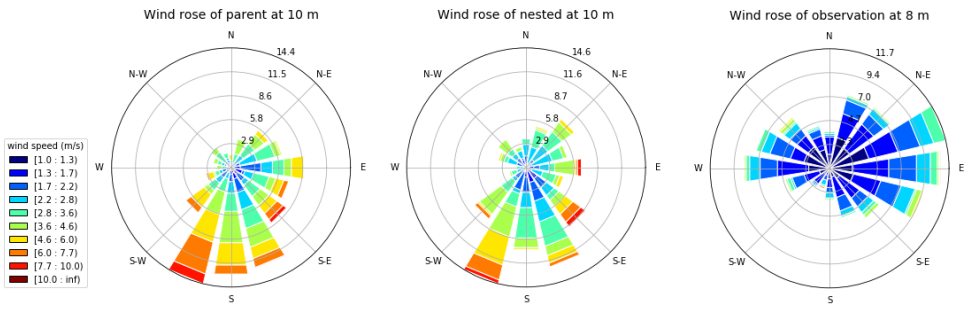

Figure 3.2.11: Comparison of the simulated (left: parent domain; middle: nested domain) and observed (right) wind rose at the surface.

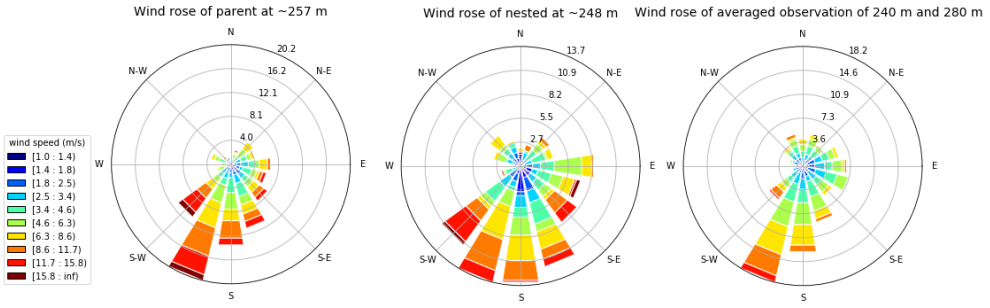

Figure 3.2.12: Same as Fig. 3.2.11, but for a different height (∼257 m).

WS. Similar results were reported in several studies (Wang et al., 2019b; Tuccella et al., 2012). The nested domain provides a slightly better simulation than the parent at 10 m, with the NMGE decreased from 2.39 to 1.79. However, no clear correlation can be seen in the scatter plot in both domains at this height.

At surface level, a key difference to the WD simulation is that far greater variability is shown in the observation. This suggests the surface wind is affected by the local factors rather than larger scale synoptic factors. The WD seems to be 'noisy' at this level, which shows the values shifting through the full 360 degrees on a frequent basis.

WS is still overestimated at a hight of 260 m at night, however, the daytime simulations show good agreement with the observation. The NMGE of the parent and nested domain are 0.79 and 0.66, respectively. This suggests that the observations at higher level may capture the regional air flow. This is more obvious on the wind rose plots.

Figs. 3.2.11 and 3.2.12 compare the simulated (left and middle) and observed (right) wind rose at different heights. The modelled and observed wind roses at 260 m show a good agreement. Predominant air from SW of Beijing is captured, which agrees with the previous study (Xie et al., 2008). However, as mentioned before, WS is overestimated by WRF.

The modelled and observed wind roses at 260 m show a high agreement. Air from the southwest is reported to be the predominant synoptic scale WD at this time in Beijing (Xie et al., 2008), which is captured by both the model and the observation. However, at the ground-level, the wind is predominantly from the

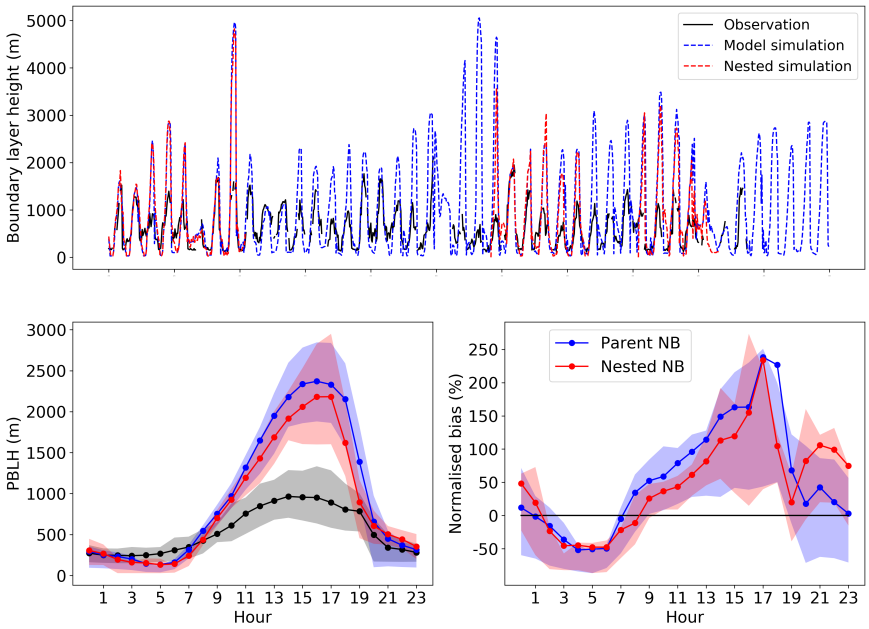

Figure 3.2.13: Comparison of the time-series and the diel cycle of the simulated (blue for the parent domain and red for the nested domain) and observed (black) planetary boundary layer height. The top panel shows the 44-day's time-series of the PBLH of the model simulation and the observation. Daily variation of the PBLH (left) and its bias (right) are plotted in the bottom panels with the 25th and 75th percentiles shaded.

east and west. The site is located in the residential area close to a major road which is the east and west direction. This suggests that the observed WD is likely to be affected by the surrounding morphology, which is hard to be captured with a 27 km or 9 km resolution model.

3.2.4 Planetary boundary layer height

Planetary boundary layer height (PBLH) is a crucial meteorological parameter in air quality modelling, which affects air pollutant dispersion, transport and surface concentrations.

The simulation of PBLH is compared with the ceilometer measurement at IAP. The modelled PBLH is significantly overestimated during daytime and underestimated at night (Fig. 3.2.13), with the normalised bias ranging from -51% to 238% in both domains. However, the high mean value of the NB in the

late afternoon in the average diel pattern can be caused by very high PBLH simulated on a few days. The mean NB at 17.00 and 18.00 are equal or even higher to the 75th percentile, which means only 25% of the overestimation in this time is higher than the mean NB.

The poor correlation ($r^2 \approx 0.23$) suggests that the model fails to capture the measurement of the PBLH at IAP. The low resolution of the simulations might contribute to this, but it is may suggest that the modelled PBLH is not comparable with the observations.

The mixing layer height is derived from the cloud base height measured by Kotthaus' group ((Kotthaus and Grimmond, 2018)), which may contain the information of other layers such as the nocturnal residual layer. This study uses YSU boundary scheme, which determines PBLH from not only wind parameters but potential temperature (Hong and Pan, 1996). It was designed to tackle the underestimation of the PBLH in the forecasting models (Hong et al., 2006).

3.2.5 Overall assessment of the meteorology

The simulated meteorological parameters are compared with the observational data in the sections above. To conclude, the model does a reasonable job in reproducing most of the meteorological quantities. Good correlations are found in temperature, relative humidity and wind simulations, although RH is systematically underestimated and WS is slightly overpredicted. This is due to that the observations at ground-level are highly affected by the local feature, which is hard to be captured in the model with resolution of 27 km and 9 km.

However, there is a substantial difference between the observed and modelled PBLH, with the PBLH simulation being overestimated by a factor of 2.5 during daytime and underestimated by a factor of 2 in the early morning. This inaccuracy will impact the vertical mixing and therefore affect the concentration of chemical tracers.

The nested simulation show slightly better agreement with the observations (apart from the wind rose, which can be due to the small dataset), however, given the high computing cost, the parent domain is good enough to simulate

reasonable meteorological conditions.

3.3 Emissions validation

As illustrated in section 2.3, the emission is an important component in WRF-Chem modelling. In the model, the emission is independent to the chemistry, however, it has a significant impact on both concentration of the chemical compounds and the chemical processes.

As introduced in section 1.1, the chemistry is usually not linear since one species can react with several other species, hence the dominating reaction may vary if the concentration of the reactant is changed. As a result, too high or too low emissions will not only directly change the mixing ratio of the species but may lead to a different chemical regime that affects the other chemistry.

Here I compare the simulated anthropogenic and biogenic emissions with the flux measurements from the campaign. The measurements were conducted at 102 m of the tower. Therefore, the total emissions injected to the model below 100 m are calculated to compare with the flux measurement.

Anthropogenic pollutants In this study, I used the Multi-resolution Emission Inventory (MEIC) 2013 version for the simulation. According to the domain resolutions, 27 km and 9 km inventories are selected. These inventories provide diel cycle and vertical distribution of the emissions, however, there are no day-to-day variations within one month. Emission inventories of June are used to generate the simulation of the summer campaign period.

The comparison of the diel cycle of CO emission is shown in Fig. 3.3.1. The modelled emissions are in blue (27 km) and red (9 km), while the observation is in black with the grey shades representing the 95% confidence intervals. In both outputs, CO emission increases steeply in the morning from 5.00 to 8.00, and shows dramatic drops at 18.00 to 19.00 and 22.00 to 24.00, reaching a very low level of emission ($\sim$ 3.5 mg m^{-2} hr^{-1}).

Two distinct peaks were observed: the first peak occurred at 11.00 (around 30 mg m^{-2} hr^{-1}) and the second at 17.00 (around 24 mg m^{-2} hr^{-1}). Between the two

peaks, the CO emissions dipped with a low daytime value of 16 mg m^{-2} hr^{-1}.

The modelled 27 km resolution CO emissions show some similarities to the observation, especially during night-time. During daytime, CO emissions are significantly overestimated in the parent domain, which may be partly due to the contribution of the industrial activity nearby. The measuring site is located in the residential area close to the ring road. Hence signals of CO emissions from the residential and transport sectors are the predominant components of the measurements and industrial emissions from the surrounding area have less representation (Squires et al., 2020).

On the contrary, the CO emissions of the nested domain (9 km resolution) is underestimated. This can be partly explained by the reason listed above. CO emissions from industry contribute to the 27 km resolution emission inventory but they are not included in this subgrids of the fine resolution inventory. Also, the underestimation can be associated to some issues during downscaling, which is discussed later in this section.

The NO_X emissions show a similar story (Fig. 3.3.2). The diel variations of both emission inventories show good agreement with the measurement, and the fine resolution emission is lower than the emission of the 27 km. The two peaks (at 7.00 and 17.00) were reproduced in MEIC. NO_X emission of 9 km domain shows a better agreement with the measurement, whereas the 27 km resolution emission is overestimated by a factor of 2.

Although the emission of 9 km resolution seems to agree with the flux measurement better (for CO and NO_X), Biggart reported an error of this emission inventory, which may have occurred during the downscaling process. Biggart's group found that all MEIC emissions are significantly underestimated in the cities (Beijing) but overestimated in the rural area. He suggests that the total amount of the emissions across the domain is correct but some are emitted in the wrong place, which is likely to be due to the downscaling. They have successfully redistributed the emissions for fine domains (9 km and 3 km) and validated with the flux measurement. However, this dataset is not available until the summer of 2019, which is too late for this study. Their paper is still in preparation. Oliver Wild, who is also a user of this emission inventory presented some of Biggart's results during the programme meeting. Hence, I excluded nested comparisons for the chemical species.

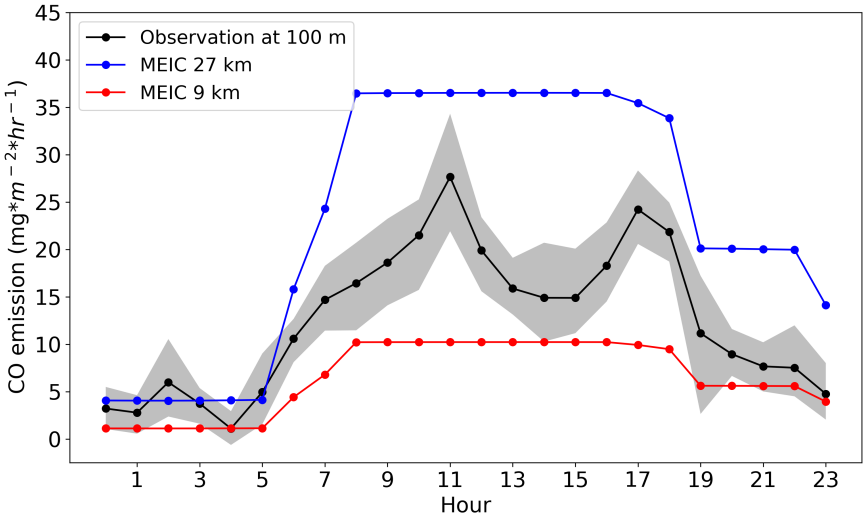

Figure 3.3.1: Diel cycle of the observed (black) and MEIC (blue) CO emissions. Observed data at 102 m are averaged over the summer campaign with the 95 % confidence intervals shaded.

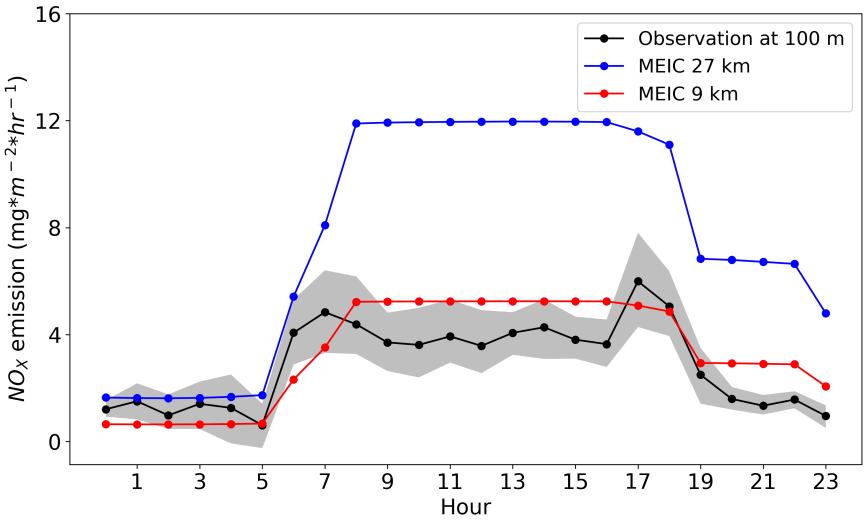

Figure 3.3.2: Same as Fig. 3.3.1, but for NO_X

To conclude, the MEIC inventory 2013 version captures the daily variation of emissions fairly well at 27 km. However, the inventory provides higher emissions than the flux measurement.

Biogenic pollutant (isoprene) Biogenic emissions are simulated by the online model MEGAN (see section 2.4). Fig. 3.3.3 compares the time-series and diel variation of isoprene emission from the MEGAN model and the observation. Time-series suggests that MEGAN is able to capture the variation of isoprene emissions over a period of time. In summer Beijing, isoprene emission is positive correlated to the leaf area, temperature and solar radiation. Hence, high emissions are observed and simulated during the hot sunny days (14th to 22nd June), whereas the emissions are significantly lower when the precipitation occured (22nd to 24th June).

The bias and diel pattern show that the model overpredicts the emissions during daytime (6.00 to 19.00). In the morning, the increase of observed isoprene emissions are not as rapid as the modelled, which is likely to be associated with the lower photosynthetic photon flux in the measurement. The site is located in a residential area with buildings surrounded that may hinder the isoprene emission. The discrepancy between the observation and simulation becomes smaller when an optimised emission factor (ε) is used with a value of 27.25 mol km^{-2} hr^{-1} instead of 36.58 mol km^{-2} hr^{-1} (Acton et al., 2020).

Overall, both anthropogenic and biogenic emissions simulation show relatively good correlations with the flux measurements. The NO_X emission comparison suggests an overestimation of NO_X in the coarse domain. However, the high agreement between the nested NO_X emission and the observation indicates that the overestimation can be an averaged result of high emissions from the surrounding grids.

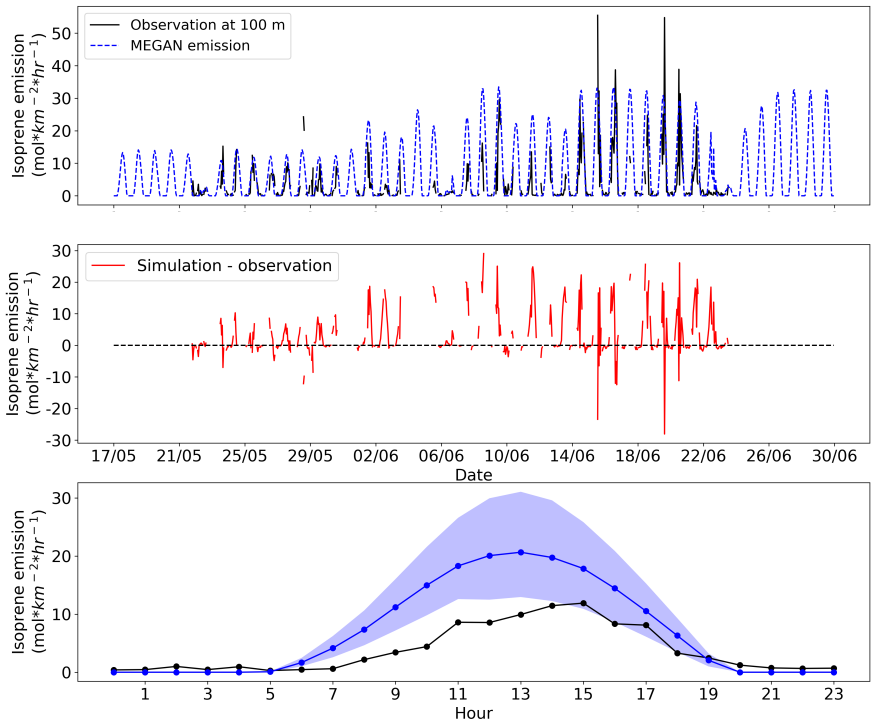

Figure 3.3.3: Comparison of the modelled (blue) and observed (black) isoprene emission time-series (top), bias (middle) and the diel cycle (bottom). The 44-day's averaged emission, as well as the 25th and the 75th percentiles (shaded area) are shown.

3.4 Validation of the chemistry

This section will discuss the ability of the model in reproducing the chemistry. This study aims to understand the isoprene related chemical impacts, which requires a reasonably accurate simulation of the background atmospheric chemistry. Here, I compared the important chemical tracers from the model outputs with the campaign measurements and the hourly record of major pollutants from the Chinese National Air Quality Monitoring Network. Individual isoprene nitrates were measured in Beijing for the first time, which will be used to validate the isoprene nitrate simulations. Since the measurements were taken place on the ground, all data presented here are from the surface layer (¡ 40 m above ground across the domain). Also, results from the nested domain run are not included due to the uncertainties in the emissions.

3.4.1 Important chemical tracers

Fig. 3.4.1 compares the modelled and the simulated CO, SO_2, NO, NO_2, O_3 and OH. Comparison of seven VOCs are shown in Fig. 3.4.2 and Fig. 3.4.3.

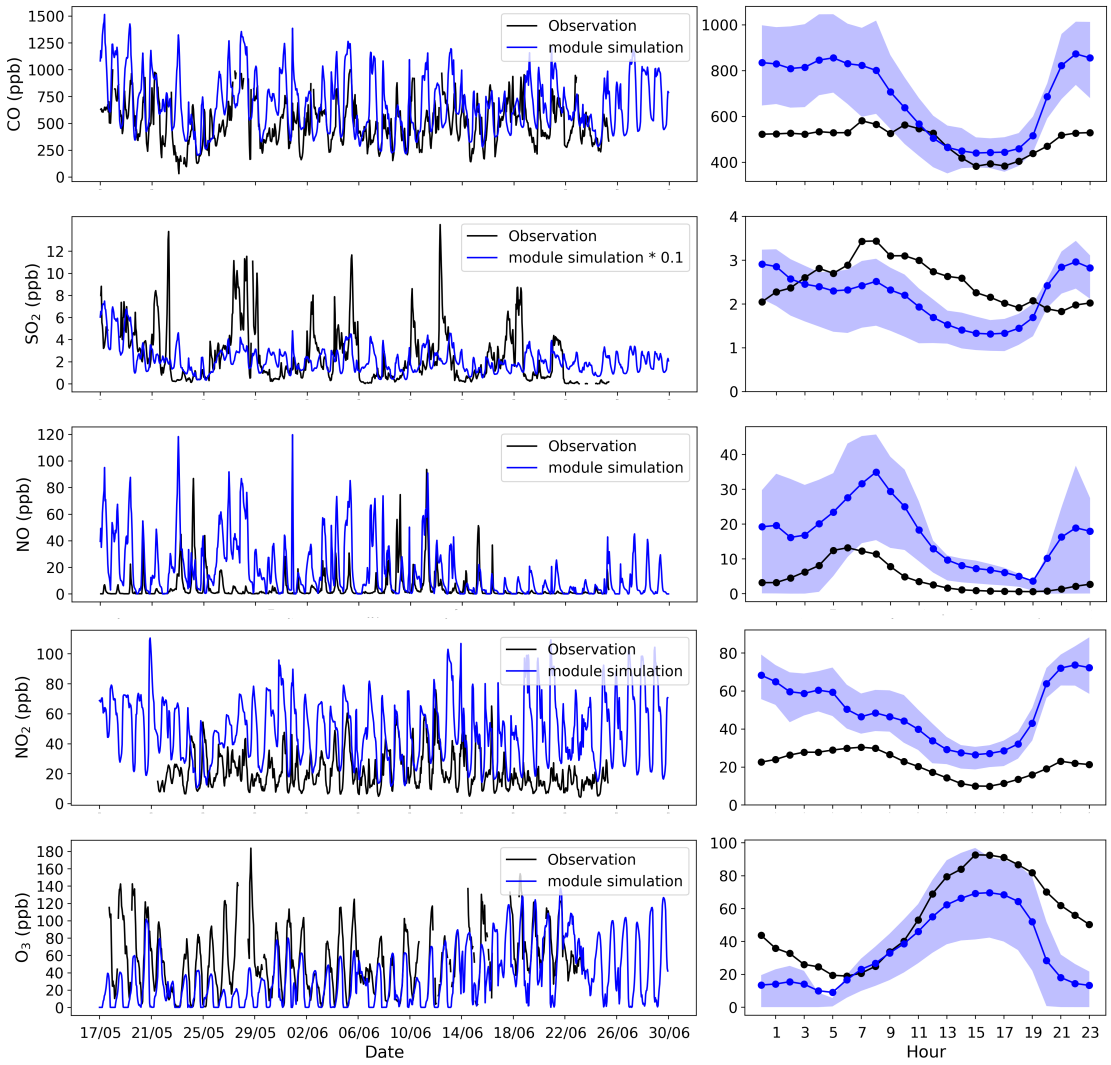

Figure 3.4.1: Comparison of time-series (left) and diel cycles (right) of the modelled (blue) and the observed (black) CO, SO_2, NO, NO_2 and O_3. A factor of 0.1 is applied for SO_2 simulation to compare the diurnal variation.

Apart from SO_2, all trace gases follow similar diel variation as observed. Compared to the observations, lower values of CO, SO_2 and NO_X are simulated in the late afternoon (15.00 to 19.00), which can be due to the dilution effect from the great overestimation of the PBLH (see section 3.2.4). Also, the steep increase in the concentration of these species from 19.00 is likely to be

associated with the collapse of PBL in the model after sunset.

CO is a primary pollutant and is relatively long lived with simple chemical reactions. Hence, the CO concentration simulations of the model reflects its ability to capture the emissions and dynamics. The time-series shows a reasonable agreement of the day-to-day variation between the simulated and the measured CO. Accumulation of CO is seen during the pollution episode (25th to 29th May) from both datasets. However, CO concentrations are considerably overestimated at night and in the early morning (19.00 - 11.00). In the parent domain, CO emission is overpredicted from 6.00 to 23.00 (Fig. 3.3.1), which is likely to result in high concentrations of CO. In noon time, this overestimation is balanced out with the high PBLH in the model. During night, the shallow PBLH leads to considerable overestimation of CO.

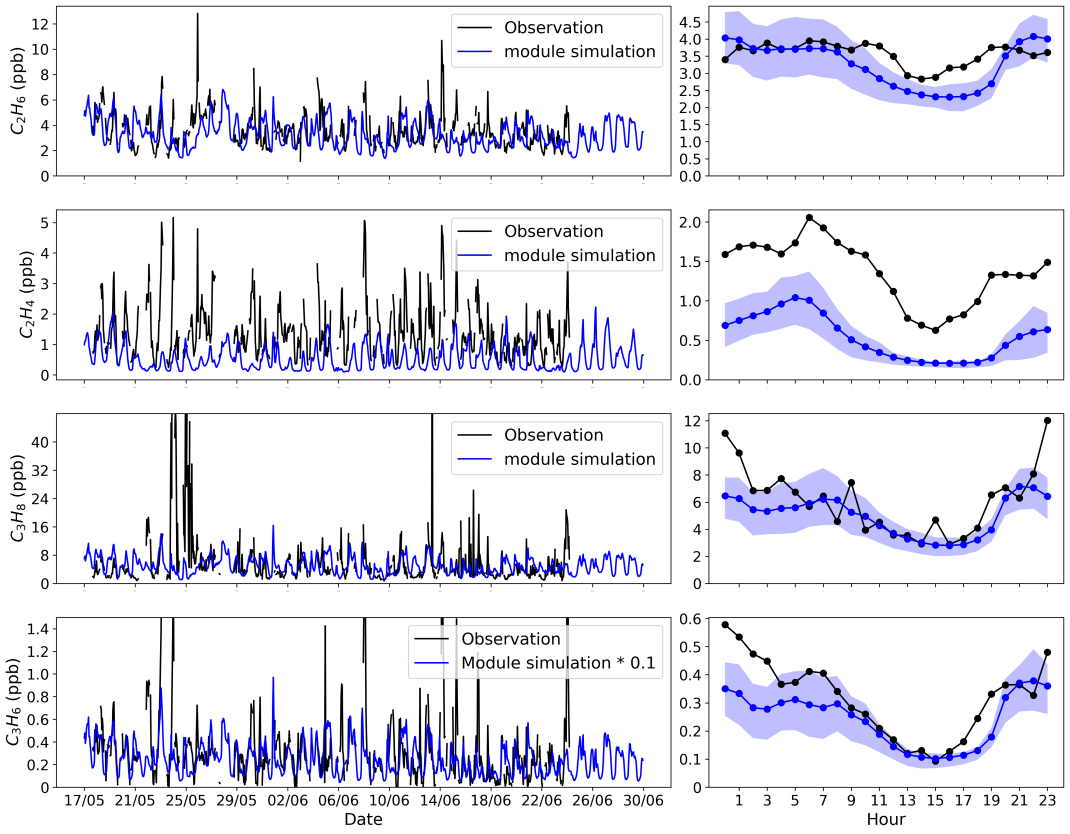

Figure 3.4.2: Same as Fig. 3.4.1, but for ethane (C_2H_6), ethene (C_2H_4), propane (C_3H_8) and propene (C_3H_6). A factor of 0.1 is applied for C_3H_6 simulation to compare the diurnal variation.

NO and NO_2 are overestimated during the whole period, so as their emissions.

Several studies reported the higher simulation of NO_X in China (Li et al., 2018b; Mo et al., 2018). Again, the diel variations of NO_X and SO_2 are likely to be dominated by the PBLH and emissions.

O_3 as a secondary pollutant, its mixing ratio is highly dependent on the concentration of its precursors, which are NO_X and VOCs (introduced in section 1.1). The high NO_X concentration, especically NO concentration, making Beijing a high NO_X environment in which O_3 is lost through reaction with NO. The slow increase of O_3 from 7 to 11 is likely due to O_3 being mixed in from the residual layer above as PBLH increases. At night, when photochemical reactions stop, the presence of NO is a sink of O_3, so an inverse pattern is expected.

Another possible reason for the underestimation of O_3 during daytime is the underestimation of VOCs, which may be a result of very high PBLH simulated in the model.

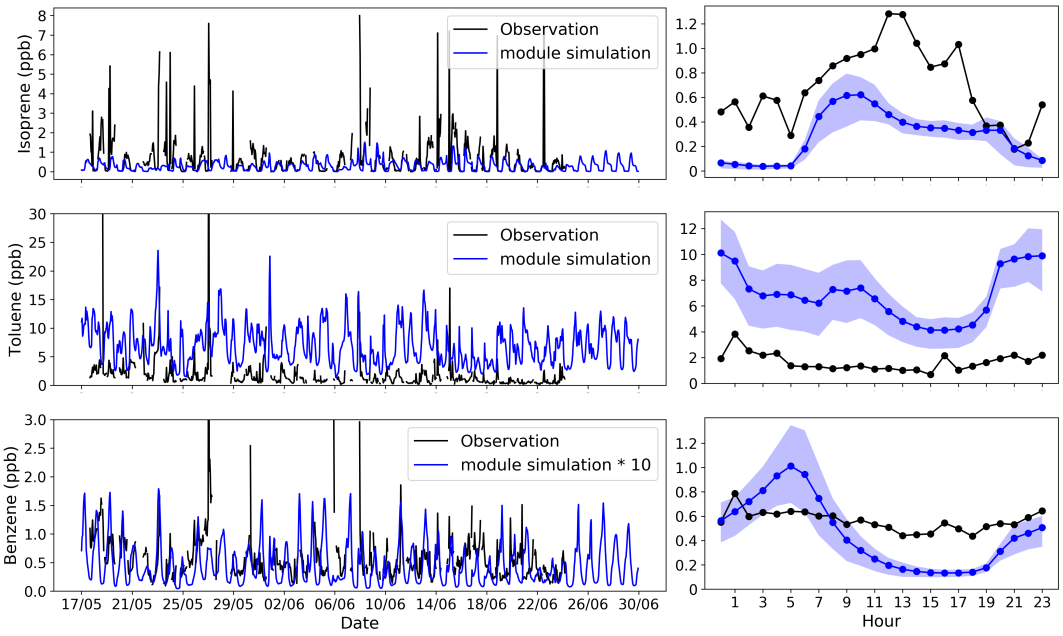

Figure 3.4.3: Same as Fig. 3.4.1, but for isoprene, toluene and benzene.A factor of 10 is applied for benzene simulation to compare the diurnal variation.

The diel patterns of anthropogenic VOCs (AVOCs) are similar. In the model most of the VOCs are lumped, with no individual concentrations. Here, ethane, ethene, propane, propene, isoprene, benzene and toluene are selected for the comparison since they are not lumped in the model. AVOCs show a slight

increase in the morning and a decreasing trend after sunrise with high PBLH. After sunset, their concentraion shoots up due to the collapse of PBLH.

Isoprene shows a different pattern. As a biogenic VOC (BVOC), the emission of isoprene is a function of radiation and temperature. A steep increase in isoprene mixing ratio is simulated and observed from 5, which agree with the rising temperature and radiation. Isoprene observation peaks at noontime with the concentration of 1.4 ppb, which agrees with the previous measurements in northern China (Mo et al., 2018). Since the emission of isoprene is overestimated the underestimation of isoprene concentration at mid-day is likely to be due to the high PBLH.

Isoprene mixing ratio simulation is very low after sunset due to the lack of emission and the high reactivity. However, a sufficient amount of isoprene is measured at night during the campaign, which is believed to be emitted from the vehicle exhaust. The nighttime isoprne emissions are not included in the emission inventory.

Fig. 3.4.4, Fig. 3.4.5 and 3.4.6 compare the averaged model simulation at surface level with the hourly data recorded from the air pollution monitoring networking in China. Data of 54 cities across China are selected in this comparison

The contour map shows the concentration of the species at 0.00 or 12.00, which is averaged over the 45-day period. Observation data from 54 cities were overlayed on top of the contour map and coloured with the same colour scale. Since all the monitoring stations are ground based, only the lowest model layer is used.

Compared to the observations, CO is overestimated in north China during night, but good agreement is shown for the daytime. Several hotspots are not captured in the model, which may be averaged out with the 27 km resolution. Similar results were found previously over eastern China (Zhou et al., 2017). NO_2 and O_3 simulations agree well with the observations at noontime. However, NO_2 is considerablely overestimated at nighte in nothern China, where O_3 is significantly underestimated. This is likely to be due to the titration effect of the high NO_X in the model.

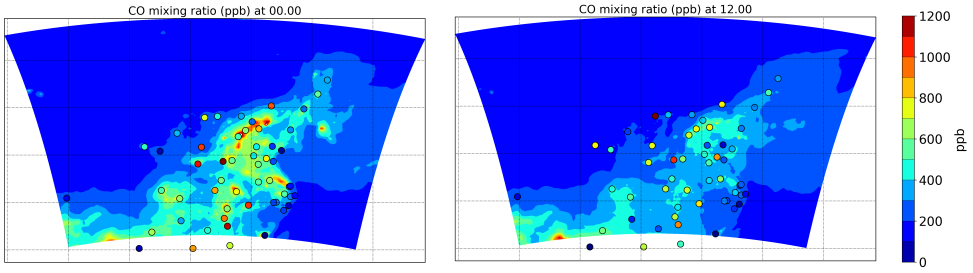

Figure 3.4.4: Averaged contour maps of CO simulation at 0 and 12 with the observations overlayed.

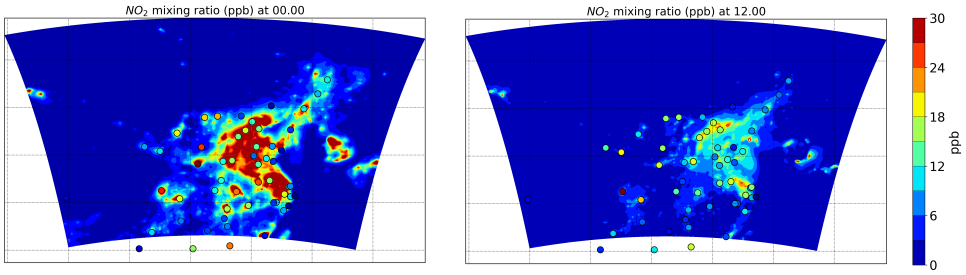

Figure 3.4.5: Same as Fig. 3.4.4, but for NO_2.

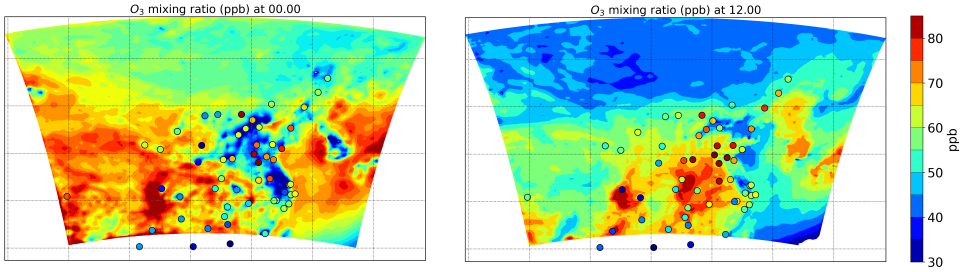

Figure 3.4.6: Same as Fig. 3.4.4, but for O_3.

Variable	Obs Mean	Mod Mean	r	MB	NMB (%)
CO (ppb)	496	679	0.38	171	53.7
NO (ppb)	4.47	169	0.26	13.4	2590
NO_2 (ppb)	21.1	49.1	0.27	25.8	172
SO_2 (ppb)	2.49	21.7	0.25	18.9	8063
O_3 (ppb)	54.2	35	0.59	−22.3	−29.1
OH (m^{-3})	$4.98E6$	$9.76E5$	0.88	$-4.2E6$	−80.2
isoprene (ppb)	0.683	0.287	−0.033	−0.406	219
isoprene day (ppb)	1.03	0.449	0.018	−0.480	−31.6
C_2H_6 (ppb)	3.57	3.26	0.11	−0.315	9.92
C_2H_4 (ppb)	1.39	0.542	0.075	−0.864	−50.7
C_3H_8 (ppb)	6.19	5.01	−0.015	−1.22	50.9
C_3H_6 (ppb)	0.326	2.43	−0.1	2.15	1988
toluene (ppb)	1.67	6.86	−0.044	5.17	711
benzene (ppb)	0.564	0.045	−0.034	−0.519	−89.9
xylene (ppb)	0.846	5.01	−0.044	4.18	894

Table 3.4.1: Comparison of WRF-Chem simuation of Beijing against the campaign measuremets at the IAP site. Only daytime isoprene concentrations are included for the isoprene day calcuation.

The table above shows the statistical evaluation of the trace species simulations against the campaign measurements in Beijing. The mean value, the correlation between the two datasets, mean bias and normalised mean bias are calculated.

CO and NO_2 are slightly overestimated while NO and SO_2 are significantly overpredicted in Beijing. Since NO_X concentration is higher in the model and Beijing is located in the VOC-limited regime, lower O_3 concentraion is expected, which is consistant with the calculated MB and NMB.

For some species such as isoprene, C_2H_6 and C_3H_8, the negative MB is calculated to be negative whereas NMB is postive. This is because of the presence of the very low nighttime concentrations in the observations. In general, these VOCs are underestimated. A massive NB can be calculated if the nighttime observation of the VOCs concentrations is very low while a small peak is simulated in the model. A positive value of NMB is then obtained when NB values are averaged.

3.4.2 Isorpene nitrates chemistry

In section 2.5, I discussed the development of M4 and mentioned that one updated version of MIM (MIM 2014) was implemented to M4. Fig. 3.4.7 shows the hydroxy isoprene nitrates (hy-INs) simulations with the original MIM2 chemical mechanism. As expected, β-INs (IN-(1,2) and IN-(4,3)) concentrations build up through the morning and peak at 1.3 ppt at noontime since it is a product of OH-initiated isoprene peroxy radicals.

However, this is not the case for δ-INs (IN-E/Z(1,4) and IN-E/Z(4,1)). A larger peak of δ-INs is simulated at 21.00 with a value of 4 ppt. This pattern is not observed in IN measurements/chamber studies, nor modelling studies.

I noticed that hy-INs can be formed in the mechanism with the RO_2 cross-body reaction ($RO_2 + RO_2$) of the nitrated isoprene peroxy radical (ISOPNO3), which is

$$\mathrm{ISOPNO3} \xrightarrow{\mathrm{k}} 0.8\,\mathrm{NC4CHO} + 0.02\,\mathrm{ISOPCENO3} + 0.18\,\mathrm{ISOPCZNO3} + 0.6\,\mathrm{HO_2} \tag{3.4.1}$$

where k is $1.3\times10^{-12} \times RO_2$, and RO_2 is the sum of all organic peroxy radicals including LISOPACO2, ISOPBO2, ISOPDO2, ISOPNO3, LHC4ACCO3, LC578O2, C59O2, LNISO3, LHMVKABO2, LMVKOHABO2, MACO3, MACRO2, $CO_2H_3CO_3$, HYPROPO2, PRONO3BO2, CH_3CO_3, $HOCH_2CO_3$, $HCOCO_3$ and CH_3O_2. It is clear that 20% δ-INs (2% ISOPCENO3 and 18% ISOPCZNO3) are formed via this reaction.

In the original mechanism of MOZART-4, the RO_2 cross-body reactions only happen between the peroxy radical with CH_3O_2 and CH_3CO_2, for example, ISOPO2 + CH_3O_2 and ISOPO2 + CH_3CO_2. This might suggest that in MOZART-4 mechanism, CH_3O_2 and CH_3CO_2 may represent the lumped RO_2 that participate in the cross-body reactions rather than these two species. Hence, the RO_2 to calculate k may double count the concentration of total RO_2 leading to a faster reaction rate coefficient.

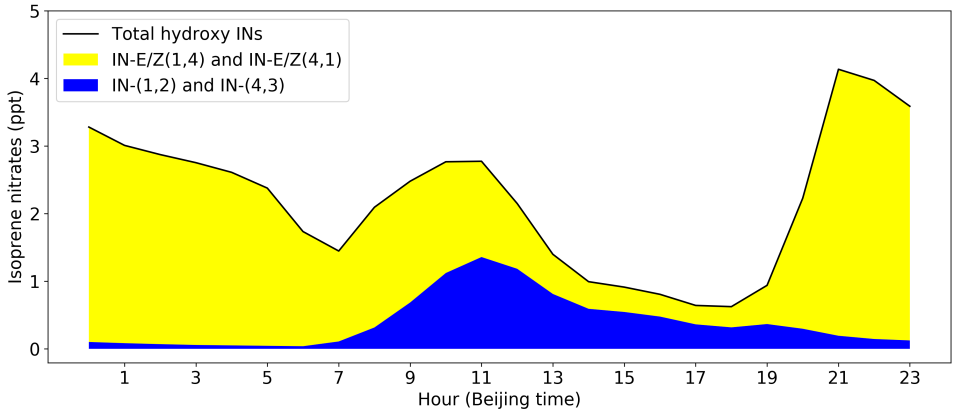

Figure 3.4.7: Accumulative diel cycle of hy-INs simulations in Beijing. The β-INs are coloured in blue while δ-INs are in yellow.

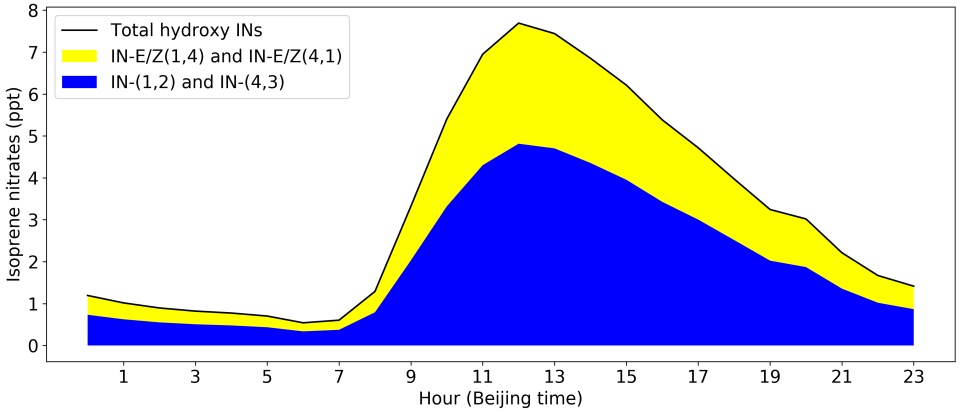

Figure 3.4.8: Same as Fig. 3.4.7, but after modification of RO_2 self- and corss-reactions.

Reaction 3.4.1 is then replaced by the following two reactions recommended by the group that developed MIM2 in an unpublished work in 2014.

$$\begin{aligned}\mathrm{ISOPNO3} + \mathrm{CH_3O_2} \xrightarrow{k_2} 0.75\,\mathrm{CH_2O} + 0.75\,\mathrm{NC4CHO} + \mathrm{HO_2} + 0.25\,\mathrm{CH_3OH} \\ + 0.031\,\mathrm{LISOPCENO3} + 0.219\,\mathrm{LISOPCZNO3}\end{aligned} \tag{3.4.2}$$

where k_2 is 1.3×10^{-12} cm^3 molecule^{-1} s^{-1}.

$$\mathrm{ISOPNO3} + \mathrm{CH_3CO_3} \xrightarrow{k_3} \mathrm{HO_2} + \mathrm{NC_4CHO} + \mathrm{CH_3O_2} + \mathrm{CO_2} \tag{3.4.3}$$

where k_3 is 1.1×10^{-11} cm^3 $molecule^{-1}$ s^{-1}.

Similar changes are made for the cross-body reactions of other peroxy radicals implemented from MIM2.

The simulation of hy-INs with the updated mechanism is shown in Fig. 3.4.8. A pronounced change of the diel pattern of δ-INs (yellow) is simulated. All hy-INs peaks at noontime with the maxima of about 5 ppt of β-INs and approximate 3 ppt of δ-INs. Similar patterns are modelled by Lee et al., (2014).

The increase in hy-INs concentration is because the reaction between ISOPO2 and NO is encouraged since less ISOPO2 are lost through reaction with RO_2. Fig. 3.4.9 illustrates a slight enhancement of O_3 (approximate 5 ppb) in the afternoon with the new chemistry. Given that the diel cycle is averaged throughout 45-days, the updated RO_2 cross-body reactions do impact the simulation of O_3 considerably. Hence, the updated version of MIM2 is applied for this study.

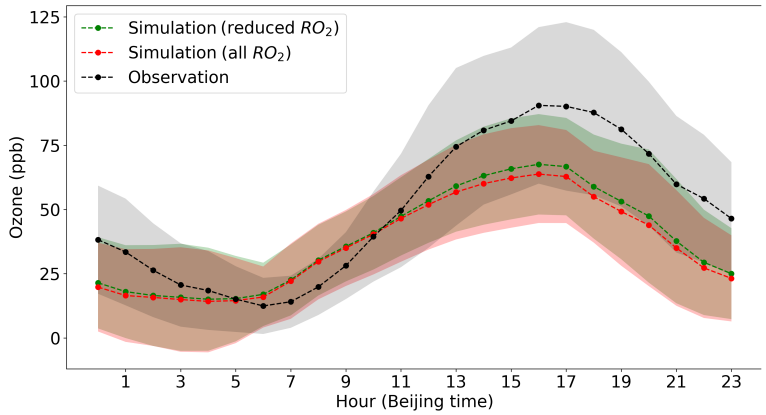

Figure 3.4.9: Comparison of the diel cycle of the observed (black) and simulated (red: MIM2 mechanism; green: updated MIM mechanism) O_3 in Beijing. The standard deviation is shaded.

Isoprene nitrates (INs) were measured at the IAP site and this is the first GC-MS system that is able to measure the individual IN isomers. Fig. 3.4.10 compares the timeseries and the diel variation of three major INs (IN-(1,2), IN-(4,3) and IN-al) simulations with the observations. To make the two dataset comparable, factors of 3 and 0.1 are applied in plotting the simulated IN-(1,2)

and IN-al, which indicates that IN-(1,2) is underestimated by a factor of 3 and the modelled IN-al is a magnitude higher than the measurement.

All three timeseries show a good correlation between the model simulations and the observations, with the correlation coefficient (r) of 0.52, 0.67 and 0.42. The day-to-day variations are also captured such as 10th to 22nd June.

The model diel variations show a similar pattern to the observations when the factors applied. The hydroxyl nitrates (IN-(1,2) and IN-(4,3)) are mainly formed via OH pathway, so they peak during day. While the higher value of the aldehydic nitrates are seen at early night when NO_3-isoprene oxidation dominates the isoprene oxidation.

In a qualitative sense, this good agreement indicates that the model is able to simulate the key chemical processes of isoprene and INs. However, quantitatively, the IN-al is overpredicted by an order of magnitude and IN-(1, 2) is underestimated by a factor of 3. This may be due to the uncertainties of the formation branching ratio between nitrates in the chemistry and/or the uncertainties in the decomposition rate (deposition and photolysis) of these nitrates.

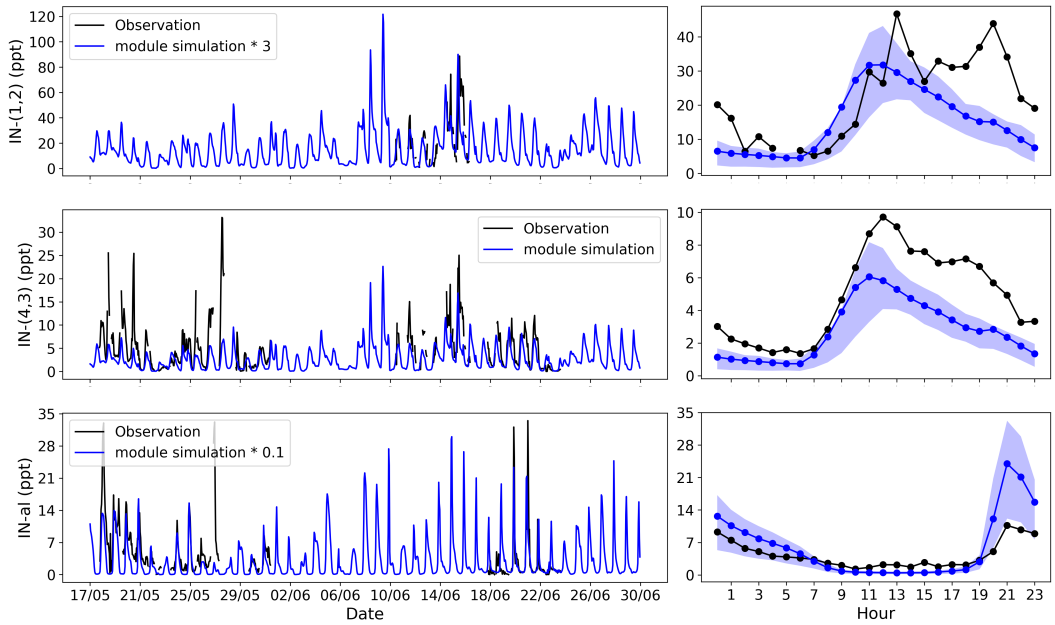

Figure 3.4.10: Same as Fig. 3.4.1, but for IN-(1,2), IN-(4,3) and IN-al. Factors of 3 and 0.1 are applied for IN-(1,2) and IN-al simulations respectively.

3.4.3 Conclusion

This chapter validates the skills of the model in reproducing the reality from three perspectives: meteorological parameters, emissions and chemical tracers. Different data were used for the assessment.

Both parent and nested model run seem to reproduce the meteorological parameters reasonably well. Good agreement between the simulated and observed timeseries and diel pattern of temperature and relative humidity in Beijing are shown. Also, the results become better at higher altitudes since the local factors are eliminated, especially for the wind speed (WS) and direction (WD) verifications. At the surface level WS and WD are greatly affected by the local features, which is hard to be captured by the regional model. With an altitude of aound 250 m, the simulated WS and WD agree well the observations. However, most of the chemical tracers are measured at the ground-level, which is likely to be influenced by the local transport.

Planetary boundary layer height (PBLH) is an important parameter since it represents the intensity of the vertical mixing. PBLH is poorly captured by the model in both domains. The daytime PBLH is overestimated by a factor of 2.5, whereas a very shallow PBLH is modelled at night. That is to say, the concentrations of chemical tracers are diluted during daytime and concentrated at night. Since chemistry is not linear, this change can alter the chemcial regime significantly. Compared to the results of the parent domain, some improvements are seen with higher resolution simulations, however, the coarse domain seems to be good enough in reproducing the meteorology.

Regardless of the absolute values, the diurnal patterns of anthropogenic and biogenic emissions show good agreement with the flux measurements. However, the anthropogenic emissions of 27 km resolution seem to be higher than the flux measurement in Beijing. The emission of the 9 km resolution is considerably lower, which is suggested to be an error during downscaling. Hence, the nested domain run is excluded from the analysis. NO_X emission is overestimated in Beijing according to the inventory, as a result, O_3 is likely to be underestimated in the model.

The simulated chemical species are compared with the field measurements at IAP and the data from air quality monitoring network. As expected, an

overestimation of the primary pollutants is seen at night and an underestimation during the daytime in Beijing, which is a result from the PBLH variation. Geographically, the NO_2 and O_3 simulation at noontime shows good agreement with the surface monitoring data in 54 cities.

The diel pattern of INs is found to be sensitive to the RO_2 cross-body reactions. Good agreement on the diel pattern of the INs are shown, although the absolute values are off. This may suggest the uncertainties in the INs yields in the current chemical mechanism.

Though not all the parameters and concentrations are well captured, this model is still adequate for this study because it offers a reasonable simulation of the meteorological and chemical environment. Good agreements of the diel patterns suggest that the model is able to simulate the main chemcial processes.

4

Insight into isoprene chemistry and its impact

4.1 Introduction

Having shown the model skill in the previous chapter, this chapter aims to understand the detailed isoprene chemistry and its simplified chemical mechanisms in a numerical model by comparing results from runs with different chemical treatments.

As described in section 2.4.3, a chemical mechanism (M4) with more explicit INs chemistry has been developed by adding isoprene related reactions in MIM2 and MCM to the MOZART-4 mechanism in WRF-Chem. To investigate the impact of the complexity of isoprene chemistry in model simulations, a comparison between M4 (Run 1, see section 2.6) and MOZART-4 (Run 3) is presented in section 4.2.

Section 4.3 discusses the contribution of isoprene in both mechanisms by comparing the results with (Run 1 and Run 3) and without (Run 4) isoprene chemistry. M4 and MOZART-4 mechanisms are expected to predict identical results when no isoprene is involved in the chemistry because the only differences between the two mechanisms are isoprene oxidation processes. This is confirmed by a 7-day test. Hence, Run 3 can represent simulations with no isoprene chemistry from both mechanisms.

In both mechanisms, isoprene is not a secondary product of any reactions, so I 'turned off' the isoprene chemistry simply by reducing its emission to zero. For the biogenic emissions, the emission factor of isoprene (MSEBIO_ISOP) in the

emission file (wrfbiochemi_d01) is set to nought over the entire domain. All anthropogenic emissions of isoprene in wrfchemi_00z_d01 and wrfchemi_12z_d01 files are replaced by zero. Also, isoprene is excluded from the input file of producing fire emissions. At the same time, no initial value and boundary conditions are created for isoprene. Run 3 is generated with these files.

The impact of INs chemistry is discussed in section 4.4. In this section, I compared results with full isoprene chemistry (Run1 and Run2), with chemical mechanisms generating no hydroxyl INs (hy-INs) (Run 4 and Run 5) and with the mechanism excluding all INs (Run 6).

As mentioned in section 2.5, different hy-INs isomers are formed via isoprene peroxy radicals (RO_2) and NO reactions with various branching ratios – α. The branching ratio of NO_2 and carbonyls formation through these reactions are 1-α. In Run 4 and Run 5, I set the α of all hy-INs to zero in both mechanisms, which means 100% NO is converted to NO_2 by isoprene peroxy radicals ($ISOPO_2$) derived from OH reaction with isoprene.

Based on Run 5, I also removed aldehydic IN (al-IN) with the same method in the MOZART-4 chemical mechanism creating a mechanism with no INs formation at all (Run 6). The comparison between Run 5 and 6 indicates the contribution of al-IN.

However, I failed to exclude the al-IN in the M4 mechanism. In M4, all al-INs are lumped as NC4CHO, which is produced through a) nitrooxy peroxy radical (NRO_2) reaction with NO, NO_3, OH and RO_2, and b) photolysis of the nitrated hydroperoxide (NROOH) which is formed via the reaction between NRO_2 and HO_2 (Appendix A). That is to say, NC4CHO is an important intermediate involved in all branching reactions of NO_3 initiated isoprene oxidation processes.

NC4CHO is lost through photolysis and reacting with OH, O_3 and NO_3. The products of these reactions are different from each other. Hence, it is impossible to summarize the degradation products of NC4CHO. As a result, al-IN cannot be removed or replaced by its subsequent products in M4 chemical mechanism.

The final section (section 4.5) of this chapter summarizes the results of the previous three sections.

It is worth mentioning that the model domain covers not only China but Mongolia, South Korea, North Korea and part of Russia, Japan, Kazakhstan, India and Myanmar (Fig.4.1.1). The focus of this study is on the impact of isoprene in China, hence the results of these areas will not be discussed in the following chapters. The North China Plain (NCP) and Yangtze River Delta (YRD) regions are two of the most populated and developed city clusters in China, and the chemistry there are discussed in detail.

All contour maps presented in chapter 4 and 5 are plotted with the data from the surface layer (¡ 40 m above the ground) if no altitude is specified. Since isoprene and RO_2 are highly reactive, most of their chemistry is expected to happen in the surface layer. Hence the surface level is selected for most of the analysis.

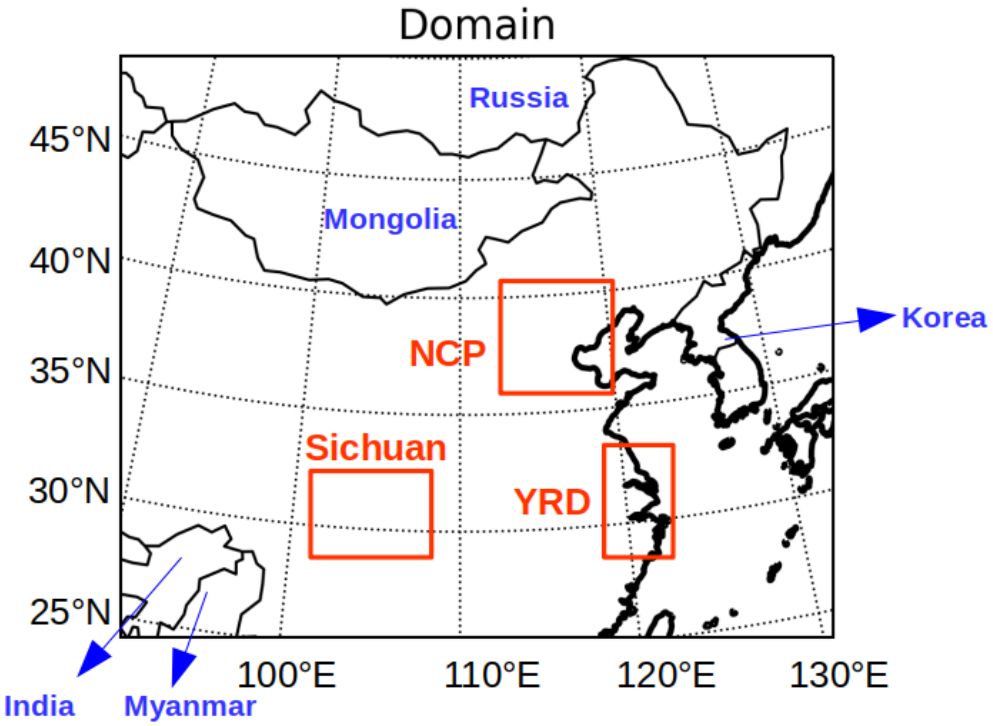

Figure 4.1.1: Map of the domain area. Sichuan province, NCP and YRD regions are in the red boxes. The countries are noted in blue.

4.2 Comparison of the two chemical mechanisms

This section will compare the model results generated with M4 and MOZART-4 chemical mechanisms, and assess the ability of the two mechanisms by comparing with the observations.

Like other chemical mechanism developed for global climate transport model, MOZART-4 mechanism lumps many organic species including isoprene derived species, to reduce the computational cost. For isoprene chemistry, the peroxy radicals, nitrates and many important carbonyls are lumped in MOZART-4. These species represent compounds with different structures and chemical properties. Hence, MOZART-4 chemical mechanism may be not able to reproduce the nonlinear chemistry of isoprene.

Compared to MOZART-4, M4 mechanism includes more isoprene derived products and has more explicit chemical processes of isoprene chemistry. The different simulations of the two mechanisms suggest the impact of the complexity of isoprene chemistry on the tropospheric chemical systems.

I start with the comparison of the isoprene derived species because their chemical fates are the only differences between the two mechanisms (section 4.2.1). The impacts of the different presentations of isoprene chemistry on inorganic species are discussed in section 4.2.2. The inorganic chemistry is the 'base' of one mechanism and the changes in these species will affect the organic compounds. Section 4.2.3 shows results of chemicals involved in the important tropospheric organic chemical systems including the formation of O_3. To investigate the NO_X recycle process between the two mechanisms, the tagging method (see section 4.2.4 for detail) is applied, which can quantitively study the behaviour of NO_X in different branching reactions of isoprene.

4.2.1 Isoprene derived species

This section aims to understand the disparity of isoprene and its derived species simulated by the two chemical mechanisms and the chemical reason behind it.

The 45 days averaged contour map of isoprene and its changes are shown in Fig.4.2.1. High isoprene mixing ratios are simulated in northeast and south China (part of the YRD region), and hotspot is also seen in the NCP region. More broadleaf forest coverage are reported in these regions (Li et al., 2014). However, the average isoprene mixing ratio is lower than 0.2 ppb over most of China. Compared to the simulations in MOZART-4, slightly lower isoprene (less than 10%) is calculated with M4 in the east of China and higher isoprene mixing ratios appear in the west and south of China. The emissions of isoprene remain the same for these two runs, so the differences between the two simulations suggest the different loss rate of isoprene.

There are three major oxidation pathways of isoprene (ISOP in the mechanism) included in both mechanisms, which are by OH, NO_3 and O_3. These reactions in the two mechanism are listed below.

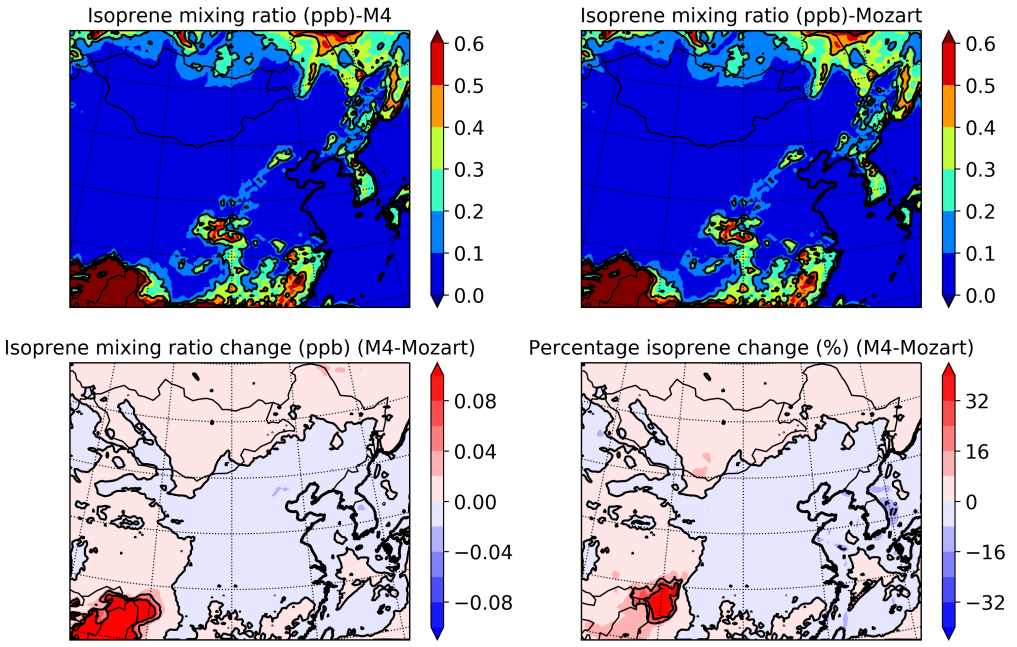

Figure 4.2.1: Contour maps of the average isoprene distribution simulated by M4 (upper left) and MOZART-4 (upper right) chemical mechanisms and the differences between the two (the absolute variation (lower left) and the percentage change (lower right)).

In M4:

$$\mathrm{ISOP + OH \xrightarrow{k_1} 0.4\,LISOPACO2 + 0.35\,ISOPBO2 + 0.25\,ISOPDO2} \quad (4.2.1)$$

where LISOPACO2, ISOPBO2 and ISOPDO2 are the three hydroxyl peroxy radical isomers. The reaction rate coefficient (k_1) of reaction 4.2.1 is $2.7\times10^{-11} \times e^{(390/T)}$ cm^3 molecule^{-1} s^{-1}. Here T is the temperature in the unit of K.

$$\begin{aligned}\mathrm{ISOP + O_3 \xrightarrow{k_2}{}} & \mathrm{0.051\,CH_3O_2 + 0.16\,CH_3CO_3 + 0.054\,LHMVKABO2} \\ & \mathrm{+ 0.52\,CO + 0.069\,HCOOH + 0.11\,H_2O_2} \\ & \mathrm{+ 0.32\,MACR + 0.13\,C_3H_6 + 0.26\,HO_2 + 0.255\,CO_2} \\ & \mathrm{+ 0.75\,CH_2O + 0.041\,MACO_2H + 0.27\,OH + 0.24\,MVK}\end{aligned} \quad (4.2.2)$$

where k_2 is $7.9\times10^{-15} \times e^{(-1913/T)}$ cm^3 molecule^{-1} s^{-1}.

$$\mathrm{ISOP + NO_3 \xrightarrow{k_3} ISOPNO3} \quad (4.2.3)$$

where ISOPNO3 is the nitrated isoprene peroxy radical and k_3 is $3.03\times10^{-12} \times e^{(-446/T)}$ cm^3 molecule^{-1} s^{-1}.

In MOZART-4:

$$\mathrm{ISOP + OH \xrightarrow{k_4} ISOPO2} \quad (4.2.4)$$

where ISOPO2 is the lumped hydroxyl peroxy radical of isoprene. The k_4 is $2.54\times10^{-11} \times e^{(410/T)}$ cm^3 molecule^{-1} s^{-1}.

$$\begin{aligned}\mathrm{ISOP + O_3 \longrightarrow{}} & \mathrm{[k_5]\,0.4\,MACR + 0.2\,MVK + 0.07\,C_3H_6 + 0.27\,OH + 0.06\,HO_2} \\ & \mathrm{+ 0.6\,CH_2O + 0.3\,CO + 0.1\,O_3 + 0.2\,MCO_3 + 0.2\,CH_3COOH}\end{aligned} \quad (4.2.5)$$

where k_5 is $1.05\times10^{-14} \times e^{(-2000/T)}$ cm^3 molecule^{-1} s^{-1}.

$$\mathrm{ISOP + NO_3 \xrightarrow{k_6} ISOPNO3} \quad (4.2.6)$$

where k_6 is euqal to k_3.

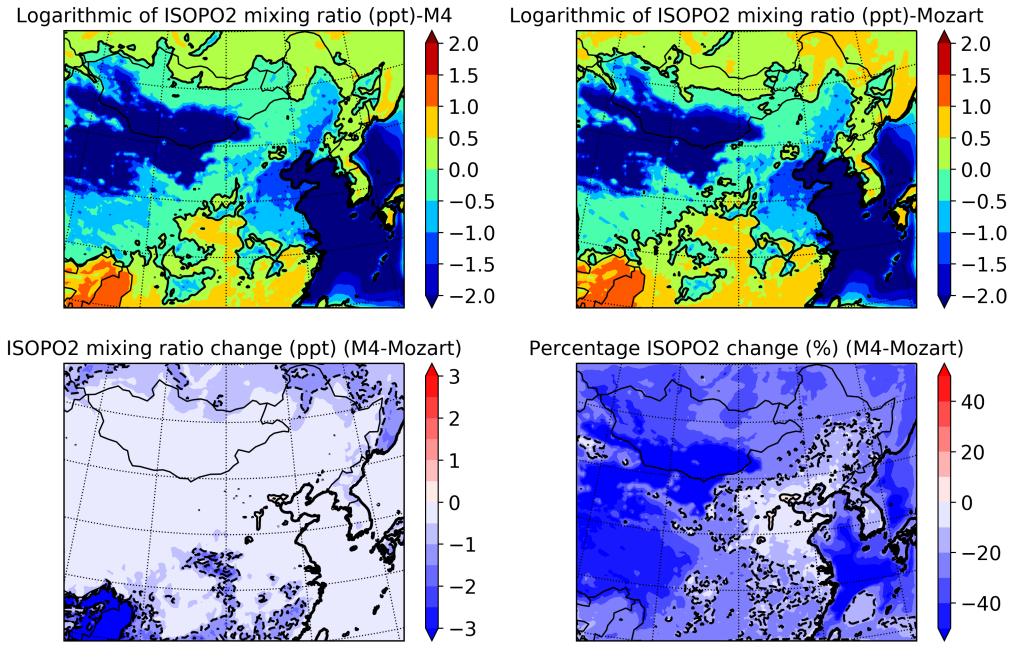

Figure 4.2.2: Same as Fig.4.2.1, but for the hydroxy peroxy radicals of isoprene with the logarithmic scale due to the wide range of values over the domain.

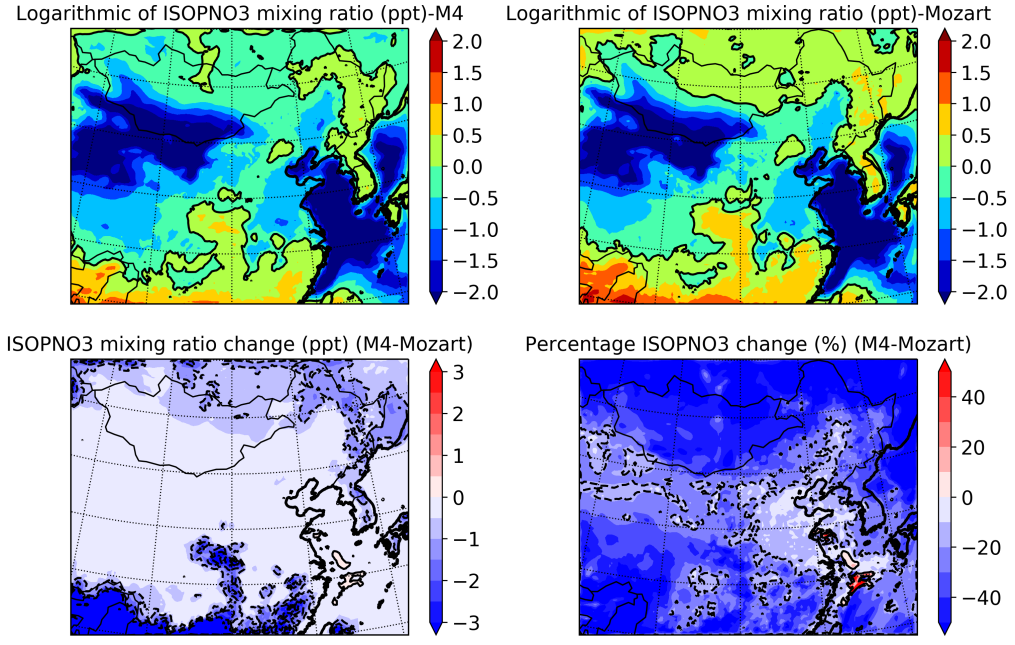

Figure 4.2.3: Same as Fig.4.2.2, but for the nitrated peroxy rdicals of isoprene.

It is clear that isoprene-NO_3 reaction is the same in the two mechanisms, whereas isoprene oxidation by OH and O_3 are simulated differently. The product of ISOP-OH reaction in MOZART-4 mechanism (ISOPO2) is speciated into three isomers in M4, which have distinct subsequent reactions. At 298 K, the reaction rate coefficients of ISOP-OH reactions are close to each other with

the MOZART-4 value larger by 0.6% and this difference is decreasing with higher temperature. More peroxy radicals (RO_2) are formed with the reaction between ISOP and O_3 in M4 than in MOZART-4. The rate coefficient of this reaction in M4 is 0.7% higher than it is in MOZART-4 at 298 K.

However, even with similar (or the same) k, the actual rate of the OH, O_3 and the NO_3 reactions with isoprene in the two mechanisms can vary due to changes in the concentration of the reactants. As a result, it is necessary to understand the behaviour of these inorganic species before interpreting the changes in isoprene.

Both hydroxyl peroxy radicals (ISOPO2, Fig.4.2.2) and nitrated peroxy radicals (ISOPNO3, Fig.4.2.3) of isoprene are lower in the run with more explicit isoprene chemistry over China. There are three potential reasons for this. Firstly, in MOZART-4, isoprene chemistry is compact with most of the intermediates lumped as one species. As a result, total peroxy radicals of isoprene (ISOPRO2 = ISOPO2 + ISOPNO3) in MOZART-4 can represent not only the peroxy radicals of isoprene but some shorter chain RO_2 that are the products of isoprene oxidation.

Also, as shown above, ISOPO2 and ISOPNO3 are products of ISOP-OH and ISOP-NO_3 reactions which is competing with the reaction between isoprene and O_3. That is to say, the lower simulation of ISOPRO2 might be partly due to the declined production if O_3 is enhanced in M4, which is the case here.

Moreover, the chemical fates of ISOPRO2 are represented differently in the two mechanisms. ISOPBO2 is selected as an example of ISOPO2 in M4 to compare with the ISOPO2 in MOZART-4. The ISOPO2 in both mechanisms can react with NO, NO_3, HO_2, CH_3O_2 and CH_3CO_3 and the biggest difference is the ISOPO2-HO_2 reactions, which is listed below.

In M4:

$$\mathrm{ISOPBO2} + \mathrm{HO_2} \xrightarrow{\mathrm{k_7}} \mathrm{ISOPBOOH} \tag{4.2.7}$$

where k_7 is $2.05\times10^{-13} \times e^{(1300/T)}$ cm^3 $molecule^{-1}$ s^{-1}.

In MOZART-4:

$$\mathrm{ISOPO2} + \mathrm{HO_2} \xrightarrow{\mathrm{k_8}} \mathrm{ISOPOOH} \tag{4.2.8}$$

where k_8 is $8.00\times10^{-13} \times e^{(700/T)}$ cm^3 $molecule^{-1}$ s^{-1}.

At 298 K the k_7 (1.61×10^{-11} cm^3 $molecule^{-1}$ s^{-1}) is about twice as much as k_8 (8.38×10^{-12} cm^3 $molecule^{-1}$ s^{-1}), which can contribute to the low ISOPO2 in M4. The k_7 is also consistent with the measurement by Boyd et al. (2003).

The ISOPNO3 simulation in M4 is even lower than ISOPO2. ISOPO2 and ISOPNO3 show similar concentrations in the run with MOZART-4 chemistry, whereas in the run with M4 mechanism the ISOPNO3 is lower by about 70% of the ISOPO2 mixing ratios in south China. Since the productions of ISOPO2 (reaction 4.2.1 and reaction 4.2.4) and ISOPNO3 (reaction 4.2.3 and reaction 4.2.6) in the two mechanisms are with a similar rate coefficient, the low ISOPNO3 concentration suggests addtional sink of it in M4 mechanism, which is by reacting with CH_3O_2 and CH_3CO_3.

$$\begin{aligned}\mathrm{ISOPNO3} + \mathrm{CH_3O_2} \xrightarrow{\mathrm{k_9}} 0.75\,\mathrm{CH_2O} + 0.75\,\mathrm{NC4CHO} + \mathrm{HO_2} + 0.25\,\mathrm{CH_3OH} \\ + 0.031\,\mathrm{LISOPCENO3} + 0.219\,\mathrm{LISOPCZNO3}\end{aligned} \tag{4.2.9}$$

where k_9 is 1.3×10^{-12} cm^3 $molecule^{-1}$ s^{-1}.

$$\mathrm{ISOPNO3} + \mathrm{CH_3CO_3} \xrightarrow{\mathrm{k_{10}}} \mathrm{HO_2} + \mathrm{NC_4CHO} + \mathrm{CH_3O_2} + \mathrm{CO_2} \tag{4.2.10}$$

where k_{10} is 1.1×10^{-11} cm^3 $molecule^{-1}$ s^{-1}.

These reactions do not exist in the MOZART-4 mechanism resulting in a disparity between ISOPNO3 simulations, especially in areas with low NO_X emissions where the radical cross-body reactions become an important sink of ISOPNO3. That is to say, a more considerable impact of implementing the explicit isoprene chemistry will be on the low NO_X environment.

Higher isoprene hydroperoxides (ISOPOOH) are simulated with M4 over most of the domain (Fig.4.2.4), especially in the northeast and south of China with high isoprene emissions and low NO_X emissions. This is not a surprise since ISOPOOH is the product of the accelerated ISOPRO2-HO_2 reaction, which is of great importance in the ISOPO2 degradation in low-NO high-isoprene regions. However, the maximum percentage difference (over 120%) appears in the NCP regions in China. This is due to the low ISOPOOH formation simulated with MOZART-4 chemistry in this area reaction 4.2.8.

The fate of ISOPOOH is also developed differently in the two mechanisms. The dominant sink of ISOPOOH in the atmosphere is reaction with OH due to its very fast rate coefficient (listed below).

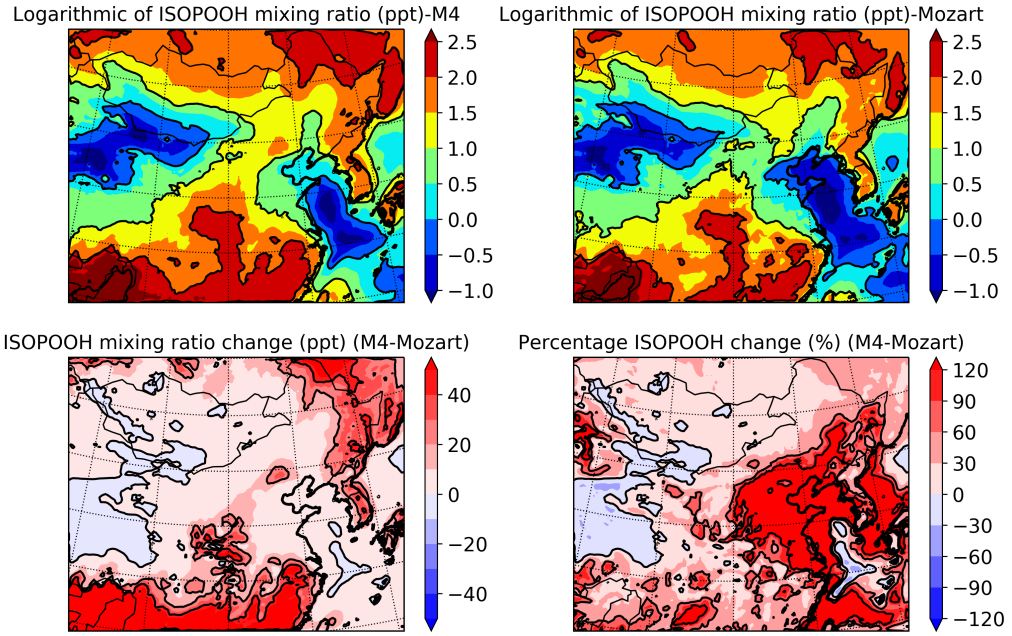

Figure 4.2.4: Same as Fig.4.2.2, but for the isoprene hydroperoxides.

In M4:

$$\text{LISOPACOOH} + \text{OH} \xrightarrow{k_{11}} 0.95\,\text{MACROH} + 0.95\,\text{OH} + 0.95\,\text{CH}_2\text{O} + 0.05\,\text{H}_2\text{O} + 0.05\,\text{LISOPACO2} \tag{4.2.11}$$

where k_{11} is 1.54×10^{-10} cm^3 molecule^{-1} s^{-1}.

$$\text{ISOPBOOH} + \text{OH} \xrightarrow{k_{12}} 0.92\,\text{LIEPOX} + 0.92\,\text{OH} + 0.08\,\text{H}_2\text{O} + 0.08\,\text{ISOPBO2} \tag{4.2.12}$$

where k_{12} is 5.0×10^{-11} cm^3 molecule^{-1} s^{-1}, LIEPOX is the lumped isoprene expoxydiols (IEPOX).

$$\text{ISOPDOOH} + \text{OH} \xrightarrow{k_{13}} 0.92\,\text{LIEPOX} + 0.92\,\text{OH} + 0.08\,\text{H}_2\text{O} + 0.08\,\text{ISOPDO2} \tag{4.2.13}$$

where k_{13} is 1.07×10^{-10} cm^3 molecule^{-1} s^{-1}.

$$\text{NISOPOOH} + \text{OH} \xrightarrow{k_{14}} \text{NC4CHO} + \text{OH} \tag{4.2.14}$$

where k_{14} is 1.03×10^{-10} cm^3 molecule^{-1} s^{-1}, NC4CHO is the lumped al-INs.

In MOZART-4:

$$\text{ISOPOOH} + \text{OH} \xrightarrow{k_{15}} 0.5\,\text{XO2} + 0.5\,\text{ISOPO2} \tag{4.2.15}$$

where k_{15} is $1.52\times10^{-11} \times e^{(200/T)}$ cm^3 molecule^{-1} s^{-1} (2.97×10^{-11} cm^3 molecule^{-1} s^{-1} at 298 K), XO2 is lumped peroxy radical from OH reacting with unsaturated hydroxycarbonyls.

As mentioned above, ISOPO2 can react with NO, NO_3, HO_2 and other RO_2. Hence, the faster ISOPO2-HO_2 in M4 becomes more competitive to the other branchings. As a reault, less methyl vinyl ketone (MVK), methacrolein (MACR) and INs are formed in M4 since the ISOPO2-NO pathway is less competitive. These results are shown in Figs.4.2.5, 4.2.6 and 4.2.7.

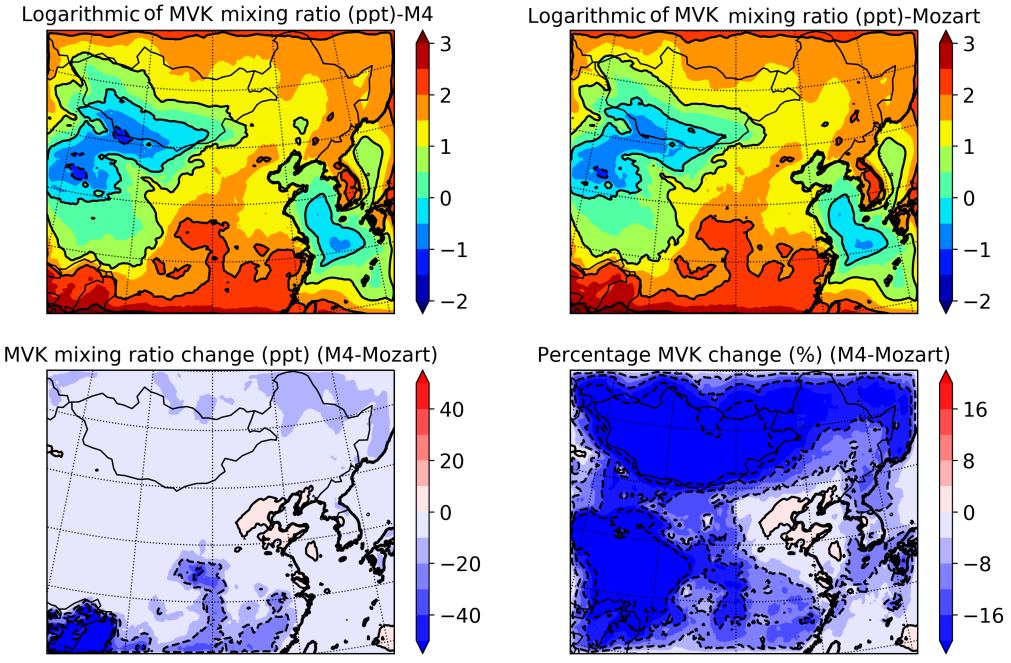

Figure 4.2.5: Same as Fig.4.2.2, but for the MVK.

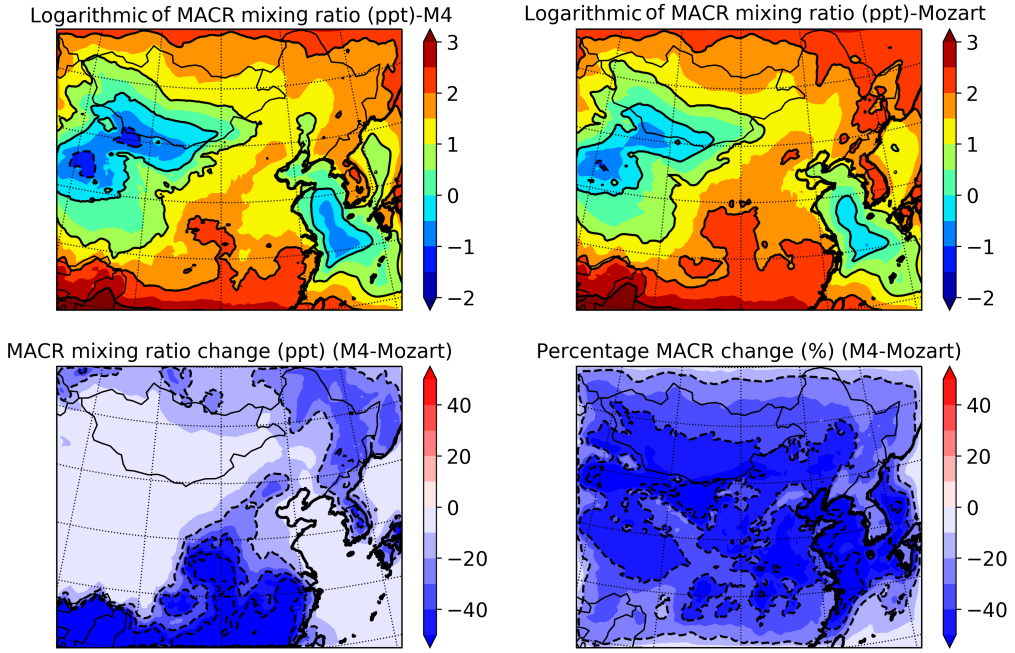

Figure 4.2.6: Same as Fig.4.2.2, but for the MACR.

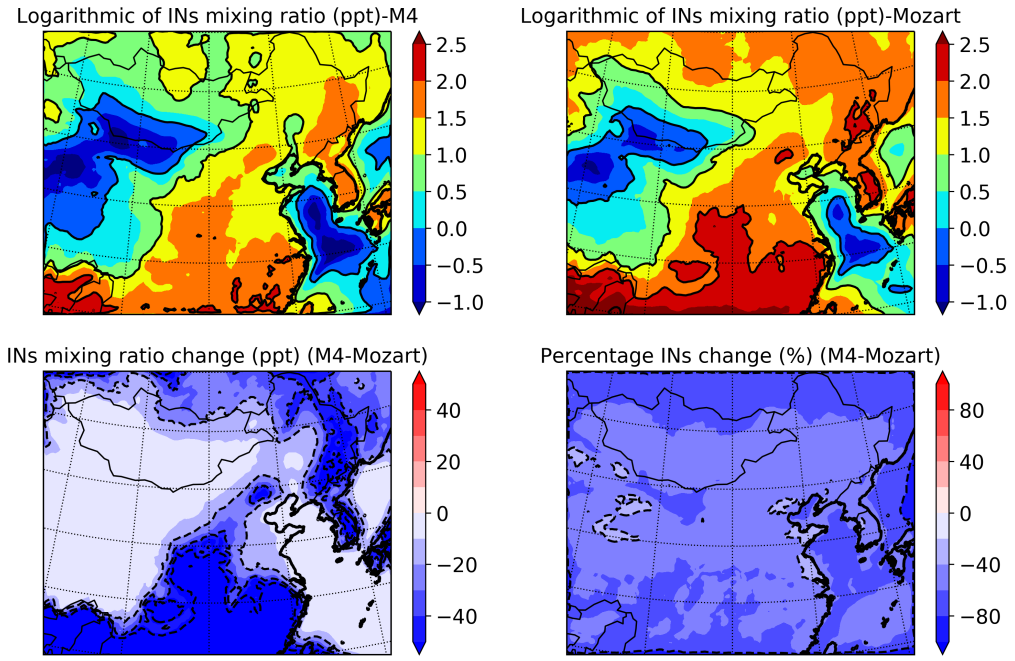

Figure 4.2.7: Same as Fig.4.2.2, but for the total isoprene nitrates.

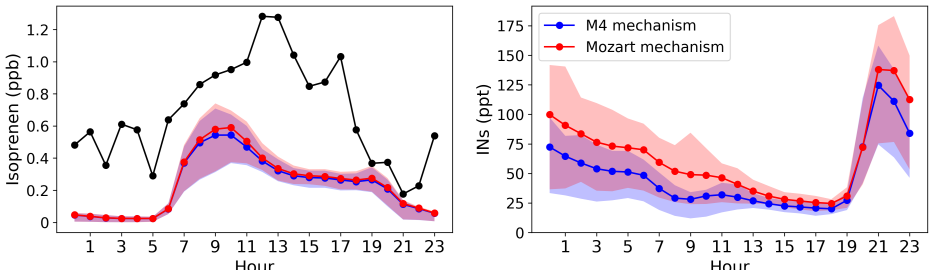

Figure 4.2.8: Averaged diel cycle of the observed (black) and simulated (blue for M4 and red for MOZART-4) isoprene (left) and INs (right) mixing ratios in Beijing during the campaign period. The shaded areas are the 25th and the 75th percentiles from each run.

The averaged diurnal cycle of isoprene and INs in Beijing over the 45-day period are shown in Fig.4.2.8. The isoprene simulations from the two runs are similar to each other. Slightly lower concentration of isoprene is predicted with M4 in the morning. As discussed earlier, the reaction rate coefficient of the first generation of isoprene oxidation is similar in the two mechanisms, which suggests that this difference is likely to be due to the variation of the concentration of its oxidants (see section 4.2.2 for detail).

Both runs simulate a similar diel pattern of INs, which suggest that the major chemical processes of INs are simulated similarly in the two chemical mechanisms. INs concentrations simulated by both mechanisms decrease over the day and reach the minima at 18.00. A steep increase of INs from 19.00 to 21.00 is modelled with the INs mixing ratio changes from 25 ppt to over 100 ppt. This dramatic increase is likely to be due to the changes in the boundary layer height, which traps INs in a 5 times shallower boundary layer from 19.00 to 21.00.

Hydroxy INs(hy-INs) are formed mainly during the daytime through the OH initiated oxidation pathway of isoprene. In the early night, NO_3 can react with the residual isoprene forming ISOPNO3, which can lead to the production of aldehydic INs (al-INs). Since the ISOPO2 generated in the NO_3 initiated chemistry is already nitrated, the branching ratio of al-INs formation is about 10 times higher as the ratio of hy-INs.

The higher INs concentrations simulated in Run 3 can suggest a larger formation of INs in MOZART-4, which is consistent with the earlier discussion.

Also, in MOZART-4, INs is not only derived from isoprene but also from the lumped monoterpene, which includes alpha-pinene, beta-pinene, limonene and myrcene. Hence higher concentrations of INs are calculated by MOZART-4 is understandable. The difference between the two simulations becomes smaller through the day, which suggesting the loss of INs in MOZART-4 is faster than they are in M4.

4.2.2 Important chemical tracers of O_3 formation

This section presents the discussion of the important organic species that are related to the O_3 formation mechanism.

The changes of total VOCs (including isoprene) are illustrated in the Fig.4.2.9. The concentrations of VOCs are lower by up to 2% in simulation with M4 mechanism over east China than they are calculated with MOZART-4 mechanism. Small changes on VOCs are within my expection since the only difference between the two run is the treatment of isoprene oxidation chemistry. In west China, slightly more VOCs are simulated with more explicit isoprene chemistry. The change of VOCs can be attributed to the oxidation capacity of the atmosphere. Hence, higher concentrations of oxidants (such as OH and O_3) are expected in east China in M4 simulation, which is consistent with Fig.4.2.12) and Fig.4.2.20) in the next section.

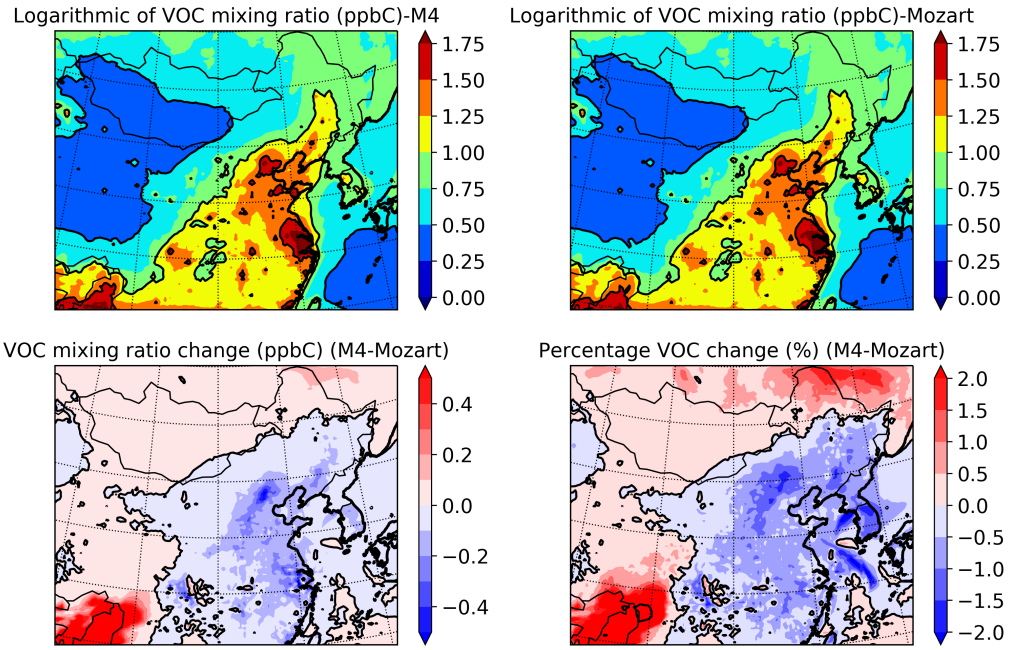

Figure 4.2.9: Same as Fig.4.2.2, but for the VOCs.

CH_3O_2 and CH_3CO_3 are two crucial peroxy radicals that involved in RO_2 cross-body reactions in the mechanisms. As a result, they are selected as example of RO_2 variation between the two outputs. Fig.4.2.10 and Fig.4.2.11 show the CH_3O_2 and CH_3CO_3 simulations with the two mechanisms, as well as the differences between the two. Higher CH_3O_2 and CH_3CO_3 are calculated over most of the domain with M4 chemical mechanism. In MOZART-4, these two RO_2 participate in around 40 reactions of other RO_2 and the decomposition of organic nitrates. More RO_2 and nitrates from isoprene oxidation intermediates are included in M4, including additional over 30 reactions of CH_3O_2 and CH_3CO_3. Hence, more RO_2 are cycled and formed in M4 chemistry. Similar results are reported by Archibald et al. (2010) with the box model comparison.

Moreover, some of the RO_2 cross-body reactions have been modified with higher RO_2 yields in M4 mechanism.

In MOZART-4:

$$\mathrm{MCO3} + \mathrm{HO_2} \xrightarrow{k_{16}} 0.25\,\mathrm{O_3} + 0.25\,\mathrm{CH_3COOH} + 0.75\,\mathrm{CH_3COOOH} \qquad (4.2.16)$$

Whereas in M4:

$$\mathrm{MCO3} + \mathrm{HO_2} \xrightarrow{k_{17}} 0.44\,\mathrm{OH} + 0.15\,\mathrm{CH_3CO_3} + 0.29\,\mathrm{CH_3O_2} + 0.29\,\mathrm{CO} + 0.44\,\mathrm{CH_2O} + 0.44\,\mathrm{CO_2} + 0.15\,\mathrm{MACO2H} + 0.15\,\mathrm{O_3} \qquad (4.2.17)$$

The concentration of RO_2 is important in O_3 formation since the reaction between RO_2 and NO can produce NO_2 without destruction of O_3. In the high NO_X environment (NCP and YRD regions), the enhanced RO_2 can encourage the formation of O_3 (Fig.4.2.12) by converting more NO to NO_2. This can contribute to the high O_3 concentration in these regions in the run with explicit isoprene chemistry.

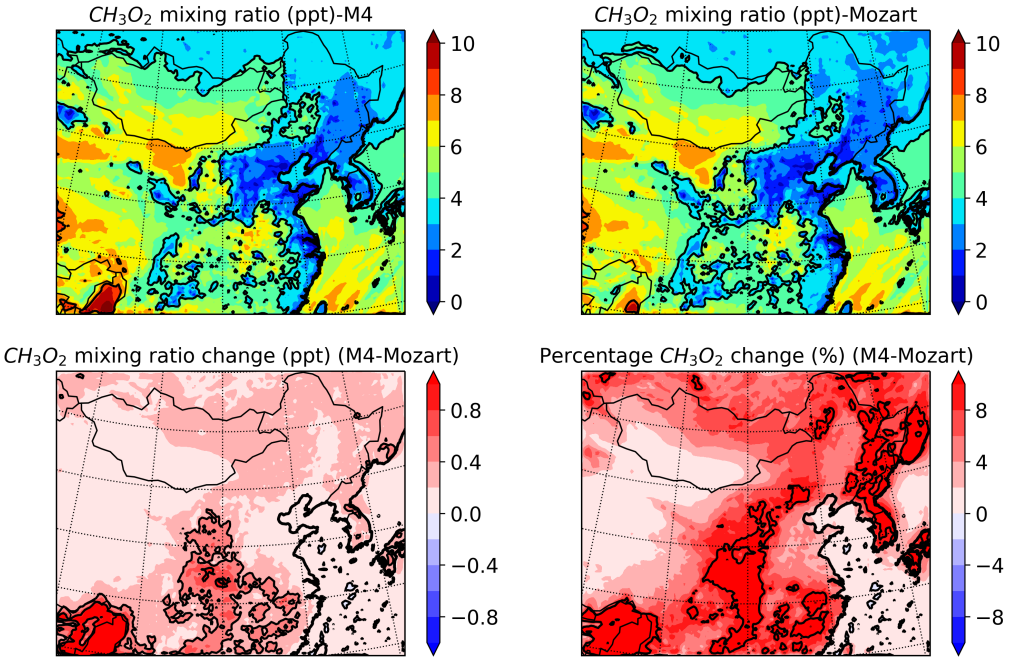

Figure 4.2.10: Same as Fig.4.2.1, but for the CH_3O_2.

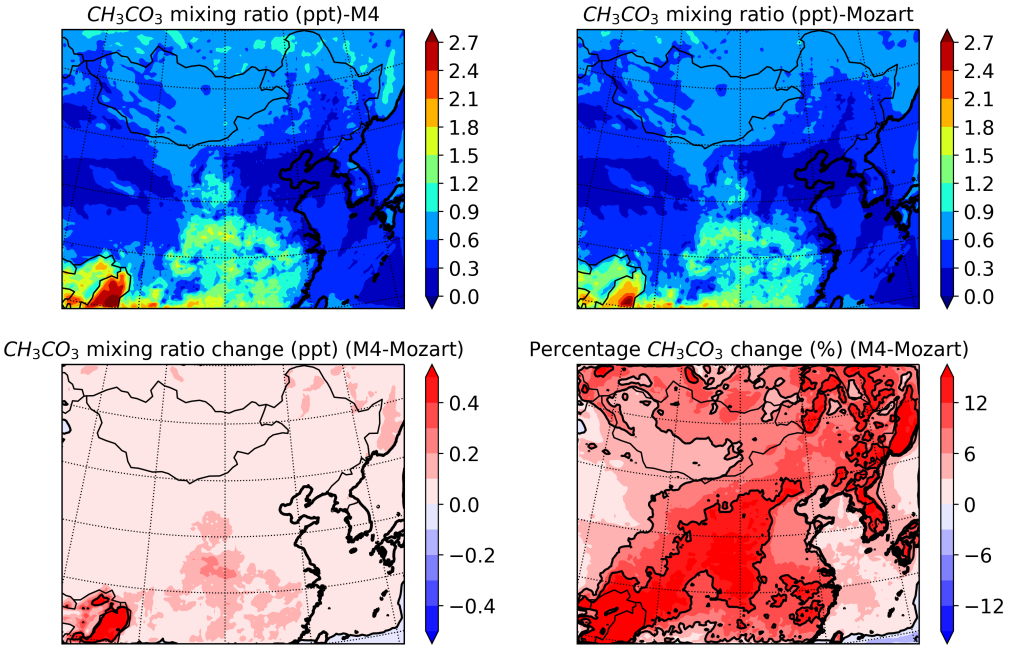

Figure 4.2.11: Same as Fig.4.2.1, but for the CH_3CO_3.

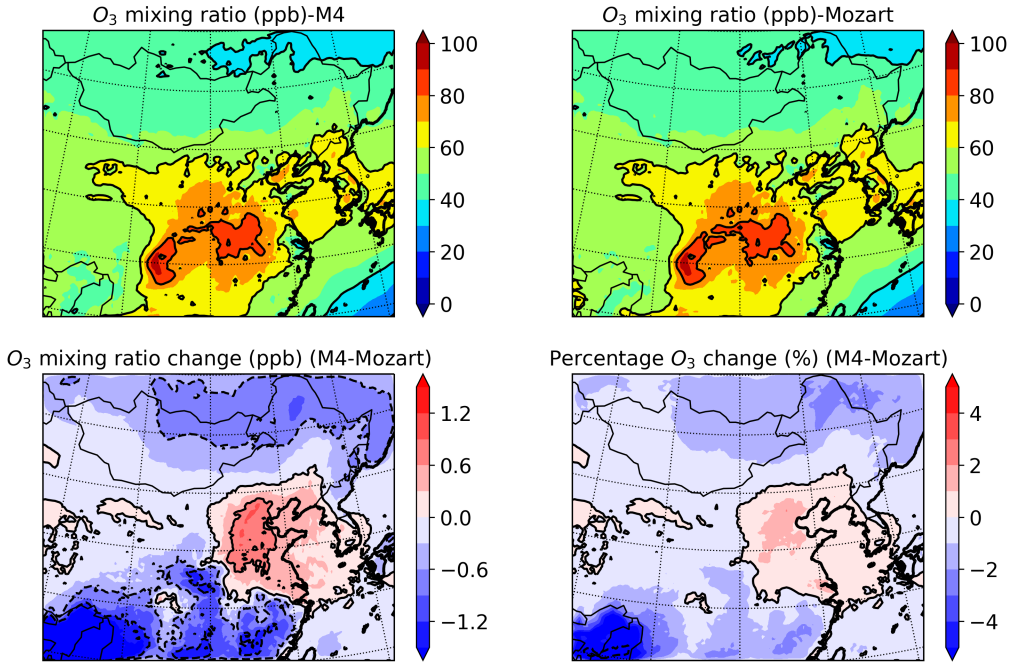

Figure 4.2.12: Same as Fig.4.2.1, but for the O_3.

However, this is not the case in the low NO_X environment. In regions with low NO_X mixing ratios, such as west of China, the formation of hydroperoxides (ROOH) becomes an important sink of RO_2 competing with the RO_2-NO pathway reaction 4.2.18. As a result, O_3 formation is hindered leading to lower O_3 concentrations.

$$CH_3O_2 + HO_2 \xrightarrow{k_{18}} CH_3OOH(+O_2) \qquad (4.2.18)$$

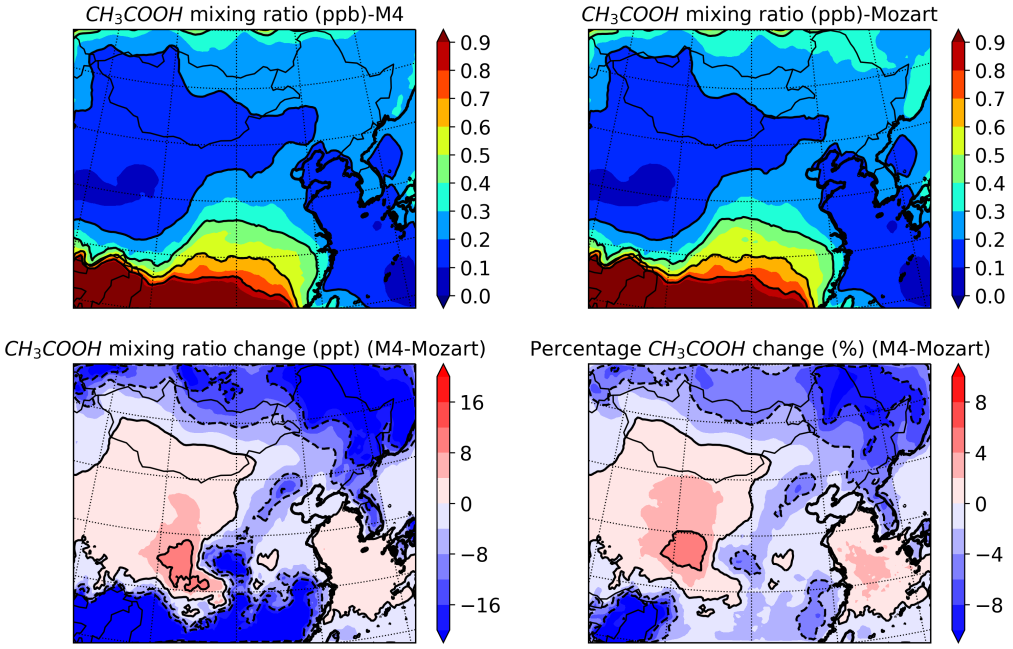

Figure 4.2.13: Same as Fig.4.2.1, but for the CH_3COOH.

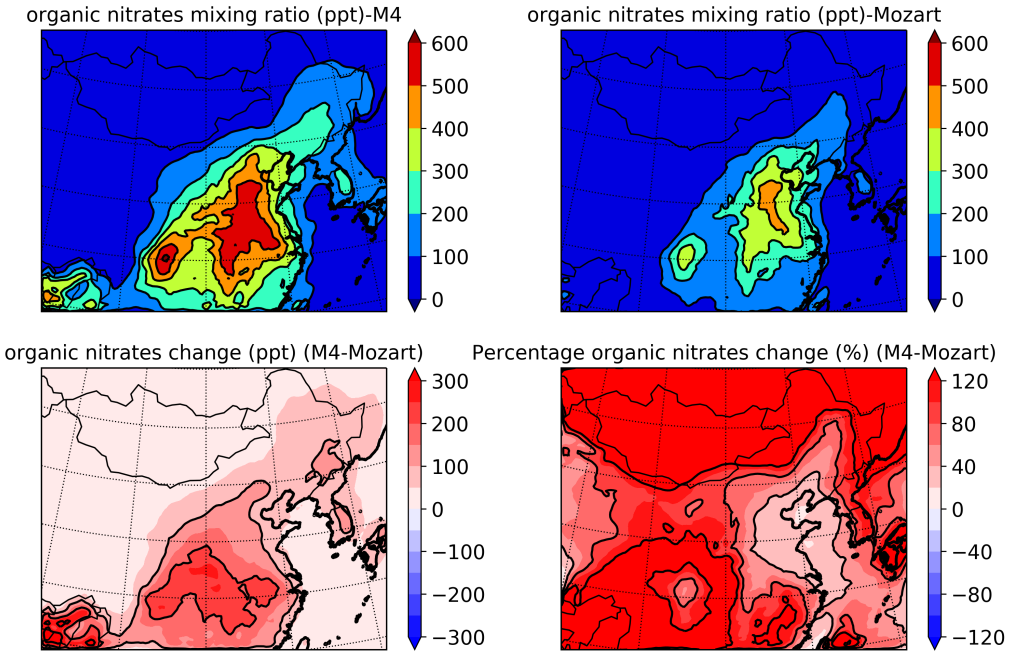

Figure 4.2.14: Same as Fig.4.2.1, but for the organic nitrates.

O_3 is the primary source of OH in the atmosphere, so the variation of O_3 can impact the distribution of OH (Fig. 4.2.20). That is to say, in Run 1, the higher O_3 in NCP and YRD regions may contribute to enhanced OH in east China, whereas the lower OH number density may be partly owing to the declined O_3 concentrations in west China.

The variation of CH_3COOH (Fig.4.2.13) is consistent with the previous discussions. Higher CH_3COOH concentrations are modelled in regions with low NO_X mixing ratios (< 1 ppb). CH3COOH can be removed from the atmosphere easily through deposition. Hence it can be considered as a sink of RO_2 in the model, especially for one CH_3COOH molecule formed two RO_2 are consumed. Since the formation of CH_3COOH reduces RO_2 concentration making O_3 production inefficient, an opposite pattern to O_3 changes are shown in the middle of China in Fig.4.2.12.

In south China, both ROOH species and O_3 show lower values, whereas RO_2 species are not (Fig. 4.2.10 and Fig. 4.2.11). As introduced in the first chapter, the RO_2-NO reaction can also form organic nitrates, which temporarily terminates the O_3 production by tying the NO_X into the nitrate functional group.

Fig.4.2.14 and Fig.4.2.15 illustrate the distribution and variability of the organic nitrates and peroxyacetyl nitrate (PAN), respectively. The 'organic nitrate' here is not all the nitrates in the model. The INs and PAN are excluded and analysed separately and the rest organic nitrates are sumed up and referred as the 'organic nitrates' for the discussion in the following text. Both of them are simulated with higher values in Run 1, especially for the organic nitrates, which can reach twice as much as it is in Run 3 over south of China. PAN is mainly produced with the reaction between CH_3CO_3 with NO_2. Hence, the maximum increase of PAN appears in the southwest of China where has sufficient amount of CH_3CO_3 and NO_2. Same story are seen in the organic nitrates.

The modelled and observed the diel cycle of VOCs (left) and O_3 (right) in Beijing are shown in Fig.4.2.16. Simulations of two mechanisms are very similar and the 25th and the 75th percentiles almost overlap with each other. Due to the slightly higher OH during the daytime, the concentration of total VOCs in M4 is marginally lower than it is in MOZART-4. Again, this change is so small that is not comparable with the disparity between the simulated and measured

VOCs.

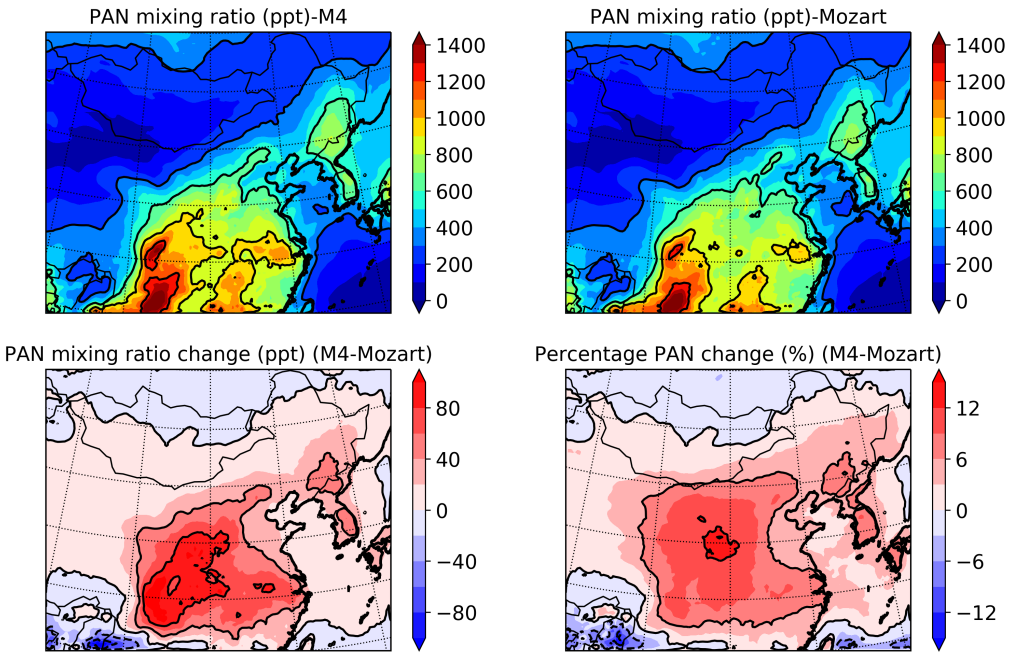

Figure 4.2.15: Same as Fig.4.2.1, but for the PAN.

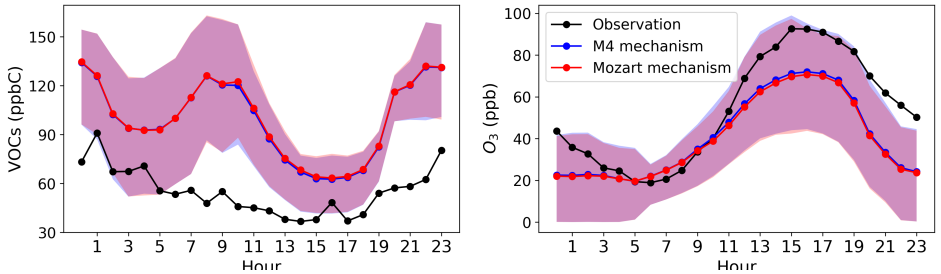

Figure 4.2.16: Same as Fig.4.2.8, but for VOCs (left) and O_3 (right).

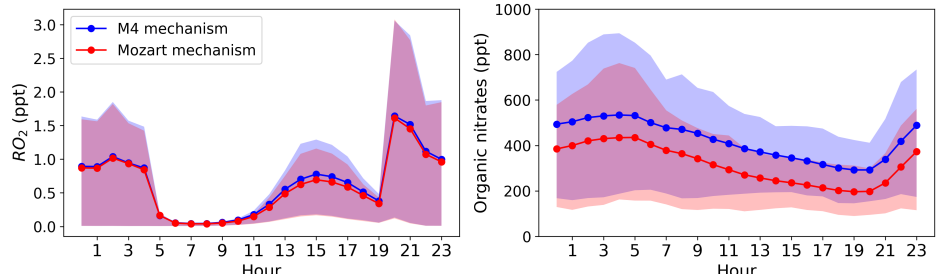

Figure 4.2.17: Same as Fig.4.2.8, but for RO_2 (left) and organic nitrates (right).

As discussed earlier in this section, owing to the increasing RO_2 in NCP region (where Beijing is located) in Run 1, O_3 production can be more efficient leading to a slightly higher O_3 during the day. However, on average, this variation is less than 1 ppb and 2% of its mixing ratio. The averaged percentage changes in O_3 over China included in the domain are within ±4% (Fig.4.2.12). Hence, I can conclude that the original MOZART-4 chemical mechanism is adequate for O_3 predictions in China.

However, significant differences appear in some organic species such as organic nitrates. Fig.4.2.17 shows the diurnal variation of RO_2 (left) and organic nitrates (right). The slight incremental of RO_2 in Run 1 is consistent with the higher OH during the daytime (Fig.4.2.22). The enhancement of OH and RO_2 may lead to a higher oxidation capacity of the atmosphere, which can affect the chemical kinetics.

Two peaks are simulated of RO_2: one occured at 15.00 with the value of 0.8 ppt, and the other one appeared at 20.00 with the maximum value of 1.7 ppt. RO_2 is formed and accumulated during daytime with increasing intensity of the solar radiation and reached its daytime peak at 15.00. Again, the steep increase of RO_2 concentration after sunset is due to the collapse of the boundary layer height in the model. RO_2 concentration decreases rapidly from 4 to 5 with the increasing PBLH.

Compared to Run 3, organic nitrates concentrations simulated with M4 are about 200 ppt higher through the day in Beijing. Given that the loss process of the organic nitrates remains unchanged in M4, the variation of its concentration suggest additional sources of organic nitrates. The primary sources of organic nitrates in MOZART-4 are from the oxidation of C_3H_6 and big alkanes, whereas in M4, in addition to these, organic nitrates are also formed during the degradation of INs (IN-E/Z(1,4), IN-E/Z(4,1) and al-INs). This suggests that less NO_X is recycled back to the atmosphere via INs in M4, which agrees with the results shown in the section 4.2.4.

In both mechanisms, the organic nitrates is a lumped species that represent various nitrates and is hard to identify its composition. As a result, there is no observation to validate the simulations. So, including more explicit isoprene chemistry does has an impact on the organic chemistry, however, due to the difficulties in validation, whether this impact is an improvement or not is unclear.

4.2.3 Inorganic chemistry

Fig.4.2.18 shows the averaged NO_X simulations of M4 and MOZART-4 mechanism and the differences between the two. The results show high agreement. The percentage differences of NO_X is lower than 5% over most of China. Apart from some regions in west China, NO_X predicted with M4 mechanism is slightly lower with a maximum difference of -0.4 ppb in the cities in the North China Plain (NCP).

As introduced in section 4.2.1, the only primary loss of NO_X is by reacting with OH forming HNO_3 which has a high deposition rate. Hence, this decrease of NO_X can be a result from an enhancement of OH (Fig.4.2.20, daytime only) leading to increasing HNO_3 formation (Fig.4.2.19) in the benchmark run.

The changes in OH (Fig.4.2.20) and HO_2 (Fig.4.2.21) generally match up. Slightly higher mixing ratios are simulated in Run 1 over east of China, especially in the Taihang mountain area. The similar pattern between OH and HO_2 variation suggests that the HO_X chemistry are represented similarly in both mechanisms, which is understandable since the inorganic chemistry (including the main HO_X partitioning reactions) and organic chemistry for VOCs (OH-VOCs reaction) excluding isoprene have not been modified. Even for isoprene, the reaction rate coefficients between OH initiated oxidation reaction (OH-isoprene) in the two mechanisms are close to each other: 2.7e-11 in M4 and 2.54e-11 in MOZART-4.

Given that HO_X partitions are consistent in M4 and MOZART-4 mechanism in the east of China, the variation of OH and HO_2 can indicate a different balance between their sources and sinks. The increases of HO_X in the east of China reflect that more HO_X are formed than they are lost with explicit isoprene chemistry, which is highly related to the distribution of O_3 and behaviour of the organic species such as RO_2 and nitrates. Hence this will be discussed in detail in the next section with the organic species.

In Tibet regions in the west of China, the average daytime OH number densities are decreased whereas HO_2 mixing ratios are not. This might be attributed to the different RO_2 reactions in the two mechanisms in very low NO_X regions, which will also be discussed in the next section.

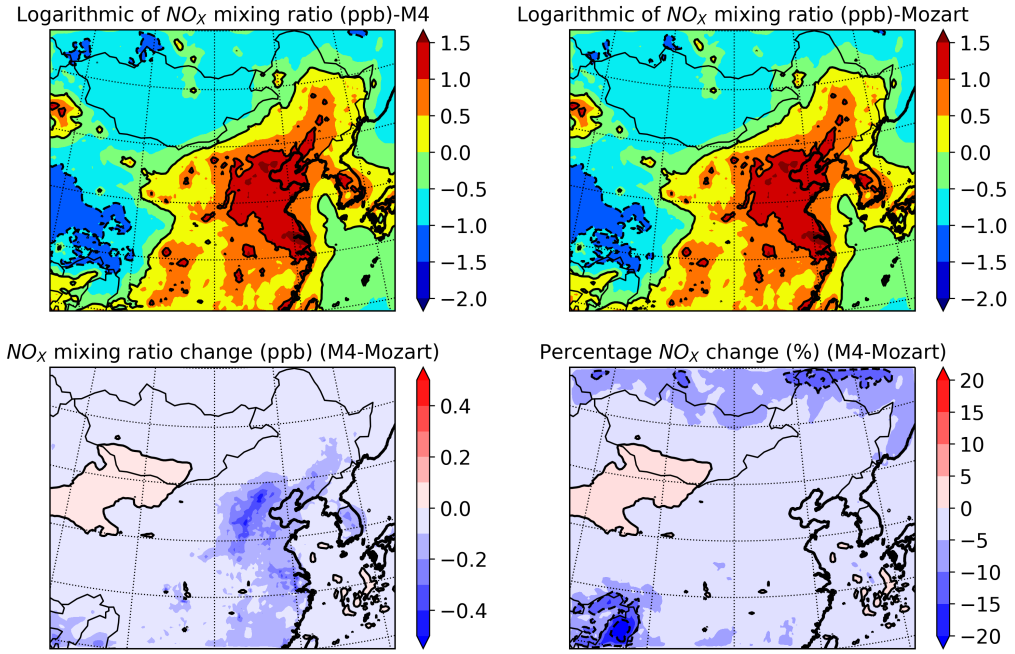

Figure 4.2.18: Same as Fig.4.2.2, but for the NO_X.

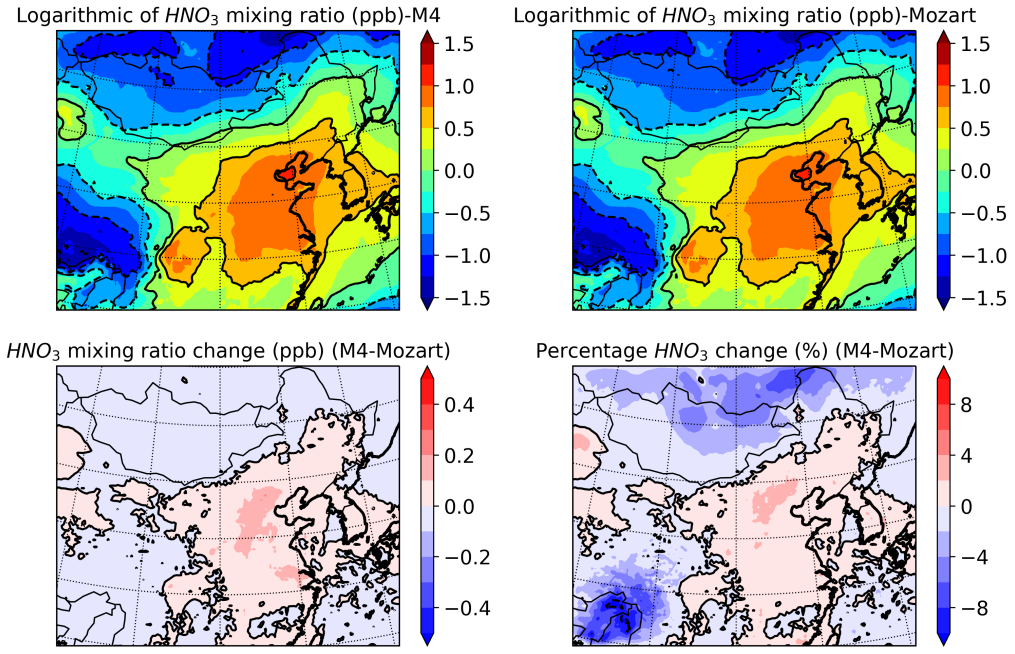

Figure 4.2.19: Same as Fig.4.2.2, but for the HNO_3.

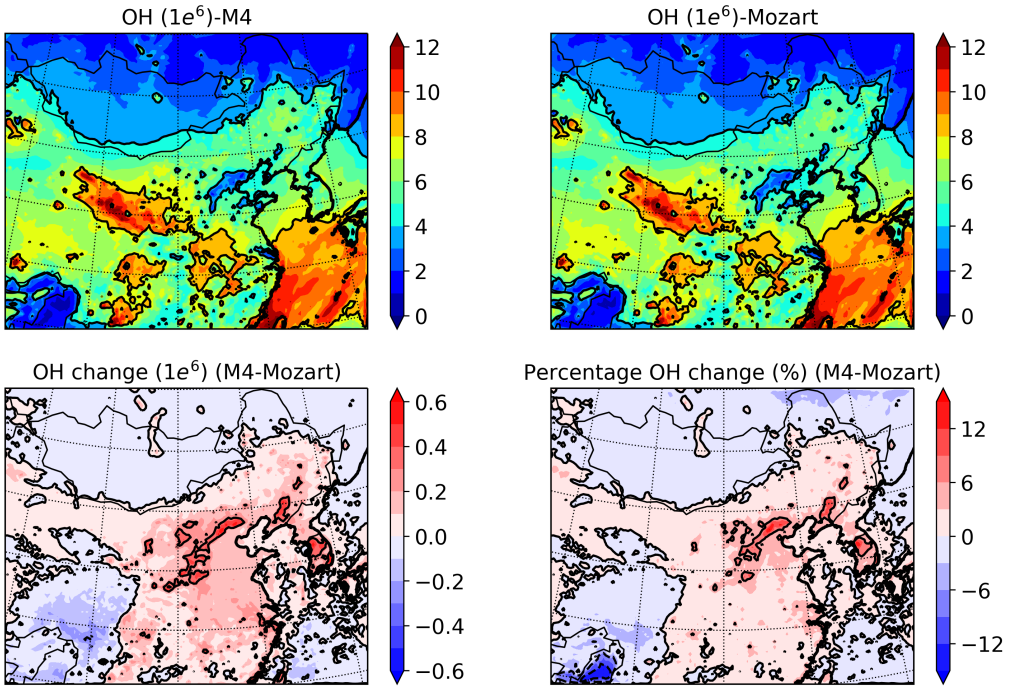

Figure 4.2.20: Same as Fig.4.2.1, but for the daytime OH with a linear scale in the unit of number density.

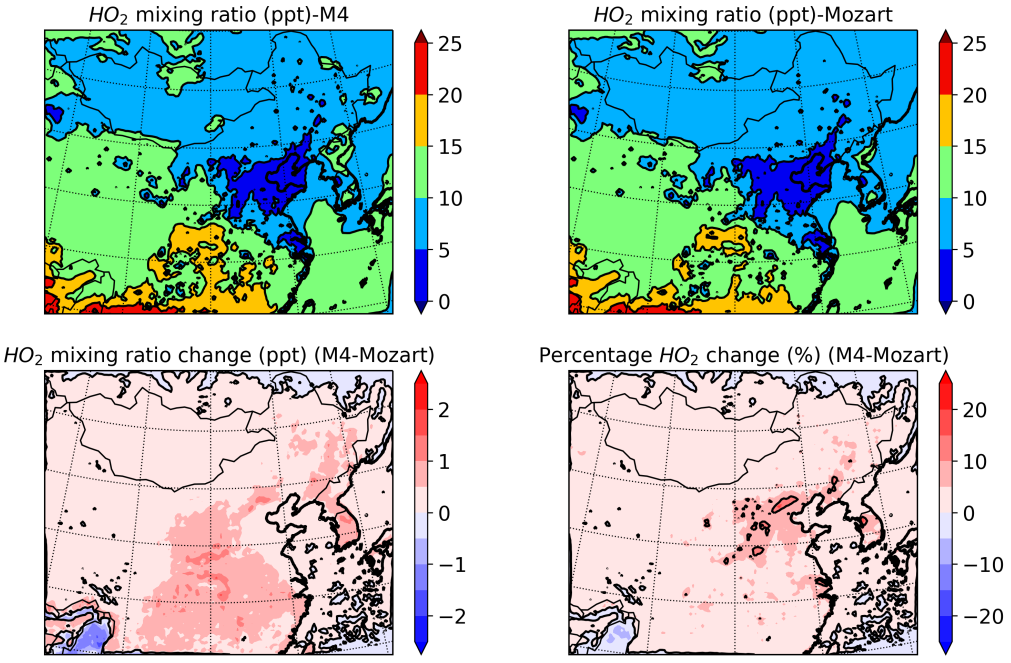

Figure 4.2.21: Same as Fig.4.2.1, but for the HO_2.

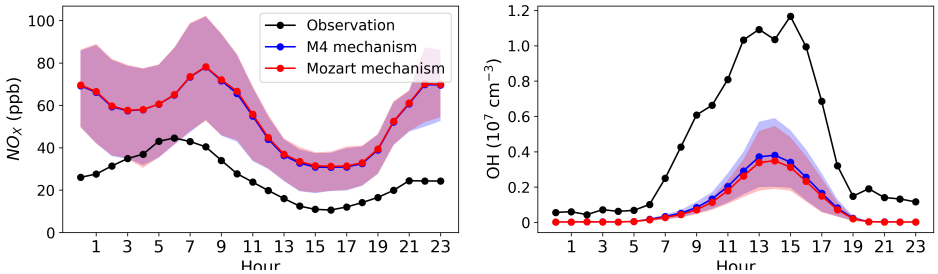

Figure 4.2.22: Same as Fig.4.2.8, but for NO_X mixing ratios (left) and OH number density (right).

The comparison of the diel patterns of NO_X and OH in Beijing are shown in Fig.4.2.22. The variations of NO_X simulations between the two mechanisms are small, which is consistent with the previous discussion. M4 mechanism provides a slightly lower prediction of NO_X during the daytime. However, this is too small to be compared with the disparities between the observations and the simulations.

Similar results are shown in the OH simulations. The daytime OH in Run 1 is higher than it is in Run 3, and is closer to the observations. But there is still a big gap between the modelled results and the measurement. Hence, I conclude that there is a minor impact of explicit isoprene chemistry on the simulations of inorganic chemistry in Beijing.

4.2.4 NO_2 released from isoprene

Isoprene is a reactive BVOCs that is of great importance in O_3 formation in the troposphere when NO_X is present. However, as mentioned in section 1.1.1, the recycling of NO_X via different ISOPO2 and INs isomers are not well understood due to large uncertainties. In this study, the tagging method is applied to quantitatively trace the NO_X cycled through various isoprene and INs oxidation pathways. The comparison of NO_X cycling between rural and urban environments can also indicate different pathways that dominate isoprene oxidation and O_3 production under low and high NO_X environment. Briefly, the tagging method is to manually add in new chemical tracers, which do not affect the standard chemistry (Emmons et al., 2012). The tags implemented in this study are introduced here.

The NO_2 converted by isoprene oxidation products are calculated with a tag

tracer - NO_{2tot}. NO_{2tot} is generated at the same rate as the NO_2 formation in the reactions of species that source from isoprene only. For species such as CH_3O_2 and CH_3CO_3 that are products of isoprene and other organic compounds, NO_{2tot} is not included in the NO_X recycling induced by them since it is hard to proportion the contribution from isoprene.

The reactions between isoprene and OH, O_3 and NO_3 are listed in section 4.2.1 (reaction 4.2.1 to reaction 4.2.6). Three ISOPO2 and one ISOPNO3 are produced in M4, and each of these peroxy radicals represents an oxidation branch of isoprene. Hence, four tag tracers (NO_{2ac}, NO_{2b}, NO_{2d} and NO_{2n}) are implemented to these branches accordingly.

In isoprene chemistry, NO_2 is mainly converted via reactions between NO and ISOPO2. INs can also be the potential source of NO_2 during its decomposition. NO_2 tags are therefore added in these reactions.

There are four hy-ISOPO2 isomers can be formed with OH initiated pathway depending on the location of OH addition. In the M4 chemical mechanism, three of them are included, which are named ISOPACO2, ISOPBO2 and ISOPDO2. Moreover, one nitrated isoprene peroxy radical (NISOPO2) is formed via the isoprene-NO_3 reaction. The subsequent chemistry of these four isoprene peroxy radicals isomers is different from each other, as well as the amount of NO_X being recycled.

Hence, apart from the NO_{2tot} tag counting total NO_2 formed directly from isoprene chemistry, four tags are included to quantify NO_2 recycled through different branches of ISOPO2. Seven INs are implemented in M4, however, only six tags (NO_{2ae}, NO_{2az}, NO_{2ce}, NO_{2cz}, NO_{2bn} and NO_{2dn}) of hy-INs are included since all NO_{2n} are formed via degradation of al-INs in M4. In total, 11 tags are designed for M4 chemical mechanisms to quantify and locate the NO_2 recycled by different parts of the isoprene chemistry.

Isoprene chemistry in MOZART-4 chemical mechanisms is simpler with hy-ISOPO2 isomer and INs lumped. As a result, in total four tags are designed to represent the NO_2 produced by isoprene, hy-ISOPO2, ni-ISOPO2 and INs.

The distributions of NO_{2total} simulations in the two runs show similar patterns (Fig.4.2.23). More NO_{2total} are produced in south China (> 10 ppt), where the isoprene concentrations are higher. Compared to MOZART-4 simulation, M4 predicts more NO_{2total} in very low NO_X environment (over the Yellow Sea and Tibet highland) and less NO_{2total} in environments with high isoprene emissions (south China). That is to say, the NO_{2total} is more evenly distributed in Run 1, which may indicate that more NO_X are recycled through relatively longer-lived products derived by isoprene. This is consistent with the complex chemistry of isoprene in M4.

In south China, the NO_{2total} is lower than 30 ($10^{1.5}$) ppt in most regions, whereas the NO_X mixing ratios in the atmosphere is around 1-3 ppb in this area (Fig. 4.2.18). Hence, the O_3 formation from direct isoprene chemistry can be relatively small. The NO_2 formed from the direct chemistry of isoprene (NO_{2total}) can have an even smaller contribution to the total NO_X in north China where is abundant in NO_X. It is worth mentioning that the NO_{2total} plotted here is not the total NO_X involved in the isoprene degradation, but NO_2 converted by species only derived from isoprene. Shorter chain organic products formed by isoprene can also convert NO to NO_2. Nevertheless, these organic species have sources other than isoprene, which makes their contribution hard to quantify. In the next section, the contribution of the full isoprene chemistry is studied with a special treatment of isoprene.

The formation of O_3 from the NO_{2total} is plotted in Fig.4.2.24. In the middle of China and YRD regions, the NO_{2total} is responsible for up to 3 ppb O_3 formation on the 45 days' average. The contribution of the NO_X recycling processes in isoprene chemistry can be less significant in north China due to the low emissions of isoprene and high background concentration of NO_X.

Interestingly, lower NO_{2total} are simulated in south China in Run 1, but the O_3 formations by isoprene are higher. As listed above, O_3 react with NO_{2total} and O_{total} with no O_{3total} formation. More O_3 is simulated in Run 3 in south China, which could result in lower O_{3total} production. The lower O_{3total} over East China Sea while NO_{2total} are higher in Run 1 can also be explained by the high

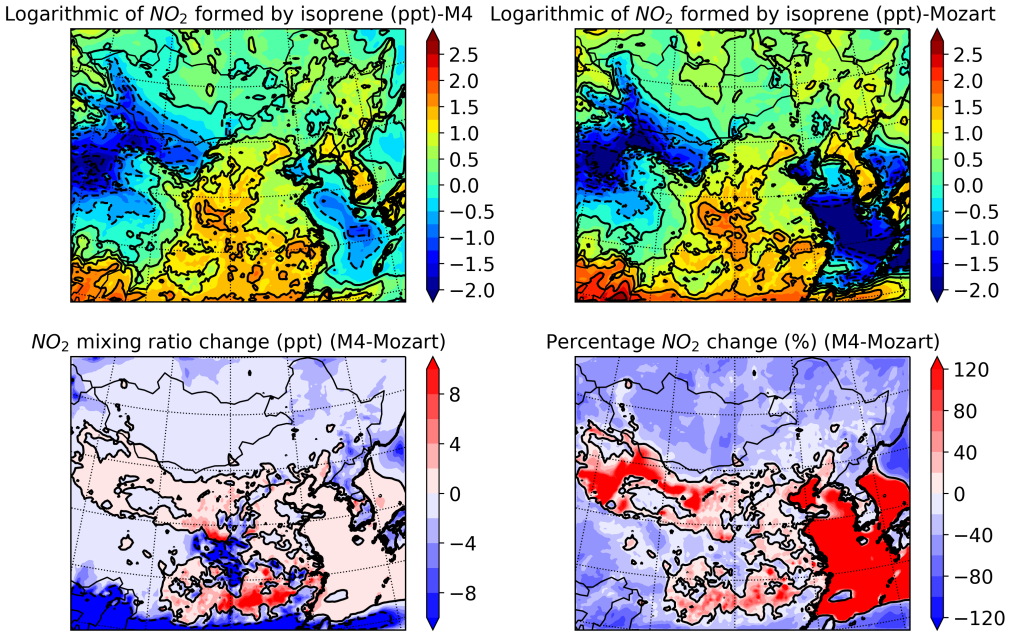

Figure 4.2.23: Same as Fig.4.2.2, but for the total NO_2 recycled directly from isoprene (NO_{2total}).

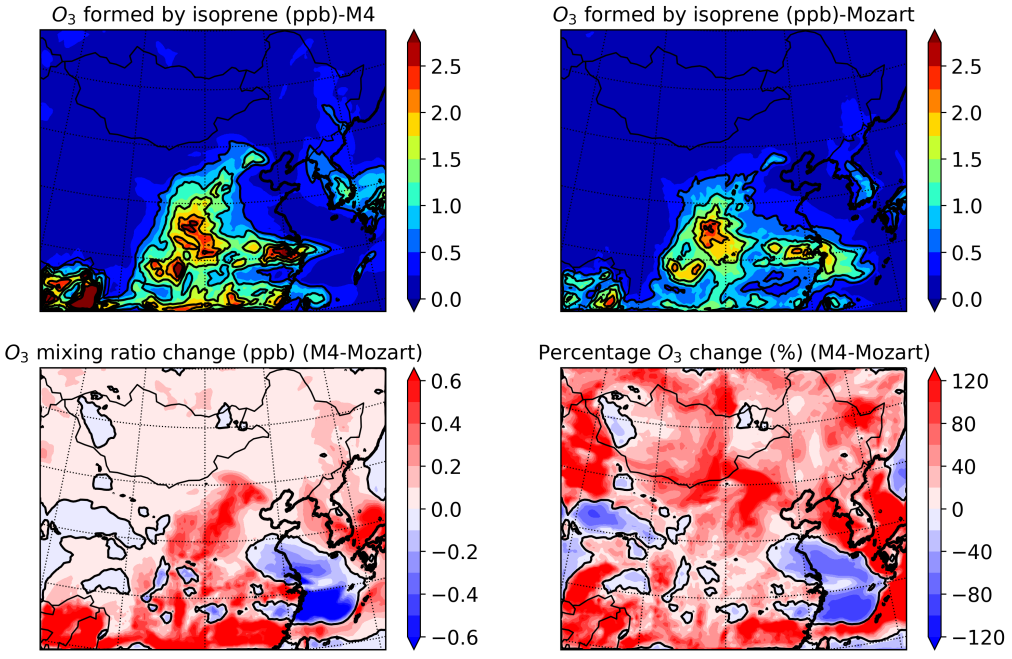

Figure 4.2.24: Same as Fig.4.2.18, but for the O_3 produced by the total NO_2 tag.

O_3.

Fig.4.2.25 and Fig.4.2.26 compare the sum of NO_2 released by all INs (NO_{2INs}) and the O_3 produced with this NO_2. It is notable that NO_{2INs} in Run 3 is about one order of magnitude higher than it is in Run 1 over most of China. As mention in the previous chapter, the INs in MOZART-4 also include nitrates from other VOCs, so the total INs concentration in MOZART-4 is higher than the sum of all INs in M4, which may lead to an increase of NO_2 recycle. Also, no shorter chain organic nitrates are formed during the degradation of INs in MOZART-4 releasing more NO_2.

However, slightly higher NO_{2INs} is calculated with M4 mechanism over the East China Sea and the Sea of Japan. This might indicate some longer-lived INs are transported to these areas and recycled NO_2 there.

Similar to Fig.4.2.24, O_3 is mainly produced over the middle of China and YRD regions. The difference in the O_3 productions is the opposite of the difference in the NO_{2INs} concentrations in most of the domain.

The simulations of NO_{2INs} concentrations in most of the domain are lower than 10 ppt in both runs, and their contribution to O_3 production is ppt level on average. Hence, based on the tagging results, the contribution of INs to NO_X recycle and O_3 formation is confirmed to be very small.

The diel cycle of NO_2 and O_3 tags via different isoprene oxidation pathways in Beijing are illustrated in Fig.4.2.27 The shaded areas represent the proportions of NO_2 recycled and O_3 generated through each branch.

The NO_{2ac} makes approximately half of the NO_{2total} during the daytime, followed by NO_{2b} and NO_{2d} contributing to about 25% and 17% of the NO_{2total}. There is a small amount of NO_2 recycled by the species produced in more than one branches, which is not coloured in the diurnal cycle.

The night-time chemistry of isoprene is very different from the day. The NO_2 cycled via NO_3 initiated isoprene oxidation pathway becomes more important after 16.00 in the afternoon reaching the maxima of over 30 ppt at 19.00. During the night (21.00 - 3.00), NO_{2n} contributes almost 100% to the $NO_{2\text{total}}$.

Low concentrations of $NO_{2\text{total}}$ (< 5ppt) are calculated after mid-night, which drop to near zero value at 4.00 in the morning. This reduction can indicate that the ni-ISOPO2 are depleted completely via reactions with NO and NO_3. With the sunrise, hy-ISOPO2 isomers are formed with OH initiated oxidations resulting in increasing NO_2 recycling (15 -20 ppt) during the morning. In the afternoon $NO_{2\text{total}}$ shows a small decrease with less radiation. However, a dramatic increase of $NO_{2\text{totoal}}$ (up to 40 ppt) is seen at 18.00, which can be due to the changes in mixing led by the collapse of boundary layer simulations. The rapid reaction between isoprene and NO_3 may also contribute to this change.

However, the high NO_{2n} during the night leads to O_3 loss rather than O_3 production since photolysis of NO_2 cannot happen at night. The proportions of O_3 production via different hy-INs are similar to their shares in NO_X recycling. This is not a surprise as the subsequent reactions of the NO_X tags are the same.

The rate of O_3 production is mainly affected by the intensity of radiation. As a result, the night-time production of O_3 should be close to zero, while the production increases with radiation intensity after sunrise reaching the peak in the afternoon. The diel patterns in Fig.4.2.27 are consistent with expectations. In Beijing, with about 20 ppt of NO_2 being recycled, O_3 production increased by up to 1.6 ppb.

The diel pattern of NO_2 recycled by different INs are shown in Fig 4.2.28, as well as the O_3 produced with NO_2 of each IN. Although IN-(1,2) (ISOPBNO3) is the most abundant INs in isoprene chemistry, it does not release as much NO_2 as the IN-(4,3) ($NO_{2\text{dn}}$). IN-E/Z(1,4) (lumped ISOPANO3) and IN-E/Z(4,1) (lumped ISOPCNO3) contribute to a smaller amount of NO_2 partly due to the lower concentration of these two nitrates. Section 3.4 introduced that ISOPCNO3 can also be formed by the reaction between ni-ISOPO2 and RO_2, resulting in the peak of $NO_{2\text{cn}}$ at early night.

Although compared to $NO_{2\text{dn}}$, $NO_{2\text{bn}}$ concentrations are slightly lower during

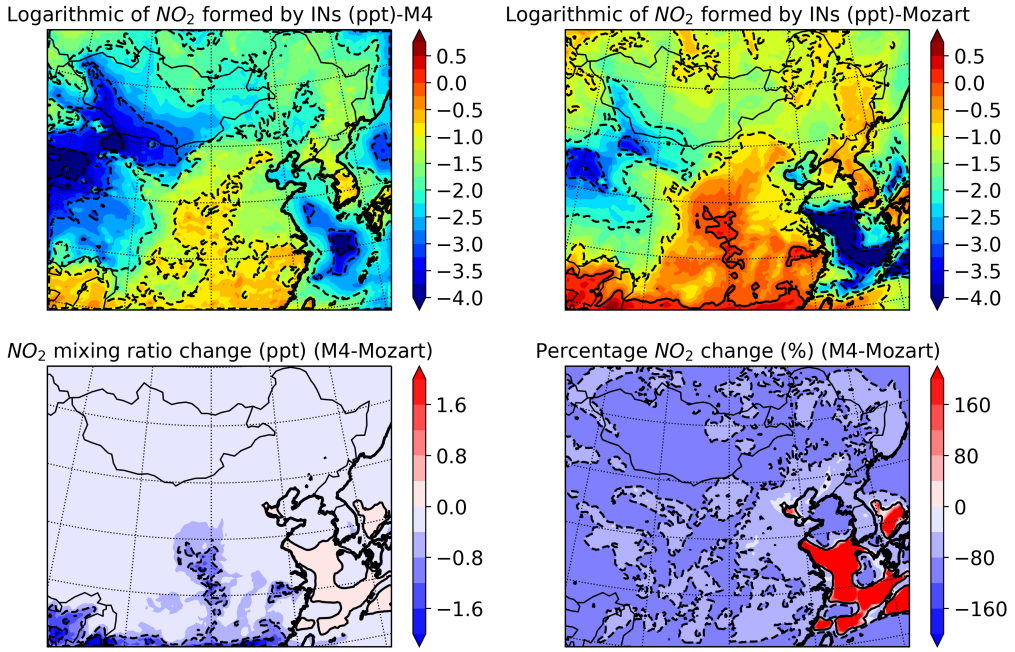

Figure 4.2.25: Same as Fig.4.2.18, but for the total NO_2 recycled directly from INs.

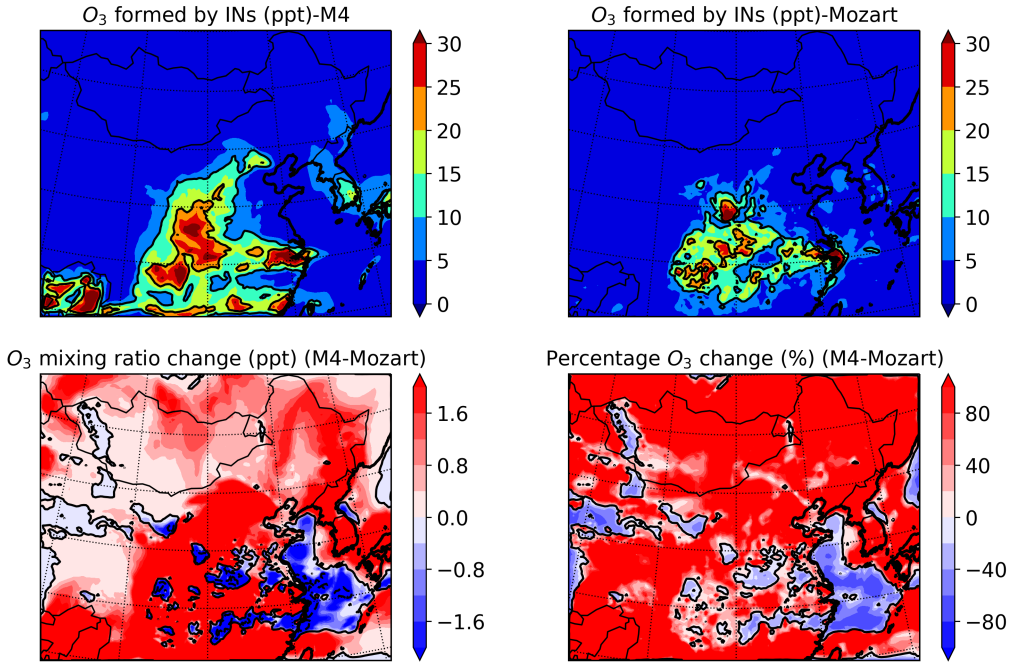

Figure 4.2.26: Same as Fig.4.2.18, but for the O_3 produced by the NO_2 tag of INs.

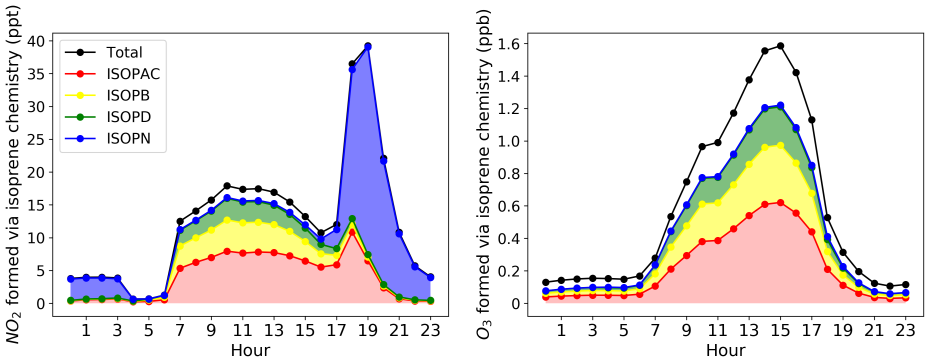

Figure 4.2.27: Diel patterns of the NO_2 (left) and O_3 (right) formed via different oxidation branchings of isoprene in Beijing.

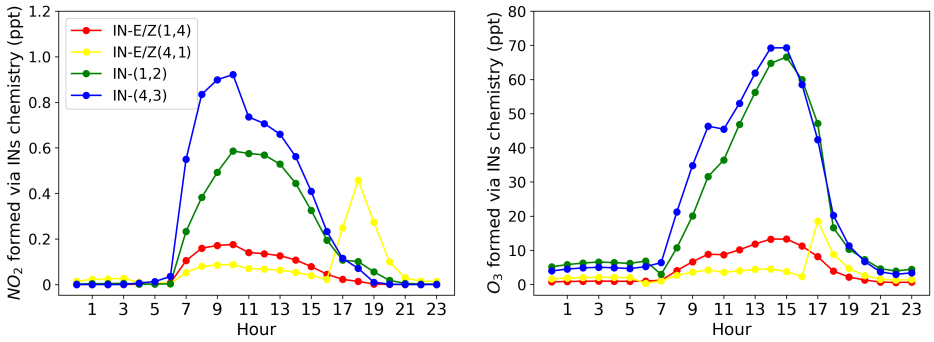

Figure 4.2.28: Same as Fig.4.2.27, but for the INs.

the day, their contributions to O_3 formation are close to each other, which peak at 14.00-15.00 in the afternoon with the value of approximately 70 ppt. O_{3an} shows similar diurnal pattern as the O_{3bn} and O_{3dn} but with a lower value. The diel variation of O_{3cn} is slightly different from the others due to the unique formation of ISOPCNO3 from NO_3 initiated chemistry.

4.3 Impact of full isoprene chemistry

4.3.1 HO_X and RO_2 systems

This section compares the results simulated with and without isoprene emissions by both mechanisms, so the contribution of isoprene to various chemical systems can be studied.

In Run 4, 100% of isoprene is removed from the system, which is confirmed by Fig.4.3.1. Consequently, all oxidation products derived only from isoprene (such as ISOPO2, ISOPOOH) remain zero for the whole studying period in Run 4. As mentioned in the section 2.5, the only difference between the M4 and MOZART-4 mechanisms is the isoprene oxidation chemistry. Hence, when isoprene is excluded in the run, the results simulated from both chemical mechanism are the same, which is confirmed with a 7-day run test.

Fig.4.3.2 illustrates the changes in O_3 concentration due to the presence of isoprene. Isoprene chemistry is stimulated to has a positive influence on the O_3 concentration over most of China and the Yellow Sea in both mechanisms. Significant enhancement of O_3 is found in the middle of China including regions in Henan, Anhui Hubei, Hunan and Sichuan provinces, in which the increase of O_3 concentration can be up to 10 ppb (18%) and even higher than it is in the NCP and YRD regions. This can be a result of lower isoprene emissions in the cities. Still, on average isoprene is responsible for about 10% of total O_3 concentrations in NCP and YRD regions.

This value is comparable with the previous reported isoprene contribution on O_3 in different locations. 9 - 12% O_3 was attributed to isoprene over US with a modelling study (Zhang et al., 2017b) and 14.1% were analysed for Rio de Janeiro (da Silva et al., 2018).

Both mechanisms simulate similar results in O_3 variation. However, it is notable that larger disparities are shown in low-NO_X and high isoprene emission regions such as southwest of China. In these regions, the O_3 formation is limited by the amount of NO_X rather than RO_2. Hence, instead of a precursor, isoprene acts like a sink of O_3 resulting in lower mixing ratios. The formation of organic nitrates can also contribute to this decrease in O_3. The behaviour of nitrates is discussed in 4.3.2.

Simulations of OH and HO_2 changes in the two mechanism matches well (Fig.4.3.3 and Fig.4.3.4). By including isoprene, OH concentration declines over a great area of the domain, apart from the NCP and YRD regions in the east of China, the northwest of China and the Yellow Sea. OH concentration change is a balance between its production and its loss. O_3 as the primary source of OH, is enhanced in most of China leading to an upsurge of OH production. Hence, in low isoprene emission regions, more OH is generated than it is reacted by isoprene, resulting in enhancement of OH. On contrary, in south China, a large amount of isoprene is emitted depleting the OH there.

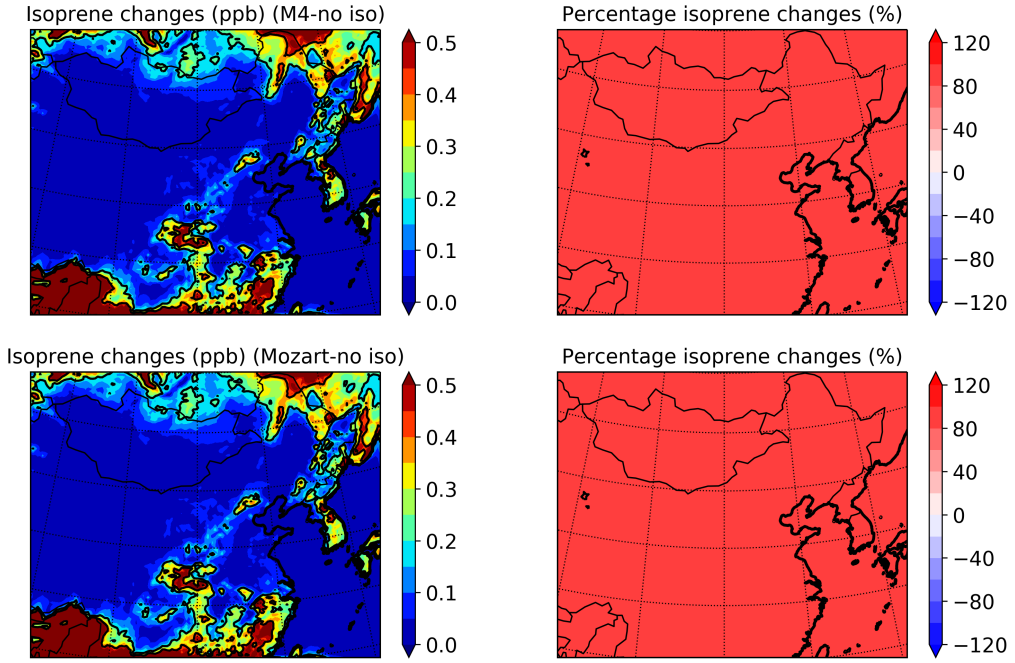

Figure 4.3.1: Contour maps of the averaged change (left) and percentage change (right) of isoprene between runs with and without isoprene. Top panels are generated with M4 chemical mechanism while lower panels are with MOZART-4 mechanism.

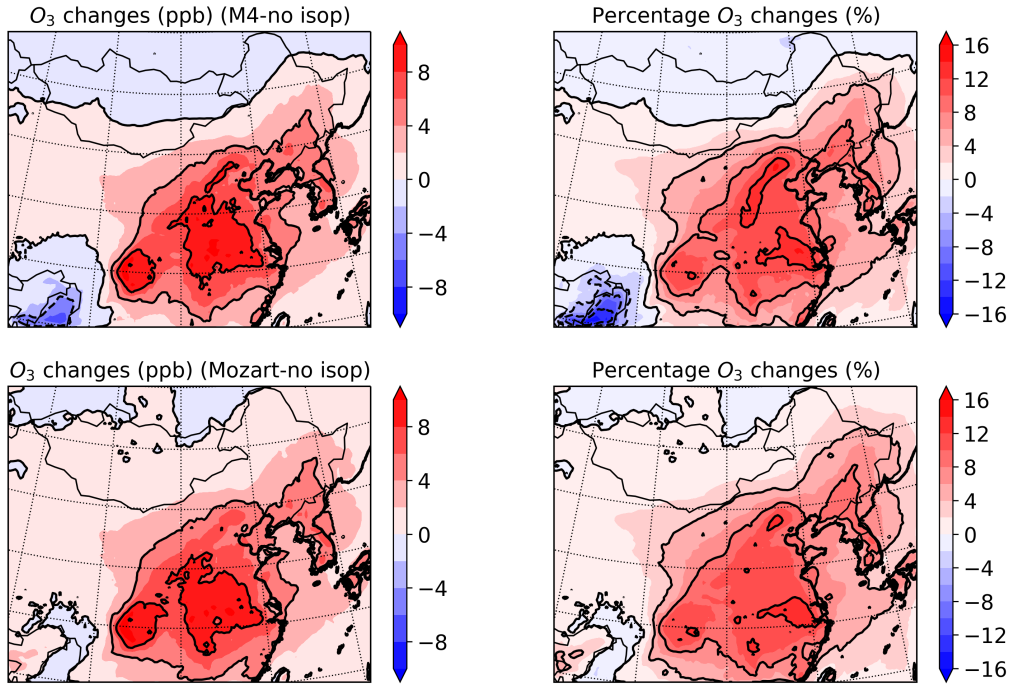

Figure 4.3.2: Same as Fig.4.3.1, but for the O_3.

Based on the M4 mechanism, isoprene chemistry contributes to over 40% of HO_2 concentration in NCP regions and Shanghai. The contribution calculated by MOZART-4 mechanism is slightly lower than M4 mehcnaism, but it is still of great importance to the HO_2 distribution. The large increase in HO_2 can affect the local organic and inorganic chemistry. reaction 4.2.18 becomes a competitive sink of RO2, which can affect the distribution of organic nitrates (discussed in the following section).

The differences in CH_3O_2 (Fig.4.3.5) and CH_3CO_3 (Fig.4.3.6) between runs with and without isoprene emissions are consistent in the two chemical mechanisms. Both results suggest that isoprene is an important source of RO_2 over east China. This increase in RO_2 can give rise to the enhancement of O_3 in this region where sufficient amount of NO_X is presence.

4.3.2 NO_X and NO_Y

Slightly higher mixing ratios of NO_X are simulated over most of China with isoprene emissions (Fig.4.3.7). The change of HNO_3 (not shown) shows a similar pattern as NO_X, so the variation of HNO_3 is not the reason for the increment in NO_X. As discussed in the previous section, up to 40% more RO_2 and HO_2 are produced during the degradation of isoprene. Hence, more RO_2 are lost through RO_2-HO_2 reactions and RO_2 cross-body reactions making RO_2-NO and RO_2-NO_3 reactions less competitive. The concentration of NO_X is therefore increased with less NO_X being converted to NO_Y by RO_2.

Fig.4.3.8 shows the impact of isoprene chemistry on the NO_3 distributions. With isoprene emission included, a slight increase in NO_3 concentration ($<$ 10%) is simulated over NCP and YRD regions in east China, part of west China and Sichuan province in middle China. Significant decreases in NO_3 ($>$ 30%) are shown in the rest of the domain.

NO_3 is a product of NO_2 and O_3 reaction. Higher NO_2 and O_3 are simulated in the runs with isoprene, which can increase the production of NO_3. However, at the same time, the loss of NO_3 is also larger due to the enhanced HO_2, isoprene and RO_2. Hence, in high NO_X emission and low isoprene emission areas, more NO_3 are formed than its loss through the minor changes of isoprene, which is consistent with the environment in the east and the middle of China.

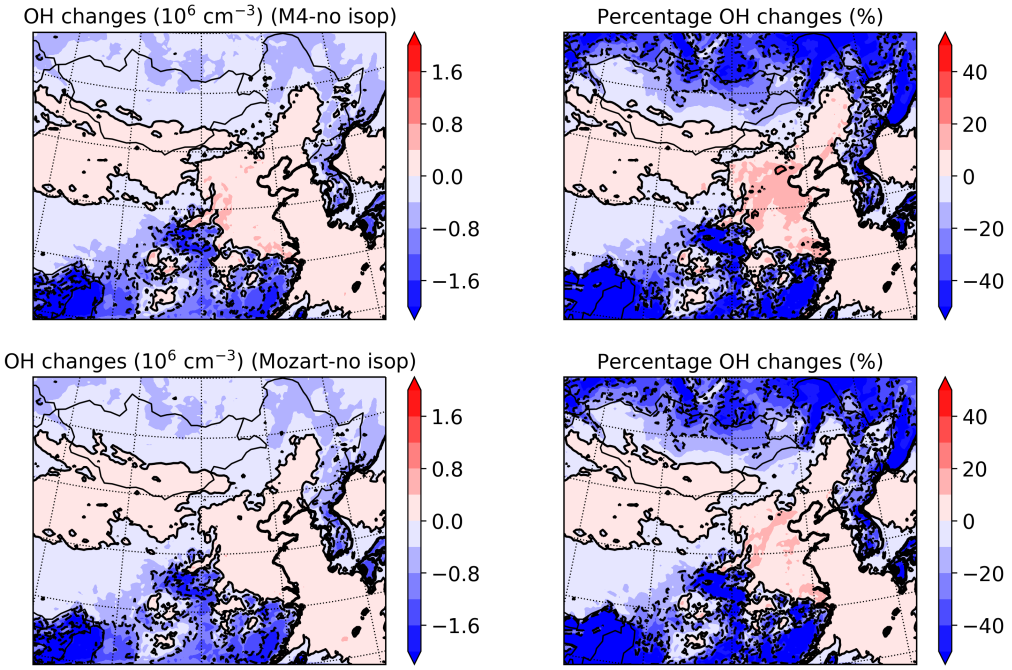

Figure 4.3.3: Same as Fig.4.3.1, but for the OH.

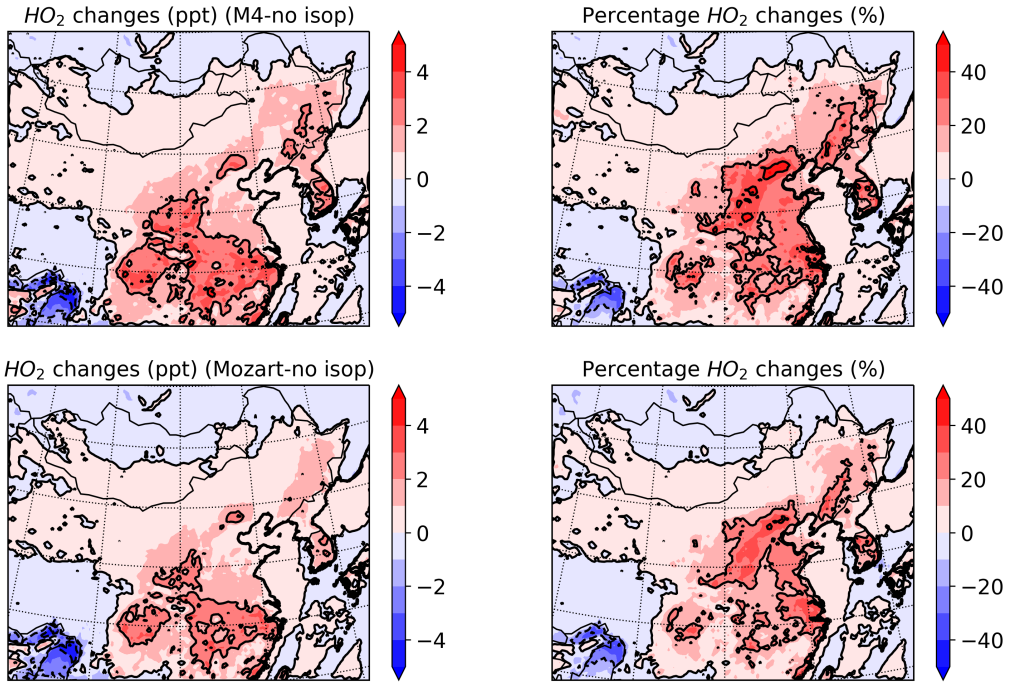

Figure 4.3.4: Same as Fig.4.3.1, but for the HO_2.

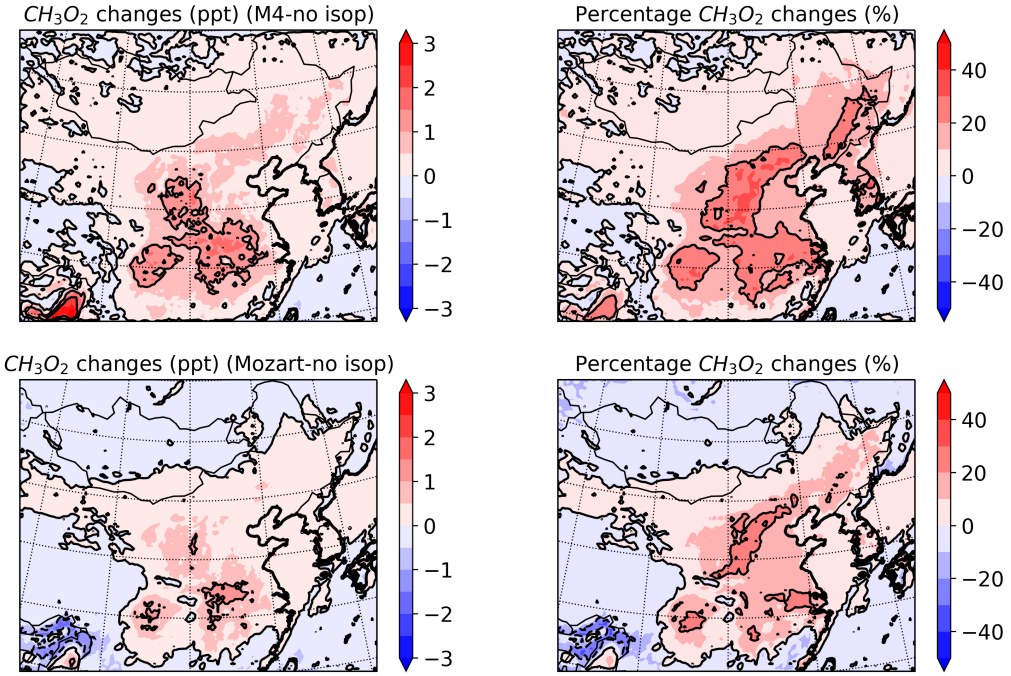

Figure 4.3.5: Same as Fig.4.3.1, but for the CH_3O_2.

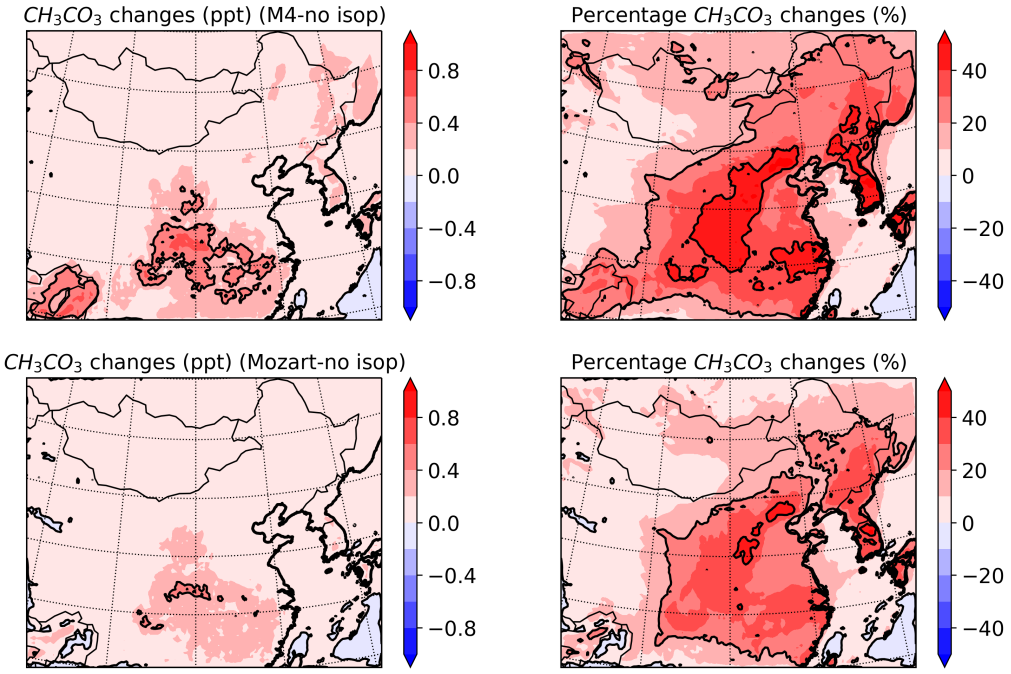

Figure 4.3.6: Same as Fig.4.3.1, but for the CH_3CO_3.

The changes in organic nitrates (Fig.4.3.9) are modelled differently with M4 and MOZART-4 mechanism. In M4 mechanism, isoprene chemistry is modelled to have a positive impact on the organic nitrates over the whole domain with a maximum contribution of 300 ppt in the middle of China. In contrast, a slight decrease of organic nitrates is calculated over most of China with MOZART-4. In M4, organic nitrates can be formed during the degradation of INs and reactions between the intermediates of isoprene and NO. These two paths are not included in the MOZART-4 mechanism. Hence, with isoprene included, more organic nitrates can be generated during the oxidation of isoprene in M4, whereas in MOZART-4 the ISOPO2-NO reaction is competing with the formation of organic nitrates leading to a reduction in its concentrations. Also, as discussed in the previous section, more RO_2 can be lost through reactions with HO_2 which may contribute to lower organic nitrates concentrations.

Another possible reason of high organic nitrates is that the deposition rates of IN isomers are low in M4, which may eventually increase the production of organic nitrates. New IN isomers are included in M4, however, little information was available to define its deposition. Deposition rate recommended by Sander (2015) is used in this study, which is lower than the generic rate.

The changes in PAN (Fig.4.2.15) are similar in both mechanisms - an increase over most of domian, especially in east China. PAN is formed with a reaction between CH_3CO_3 and NO_2. The variations of its precursors are simulated with similar results, so it is not a suprise to have the similar prediction of PAN.

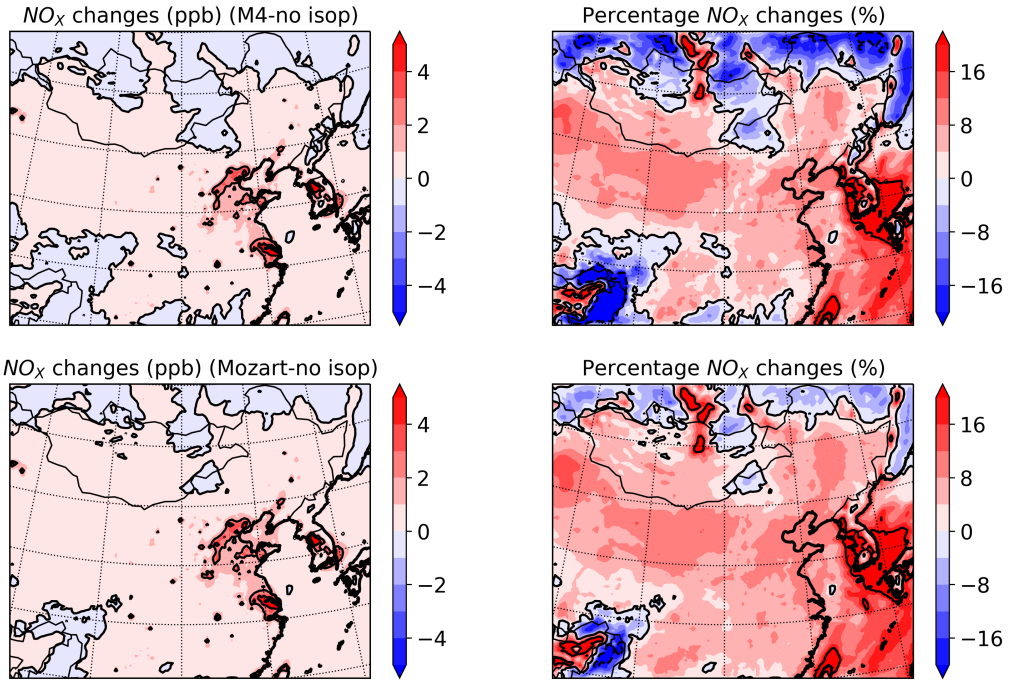

Figure 4.3.7: Same as Fig.4.3.1, but for the NO_X.

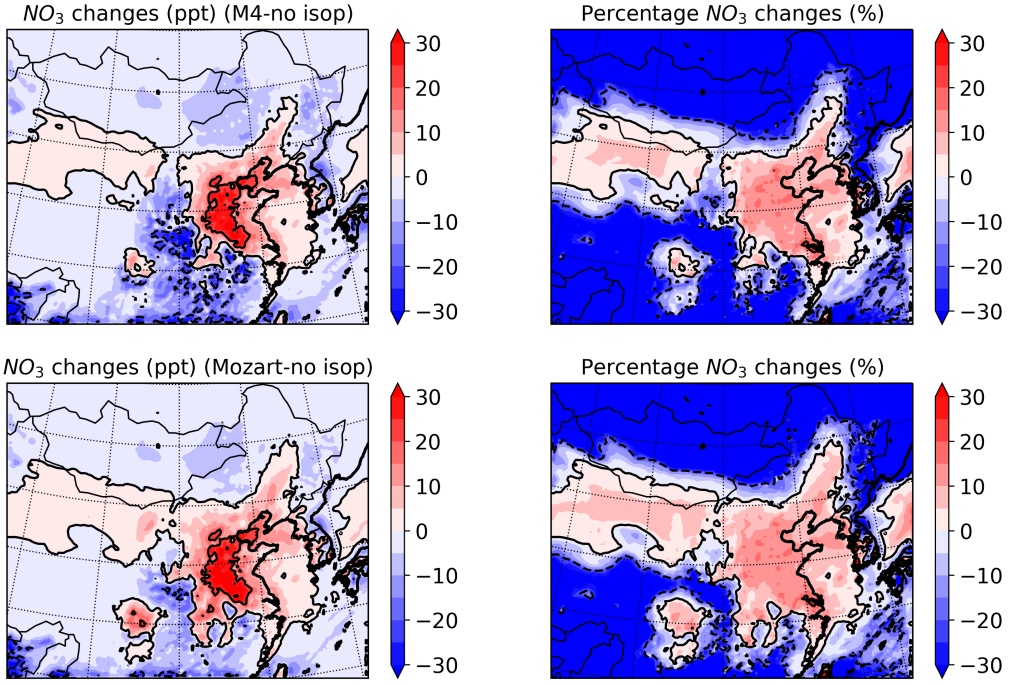

Figure 4.3.8: Same as Fig.4.3.1, but for the NO_3.

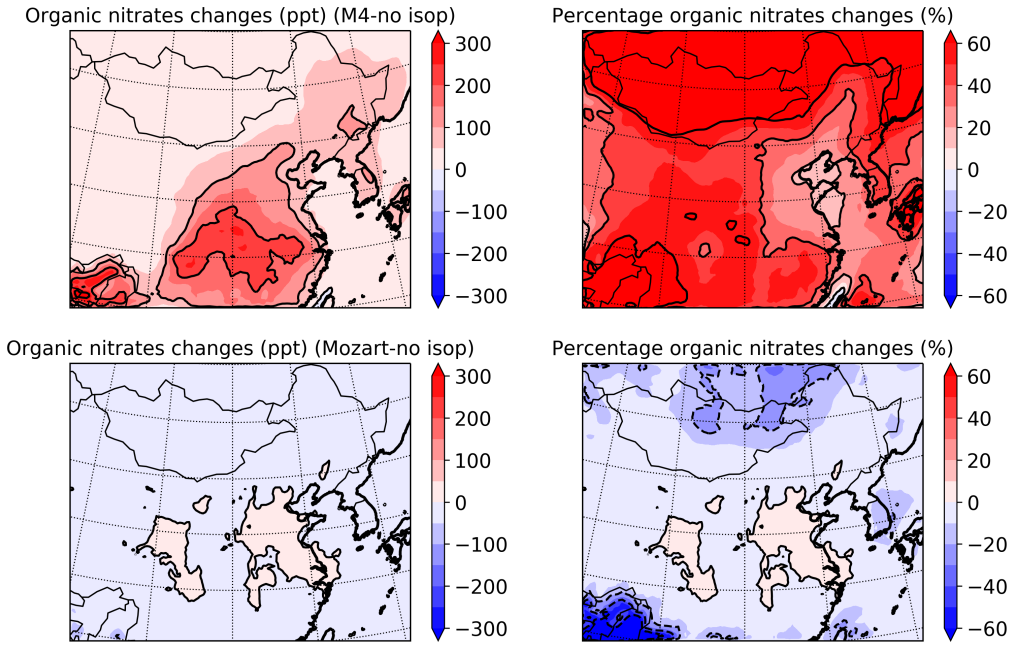

Figure 4.3.9: Same as Fig.4.3.1, but for the organic nitrates.

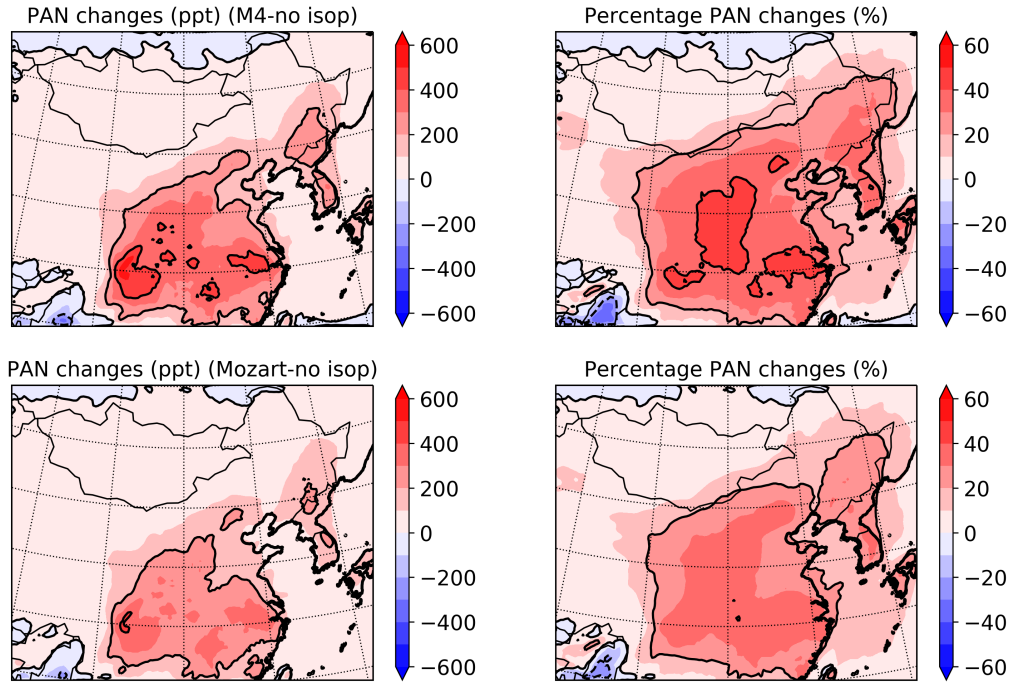

Figure 4.3.10: Same as Fig.4.3.1, but for the PAN.

4.4 Impact of INs chemistry

4.4.1 NO_X and NO_Y

In this section, I compare results with different treatments on INs. The contribution of hy-INs in M4 and MOZART-4 mechanisms are compared in the top two panels of each figure. The lower panel shows the impact of both hy-INs and al-INs in MOZART-4. As explained in section 4.1, the al-INs in M4 cannot be replaced, so the al-INs chemistry cannot be studied using this method.

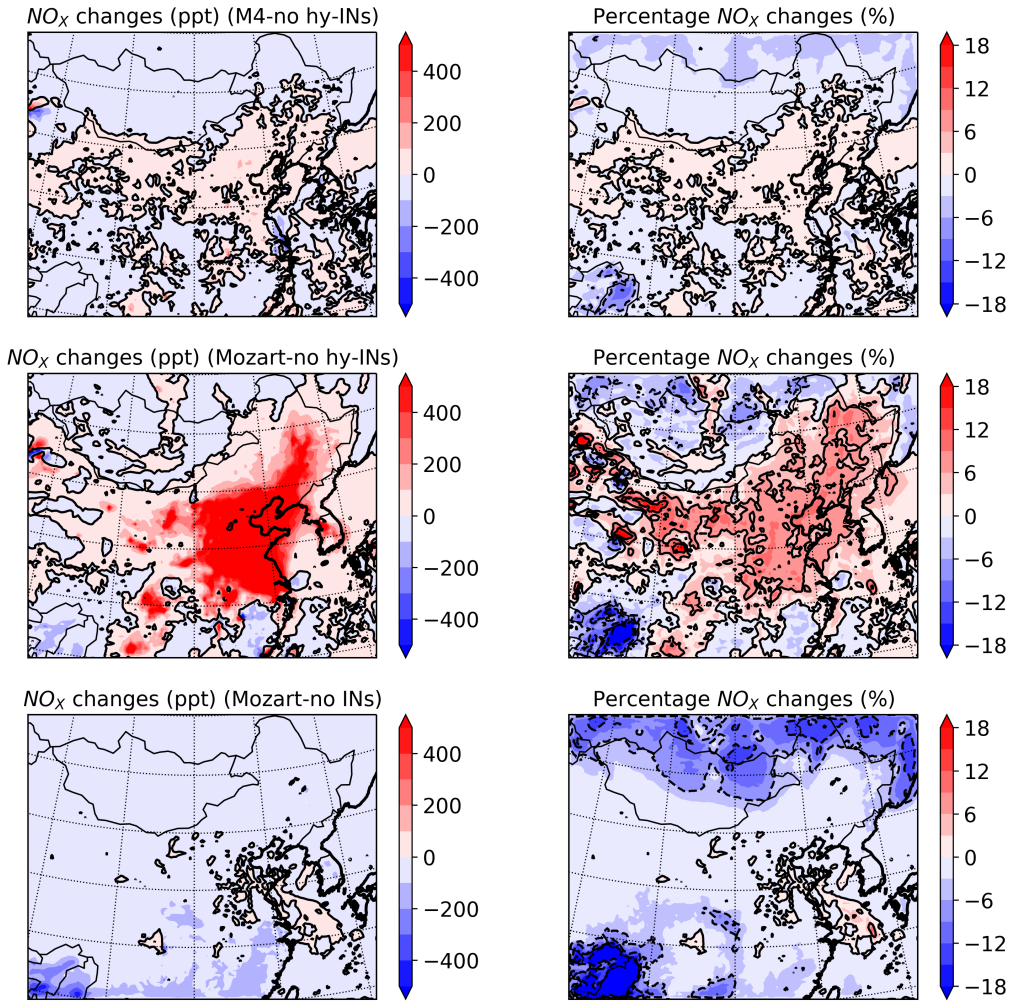

Figure 4.4.1: Contour maps of the change (left) and percentage change (right) of NO_X between runs with different treatment of INs chemistry. Top two panels are generated by subtracting simulations with no hy-INs in M4 and MOZART-4 chemical mechanism from the Run 1 and Run 2, respectively. The bottom panel shows the impact of both hy-INs and al-INs in the MOZART-4 chemical mechanism.

Excluding INs in the chemistry is expected to accelerate the NO_X recycling and increase NO_X (Fig.4.4.1) concentrations since less NO_X is lost in nitrate formation. Up to 300 ppt of NO_X is reduced by hy-INs in south and west China. However, this is not true for the whole of China. In north China, hy-INs have a positive impact on NO_X values. The reason behind this increase is a result of interactions between various systems, that will be discussed in the next section.

The increase of NO_X generated by M4 is much smaller than it is predicted by MOZART-4, which indicates that NO_X recycled by the subsequent chemistry of hy-INs in M4 is less than it is in MOZART-4. This is confirmed by the significantly increased concentration of organic nitrates in M4 (Fig.4.4.2).

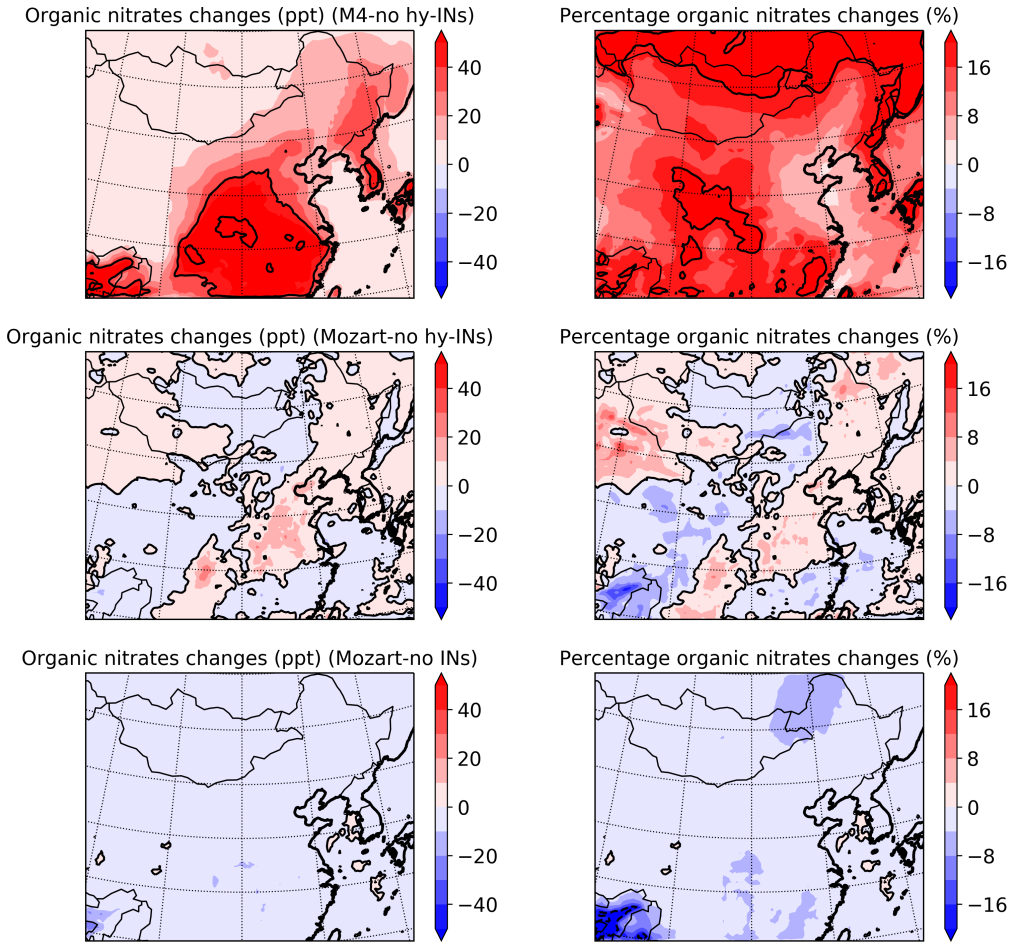

Figure 4.4.2: Same as Fig.4.4.1, but for the organic nitrates.

As expected, the total INs is simulated to have a negative impact on the NO_X concentrations over the land in MOZART-4 mechanism. Over the sea, where the emissions of NO_X and VOCs are very low, the changes in chemistry can be

less important compared to changes in transport. With INs formation, the short-lived NO_X can be tied into the relatively longer-lived nitrate functional group and released during the transportation of INs. The increase of NO_X over the East China Sea may indicate this process.

The variation of organic nitrates shows different patterns in the two mechanisms (Fig.4.4.2). In M4 mechanism, organic nitrates are formed during the degradation of hy-INs, so as a source of organic nitrates, an enhancement of organic nitrates is calculated over the entire domain with hy-INs formation.

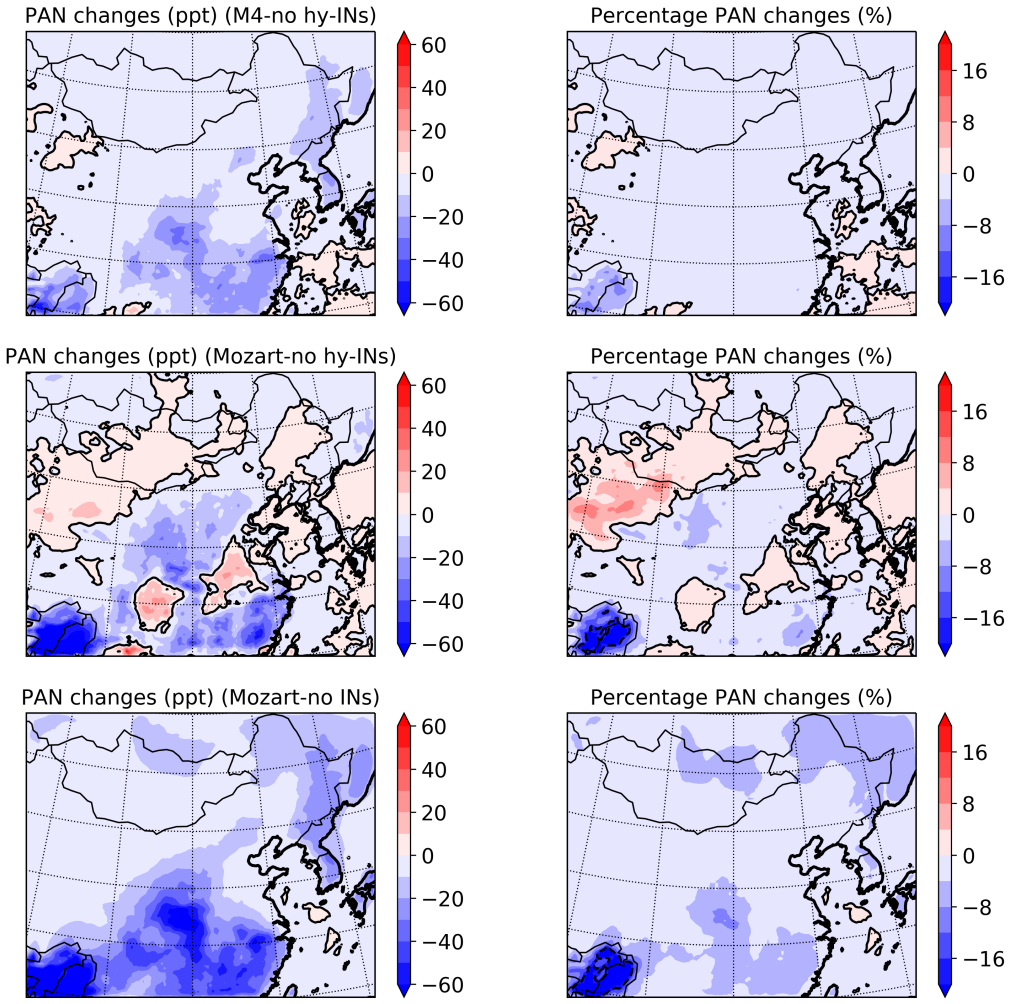

Figure 4.4.3: Same as Fig.4.4.1, but for the PAN.

However, this is not the case in MOZART-4 chemistry. No organic nitrates are formed in the subsequent chemistry of INs in MOZART-4. Hence, the formation of hy-INs is competing with organic nitrate production, which is consistent with the lower organic nitrates mixing ratios over the middle and the

southeast of China. In the northeast and the southwest of China, organic nitrates show an increase in concentrations owing to the enhanced NO_X (Fig.4.4.1). The formation of al-INs further reduces NO_X concentrations in the atmosphere leading to a reduction in the organic nitrates formation.

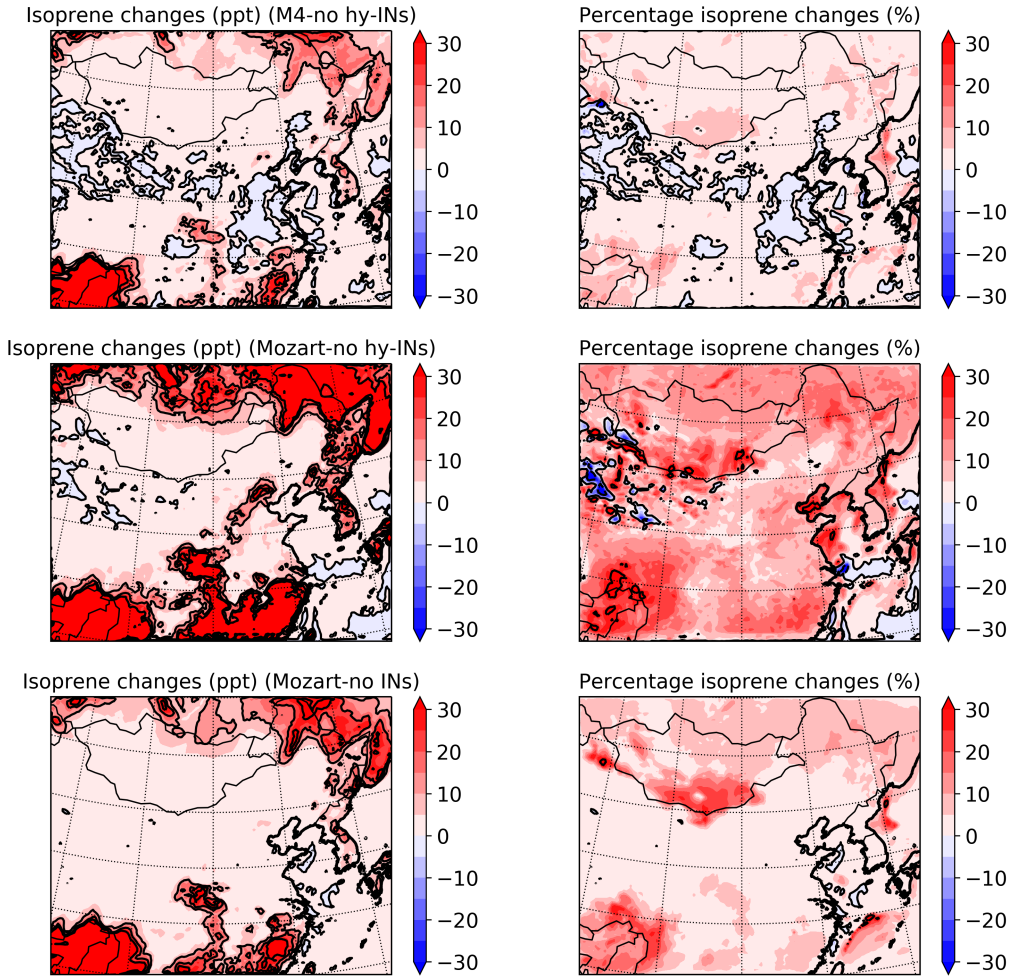

Figure 4.4.4: Same as Fig.4.4.1, but for the isoprene.

The changes of PAN (Fig.4.4.3) in MOZART-4 mechanism is very closed to the changes in organic nitrates indicating similar chemical processes. Unlike organic nitrates, a negative contribution of hy-INs to PAN is simulated over most of mainland China. PAN is formed with reactions between CH_3CO_3 and NO_2. With hy-INs formation, lower NO_X is simulated over south China in M4, which is partly the reason for the reduction in PAN. Moreover, lower CH_3CO_3 is simulated in M4 with hy-INs discouraging the formation of PAN.

4.4.2 Important organic species.

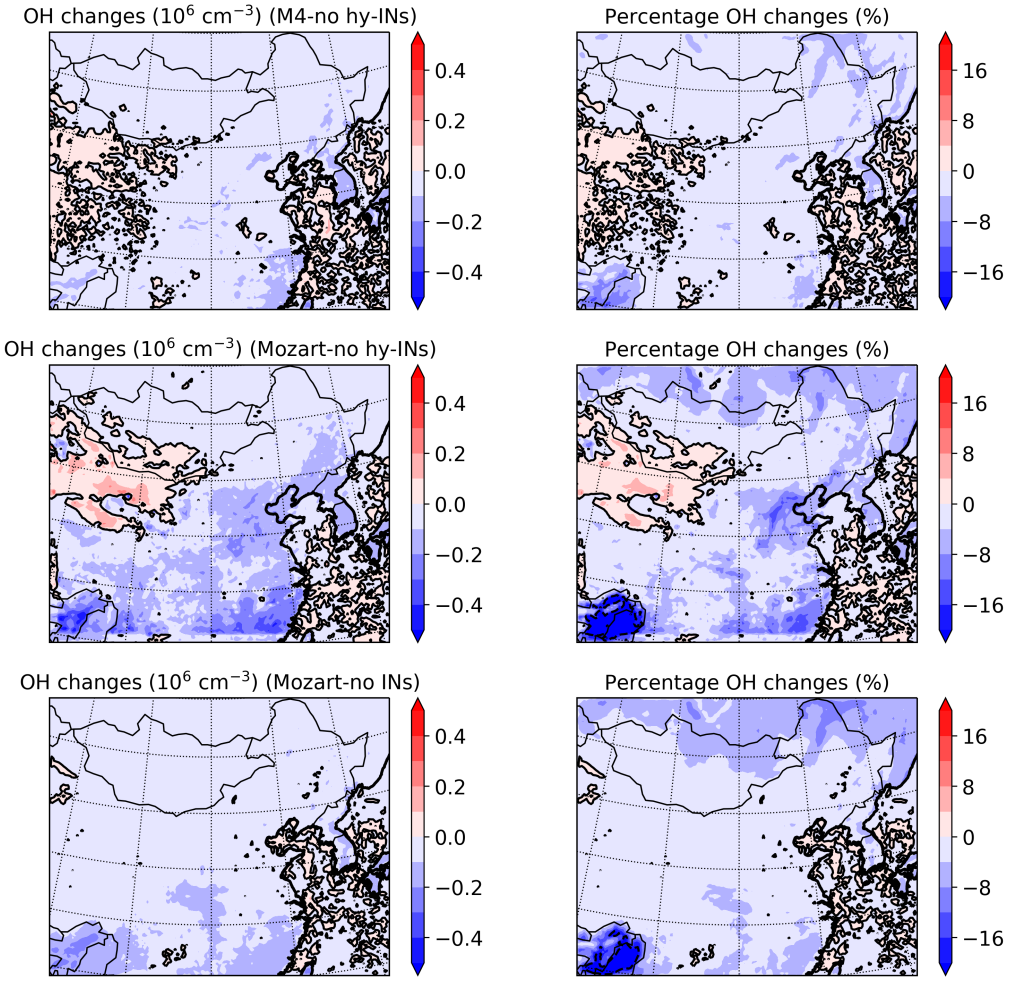

Figure 4.4.5: Same as Fig.4.4.1, but for the OH.

Fig.4.4.4 shows the changes in isoprene mixing ratio induced by the formation of INs. Increased isoprene over most of the domain is calculated in both M4 and MOZART-4 chemical mechanisms when INs are formed. This is understandable since the formation of INs hinders the O_3 production via ISOPO2 and NO reaction. O_3 is the major source of OH production in the troposphere. Hence, lower OH concentration (Fig.4.4.5) can lead to a slower OH-isoprene reaction remaining more isoprene in the atmosphere.

Interestingly, compared to generating all INs, including only hy-INs has a more significant impact on isoprene. CH_3O_2 (Fig.4.4.7) is a product of al-INs chemistry. As a reactive RO_2, CH_3O_2 can react with NO rapidly during day and night, which can not only lead to O_3 formation, but also competes with O_3-NO reaction reducing O_3 depletion. Hence, with the al-INs included, the

reduction in O_3 becomes smaller over most of the domain in MOZART-4 leading to less significant changes in OH and isoprene.

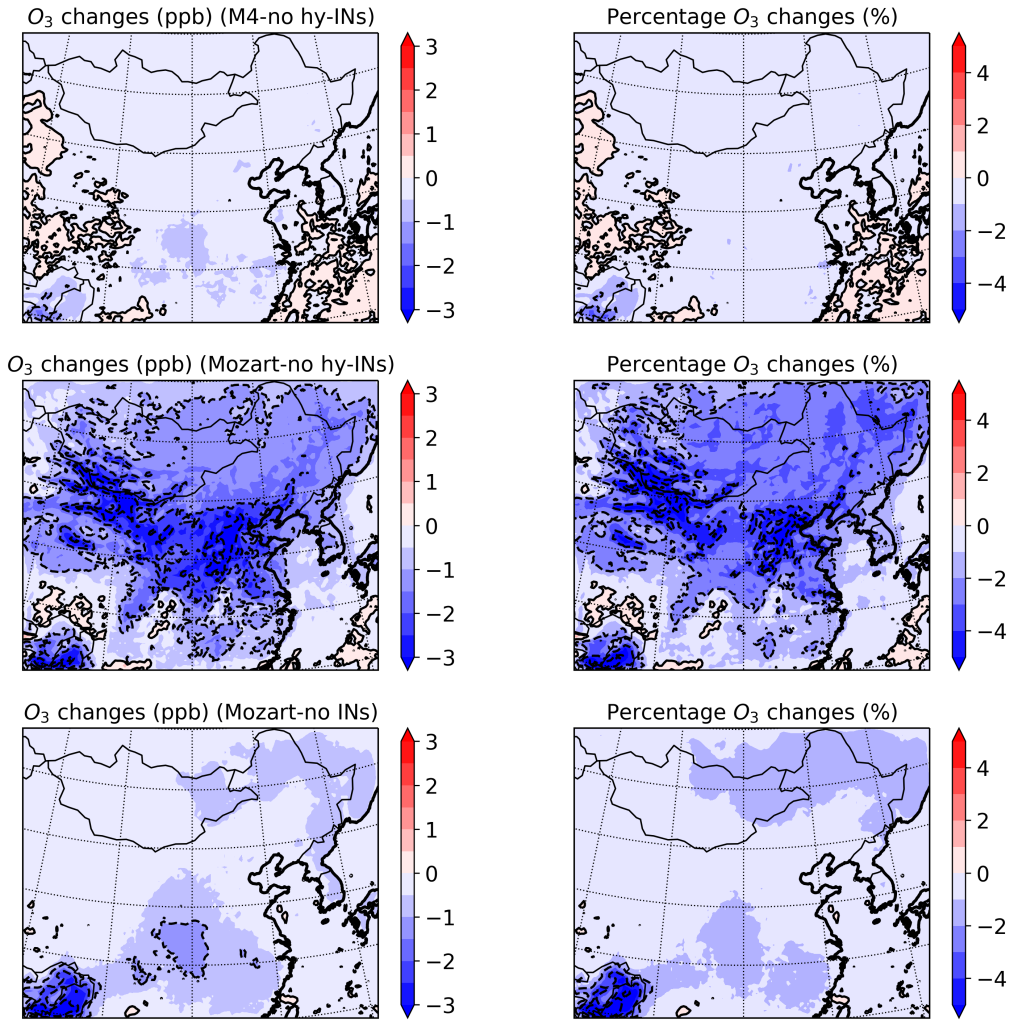

Figure 4.4.6: Same as Fig.4.4.1, but for the O_3.

The impact of hy-INs on OH are simulated similarly with both mechanisms Fig.4.4.5. Hy-IN has a negative impact on the OH over most of China apart from the west of China. Since reacting with OH is a primary sink of hy-INs. It is not a surprise to see a negative impact.

However, the variation of O_3 shows a great difference between the two mechanisms Fig.4.4.6, which again is due to the changes in RO_2. Both CH_3O_2 and CH_3CO_3 (Fig.4.4.7 and Fig.4.4.8) simulated in M4 mechanism are higher than they are in MOZART-4 leading to a more efficient O_3 production in M4.

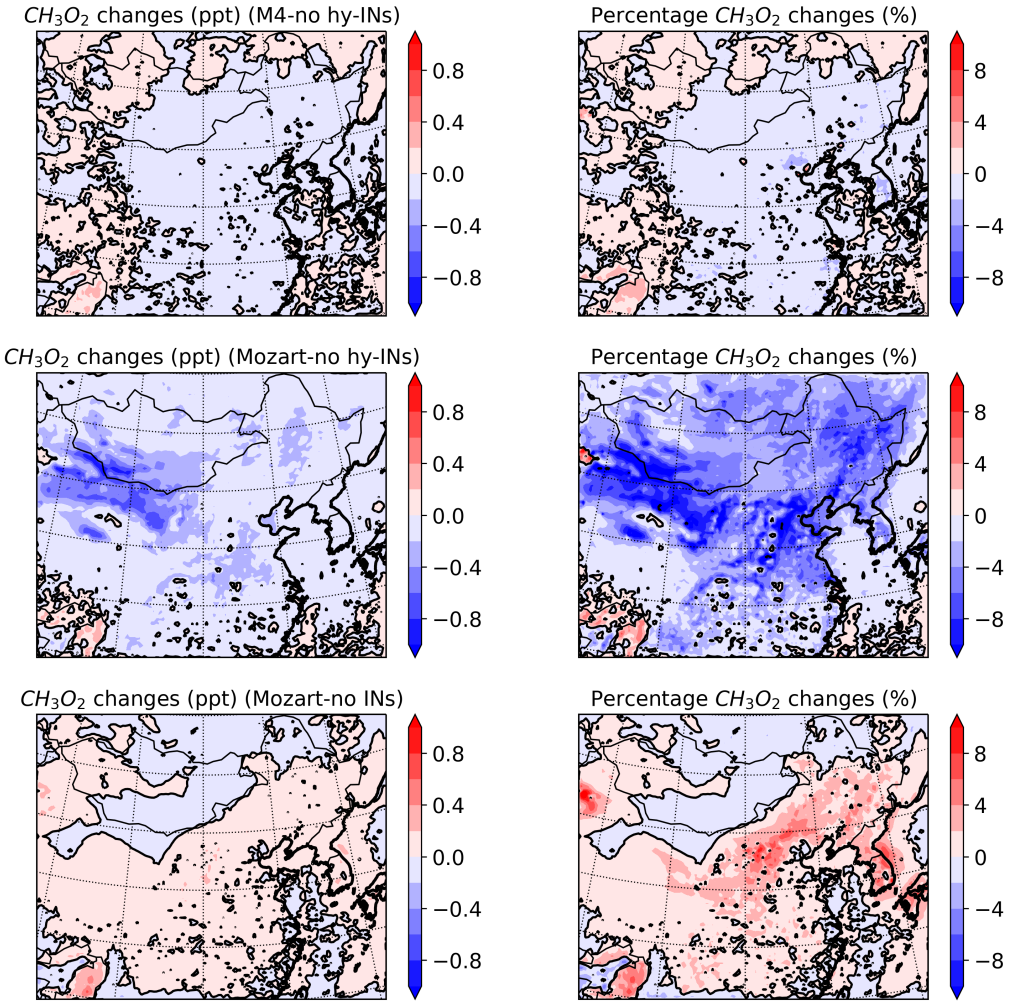

Figure 4.4.7: Same as Fig.4.4.1, but for the CH_3O_2.

4.5 Conclusion

This chapter discussed the detailed isoprene chemistry and its impact on various chemical systems simulated by M4 and MOZART-4 chemical mechanisms. Tags are added to quantitatively study and compare the NO_2 recycled via different branches of isoprene and INs chemistry. However, tags cannot be implemented to some products that are not only produced by isoprenes, such as shorter chain peroxy radicals, nitrates and aldehydes. Hence, run with no isoprene and no INs are designed to investigate the impact of isoprene and INs on the chemical systems.

Section 4.2 compares the simulations with M4 and MOZART-4 chemical mechanism. Very similar results of NO_X, HO_X, VOCs and O_3 concentrations are calculated by both mechanisms over the whole domain. In Beijing, the

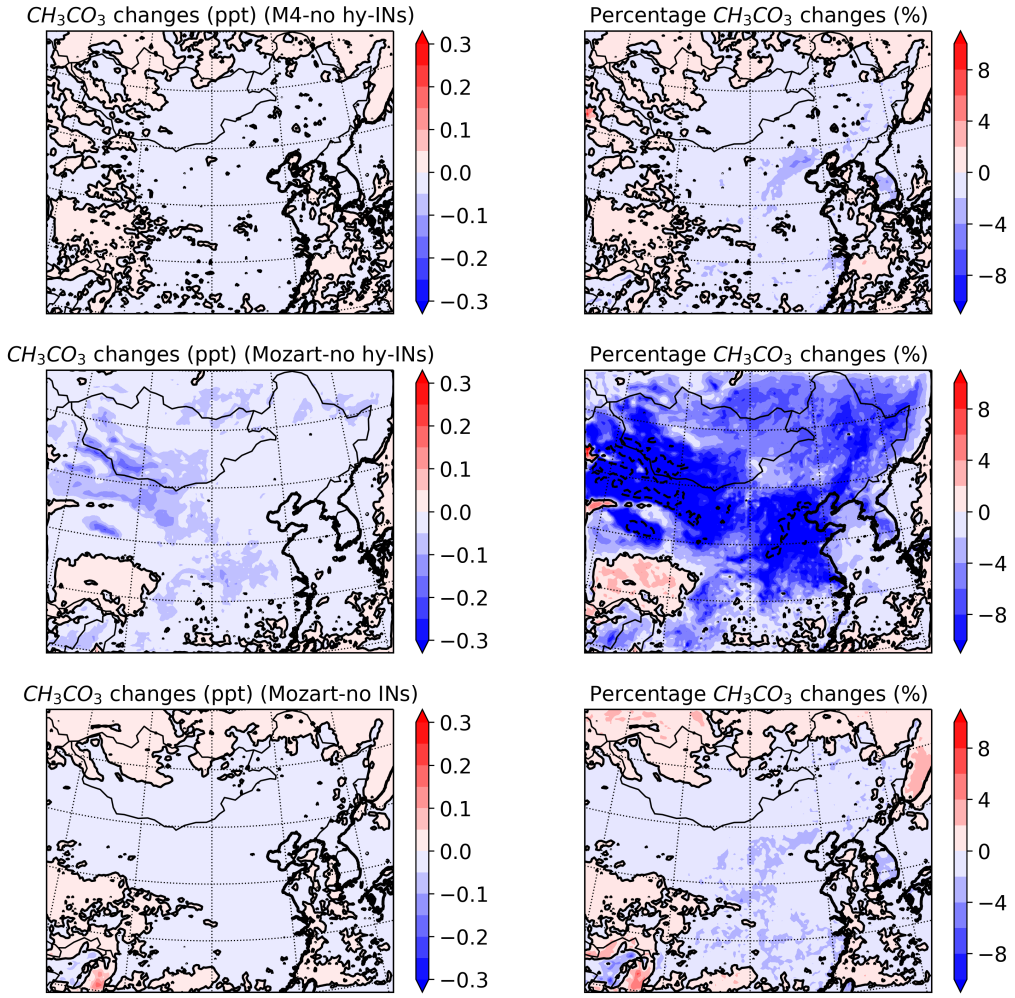

Figure 4.4.8: Same as Fig.4.4.1, but for the CH_3CO_3.

averaged diel patterns of O_3, NO_X and OH from Run 1 almost overlaps Run 3. Hence, the improvement of M4 in generating better O_3 simulations is not significant.

However, detailed isoprene chemistry in M4 treats RO_2 differently from MOZART-4. More RO_2 are produced during isoprene oxidation resulting in an upsurge of RO_2 concentration over most of the domain affecting the kinetics of chemistry. In the NO_X-rich environment, increasing RO_2 lead to enhancement of O_3, which could produce more OH thereby changing the VOC and NO_X concentrations.

The products of INs degradation are different in the two mechanisms. Organic nitrates are produced in reactions between INs and OH in M4, while it is not in MOZART-4. This difference not only impacts the simulation of organic nitrates

concentrations but also affects the NO_X recycling. In general, more NO_2 are recycled by isoprene and INs in MOZART-4 chemistry. However, the O_3 production from the NO_2 is lower than it is in M4 due to the larger sink of NO_2 in MOZART-4.

NO_X recycled via different branches of isoprene chemistry is also studied with tags. The total recycled NO_2 reaches the first peak at noontime with the value of roughly 20 ppt. The NO_2 concentration here is the balance between the production and the loss. In the model, more NO_2 has been released from the isoprene derived species, and about 1.6 ppb of O_3 is produced at noontime. At 19.00 in the evening, a great amount of NO_2 is formed via ni-ISOPO2, however, much less O_3 is produced since no photochemistry is happening.

NO_2 recycled via different INs isomers are also quantified. ISOPBNO3 and ISOPDNO3 contribute to 80% and 90% of isoprene derived NO_2 formation and O_3 production during the day. Since ISOPCNO3 can be formed with ni-ISOPO2 and RO_2 reactions, the diurnal pattern of NO_2 recycled by ISOPCNO3 is different from the other hy-INs.

Section 4.3 compares the impact of isoprene chemistry in both mechanisms. In simulations generated with both mechanisms, isoprene chemistry contributes to up to 18% of total O_3 concentration over east China.

The variations of most species from the two chemical mechanisms are similar to each other, including HO_X, NO_X and PAN. However, more RO_2 and organic nitrates are simulated in M4, which suggest that RO_2 and organic nitrates are cycled in the more explicit isoprene chemical mechanism.

Section 4.4 evaluates the impact of INs on different systems. As expected, the formation of INs has a small negative impact on O_3 over most of mainland China due to the reduction in NO_X. The degradation of hy-INs is represented differently in the two mechanisms leading to the discrepancies in O_3 simulation. Also, a slight increase of O_3 over East China Sea is modelled, which may be due to the NO_X released by hy-INs.

5

Perturbation studies

5.1 Introduction

The detailed isoprene chemistry and its impacts are discussed in the previous chapter by comparing the model results generated with different chemical treatments. It is clear that this chemistry is not linear and is sensitive to local NO_X-VOC regimes. Since isoprene and NO_X are two important precursors of O_3, their behavior can affect O_3 distribution.

In this chapter, I aim to understand further the isoprene chemistry and its impacts under various NO_X-VOC conditions but with a different approach - changing the emissions of NO_X and isoprene. Run 1 is still considered as the 'benchmark' run, and three sensitivity test runs are set up using the same configuration as Run 1 but different emission scenarios.

During the past several years, China started to apply rigorous emission strategies across the country to improve air quality. Compared to the value in 2010, decreases in NO_X emissions are reported by Sun et al. (2018) (18.7% 2010-2015), Liu et al. (2016) (15%, 2010-2015), and Zheng et al. (2018) (17% 2010-2017). Also, this decreasing trend of NO_X emission is expected to have continued in subsequent years to meet the emission target of China. However, as mentioned in the previous chapter, the reduction of NO_X does not always lead to lower concentrations of secondary pollutants such as O_3, but can enhance its mixing ratio in certain areas.

The first sensitivity test (ST1) is therefore designed to investigate the effect of the decreasing NO_X emissions. In ST1 NO_X emissions are reduced by 25%. As mentioned in section 2.4.3, WRF-Chem reads in anthropogenic emissions from

the *wrfchemi* files. A factor of 0.75 is applied to the NO and NO_2 emissions over the entire domain when generating the *wrfchemi* files for ST1. The rest of the settings remain the same as Run 1.

ST2 is designed to examine the impacts of a 50% isoprene emission increase. Li and Xie (2014) reported a 41.60% increase in isoprene emission over the past 23 years owing to the enhanced forest volume in China. The Three-North Shelter Forest Program is a series of human-planted forest strips in north China to prevent expansion of the desert. This program started in 1978 and is planned to be completed around 2050. Due to this program, isoprene emission flux increased up to 58% between 1982 and 2010 in the central north China region (Zhang et al., 2016; Chen et al., 2018).

Modification of the isoprene emission in WRF-Chem is not as straightforward as changing NO_X emissions since it is calculated online by MEGAN during the model run (section 2.4.3). The function of biogenic emissions is defined in the file *module_bioemi_megan2.F* under the *chem* directory of WRF. To increase the isoprene emission by 50%, I applied a scaling factor of 1.5 to the line:

E_megan2(is_isoprene) = adjust_factor(imgn_isop) × msebio_isop(i,j) × 1.5

This value is then passed to the emission variable e_bio(i, j, p_isopr) by the lines below:

gas_emis = mozcart_per_megan(is_isoprene) × E_megan2(p_of_megan2mozcart(is_isoprene))

e_bio(i, j, p_isopr-1) = e_bio(i, j, p_isopr-1) + gas_emis × convert2

In this way, an increased isoprene emission is read in by the chemical solver without affecting other biogenic emissions.

ST3 combines the scenarios from ST1 and ST2. In this test, isoprene emission is increased by 50% while NO_X emission is reduced by 25%.

The results of ST1, ST2 and ST3 are discussed in section 5.2, 5.3 and 5.4, respectively. Section 5.5 gives a brief review of the chapter.

5.2 Sensitivity test 1: reduced NO_X emissions

5.2.1 Change of inorganic NO_Y

The NO_X emissions are reduced by 25% in this test all over the domain, however, the decline of the NO_X concentrations is not 25% everywhere (Fig. 5.2.1). In the North China Plain (NCP) and Yangtze River Delta (YRD) which are considered as high NO_X environments, NO_X mixing ratios decreased by over 30%, whereas, in the west of China, the change of NO_X mixing ratio is lower than 20%. The pattern of the absolute difference of NO_X is consistent with the locations of major cities, which indicates that more NO_X is lost in the places with higher anthropogenic emission signals.

NO_2 can be converted to NO_Z (NO_Y - NO_X) by reacting with oxidants including OH, O_3 and RO_2, and this is the primary loss path of NO_X in the model. As mentioned in the section 1.1.1, HNO_3 is a product of OH and NO_2 reaction. Hence, the decrease of NO_X hinders the formation of HNO_3, so it decreases across the whole of the domain (Fig. 5.2.2). Also, less OH is lost through this reaction, which results in an enhancement of OH over NCP region (Fig. 5.2.7).

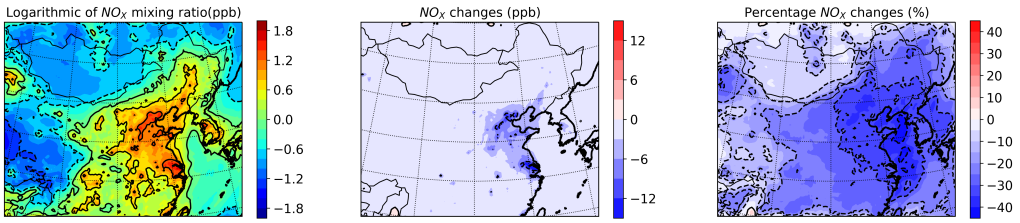

Figure 5.2.1: Contour maps of the average NO_X distribution with the ST1 emission scenario (left) and the absolute difference (middle) and the percentage change (right) between ST1 and the benchmark run. The NO_X mixing ratio is displayed on the logarithmic scale due to the wide range of values over the domain.

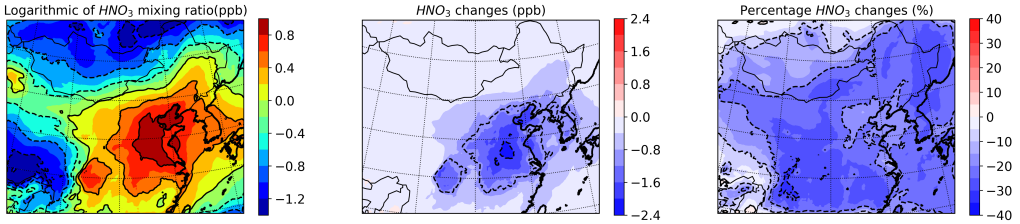

Figure 5.2.2: Same as Fig.1, but for the HNO_3.

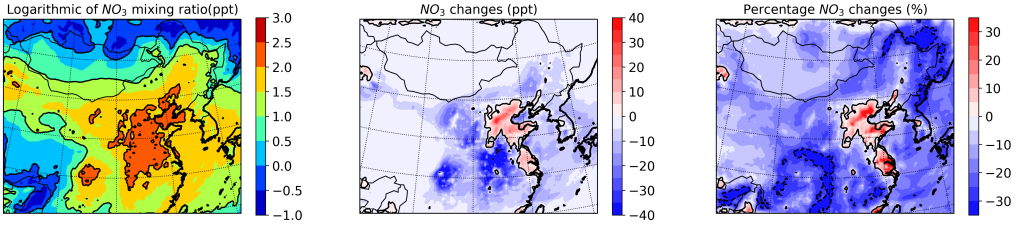

Figure 5.2.3: Same as Fig.1, but for the NO_3.

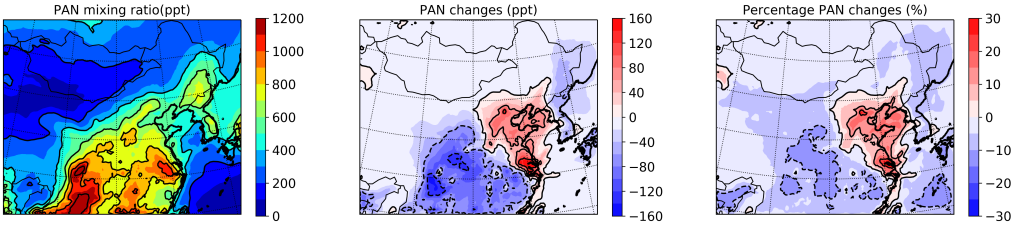

Figure 5.2.4: Same as Fig.1, but for the PAN with linear scale.

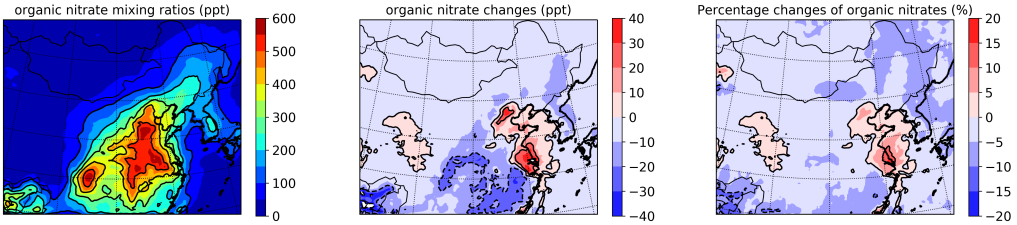

Figure 5.2.5: Same as Fig.1, but for the organic nitrates with linear scale.

Figs. 5.2.3, 5.2.4 and 5.2.5 illustrate the distribution and variation of NO_3, PAN and organic nitrates under this emission scenario. These three species show decreases across most of the domain, which is consistent with the reduction of one of their main precusors – NO_X. However, counter to this there is an increase in these species in the NCP and YRD. The reason for this increase will be discussed in the next section with other organic species. Nevertheless, it seems that it is the increase in the formation of these NO_Z species that is the reason for the decrease in NO_X being greater than 25%

The major source of NO_3 is the oxidation of NO_2 by O_3. The O_3 mixing ratio is enhanced in the NCP region (Fig. 5.2.8) while NO_2 is not, so the net effect on NO_3 is a balance between these two competing changes. NO_3 is involved in a reversible reaction: the NO_2, NO_3 and N_2O_5 reaction ($NO_2 + NO_3 \rightleftharpoons N_2O_5$). The lower NO_2 concentration shifts the equilibrium towards the left, resulting in an increase of NO_3.

The maxma percentage decrease of NO_X is simulated over the Yellow Sea (43%), which is a combined effect of nitrates formation and the low NO_X mixing ratio in the first place.

5.2.2 The NO_X, VOCs and O_3 chemistry

After examining the behaviour of inorganic NO_Y, this section looks into the interactions between NO_X, VOCs and O_3. Here, I discuss the variation of VOCs first since VOCs are primary pollutants while O_3 is a secondary product with complex processes in both formation and decomposition.

Fig. 5.2.6 shows the total VOCs (including both AVOCs and BVOCs) concentration and difference in ppb carbon, as well as the percentage change. VOCs show a reduction (up to 2.6 ppbC) in the NCP and YRD and a slight increase (up to 0.8 ppbC) over the rest of the mainland China. Since the emissions remain the same as in the benchmark run, this variation suggests a different chemical loss rate of VOCs.

The oxidation of hydrocarbons is dominated by OH reaction during the daytime and reacting with NO_3 is the primary sink of hydrocarbons after sunset. O_3 is another important oxidant of them, and the reactions between O_3 and hydrocarbons occur during day and night. However, O_3 is also a product of VOCs oxidation making this chemistry less straightforward.

Both OH (daytime only) and NO_3 show increases in mixing ratios in the NCP and YRD regions and slight decreases over a great area of the rest of China. The changes in OH and NO_3 concentration are opposite to the variation of VOCs, which suggesting that OH and NO_3 may contribute to the VOCs changes.

Also, with more hydrocarbons being oxidised, an enhancement of the organic peroxyl radicals (RO_2) is simulated (Fig. 5.2.9), which can enhance O_3 formation and OH recycling.

PAN and organic nitrates are formed via RO_2 and NO_X reactions. In NCP and YRD regions, the enhanced OH rapidly react with VOCs (mainly AVOCs) forming RO_2. Hence, more RO_2 can react with NO_X leading to an enhancement

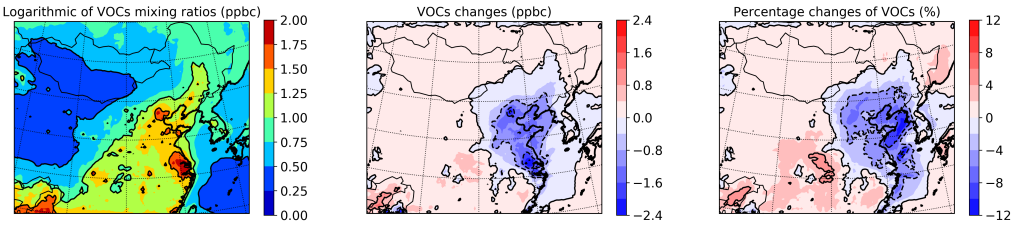

Figure 5.2.6: Same as Fig.1, but for VOCs.

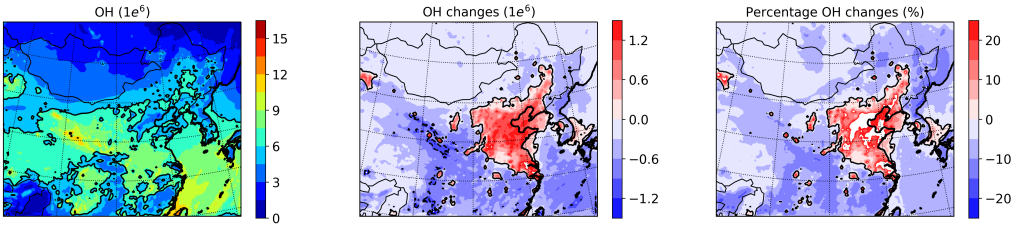

Figure 5.2.7: Same as Fig.1, but for the daytime OH with linear scale.

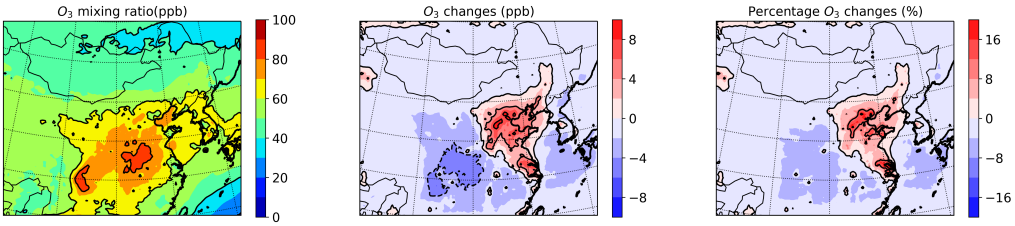

Figure 5.2.8: Same as Fig.1, but for O_3 with linear scale.

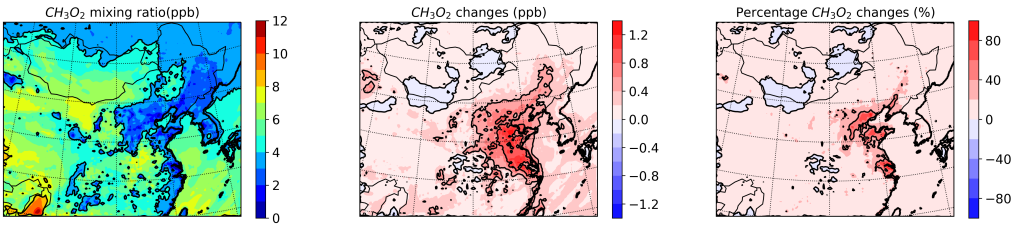

Figure 5.2.9: Same as Fig.1, but for CH_3O_2 with linear scale.

of PAN and organic nitrates (Figs. 5.2.4 and 5.2.5).

The changes in NO_X and VOCs variation can now be considered in the context of explaining the changes of O_3. However, this chemistry is not linear and can be affected by the NO_X-VOCs regimes. As mentioned in section 1.1, depending on the NO_X and VOCs concentrations, three regimes are defined, which are NO_X-limited, VOCs-limited and the transition regime.

The formaldehyde (HCHO) NO_2 ratio (FNR) is a commonly used factor to

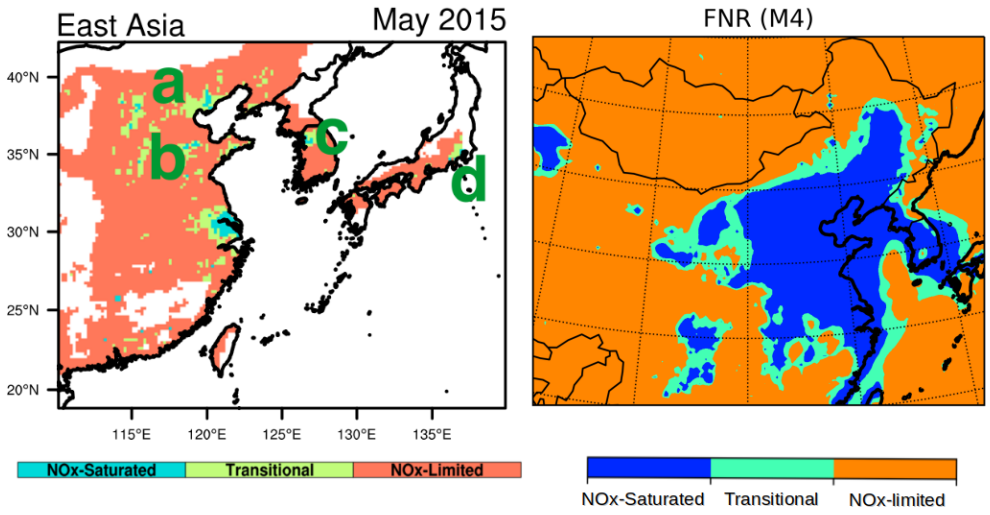

Figure 5.2.10: Comparison between the observed (left, for May 2015, (Jin et al., 2017)) and modelled (right, for 16th May to 30th June 2017) O_3 production regimes depending on the FNR values.

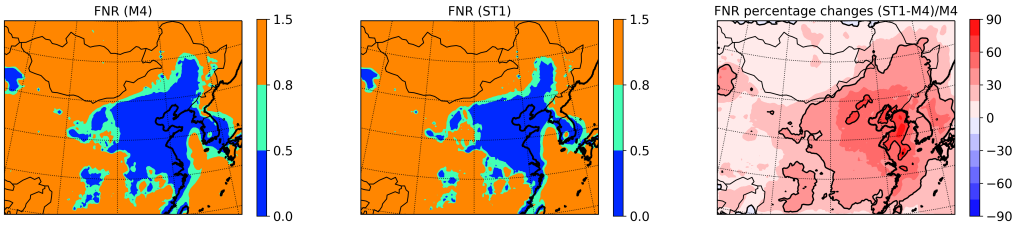

Figure 5.2.11: Contour maps of the averaged FNR of the benchmark run (left), of ST1 (middle) and the percentage difference (right) between the two.

indicate various NO_X-VOCs conditions (Jin and Holloway, 2015; Witte et al., 2011). However, different emission characteristics can influence the threshold value for determining the regimes. Here, I take the FNR < 0.5 as the VOCs-limited regime, FNR > 0.8 as the NO_X-limited regime, and $0.5 <$ FNR < 0.8 as the transitional regime, where O_3 production is sensitive to both NO_X and VOCs. These values are validated for east Asia by comparing the satellite data with the global model simulations (Jin et al., 2017). Fig. 5.2.10 compares the O_3 production regimes from satellite observations and the model simulations. The simulated FNR values seem to be lower than the observed resulting in a larger VOCs-limited region. This is understandable since NO_X are overestimated (section 3.4) in the model. However, the location of low FNR values are captured by the model and the general pattern between the two shows similarity to some extent. Also, with reduced NO_X emissions, O_3 concentraion increased in the VOCs-limited region defined here, which indicates that appropriate threshold values are used.

Fig. 5.2.11 illustrates the comparison of the spatial distribution of FNR between the two emission scenarios. Since FNR is < 0.5 in the NCP and YRD regions, it suggests that the OH-NO_2 reaction is a significant sink for OH and this will lead to inefficient O_3 production. Also, the NO titration effect is of great importance for O_3 decomposition in this regime. Reducing the NO_X emissions not only impedes the formation of HNO_3 releasing OH radicals, which in turn leads to more RO_2, but also reduces the NO-O_3 reaction. As a result, the O_3 concentration is increased due to both enhanced production and reduced loss. Wang et al. (2019a) found that part of NCP and YRD are VOCs-sensitive regions and control measures only focused on NO_X aggravate O_3 pollution. Similar results are reported by previous studies in several Chinese cities including Beijing (Zhang et al., 2014), Nanjing (An et al., 2015), Shanghai (Tie et al., 2013) and Chengdu (Tan et al., 2018).

However, this is not the case everywhere. O_3 decreases (up to 6 ppb) in the middle of China (most of the Hubei and Sichuan province) in this test. After reducing NO_X emissions by 25%, these areas shift from VOCs-sensitive (blue) to transition (green), or even NO_X-sensitive environment (orange). That is to say, significant amounts of RO_2 are formed but there is a lack of NO_X such that O_3 production is limited by NO_X. Thus, a lower NO_X concentration hinders the O_3 formation, resulting in a reduction of O_3.

5.2.3 Isoprene chemistry

The isoprene variation (Fig. 5.2.12) is similar to the total VOCs: decreases over the NCP and YRD due to the increased OH and O_3, and slight enhancement over most of the rest of mainland China.

However, the isoprene nitrates (INs) (Fig. 5.2.13 and Fig. 5.2.14) illustrate a different pattern from the organic nitrates and PAN (Fig. 5.2.5 and Fig. 5.2.4). Both hy-INs and al-INs are simulated with lower values in the NCP region and higher in the northwest of China with the reduction of NO_X emissions, whereas significant enhancement (up to 30%) of PAN and organic nitrates are simulated in the NCP region and slight decrease of them are modelled in the northwest of China. This can be due to several reasons. The concentration of INs shows the balance between its production and its loss. INs are produced when isoprene peroxy radicals ($ISOPO_2$) react with NO. $ISOPO_2$ are enhanced due to the increased OH-isoprene reaction, but this is countered by the reduction in NO_X concentration. Moreover, the oxidation of OH is one of the major sinks of the

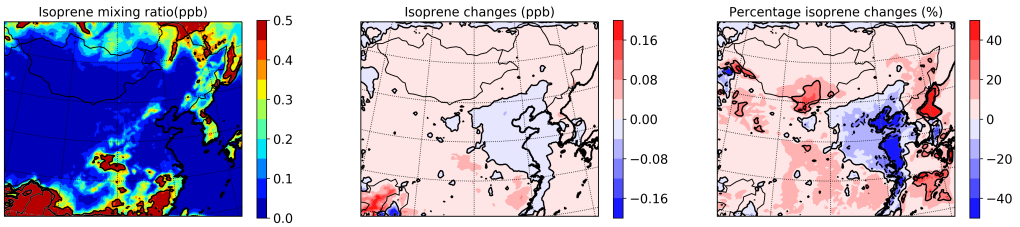

Figure 5.2.12: Same as Fig.1, but for the isoprene.

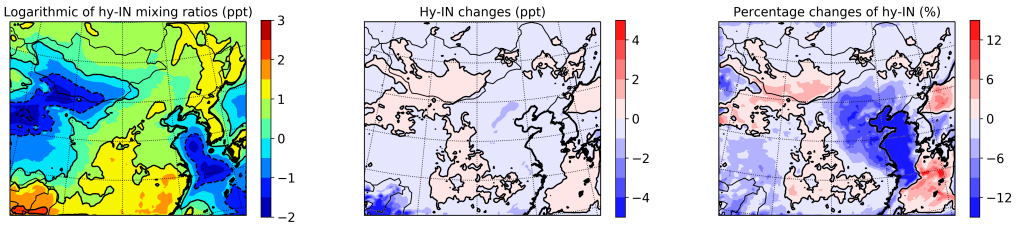

Figure 5.2.13: Same as Fig.1, but for the hy-INs.

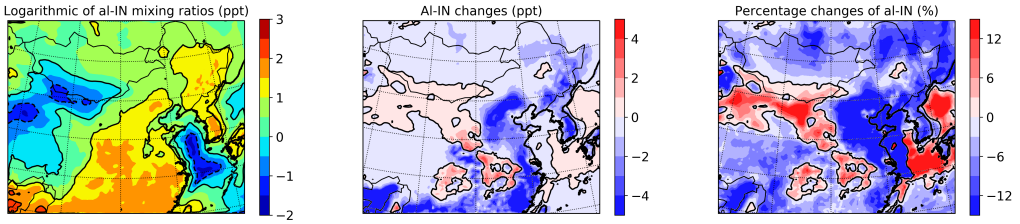

Figure 5.2.14: Same as Fig.1, but for the al-INs.

INs. Hence, the increase of OH will lead to faster loss of INs. The organic nitrates and PAN are less reactive than INs, as a result, the destruction of them through the enhanced OH are not much as it is for INs.

Another possible reason for the INs variations differ from the organic nitrtes is that INs are formed from a biogenic VOC - isoprene, which is not emitted as much as the other anthropogenic VOCs (AVOCs) in urban areas. Since NO_X and the AVOCs are co-emitted, in the NCP and YRD region, the increasing OH due to change of NO_X emission can produce more RO_2 from the AVOCs than the $ISOPO_2$ making INs formation less competitive to the formation of other organic nitrates.

5.3 Sensitivity test 2: incremental isoprene emission

5.3.1 Isoprene chemistry and its impact

In this test, an increase of 50% of the biogenic isoprene emission is applied to the whole domain. The anthropogenic emission of isoprene remains unchanged due to the small portion compared to the biogenic source.

Fig. 5.3.1 shows the average concentration and the change in isoprene. In the majority of China, the isoprene increment is less than 0.1 ppb due to the low emission in the first place. However, this increase does have an impact since this magnitude of isoprene change can be double the mixing ratio (100% increase) in some places. Larger increases are seen in the middle (Shaanxi province) and the South (Jiangxi and Fujian province) of China.

Once emitted to the atmosphere, isoprene rapidly reacts with OH, O_3 and NO_3. The variations of these three species are illustrated in Figs. 5.3.2, 5.3.3 and 5.3.5. Again, the isoprene chemistry is not linear, as a result, the enhancement of isoprene can have different impacts on OH, O_3 and NO_3 depending on the ambient air conditions. FNR (Fig. 5.3.10) is calculated as an indicator of the O_3 sensitivity regimes to help interpret the variations.

Isoprene-OH reaction happens swiftly during the daytime, so higher isoprene emissions can lead to a reduction of OH. This is seen in most NO_X limited regimes, especially the South of China. Interestingly, higher OH concentration is simulated in NCP and YRD regions. In a VOCs-limited regime such as NCP and YRD, even a slight increase of isoprene can lead to a significant enhancement of RO_2 (Fig. 5.3.4) accelerating the formation of O_3, which is the primary source of OH. OH is therefore enhanced if the increase in its formation exceeds the increase in its sink.

With a sufficient amount of NO_X in the atmosphere, additional isoprene is expected to produce more O_3. Hence, in most of China, O_3 witnesses a higher concentration. This increment is more distinct in places with lower FNR. In contrast, in the north (Mongolia and Russia) and the southwest (India and Myanmar) of the domain, due to the very low NO_X mixing ratio, extra isoprene acts as a sink of O_3 leading to a decline in O_3 concentration.

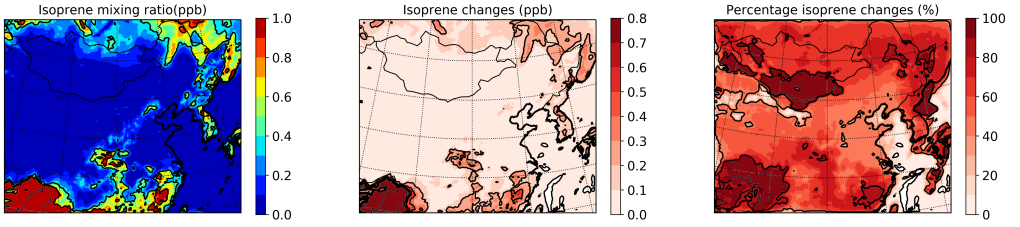

Figure 5.3.1: Contour maps of the averaged isoprene distribution with the ST2 emission scenario (left) and the absolute difference (middle) and the percentage change (right) between ST2 and the benchmark run.

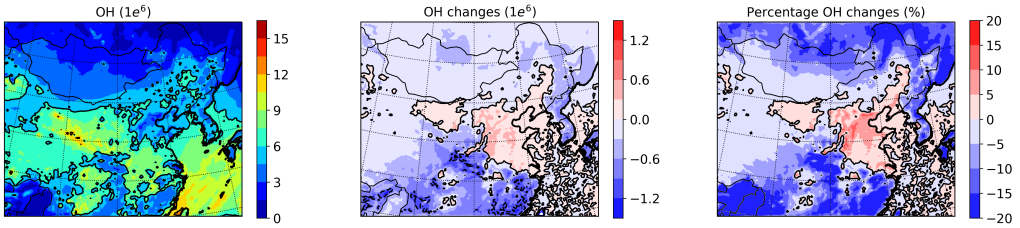

Figure 5.3.2: Same as Fig.5.3.1, but for the averaged daytime OH.

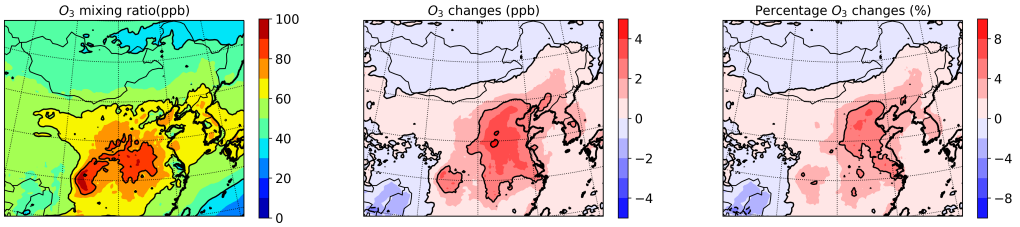

Figure 5.3.3: Same as Fig.5.3.1, but for the O_3.

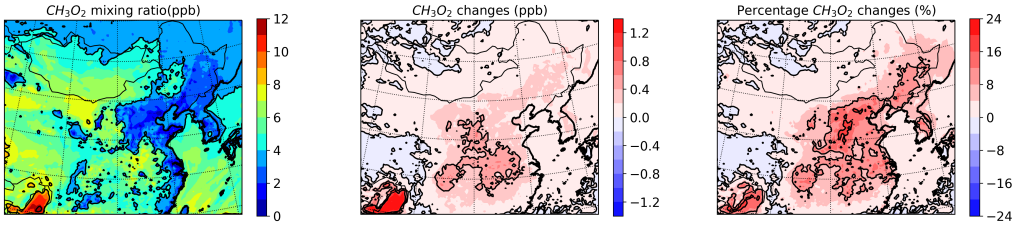

Figure 5.3.4: Same as Fig.5.3.1, but for the CH_3O_2.

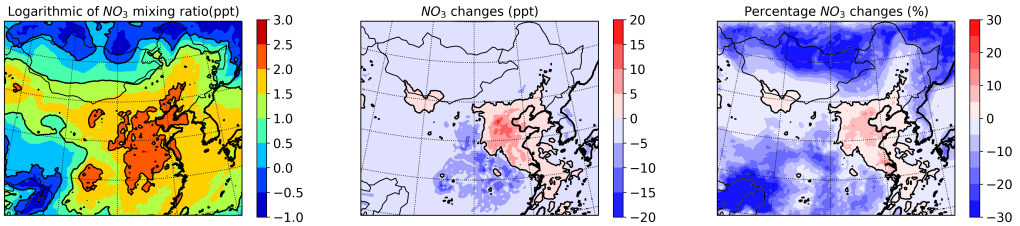

Figure 5.3.5: Same as Fig.5.3.1, but for the NO_3 with a logarithmic scale.

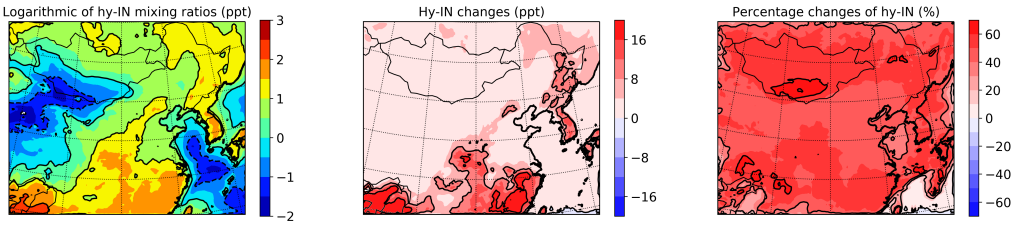

Figure 5.3.6: Same as Fig.5.3.1, but for the hy-INs with a logarithmic scale.

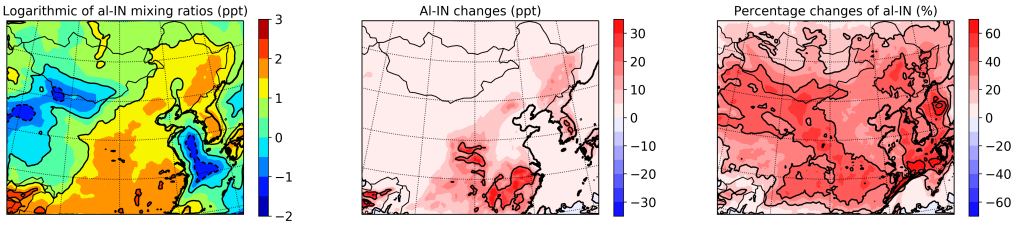

Figure 5.3.7: Same as Fig.5.3.1, but for the al-INs with a logarithmic scale.

Similar to the OH, NO_3 is of importance for isoprene loss but mainly during the night. Hence, increased isoprene can have a negative impact on NO_3 concentration. Nevertheless, more NO_3 can be produced with enhanced O_3 leading to its increment over NCP and YRD.

Both hy-INs (Fig. 5.3.6) and al-INs (Fig. 5.3.7) show a dramatic increase (up to 70%) over the domain, which could impact the NO_X (Fig. 5.3.9) distribution. The slight increase of NO_X over the sea might indicate NO_X recycling by the INs transported from the land. However, the absolute increase of INs is in ppt levels that might be negligible.

5.3.2 The NO_X, VOCs and O_3 chemistry

The change of VOCs (including both AVOCs and BVOCs) concentration (Fig. 5.3.8) is the inverse of the OH variation. Slightly lower VOCs concentrations are simulated in the NCP region and a 12% increase is modelled in the south and the north of the domain with less urbanization. Since the total VOCs emission is increased in this test, the lower mixing ratio in NCP indicates an enhancement of RO_2 (Fig.5.3.4) in the region. RO_2 are short-lived and rapidly react with NO producing NO_2 or organic nitrates. This contributes to the enhanced PAN (Fig.5.3.11) and organic nitrates (Fig.5.3.12) in China.

The transit from VOCs-limited regime to the mix-sensitivity regime can be

found in the middle of China (Sichuan province Fig. 5.3.10). This suggests that planting trees with high isoprene emission factors in Sichuan province (the middle south of China, Fig. 4.1.1) can result in more severe O_3 pollution.

Compared to the change of FNR in ST1, the increase of FNR in ST2 is less significant. This is also true for the changes of O_3 resulting from the two emission scenarios. It could imply that in a high NO_X emission environment like China, the O_3 formation is more sensitive to the variation of NO_X rather than VOCs. However, in ST1 the averaged decline of NO_X concentration in NCP is up to 18 ppb, whereas the increment of isoprene over NCP is in ppt level. Even with a very small increase of isoprene, O_3 shows an enhancement of over 4 % in the whole NCP and a maxima increase of 6 ppb in the middle of China.

In ST2, the changes of PAN (Fig. 5.3.11) show a similar pattern to the organic nitrates and O_3. PAN is produced from CH_3CO_3 and NO_2 reaction, so the concentration of PAN is expected to increase when NO_2 is enhanced. In the NCP region, more NO can be converted to NO_2 with the increased RO_2. Hence, both O_3 and PAN are produced more efficiently. Organic nitrates are the products of RO_2 and NO reactions, so its production is expected to increase over most of China due to the RO_2 increment.

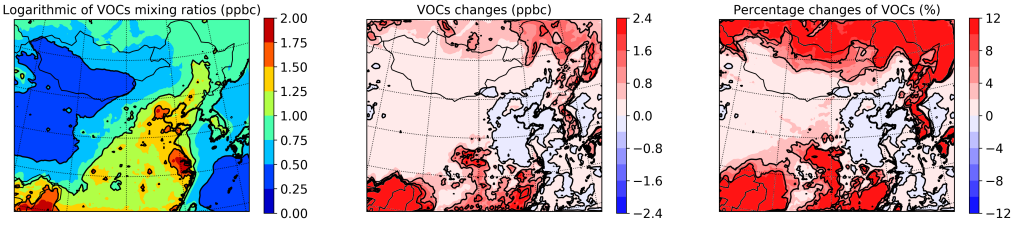

Figure 5.3.8: Same as Fig.5.3.1, but for the VOCs with a logarithmic scale.

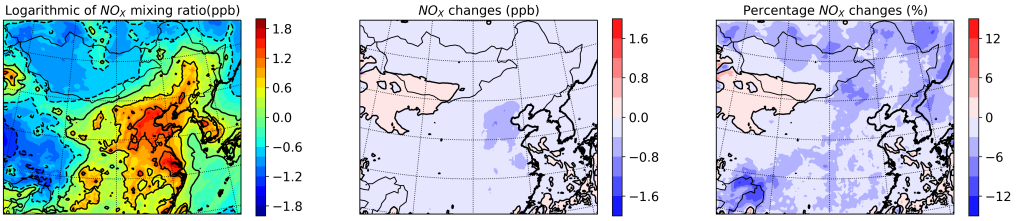

Figure 5.3.9: Same as Fig.5.3.1, but for the NO_X with a logarithmic scale.

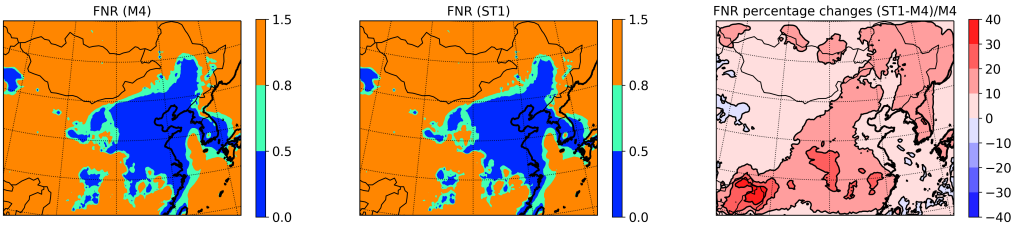

Figure 5.3.10: Same as Fig.5.2.11, but for the ST2.

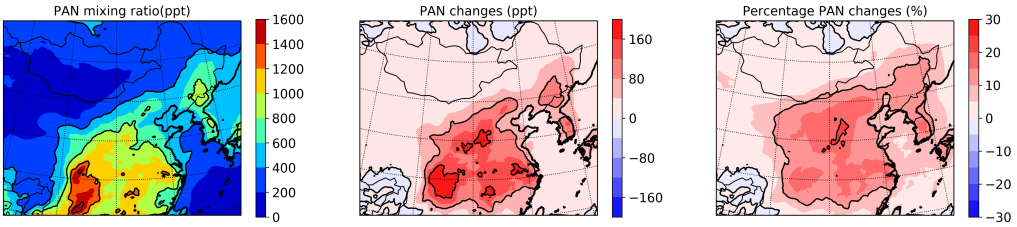

Figure 5.3.11: Same as Fig.5.3.1, but for the PAN.

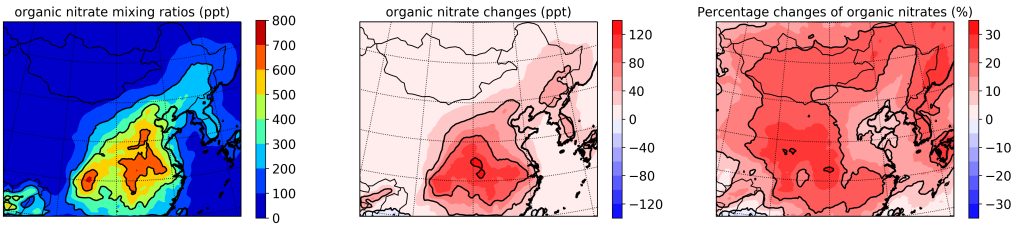

Figure 5.3.12: Same as Fig.5.3.1, but for the organic nitrates.

5.4 Sensitivity test 3: combined emission scenarios

5.4.1 The NO_X, VOCs and O_3 chemistry

ST3 combines the two emission scenarios: NO_X emissions reduced by 25 %, and isoprene emission increased by 50 %.

The change in isoprene is illustrated in Fig. 5.4.1. Isoprene is increased all over the domain apart from the Yellow Sea. Over the Yellow Sea, the emission of isoprene is very low in the first place, so the 50 % increased does not lead to a much greater source of isoprene. However, as discussed in section 5.2.1, OH concentration (Fig. 5.3.2) in this region is enhanced significantly due to the reduction in the OH-NO_2 reaction resulting from the lower NO_X emissions. This then means that the loss of isoprene via reaction with OH is increased and the net effect over the Yellow Sea is a decrease in isoprene. The increase in OH due to the lower NO_X emissions is also the reason for a lower isoprene increase in NCP compared to the rest of the domain.

The distribution and changes of NO_X are very similar to the ST1, which is understandable since its emission is reduced by 25% in both runs. The variations of OH are also simulated with good agreement of ST1. The potential reasons behind its variation are discussed in section 5.2.1 and 5.2.2.

The FNR value is increased over the whole domain. In some regions in the middle and south of China, the emission scenarios in ST3 shift the O_3 production regime from VOCs-limited to transitional and even to the NO_X-limited regime. This ratio is useful in selecting the measures for O_3 control.

Total VOCs mixing ratio is decreased over NCP, which is a result of the increased OH reaction. The emissions of all VOCs remain the same except isoprene which is increased, but lower concentrations of VOCs are simulated. This implies more RO_2 are formed in this region leading to higher O_3 formation (Fig. 5.4.6 and Fig. 5.4.7). Again, their variation patterns show great agreement with the ST1. However, the increase of O_3 concentration in the NCP and YRD regions is even higher than the sum of the changes in ST1 and ST2. Up to 26% increase of O_3 are seen in these regions. This suggests that the O_3 pollution in NCP and YRD regions is not likely to be improved if only NO_X

emission is reduced and more trees are planted. Reduction of VOCs emissions at the same time is needed for O_3 mitigation.

The changes of PAN in the ST3 are similar to the ST1, whereas the variation of organic nitrates agree with the ST2 better. The variations in concentrations of PAN and organic nitrates reflect the balance between the decrease in NO_X concentrations and the increase in RO_2 concentrations. For PAN, the enhanced CH_3CO_3 leads to higehr values over most of northern China and the YRD region with a maximum increase of 40%. In the rest of the domain, the reduction of NO_X becomes the predominant factor of the changes in PAN. Apart from ISOPO2 and CH_3CO_3, all RO_2 species are the precusors of organic nitrates including the RO_2 produced during the oxidation of isoprene-derived species. Hence, when more isoprene is injected to the model, more RO_2 species are produced leading to the increase of organic nitrates across alomost the whole domain.

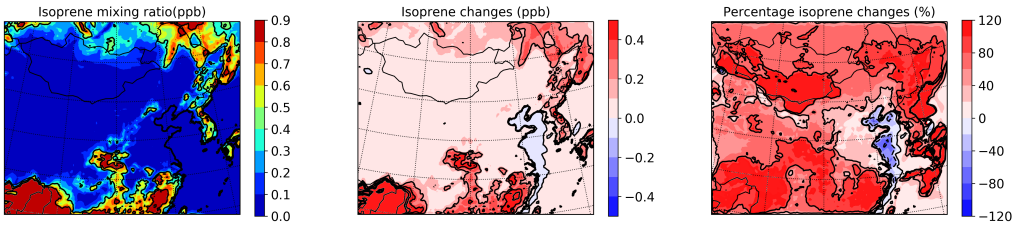

Figure 5.4.1: Contour maps of the averaged isoprene distribution with the ST3 emission scenario (left) and the absolute difference (middle) and the percentage change (right) between ST3 and the benchmark run.

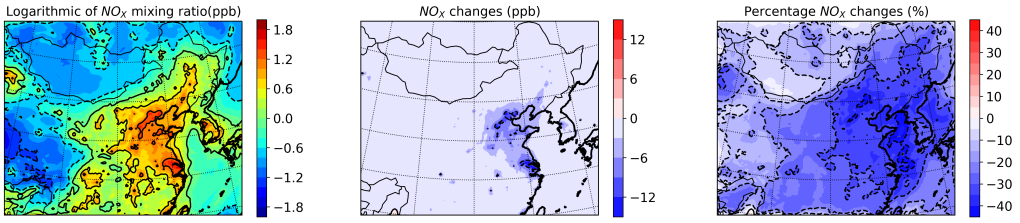

Figure 5.4.2: Same as Fig.5.4.1, but for NO_X with a logarithmic scale.

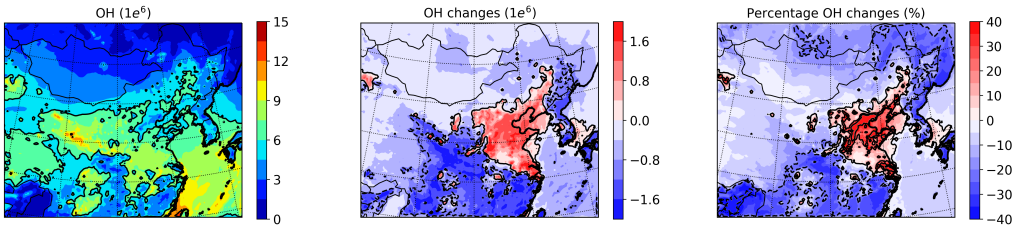

Figure 5.4.3: Same as Fig.5.4.1, but for the averaged daytime OH.

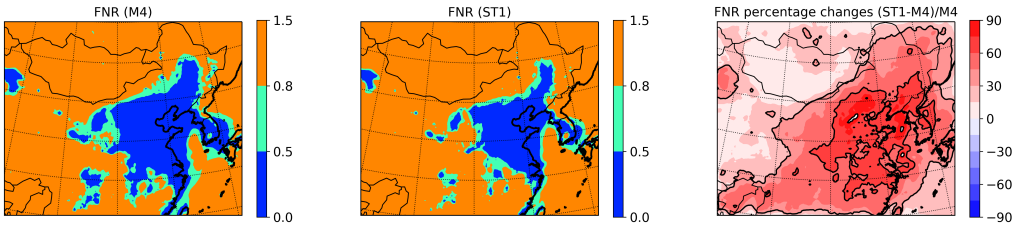

Figure 5.4.4: Same as Fig.5.2.11, but for ST3.

5.5 Comparison of three emission scenarios

Model results from three emission scenarios are discussed individually over the entire domain in the previous three sections. Here, I compare these emission conditions with each other and with the benchmark run in four locations. Three urban sites and one rural site are selected. Beijing(BJ), Shanghai(SH) and Chengdu(CD) are three megacities with a population of over 18 million in each

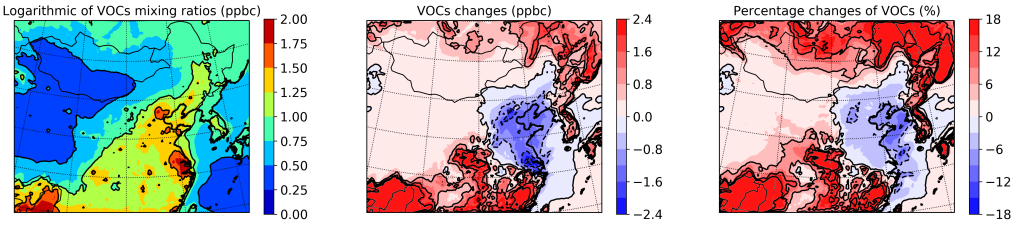

Figure 5.4.5: Same as Fig.5.4.1, but for the VOCs with a logarithmic scale.

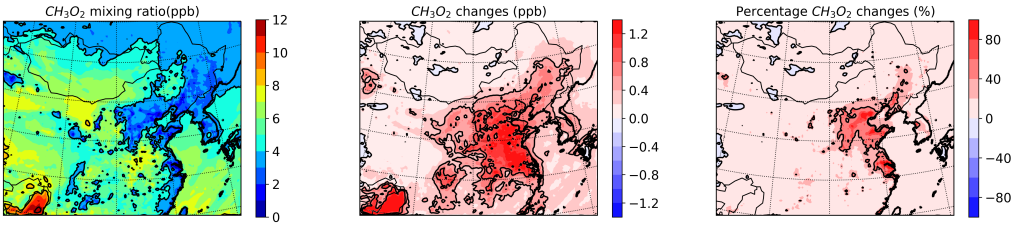

Figure 5.4.6: Same as Fig.5.4.1, but for CH_3O_2.

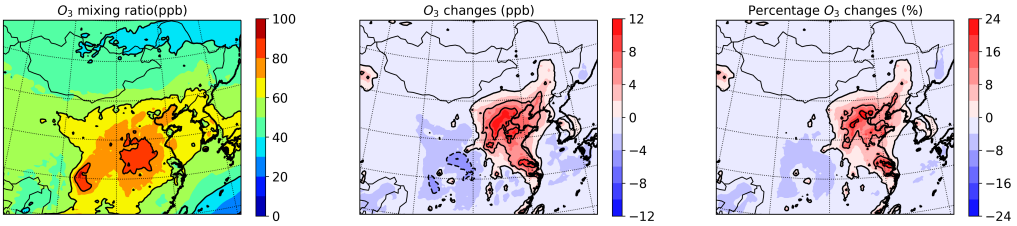

Figure 5.4.7: Same as Fig.5.4.1, but for O_3.

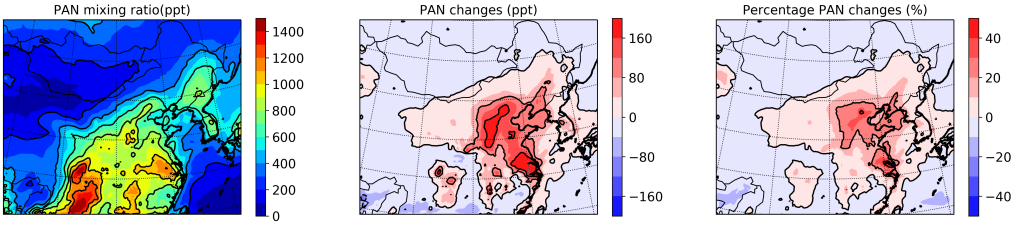

Figure 5.4.8: Same as Fig.5.4.1, but for PAN.

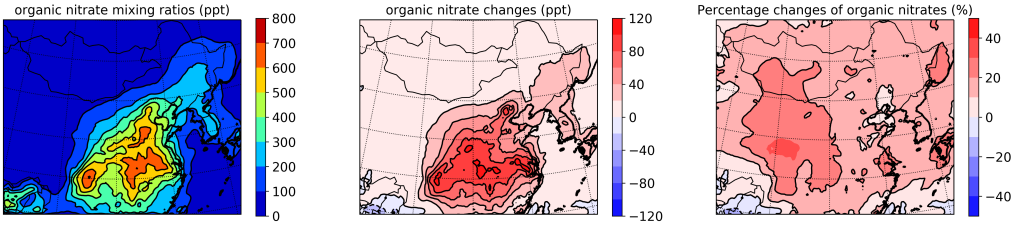

Figure 5.4.9: Same as Fig.5.4.1, but for the organic nitrates.

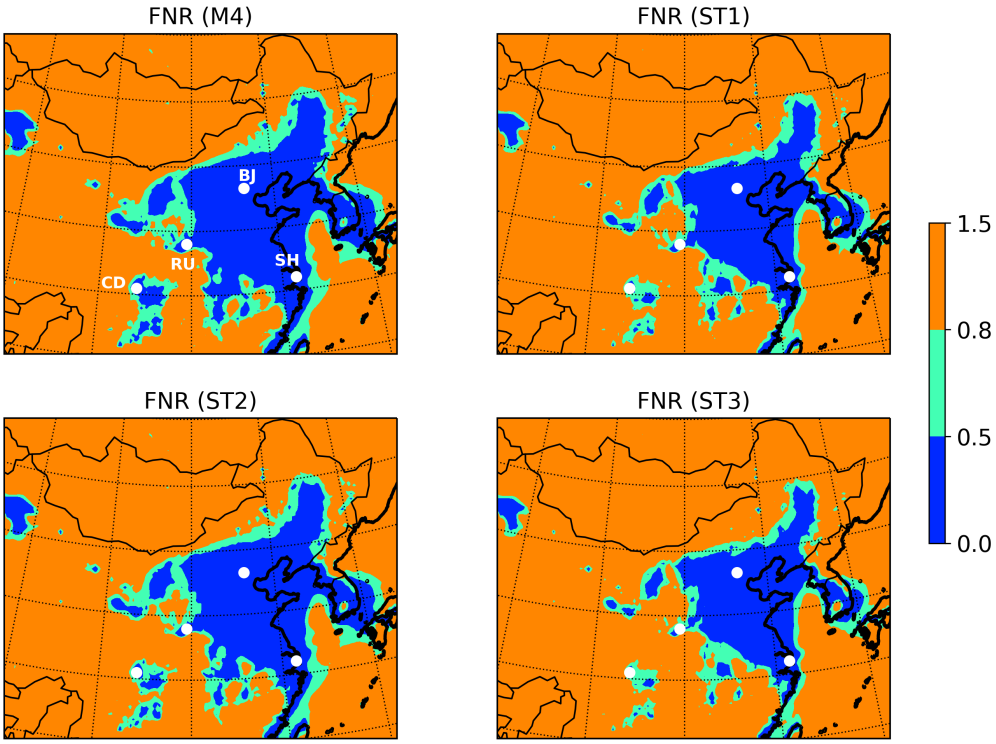

Figure 5.5.1: Contour map of FNR with four emissions scenarios. The four highlighted markers represent the location of the four sites selected.

city. Severe O_3 pollution is reported in all three cities during the summer. In contrast, one rural site(RU) close to another megacity - Xi'an is chosen to help understand the chemistry in a different NO_X-VOC regime. Fig. 5.5.1 shows the FNR generated with four emission scenarios. The location of four selected areas is highlighted with white markers.

The four sites are located in a wide area of China. Beijing and Shanghai are in the east of China close to the coast, while Chengdu and RU site are in the middle. Beijing and the RU site are considered in the north of China with dryer climate compared to Chengdu and Shanghai.

The NO_X-VOC regime for Beijing and Shanghai did not change for the three tests runs. They have always been in VOC-limited regime. Chengdu is another megacity in China, but not on the east coast. In ST3, it shifts from the VOC-limited regime to the transition regime. The rural site is specially selected due to that its NO_X-VOC regime changed from transition regime to NO_X-limited regime when different emission scenarios are applied.

5.5.1 Primary pollutants

Isoprene concentrations (Fig. 5.5.2) at the three urban sites show similar diel patterns. It peaks in the morning with increased radiation and temperature. At noontime, due to the fast oxidation by OH (Fig.5.5.6), isoprene shows a slight decrease. In Beijing and Shanghai, a second peak is simulated at around 18-19, which is a result of a steep decrease of the boundary layer height and the emission from vehicles. At all the urban sites, the highest isoprene is simulated with ST2, followed by ST3, benchmark run and ST1. Compared to ST2 and the base run, lower NO_X concentrations in ST3 and ST1 accelerate the HO_X cycle leading to enhanced OH and reduction of isoprene.

However, it is slightly dufferent in RU. Isoprene concentration in RU increases during day and reaches its maxima at 19.00 with the value of 0.6 ppb in Run 1. It then rapidly reacts with the oxidants. Unlike the urban sites, the highest concentration of isoprene is modelled in ST3, followed by ST2, ST1 and the lowest value is calculated in Run 1. Since RU is in a NO_X-limited regime, the reduction of NO_X discourages O_3 and OH formation. Hence, higher isoprene mixing ratios are simulated with lower NO_X emissions.

The total VOCs in Beijing and Chengdu show not only similar values but similar diel trends. High VOCs signals are modelled during the morning and night rush hours reaching a maximum of 130 ppbC in Beijing and 160 ppbC in Chengdu. These signals are dominated by the anthropogenic sources since the red line overlays the black. Also, it is notable that in these two sites, VOC concentrations are more sensitive to the changing of NO_X emissions (ST1), rather than the increasing of isoprene emissions (ST2).

VOCs in Shanghai at 20.00 can reach 300 ppbC, but during the day, the mixing ratios are lower than 125 ppbC. This diel pattern is different from the previous works (Han et al., 2017; Cai et al., 2010). This might be due to a very shallow PBLH at night. Also, high AVOCs emission rates were provided by the emission inventory. As I present the concentration based on number of carbons, which may exaggerate the differences in the diel cycle if more larger molecules are emitted in the early night.

Lower VOC concentrations are simulated for the selected rural site with the peak of less than 18 ppbC in the morning. At this site, the impact of increased

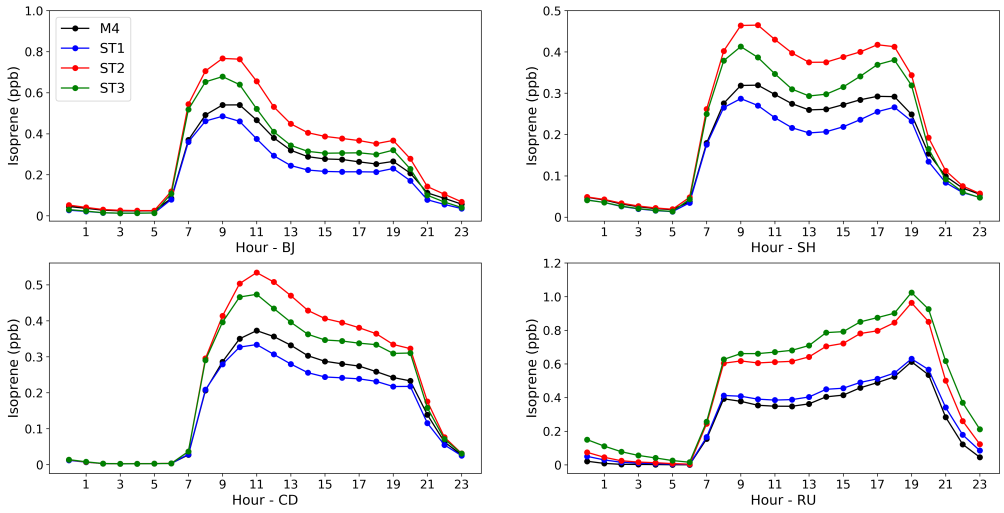

Figure 5.5.2: Diel cycle of isoprene with four emissions scenatios (benchmark(black), ST1(blue), ST2(red), and ST3(green)) in four locations.

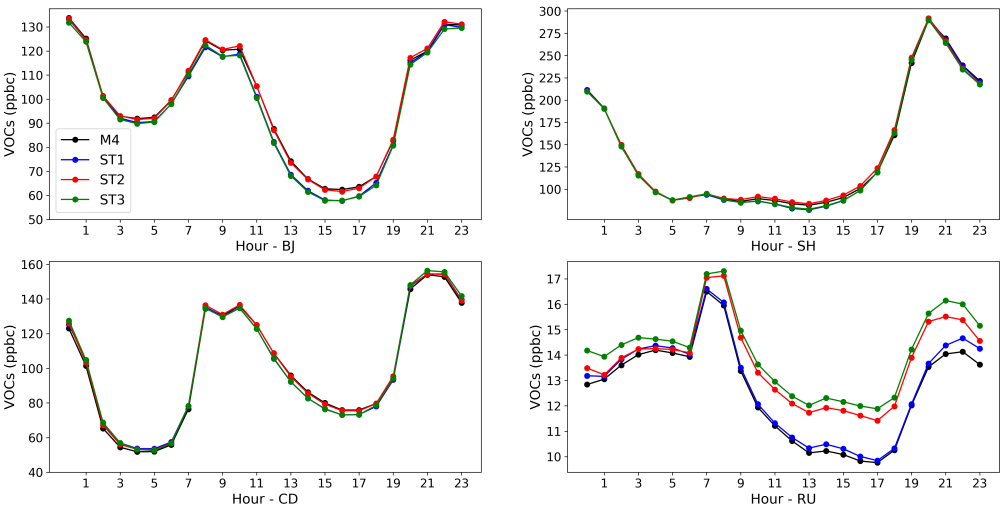

Figure 5.5.3: Same as Fig.5.5.2, but for VOCs.

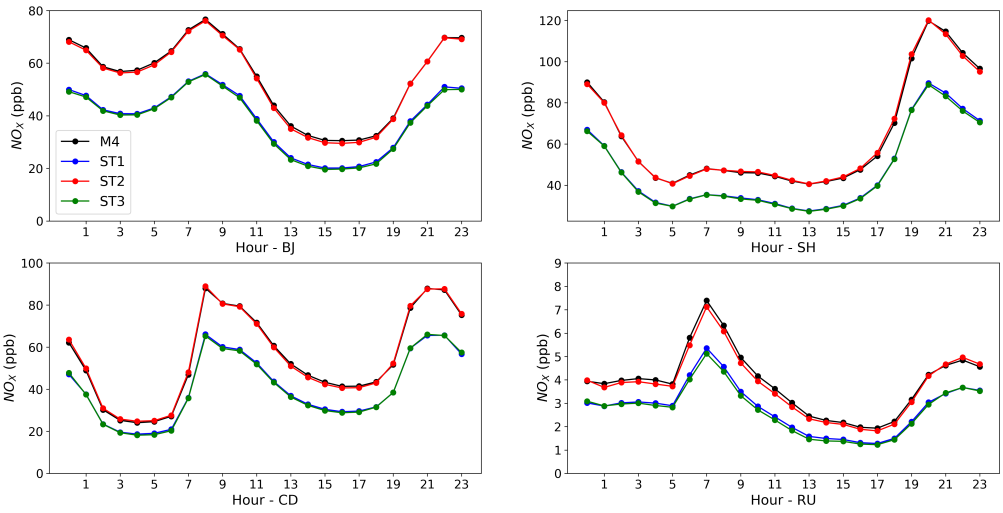

Figure 5.5.4: Same as Fig.5.5.2, but for NO_X.

isoprene emissions on the total VOCs concentrations is significant, especially at noontime.

NO_X at BJ, CD and RU show similar diel patterns, though the concentrations of NO_X in RU is approximately ten times smaller than the concentrations in the two urban sites. The morning peak of NO_X in Shanghai is not as obvious as it is at the other three sites. However, this diurnal variation is consistent to the VOCs pattern, which suggests a different diel variation of the emissions.

5.5.2 The NO_X, VOCs and O_3 chemistry

With the knowledge of the primary pollutants, the complex O_3 formation system can be interpreted. At all sites, O_3 (Fig. 5.5.5) peaks in the afternoon, which is consistent with the afternoon peak of the methyl peroxy radical (CH_3O_2, Fig. 5.5.8). This suggests that the maxima O_3 concentration is related to rapid RO_2 chemistry.

In urban sites, in which FNR (Fig.5.5.9) is always less than 0.5 (VOC-limited regime), it seems that the O_3 mixing ratio is more sensitive to the decrease of NO_X rather than the increase of isoprene. ST3 and ST1 predict a significant enhancement of O_3 through the day, but the red line (ST2) follows similar

values of the black line (base run). The increase of isoprene emission affects the NO_X concentrations in ppt level whereas NO_X concentrations are declined by 10-20 ppb on average with NO_X emission reduction.

Unlike the urban environment, the RU is considered to be in the NO_X limited regime during the daytime (FNR > 0.8). Hence, reduction of NO_X in ST1 and ST3 reduces the production of O_3. In RU, the NO_X-VOCs regimes changes during the day. In the base run, RU shift from transition regime to NO_X-limited regime at around 10.00 in the morning. Reducing NO_X emission and/or increasing isoprene emission pushes this shift earlier in the day limiting the O_3 formation.

In CD, the second peak of O_3 mixing ratio appears from 22.00 to 7.00, which is resulted from both meteorological and chemical reasons. Chengdu is located in the Sichuan Basin surrounded by mountains. Hence, after sunset, O_3 can be transported by the mountain breeze (Liao et al., 2017). Not only the O_3 formed in the mountains, O_3 from the residual layer can be transported to the city during night.

5.6 Conclusion

In this chapter, I present the results from three sensitivity tests of different emission scenarios. The simulations of key species and chemical systems are discussed individually in sections 5.2, 5.3 and 5.4. In section 5.5, I compared the emission scenarios in four selected locations.

In ST1, decrease of NO_X emissions can chanage the proportions of NO_X and NO_Z, and reduce the sink of OH leading to a different OH distribution affecting the subsequent chemimstry including RO_2, O_3 and nitrates production.

In VOCs-limited regions (FNR < 0.5) such as the NCP and YRD, a reduction of NO_X emission can aggravate O_3 pollution by increasing its production. Also, O_3 titration is hindered due to the decreasing NO concentration. In the transition (0.5 < FNR < 0.8) and NO_X (0.8 < FNR) regimes, O_3 concentrations are declined, which could be due to lacking NO_X in O_3 production. Hence, in rural area, reducing NO_X emissions could improve the O_3

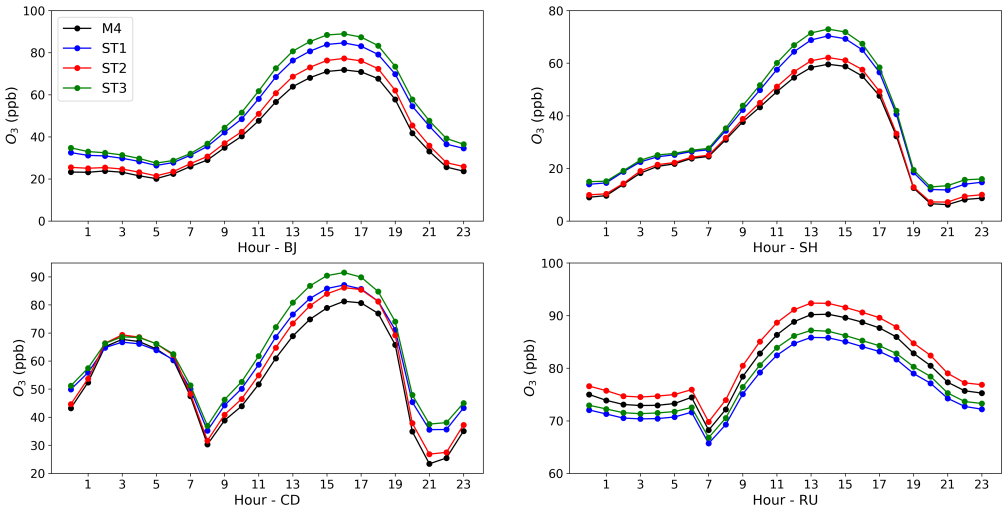

Figure 5.5.5: Same as Fig.5.5.2, but for O_3.

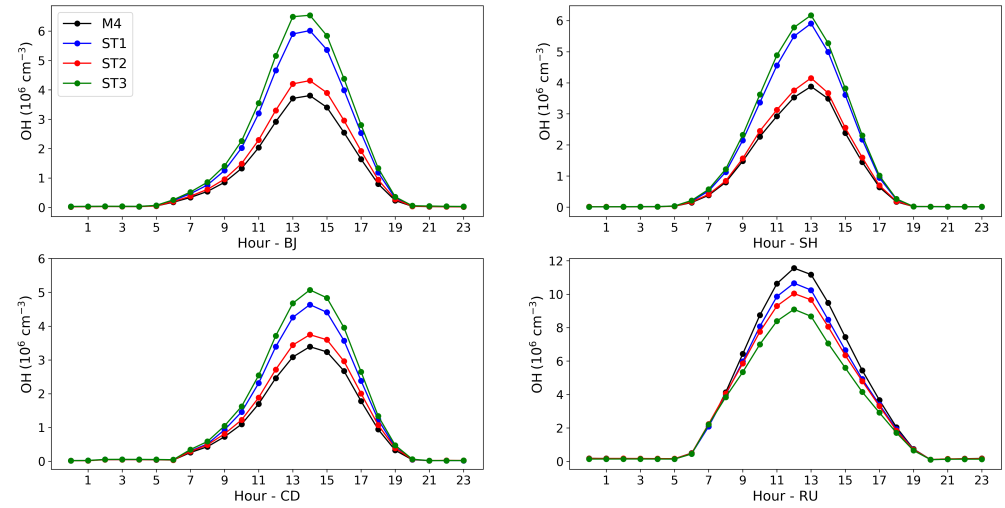

Figure 5.5.6: Same as Fig.5.5.2, but for OH.

pollution, but in the cities, O_3 concentration would not decrease with declined NO_X concentration only.

The change of isoprene mixing ratio is the opposite to the OH distribution variation due to the rapid OH-isoprene reactions. ST2 simulates the results with an increase of isoprene emission by 50%. Although isoprene reacts with OH, in VOCs-limited regimes, its enhancement could lead to increased OH

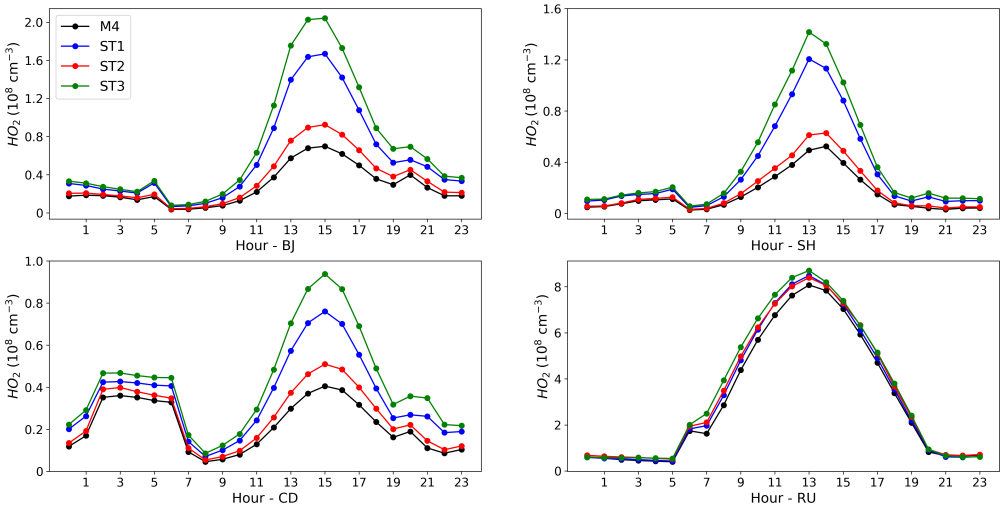

Figure 5.5.7: Same as Fig.5.5.2, but for HO_2.

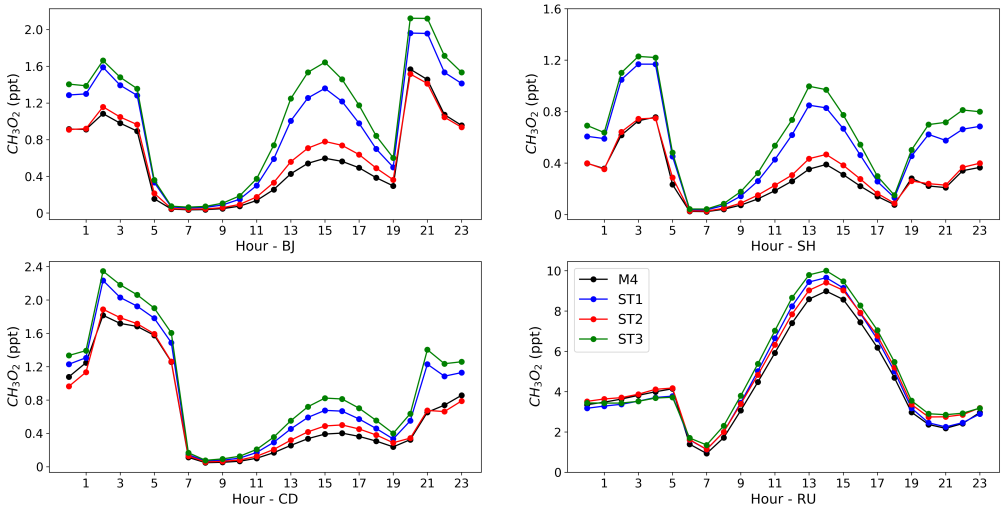

Figure 5.5.8: Same as Fig.5.5.2, but for CH_3O_2.

concentration by producing more RO_2 accelerating the HO_X recycling. Due to increase in precursors, O_3 mixing ratio is enhanced over most of mainland China. Hence, planting trees with big isoprene emission factor in the afforestation program can aggravate O_3 pollution in China.

ST3 combines the previous two emission scenarios - 25% decrease of NO_X emissions and 50% increase of isoprene emissions. The averaged O_3

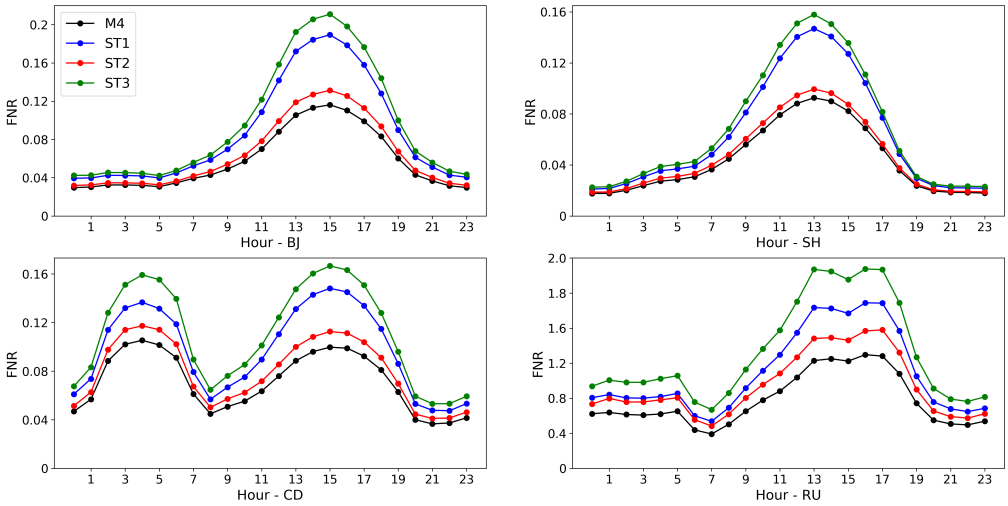

Figure 5.5.9: Same as Fig.5.5.2, but for FNR.

concentration is enhanced up to 24% in NCP and YRD with the absolute increase of up to 12 ppb. Also, FNR values show great increases over the whole domain, stuggesting that China shifts towards NO_X-limited regimes with this emission scenario.

Beijing (BJ), Shanghai (SH), Chengdu (CD) and one rural site (RU) closed to Xi'an are selected to compare the impact of ST1, ST2 and ST3. The three urban sites are in VOCs-limited regimes, so higher O_3 are simulated in ST3 and ST1, whereas the RU site shows the opposite. A second peak of O_3 appears at around 3 a.m. in CD. This might be a result of both transportation of O_3 and production via RO_2 and HO_X reactions.

6

Conclusion

In this chapter, I summarise the key findings of this study and discuss future work can be conducted base on this study.

6.1 Summary of developments and findings

In this study, several amendments were made to the chemical mechanism of Weather Research and Forecasting model with Chemistry (WRF-Chem) to include a detailed representation of isoprene oxidation chemistry and test its impact on various chemical systems. This mechanism was evaluated with the measurements and compared with other mechanisms and models. A series of tests were conducted to investigate the impact of isoprene and isoprene nitrates (INs) on the key tropospheric chemical systems including O_3 formation, NO_X recycling, HO_X cycle and RO_2 chemistry. Perturbation studies were conducted to investigate the impact of isoprene under various emission scenarios in China.

The new chemical mechanism named MOZART-MIM-MCM-MOSAIC-4bin-aq (M4) is developed and implemented into the WRF-Chem. In this new mechanism, a representation of more explicit isoprene oxidation chemistry with 61 species and 188 photolysis and chemical reactions, has been included in the MOZART-MOSAIC-4bin-aq mechanism, which originally contains 140 species and 286 gas-phase reactions. Majority of reactions are from the updated version of Mainz Isoprene Mechanism 2 (MIM) and information from the Master Chemical Mechanism v3.3.1 (MCM) are used to speciate the lumped isoprene nitrate in MIM. In total, 6 hydroxy isoprene nitrates (hy-IN) and 1 aldehydic isoprene nitrate (al-IN) are included in M4.

Another development made to the model is the inclusion of tags, which traces

the NO_2 coverted from NO by isoprene derived species. The subsequent O_3 formation from these NO_2 is also tagged. The contribution of one oxidation path of isoprene or one INs in the NO_X recycling can also be quantified with tags. NO_2 recycled from the degradation of 7 INs, 4 isoprene oxidation pathways and the oxidation of isoprene have been tagged in M4 mechanism, whereas four tags have been implemented to the MOZART-4 mechanism.

In WRF- Chem, new chemical species and reactions can be added to the mechanism via the Kinetic PreProcessor (KPP), which reads in the text files of the reactions and the rate coefficients, and produces Fortran 90 codes for the model to solve. Apart from KPP, a series of changes has been made in the chemistry related files and programs of WRF-Chem, so that the new species can be emitted, photolysed, reacted, transpoted and deposited like other chemical tracers during simulation.

The model with the M4 chemical mechanism is validated with the observational data in chapter 3 mainly on four components: meteorological parameters, emissions, background chemistry and the isoprene nitrate chemistry.

In general, the model reproduces the meteorological parameters reasonably well. The day-to-day variation and the diel cycle of temperature and relative humidity in Beijing are captured by the model with good correlations. The observation of wind speed (WS) and direction (WD) at the ground surface is greatly affected by the local features, which is hard to be captured by the regional model. At higher altitudes, a good agreement is seen between the simulated and observed WS and WD. However, most of the chemical tracers are measured at the ground-level, which means the discrepancy between the modelled and observed chemical tracers may be partly due to the differences in the transport. Planetary boundary layer height (PBLH), as an important indicator of vertical mixing, is poorly captured by the model. The daytime PBLH is overestimated by a factor of 2.5 and a very shallow PBLH is simulated at night. Hence, the concentration of chemical tracers is expected to be low during the daytime due to strong dilution and high at night. Compared to the results of the parent domain, some improvements are seen with higher resolution simulations, however, the coarse domain seems to be good enough in reproducing the meteorology.

The diurnal patterns of both anthropogenic and biogenic emissions agree with

the flux measurements well. Higher anthropogenic emissions are provided by the 27 km resolution Multi-resolution Emission Inventory for China (MEIC) in Beijing. The emission of the 9 km resolution is considerably lower, which is suggested to be an error during downscaling. Hence, the simulations of the chemical tracers of the nested domain are not shown.

The model simulations of the chemical species are compared with the measurements of the field campaigns and the data from air quality monitoring network. As expected, the model tends to overestimate the concentrations of most of the primary species at night and underestimate then during the daytime, which is partly due to the PBLH variation. Isoprene concentration is also underpredicted, which is likely to be a result of strong dilution or rapid reaction since its emission is well captured. As a secondary pollutant, the concentration of O_3 depends on its production and loss rate. Hence the underestimation of O_3 suggests either less production (probably related to the lower VOC simulation during the daytime) or overestimation of the sink (can be NO titration).

The diel pattern of INs is sensitive to the RO_2 cross-body reactions. Good agreement on the diel pattern of the INs are shown, although the absolute values are off. The ratio between (1,2)-IN to (4,3)-IN is lower in the model, which is likely to be due to the low (1,2)-ISOPO2 to (4,3)-ISOPO2 ratio.

The primary goal of this study is not to model precisely the meteorological parameters and concentration of all chemical species, but to test isoprene chemistry with reasonable chemical environments. Hence I conclude that this model is adequate for this study.

Chapter 4 aims to assess the impact of isoprene and INs on the air composition in China. Simplified (MOZART-4) and explicit (M4) mechanisms are used and the difference between the two mechanisms are investigated. Here are the key conclusions:

1. **Difference between the two mechanisms** In M4, reactions between ISOPO2 and HO_2 is faster than in MOZART-4 leading to a higher production of ISOPOOH. As a result, reactions between ISOPO2 and NO and NO_3 are slowed down resulting in low MVK, MACR and INs concentrations. In M4, more RO_2 are produced from ISOPOOH resulting

in an upsurge of RO_2 concentration, which encourages O_3 formation in the VOC-limited regimes. Also, with higher RO_2 concentrations in the model, the oxidation capacity of the modelled atmosphere ultimately increased. However, similar concentrations of NO_X, HO_X, VOCs and O_3 are simulated by the two mechanisms. The increase of RO_2 in M4 does result in a slight increase in O_3 concentration in Beijing, but only for less than 1 ppb and 2% for the 45 days average. For the whole China, the maximum averaged O_3 variation is 4%. Hence, this study suggests that MOZART-4 is adequate for O_3 simulation in China with much lower computaional cost.

2. **NO_2 recyced by isoprene** The total recycled NO_2 peaks at noontime with the value of roughly 20 ppt, which responsible for about 1.6 ppb of O_3 production. At 19.00 in the evening, a great amount of NO_2 are formed via ni-ISOPO2, however, much less O_3 is produced since no photochemistry is happening. ISOPBNO3 and ISOPDNO3 contribute to 80% NO_2 formation and 90% O_3 production during the day from isoprene oxidation. In total, isoprene chemistry contributes to up to 18% of total O_3 concentration over east China. A slight negative impact on O_3 is simulated due to inclusion of INs. However, a slight increase of O_3 over Esat China Sea is modelled, which may be due to the NO_X released by hy-INs.

3. **Impact of the full isoprene chemistry** Isoprene contributes to up to 18% of O_3 concentration in NCP regions in the M4 mechanism. IN NCP and YRD regions, up to 20% OH and RO_2 are attributed to the presence of isoprene. Slight lower O_3 concentration changes are modelled with MOZART-4 mechanism, which is consistant with the lower RO_2 variation in MOZART-4 mechanism. Simualtion of OH, HO_2 and NO_Xchanges in the two mechanisms matches well, but the organic nitrates is not the case.

4. **Impact of the INs chemistry** Slight lower (less than 4%) O_3 is sumulated with the formation of INs across the domain in both mechanisms, which leads to a decrease of OH. In both mechanisms, with hy-INs formation increased NO_X concentration which can be related to the changes in OH. In general, INs chemistry has little impact from an air quality perspective.

Three sensitivity tests are conducted in chapter 5 to investigate the reponse of O_3 to the different emission scenarios, which is useful for the O_3 mitigation policy making. Here are the key conclusions:

1. **NO_X emission reduction** For areas in the NO_X-limited regime (FNR ¿ 0.8), the decrease of NO_X hinders the O_3 production resulting in lower O_3 concentrations. On the contrary, in the VOC-limited regime (FNR ¡ 0.5) reduced NO_X concentrations leads to less titration effect of O_3 increasing its concentration. Also, the FNR values are simulated to increase over the whole domain, especially in the NCP and YRD regions.

2. **Isoprene emission increase** Increase of O_3 (up to 6%) is simulated over the most of China, especially in the VOC-limited regions. This is likely to be due to that more RO_2 are produced with higher isoprene emissions. OH concentration increases over the NCP region reacting with VOCs leading to a lower concentraion of VOCs. RO_X are cycled more efficiently under this scenario and the atmospheric oxidation capacity is expected to be higher.

3. **Comparison of the four sites** Three city sites (BJ, SH, CD) and one rural site (RU) were selected to compare the impact of the three emission scenarios. In all city sites, highest O_3 concentraions are simulated with ST3, followed by ST1, ST2 and the base run. This is consistant with the expectation since they are all located in VOC-limited regime. The O_3 concentration in the rural site decreases when the NO_X emission is reduced and including more isoprene emissions can encourage O_3 formation in this site. Reducing NO_X emission only can limit O_3 production in areas where FNR is higher than 0.5 but also can encourage O_3 production in the cities. Hence, O_3 mitigation requaires emission control of both NO_X and VOCs.

The table below summaries the key conclusions of this study and the runs to derive them.

Table 6.1.1: Synthesis of the key results of this study.

Runs	Conclusions
Run 1	Reasonably good agreement with the observations; large variation of PBLH that will impact the diel pattern of the tracers; variation of INs are captured
Run 2	No significant improvement to Run 1; issues were found in emissions
Run 1 and 3	MOZART-4 is adequate for O_3 simulation in China; M4 and MOZART treats ISOPO2 reactions differently
Run 1; 3 and 4	Isoprene chemistry contributes to 18% O_3 formation in China
Run 5; 6 and 7	NO_X recycling from INs are different in M4 and MOZART; minor impact of INs on O_3
ST1 and Run 1	Reduction of NO_X emission leads to enhancement of O_3 in NCP and YRD
ST2 and Run 1	Increase of isoprene emission leads to enhancement of O_3 in most of China
ST3 and Run 1	Under the previous two emission scenarios; O_3 increased by up to 20% in NCP and YRD
ST1; 2 and 3	Depending on the O_3 formation regimes; different locations respond differently to the emission changes

6.2 Future work

Firstly, the M4 can be compared with other mechanisms in a box model run with mixing and emission constrained. WRF-Chem is a complex model with many components. Hence many factors need to be taken into consideration when interpreting the results. Whereas these factors can be easily eliminated in the box model. Also, various NO_X-VOC regimes can be adjusted and kinetic variables such as reactivity, production rate and lifetime can be generated. Therefore, including a box model run may help understand the isoprene chemistry.

Our understanding on isoprene chemistry is continually developing. In 2016, the updated version of MIM2 was well represented and the reaction rate coefficients and the branching ratios were validated with different source and lab studies. Recently, Wennberg et al. (2018) reported the up-to-date oxidation mechanism of isoprene and some of the branching ratio and reaction rate coefficient recommended in the paper are slightly different from that has been used in this study. It would be interesting to compare results of the current M4 mechanism and the M4 mechanism with updated parameters.

The physical parameter combination of the model is not tested in this study, but suggested by the researcher (Jie Li) from IAP who have been working on the WRF simulation in China for years. Better understanding of the physical scheme configurations can be obtained by setting up serveral test runs with different configrations.

Also, increasing studies focus on biogenic secondary organic aerosols (BSOA). Fu et al. (2010) reported a 10% contribution of organic carbon (OC) from isoprene in summer China. An aerosol scheme can be developed based on M4.

Bibliography

Acton, W. J. F., Huang, Z., Davison, B., Drysdale, W. S., Fu, P., Hollaway, M., Langford, B., Lee, J., Liu, Y., Metzger, S., et al. (2020). Surface–atmosphere fluxes of volatile organic compounds in beijing. *Atmospheric Chemistry and Physics Discussions*.

An, J., Wang, Y., Li, X., Sun, Y., Shen, S., and Shi, L. (2007). Analysis of the relationship between no, no2 and o3 concentrations in beijing. *Huan jing ke xue*, 28(4):706–711.

An, J., Zou, J., Wang, J., Lin, X., and Zhu, B. (2015). Differences in ozone photochemical characteristics between the megacity nanjing and its suburban surroundings, yangtze river delta, china. *Environmental Science and Pollution Research*, 22(24):19607–19617.

Ansari, T. U., Wild, O., Li, J., Yang, T., Xu, W., Sun, Y., and Wang, Z. (2019). Effectiveness of short-term air quality emission controls: a high-resolution model study of beijing during the asia-pacific economic cooperation (apec) summit period. *Atmospheric Chemistry and Physics*, 19(13):8651–8668.

Archibald, A., Jenkin, M., and Shallcross, D. (2010). An isoprene mechanism intercomparison. *Atmospheric Environment*, 44(40):5356–5364.

Borbon, A., Fontaine, H., Veillerot, M., Locoge, N., Galloo, J., and Guillermo, R. (2001). An investigation into the traffic-related fraction of isoprene at an urban location. *Atmospheric Environment*, 35(22):3749–3760.

Boyd, A. A., Flaud, P.-M., Daugey, N., and Lesclaux, R. (2003). Rate constants for ro2+ ho2 reactions measured under a large excess of ho2. *The Journal of Physical Chemistry A*, 107(6):818–821.

Cai, C., Geng, F., Tie, X., Yu, Q., and An, J. (2010). Characteristics and source apportionment of vocs measured in shanghai, china. *Atmospheric Environment*, 44(38):5005–5014.

Carter, W. P. (2000). Documentation of the saprc-99 chemical mechanism for voc reactivity assessment. *Contract*, 92(329):95–308.

Chen, W., Guenther, A., Wang, X., Chen, Y., Gu, D., Chang, M., Zhou, S., Wu, L., and Zhang, Y. (2018). Regional to global biogenic isoprene emission responses to changes in vegetation from 2000 to 2015. *Journal of Geophysical Research: Atmospheres*, 123(7):3757–3771.

Chen, X., Hulbert, D., and Shepson, P. B. (1998). Measurement of the organic nitrate yield from oh reaction with isoprene. *Journal of Geophysical Research: Atmospheres*, 103(D19):25563–25568.

da Silva, C. M., Corrêa, S. M., and Arbilla, G. (2018). Isoprene emissions and ozone formation in urban conditions: a case study in the city of rio de janeiro. *Bulletin of environmental contamination and toxicology*, 100(1):184–188.

Damian, V., Sandu, A., Damian, M., Potra, F., and Carmichael, G. R. (2002). The kinetic preprocessor kpp-a software environment for solving chemical kinetics. *Computers and Chemical Engineering*, 26(11):1567–1579.

Dodge, M. (1977). Combined use of modeling techniques and smog chamber data to derive ozone-precursor relationships. In *International conference on photochemical oxidant pollution and its control: Proceedings*, volume 2, pages 881–889. US Environmental Protection Agency Research Triange Park, NC.

Duan, J., Peng, Y., Tan, J., Hao, J., and Chai, F. (2013). Spatial distribution characteristics of nmhcs during winter haze in beijing. *Huan jing ke xue*, 34(12):4552–4557.

Emmerson, K. and Evans, M. (2009). Comparison of tropospheric gas-phase chemistry schemes for use within global models. *Atmospheric chemistry and physics*, 9(5):1831–1845.

Emmons, L., Hess, P., Lamarque, J.-F., and Pfister, G. (2012). Tagged ozone mechanism for mozart-4, cam-chem and other chemical transport models. *Geoscientific Model Development*, 5(6):1531–1542.

Emmons, L. K., Walters, S., Hess, P. G., Lamarque, J.-F., Pfister, G. G., Fillmore, D., Granier, C., Guenther, A., Kinnison, D., Laepple, T., et al. (2010). Description and evaluation of the model for ozone and related chemical tracers, version 4 (mozart-4).

Fan, J. and Zhang, R. (2004). Atmospheric oxidation mechanism of isoprene. *Environmental Chemistry*, 1(3):140–149.

Fu, P., Kawamura, K., Kanaya, Y., and Wang, Z. (2010). Contributions of biogenic volatile organic compounds to the formation of secondary organic aerosols over mt. tai, central east china. *Atmospheric Environment*, 44(38):4817–4826.

GB3095 (2012). Ambient air quality standards [s].

Geng, F., Tie, X., Guenther, A., Li, G., Cao, J., and Harley, P. (2011). Effect of isoprene emissions from major forests on ozone formation in the city of shanghai, china. *Atmospheric Chemistry and Physics*, 11(20):10449–10459.

Gerbig, C., Schmitgen, S., Kley, D., Volz-Thomas, A., Dewey, K., and Haaks, D. (1999). An improved fast-response vacuum-uv resonance fluorescence co instrument. *Journal of Geophysical Research: Atmospheres*, 104(D1):1699–1704.

Gery, M. W., Whitten, G. Z., Killus, J. P., and Dodge, M. C. (1989). A photochemical kinetics mechanism for urban and regional scale computer modeling. *Journal of Geophysical Research: Atmospheres*, 94(D10):12925–12956.

Gong, X., Hong, S., and Jaffe, D. A. (2018). Ozone in china: Spatial distribution and leading meteorological factors controlling o3 in 16 chinese cities. *Aerosol and Air Quality Research*, 18(9):2287–2300+.

Grell, G. A., Peckham, S. E., Schmitz, R., McKeen, S. A., Frost, G., Skamarock, W. C., and Eder, B. (2005). Fully coupled "online" chemistry within the wrf model. *Atmospheric Environment*, 39(37):6957–6975.

Guenther, A., Karl, T., Harley, P., Wiedinmyer, C., Palmer, P., and Geron, C. (2006). Estimates of global terrestrial isoprene emissions using megan (model of emissions of gases and aerosols from nature). *Atmospheric Chemistry and Physics*, 6(11):3181–3210.

Guo, H., Wang, Y., and Zhang, H. (2017). Characterization of criteria air pollutants in beijing during 2014–2015. *Environmental research*, 154:334–344.

Han, D., Wang, Z., Cheng, J., Wang, Q., Chen, X., and Wang, H. (2017). Volatile organic compounds (vocs) during non-haze and haze days in shanghai: characterization and secondary organic aerosol (soa) formation. *Environmental Science and Pollution Research*, 24(22):18619–18629.

Hewitt, C. N. and Jackson, A. V. (2009). *Atmospheric science for environmental scientists*. John Wiley & Sons.

Hong, S.-Y., Noh, Y., and Dudhia, J. (2006). A new vertical diffusion package with an explicit treatment of entrainment processes. *Monthly weather review*, 134(9):2318–2341.

Hong, S.-Y. and Pan, H.-L. (1996). Nonlocal boundary layer vertical diffusion in a medium-range forecast model. *Monthly weather review*, 124(10):2322–2339.

Hopkins, J. R., Jones, C. E., and Lewis, A. C. (2011). A dual channel gas chromatograph for atmospheric analysis of volatile organic compounds including oxygenated and monoterpene compounds. *Journal of Environmental Monitoring*, 13(8):2268–2276.

Horowitz, L. W., Fiore, A. M., Milly, G. P., Cohen, R. C., Perring, A., Wooldridge, P. J., Hess, P. G., Emmons, L. K., and Lamarque, J.-F. (2007). Observational constraints on the chemistry of isoprene nitrates over the eastern united states. *Journal of Geophysical Research: Atmospheres*, 112(D12).

Hu, J., Ying, Q., Wang, Y., and Zhang, H. (2015). Characterizing multi-pollutant air pollution in china: Comparison of three air quality indices. *Environment international*, 84:17–25.

Huang, Z., Zhang, Y., Yan, Q., Zhang, Z., and Wang, X. (2016). Real-time monitoring of respiratory absorption factors of volatile organic compounds in ambient air by proton transfer reaction time-of-flight mass spectrometry. *Journal of Hazardous Materials*, 320:547–555.

Iacono, M. J., Delamere, J. S., Mlawer, E. J., Shephard, M. W., Clough, S. A., and Collins, W. D. (2008). Radiative forcing by long-lived greenhouse gases: Calculations with the aer radiative transfer models. *Journal of Geophysical Research: Atmospheres*, 113(D13).

Jacob, D. J. (1999). *Introduction to atmospheric chemistry*. Princeton University Press.

Jenkin, M., Watson, L., Utembe, S., and Shallcross, D. (2008). A common representative intermediates (cri) mechanism for voc degradation. part 1: Gas phase mechanism development. *Atmospheric Environment*, 42(31):7185–7195.

Jenkin, M. E. and Clemitshaw, K. C. (2000). Ozone and other secondary photochemical pollutants: chemical processes governing their formation in the planetary boundary layer. *Atmospheric Environment*, 34(16):2499–2527.

Jin, X., Fiore, A. M., Murray, L. T., Valin, L. C., Lamsal, L. N., Duncan, B., Folkert Boersma, K., De Smedt, I., Abad, G. G., Chance, K., et al. (2017). Evaluating a space-based indicator of surface ozone-nox-voc sensitivity over

midlatitude source regions and application to decadal trends. *Journal of Geophysical Research: Atmospheres*, 122(19):10–439.

Jin, X. and Holloway, T. (2015). Spatial and temporal variability of ozone sensitivity over china observed from the ozone monitoring instrument. *Journal of Geophysical Research: Atmospheres*, 120(14):7229–7246.

Kotthaus, S. and Grimmond, C. S. B. (2018). Atmospheric boundary-layer characteristics from ceilometer measurements. part 1: A new method to track mixed layer height and classify clouds. *Quarterly Journal of the Royal Meteorological Society*, 144(714):1525–1538.

Kuhlmann, R. v., Lawrence, M., Pöschl, U., and Crutzen, P. (2004). Sensitivities in global scale modeling of isoprene. *Atmospheric Chemistry and Physics*, 4(1):1–17.

Lee, L., Teng, A. P., Wennberg, P. O., Crounse, J. D., and Cohen, R. C. (2014). On rates and mechanisms of oh and o3 reactions with isoprene-derived hydroxy nitrates. *The Journal of Physical Chemistry A*, 118(9):1622–1637.

Li, C., Wang, J., Hu, L., Yu, L., Clinton, N., Huang, H., Yang, J., and Gong, P. (2014). A circa 2010 thirty meter resolution forest map for china. *Remote Sensing*, 6(6):5325–5343.

Li, D., Vogel, B., Müller, R., Bian, J., Günther, G., Li, Q., Zhang, J., Bai, Z., Vömel, H., and Riese, M. (2018a). High tropospheric ozone in lhasa within the asian summer monsoon anticyclone in 2013: influence of convective transport and stratospheric intrusions. *Atmospheric Chemistry & Physics*, 18(24).

Li, L., Wu, F., and Meng, X. (2013). Seasonal and diurnal variation of isoprene in the atmosphere of beijing. *Environmental Monitoring of China*, (2).

Li, L. and Xie, S. (2014). Historical variations of biogenic volatile organic compound emission inventories in china, 1981–2003. *Atmospheric environment*, 95:185–196.

Li, M., Zhang, Q., Kurokawa, J.-i., Woo, J.-H., He, K., Lu, Z., Ohara, T., Song, Y., Streets, D. G., Carmichael, G. R., et al. (2017). Mix: a mosaic asian anthropogenic emission inventory under the international collaboration framework of the mics-asia and htap. *Atmospheric Chemistry and Physics (Online)*, 17(2).

Li, N., He, Q., Greenberg, J., Guenther, A., Li, J., Cao, J., Wang, J., Liao, H., Wang, Q., and Zhang, Q. (2018b). Impacts of biogenic and anthropogenic emissions on summertime ozone formation in the guanzhong basin, china. *Atmospheric Chemistry and Physics*, 18(10):7489.

Liao, T., Wang, S., Ai, J., Gui, K., Duan, B., Zhao, Q., Zhang, X., Jiang, W., and Sun, Y. (2017). Heavy pollution episodes, transport pathways and potential sources of pm2. 5 during the winter of 2013 in chengdu (china). *Science of the Total Environment*, 584:1056–1065.

Liu, F., Zhang, Q., Zheng, B., Tong, D., Yan, L., Zheng, Y., He, K., et al. (2016). Recent reduction in no x emissions over china: synthesis of satellite observations and emission inventories. *Environmental Research Letters*, 11(11):114002.

Liu, H., Liu, S., Xue, B., Lv, Z., Meng, Z., Yang, X., Xue, T., Yu, Q., and He, K. (2018a). Ground-level ozone pollution and its health impacts in china. *Atmospheric Environment*, 173:223–230.

Liu, N., Ren, W., Li, X., Ma, X., Zhang, Y., and Li, B. (2018b). Distribution and urban–suburban differences in ground-level ozone and its precursors over shenyang, china. *Meteorology and Atmospheric Physics*, pages 1–11.

Lockwood, A., Shepson, P., Fiddler, M., and Alaghmand, M. (2010). Isoprene nitrates: preparation, separation, identification, yields, and atmospheric chemistry. *Atmospheric Chemistry and Physics*, 10(13):6169–6178.

Mathur, A., Atchison, D. A., and Scott, D. H. (2008). Ocular aberrations in the peripheral visual field. *Optics Letters*, 33(8):863–865.

McKee, D. (1993). *Tropospheric ozone: human health and agricultural impacts*. CRC Press.

MEP (2015). Monthly report on the air quality in key regions and cities of china. *Ministry of Environmental Protection*.

Mills, G. P., Hiatt-Gipson, G. D., Bew, S. P., and Reeves, C. E. (2016). Measurement of isoprene nitrates by gcms. *Atmospheric Measurement Techniques*, 9(9):4533.

Mo, Z., Shao, M., Wang, W., Liu, Y., Wang, M., and Lu, S. (2018). Evaluation of biogenic isoprene emissions and their contribution to ozone formation by ground-based measurements in beijing, china. *Science of The Total Environment*, 627:1485–1494.

Patchen, A. K., Pennino, M. J., Kiep, A. C., and Elrod, M. J. (2007). Direct kinetics study of the product-forming channels of the reaction of isoprene-derived hydroxyperoxy radicals with no. *International Journal of Chemical Kinetics*, 39(6):353–361.

Paulot, F., Crounse, J., Kjaergaard, H., Kroll, J., Seinfeld, J., and Wennberg, P. (2009). Isoprene photooxidation: new insights into the production of acids and organic nitrates. *Atmospheric Chemistry and Physics*, 9(4):1479–1501.

Perring, A., Bertram, T., Wooldridge, P. J., Fried, A., Heikes, B., Dibb, J., Crounse, J. D., Wennberg, P., Blake, N., Blake, D., et al. (2009). Airborne observations of total rono 2: new constraints on the yield and lifetime of isoprene nitrates. *Atmospheric Chemistry and Physics*, 9(4):1451–1463.

Piletic, I. R., Edney, E. O., and Bartolotti, L. J. (2017). Barrierless reactions with loose transition states govern the yields and lifetimes of organic nitrates derived from isoprene. *The Journal of Physical Chemistry A*, 121(43):8306–8321.

Popoola, O. A., Carruthers, D., Lad, C., Bright, V. B., Mead, M. I., Stettler, M. E., Saffell, J. R., and Jones, R. L. (2018). Use of networks of low cost air quality sensors to quantify air quality in urban settings. *Atmospheric Environment*, 194:58–70.

Qi, J., Zheng, B., Li, M., Yu, F., Chen, C., Liu, F., Zhou, X., Yuan, J., Zhang, Q., and He, K. (2017). A high-resolution air pollutants emission inventory in 2013 for the beijing-tianjin-hebei region, china. *Atmospheric environment*, 170:156–168.

Rollins, A. W., Kiendler-Scharr, A., Fry, J., Brauers, T., Brown, S. S., Dorn, H.-P., Dubé, W. P., Fuchs, H., Mensah, A., Mentel, T., et al. (2009). Isoprene oxidation by nitrate radical: alkyl nitrate and secondary organic aerosol yields. *Atmospheric Chemistry and Physics*, 9(18):6685–6703.

Sander, R. (2015). Compilation of henry's law constants (version 4.0) for water as solvent. *Atmospheric Chemistry and Physics*, 15(8).

Saunders, S. M., Jenkin, M. E., Derwent, R., and Pilling, M. (2003). Protocol for the development of the master chemical mechanism, mcm v3 (part a): tropospheric degradation of non-aromatic volatile organic compounds. *Atmospheric Chemistry and Physics*, 3(1):161–180.

Shi, Z., Vu, T., Kotthaus, S., Harrison, R. M., Grimmond, S., Yue, S., Zhu, T., Lee, J., Han, Y., Demuzere, M., et al. (2019). Introduction to the special issue "in-depth study of air pollution sources and processes within beijing and its surrounding region (aphh-beijing)". *Atmospheric Chemistry and Physics*, 19(11):7519–7546.

Silver, B., Reddington, C., Arnold, S., and Spracklen, D. (2018). Substantial changes in air pollution across china during 2015–2017. *Environmental Research Letters*, 13(11):114012.

Skov, H., Hjorth, J., Lohse, C., Jensen, N., and Restelli, G. (1992). Products and mechanisms of the reactions of the nitrate radical (no3) with isoprene, 1, 3-butadiene and 2, 3-dimethyl-1, 3-butadiene in air. *Atmospheric Environment. Part A. General Topics*, 26(15):2771–2783.

Smith, K. R., Edwards, P. M., Evans, M. J., Lee, J. D., Shaw, M. D., Squires, F., Wilde, S., and Lewis, A. C. (2017). Clustering approaches to improve the performance of low cost air pollution sensors. *Faraday discussions*, 200:621–637.

Sprengnether, M., Demerjian, K. L., Donahue, N. M., and Anderson, J. G. (2002). Product analysis of the oh oxidation of isoprene and 1, 3-butadiene in the presence of no. *Journal of Geophysical Research: Atmospheres*, 107(D15):ACH–8.

Squire, O., Archibald, A., Griffiths, P., Jenkin, M., Smith, D., and Pyle, J. (2015). Influence of isoprene chemical mechanism on modelled changes in tropospheric ozone due to climate and land use over the 21st century. *Atmospheric Chemistry and Physics*, 15(9):5123–5143.

Squires, F. A., Nemitz, E., Langford, B., Wild, O., Drysdale, W. S., Acton, W. J. F., Fu, P., Grimmond, C. S. B., Hamilton, J. F., Hewitt, C. N., et al. (2020). Measurements of traffic dominated pollutant emissions in a chinese megacity. *Atmospheric Chemistry and Physics Discussions*.

St. Clair, J. M., Rivera-Rios, J. C., Crounse, J. D., Knap, H. C., Bates, K. H., Teng, A. P., Jørgensen, S., Kjaergaard, H. G., Keutsch, F. N., and Wennberg, P. O. (2015). Kinetics and products of the reaction of the first-generation isoprene hydroxy hydroperoxide (isopooh) with oh. *The Journal of Physical Chemistry A*, 120(9):1441–1451.

Stevenson, D., Dentener, F., Schultz, M., Ellingsen, K., Van Noije, T., Wild, O., Zeng, G., Amann, M., Atherton, C., Bell, N., et al. (2006). Multimodel ensemble simulations of present-day and near-future tropospheric ozone. *Journal of Geophysical Research: Atmospheres*, 111(D8).

Stocker, T., Qin, D., Plattner, G., Tignor, M., Allen, S., Boschung, J., Nauels, A., Xia, Y., Bex, V., and Midgley, P. (2013). Ipcc, 2013: Climate change 2013: The physical science basis. contribution of working group i to the fifth assessment report of the intergovernmental panel on climate change, 1535 pp.

Stockwell, W. R., Kirchner, F., Kuhn, M., and Seefeld, S. (1997). A new mechanism for regional atmospheric chemistry modeling. *Journal of Geophysical Research: Atmospheres*, 102(D22):25847–25879.

Stockwell, W. R., Middleton, P., Chang, J. S., and Tang, X. (1990). The second generation regional acid deposition model chemical mechanism for regional air quality modeling. *Journal of Geophysical Research: Atmospheres*, 95(D10):16343–16367.

Sun, W., Shao, M., Granier, C., Liu, Y., Ye, C., and Zheng, J. (2018). Long-term trends of anthropogenic so2, nox, co, and nmvocs emissions in china. *Earth's Future*, 6(8):1112–1133.

Tan, Z., Lu, K., Jiang, M., Su, R., Dong, H., Zeng, L., Xie, S., Tan, Q., and Zhang, Y. (2018). Exploring ozone pollution in chengdu, southwestern china: A case study from radical chemistry to o3-voc-nox sensitivity. *Science of The Total Environment*, 636:775–786.

Taraborrelli, D., Lawrence, M., Butler, T., Sander, R., and Lelieveld, J. (2009). Mainz isoprene mechanism 2 (mim2): an isoprene oxidation mechanism for regional and global atmospheric modelling. *Atmospheric Chemistry and Physics*, 9(8).

Tie, X., Geng, F., Guenther, A., Cao, J., Greenberg, J., Zhang, R., Apel, E., Li, G., Weinheimer, A., Chen, J., et al. (2013). Megacity impacts on regional ozone formation: observations and wrf-chem modeling for the mirage-shanghai field campaign. *Atmospheric Chemistry and Physics*, 13(11):5655–5669.

Tuazon, E. C. and Atkinson, R. (1990). A product study of the gas-phase reaction of isoprene with the oh radical in the presence of nox. *International Journal of Chemical Kinetics*, 22(12):1221–1236.

Tuccella, P., Curci, G., Visconti, G., Bessagnet, B., Menut, L., and Park, R. J. (2012). Modeling of gas and aerosol with wrf/chem over europe: Evaluation and sensitivity study. *Journal of Geophysical Research: Atmospheres*, 117(D3).

Vaughan, A. R., Lee, J. D., Misztal, P. K., Metzger, S., Shaw, M. D., Lewis, A. C., Purvis, R. M., Carslaw, D. C., Goldstein, A. H., Hewitt, C. N., et al. (2016). Spatially resolved flux measurements of nox from london suggest significantly higher emissions than predicted by inventories. *Faraday discussions*, 189:455–472.

Wang, L., Zhang, Y., Wang, K., Zheng, B., Zhang, Q., and Wei, W. (2016). Application of weather research and forecasting model with chemistry (wrf/chem) over northern china: Sensitivity study, comparative evaluation, and policy implications. *Atmospheric Environment*, 124:337–350.

Wang, N., Lyu, X., Deng, X., Huang, X., Jiang, F., and Ding, A. (2019a). Aggravating o3 pollution due to nox emission control in eastern china. *Science of The Total Environment*, 677:732–744.

Wang, R., Tie, X., Li, G., Zhao, S., Long, X., Johansson, L., and An, Z. (2019b). Effect of ship emissions on o3 in the yangtze river delta region of china: Analysis of wrf-chem modeling. *Science of The Total Environment*.

Wang, T., Xue, L., Brimblecombe, P., Lam, Y. F., Li, L., and Zhang, L. (2017). Ozone pollution in china: A review of concentrations, meteorological influences, chemical precursors, and effects. *Science of the Total Environment*, 575:1582–1596.

Wang, X., Dickinson, R. E., Su, L., Zhou, C., and Wang, K. (2018). Pm2. 5 pollution in china and how it has been exacerbated by terrain and meteorological conditions. *Bulletin of the American Meteorological Society*, 99(1):105–119.

Wang, X., Liang, X.-Z., Jiang, W., Tao, Z., Wang, J. X., Liu, H., Han, Z., Liu, S., Zhang, Y., Grell, G. A., et al. (2010). Wrf-chem simulation of east asian air quality: Sensitivity to temporal and vertical emissions distributions. *Atmospheric Environment*, 44(5):660–669.

WANG, Z., LI, Y., CHEN, T., ZHANG, D., SUN, F., SUN, R., DONG, X., SUN, N., and PAN, L. (2014). Temporal and spatial distribution characteristics of ozone in beijing. *Environmental Science*, 35:4446–4453.

Wang, Z., Zhang, S., Lu, S., and Bai, Y. (2003). Screenings of 23 plant species in beijing for volatile organic compound emissions. *Huan jing ke xue*, 24(2):7–12.

Wennberg, P. O., Bates, K. H., Crounse, J. D., Dodson, L. G., McVay, R. C., Mertens, L. A., Nguyen, T. B., Praske, E., Schwantes, R. H., Smarte, M. D., et al. (2018). Gas-phase reactions of isoprene and its major oxidation products. *Chemical reviews*, 118(7):3337–3390.

Whalley, L., Furneaux, K., Goddard, A., Lee, J., Mahajan, A., Oetjen, H., Read, K., Kaaden, N., Carpenter, L., Lewis, A., et al. (2010). The chemistry of oh and ho 2 radicals in the boundary layer over the tropical atlantic ocean. *Atmospheric Chemistry and Physics*, 10(4):1555–1576.

Witte, J., Duncan, B., Douglass, A., Kurosu, T., Chance, K., and Retscher, C. (2011). The unique omi hcho/no2 feature during the 2008 beijing olympics: Implications for ozone production sensitivity. *Atmospheric Environment*, 45(18):3103–3111.

Xie, X., Shao, M., Liu, Y., Lu, S., Chang, C.-C., and Chen, Z.-M. (2008). Estimate of initial isoprene contribution to ozone formation potential in beijing, china. *Atmospheric Environment*, 42(24):6000–6010.

Zang, X., Lu, Y., Yao, H., Li, F., Zhnag, S., et al. (2015). Investigation of the temporal and spatial distribution of major pollutants in china. *Ecology and Environmental Sciences*, 24(8):1322–1329.

Zaveri, R. A. and Peters, L. K. (1999). A new lumped structure photochemical mechanism for large-scale applications. *Journal of Geophysical Research: Atmospheres*, 104(D23):30387–30415.

Zhang, L., Wang, X., Ouyang, Z., and Miao, Q. (2003). Estimation of isoprene emission from forest ecosystems in china. *Huan jing ke xue*, 24(1):8–15.

Zhang, Q., Jiang, X., Tong, D., Davis, S. J., Zhao, H., Geng, G., Feng, T., Zheng, B., Lu, Z., Streets, D. G., et al. (2017a). Transboundary health impacts of transported global air pollution and international trade. *Nature*, 543(7647):705–709.

Zhang, Q., Yuan, B., Shao, M., Wang, X., Lu, S., Lu, K., Wang, M., Chen, L., Chang, C.-C., and Liu, S. (2014). Variations of ground-level o 3 and its precursors in beijing in summertime between 2005 and 2011. *Atmospheric Chemistry and Physics*, 14(12):6089–6101.

Zhang, R., Cohan, A., Biazar, A. P., and Cohan, D. S. (2017b). Source apportionment of biogenic contributions to ozone formation over the united states. *Atmospheric Environment*, 164:8–19.

Zhang, X., Huang, T., Zhang, L., Shen, Y., Zhao, Y., Gao, H., Mao, X., Jia, C., and Ma, J. (2016). Three-north shelter forest program contribution to long-term increasing trends of biogenic isoprene emissions in northern china. *Atmospheric Chemistry and Physics*, 16(11):6949–6960.

Zhang, Y. (2010). On-line coupled meteorology and chemistry models in the us. In *Integrated Systems of Meso-Meteorological and Chemical Transport Models*, pages 15–39. Springer.

Zheng, B., Tong, D., Li, M., Liu, F., Hong, C., Geng, G., Li, H., Li, X., Peng, L., Qi, J., et al. (2018). Trends in china's anthropogenic emissions since 2010 as the consequence of clean air actions. *Atmospheric Chemistry and Physics*, 18(19):14095–14111.

Zhou, G., Xu, J., Xie, Y., Chang, L., Gao, W., Gu, Y., and Zhou, J. (2017). Numerical air quality forecasting over eastern china: An operational application of wrf-chem. *Atmospheric Environment*, 153:94–108.

Zhu, X., Tang, G., Guo, J., Hu, B., Song, T., Wang, L., Xin, J., Gao, W., Münkel, C., Schäfer, K., et al. (2018). Mixing layer height on the north china plain and meteorological evidence of serious air pollution in southern hebei. *Atmospheric Chemistry and Physics*, 18(7):4897–4910.

A

M4 chemical mechanism

This appendix lists the species and reactions that are included in the M4 chemical mechanism and the scripts processed by KPP.

A.1 Species

33 species have been added into M4 chemical mechanism.

Name	Formula	Description	Mixing ratio	Photo-lysis	Dry deposition
LISOP-ACOOH	$C_5H_{10}O_3$ lumped	hydroxyperoxides	Y	Y	Y
ISOPB-OOH	$HOCH_2C(CH_3)(OOH)CH{=}CH_2$	hydroxyperoxides	Y	Y	Y
ISOPD-OOH	$CH_2{=}C(CH_3)CHOOHCH_2OH$	hydroxyperoxides	Y	Y	Y
ISOPA-OH	$HOCH_2C(CH_3){=}CHCH_2OH$	diol	Y		
ISOPB-OH	$HOCH_2C(CH_3)OHCH{=}CH_2$	diol	Y		
ISOPD-OH	$CH_2{=}C(CH_3)CHOHCH_2OH$	diol	Y		
ISOPA-ENO3	$HOCH_2C(CH_3\ ){=}CHCH_2ONO_2$	IN-E(1; 4)	Y	Y	Y
ISOPA-ZNO3	$HOCH_2C(CH_3\ ){=}CHCH_2ONO_2$	IN-Z(1; 4)	Y	Y	Y
ISOPC-ENO3	$NO_3CH_2C(CH_3\ ){=}CHCH_2OH$	IN-E(4; 1)	Y	Y	Y
ISOPC-ZNO3	$NO_3CH_2C(CH_3\ ){=}CHCH_2OH$	IN-Z(4; 1)	Y	Y	Y

ISOPB-NO3	$HOCH_2C(CH_3)ONO_2CH{=}CH_2$	IN-(1; 2)	Y	Y	Y
ISOPD-NO3	$CH{=}C(CH_3)CHONO_2\ CH_2OH$	IN-(4; 3)	Y	Y	Y
NISOP-OOH	$O_2NOCH_2C(CH_3){=}CHCH_2OOH$	nitro hydro peroxide	Y	Y	Y
NC4C-HO	$O_2NOCH_2C(CH_3){=}CHCHO$	lumped aldehydic nitrate	Y	Y	Y
LNISO-OH	$C_5H_7NO_6$.5 lumped	nitro peroxide	Y	Y	Y
LHC4A-CCHO	$C_5H_8O_2$ lumped	carbonyls	Y	Y	
LC578-OOH	$C_5H_{10}O_5$ lumped	hydroxyperoxides	Y	Y	Y
LHC4AC-CO2H	$C_5H_8O_3$ lumped	carboxylic acids	Y		Y
LHC4AC-CO3H	$C_5H_8O_4$ lumped	percarboxylic acids	Y	Y	Y
LC5PA-N1719	$C_5H_7NO_6$lumped		Y		
HCOC5	$CH_2{=}C(CH_3)COCH_2OH$		Y	Y	Y
C59OOH	$HOCH_2C(CH3)(OOH)COCH_2OH$	hydroxyperoxides	Y	Y	Y
LISOPA-CO2	$C_5H_9O_3$lumped	hydroxyperoxy radical	Y		
ISOPB-O2	$HOCH_2CO_2(CH_3)CH{=}CH2$	hydroxyperoxy radical	Y		
ISOPD-O2	$CH_2{=}C(CH_3)CO_2CH_2OH$	hydroxyperoxy radical	Y		
NISOPO	$O_2NOCH_2C(CH_3){=}CHCH_2O_2$	nitro peroxy radical	Y		
LNISO3	$C_5H_7NO_6$.5 lumped	nitro peroxy radical	Y		
LHC4AC-CO3	$C_5H_7O_4$ lumped	hydroxy peroxyacyl radical	Y		
LC578-O2	$C_5H_9O_5$ lumped	peroxy radicals	Y		

C59O2	$C_5H_9O_5$	alkyl peroxy radicals	Y		
LIEPOX	$C_5H_{10}O_2$ lumped		Y		
LIECHO	$C_5H_8O_2$ lumped		Y	Y	
LIECO3	$C_5H_7O_5$ lumped	peroxyacyl radical	Y		
LIECO-3H	$C_5H_8O_5$ lumped	peroxy carboxilic acid	Y	Y	Y
IEC1O2	$C_5H_7O_5$		Y		
NISOP-NO3	$C_5H_8N_2O_6$ lumped		Y		
MACR-OH	$HOCH_2C(CH_3)(OH)CHO$		Y	Y	Y
MAC-O2H	$CH_2{=}C(CH_3)CO_2H$	methacroleic acid	Y		Y
RONO2	$C_4H_7NO_5$		Y		
LHMVK-ABOOH	$C_4H_8O_4$ lumped	hydroxyperoxides	Y	Y	Y
MVKOH	$CH_2{=}CHC(O)CH_2OH$	hydroxy methyl vinyl ketone	Y	Y	
LMVKO-HABOO-H	$C_4H_8O_5$ lumped	hydroxyperoxides	Y	Y	
CO2H3-CHO	$CH_3COCH_2(OH)CHO$		Y	Y	Y
CO2H3-CO3H	$CH_3COCH_2(OH)CO_3H$		Y	Y	Y
BIACE-TOH	$CH_3C(O)C(O)CH_2OH$		Y	Y	Y
HO12C-O3C4	$CH_3C(O)CH(OH)CH_2OH$		Y	Y	Y
LHMVK-ABO2	$C_4H_7O_4$ lumped		Y		
LMVKO-HABO2	$C_4H_7O_5$ lumped		Y		
CO2H3-CO3	$CH_3COCH_2(OH)CO_3$		Y		

HOCH2-COCO2H	$HOCH_2C(O)CO_2H$		Y	Y	Y
HOCH2-COCHO	$HOCH_2C(O)CHO$		Y	Y	Y
PRONO-3BO2	$CH_3CH(O_2)CH_2ONO_2$	nitro peroxy radical	Y		
PR2O2-HNO3	$CH_3CH(OOH)CH_2ONO_2$		Y	Y	Y
HCOC-O3	$HCOCO_3$	peroxy acyl radical	Y		
HCOC-O2H	$HCOCO_2H$	carboxilic acid	Y	Y	Y
HCOC-O3H	$HCOCO_3H$	peroxy carboxilic acid	Y	Y	Y
PHAN	$HOCH_2C(O)OONO_2$		Y		Y
HOCH2-CO3H	$HOCH_2CO_3H$	peroxy carboxilic acid	Y	Y	Y
HOCH2-CO2H	$HOCH_2CO_2H$	carboxilic acid	Y		Y
HOCH2-CO3	$HOCH_2CO_3$	peroxy acyl radical	Y		
CO2	CO_2		Y		

Table A.1.1: The list of species implemented into WRF-Chem.

B

Meteorological analysis

B.1 Temperature

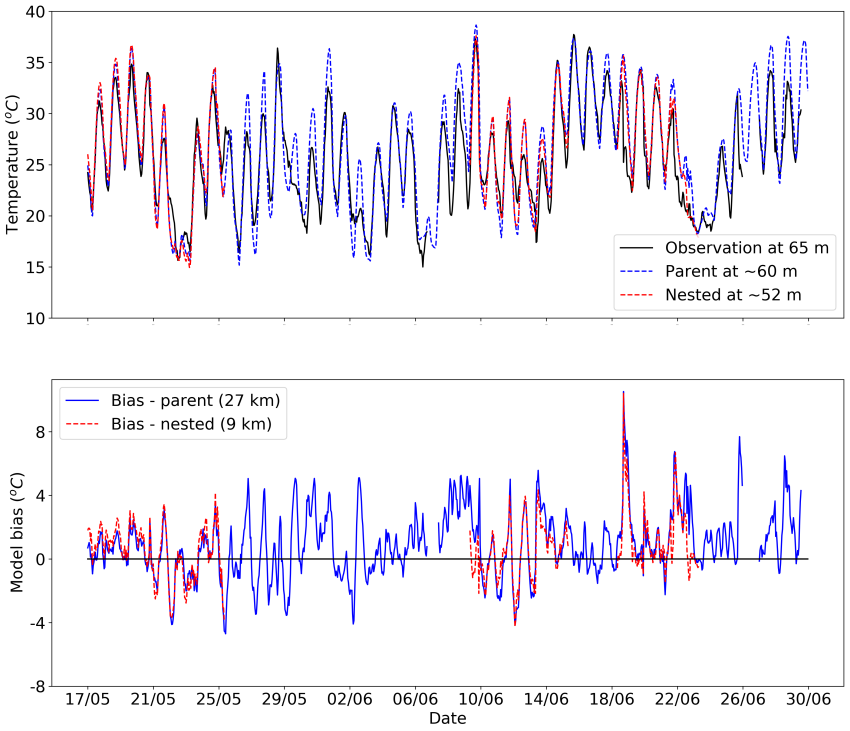

Figure B.1.1: Same as Fig.3.2.1, but for a different height (∼60 m).

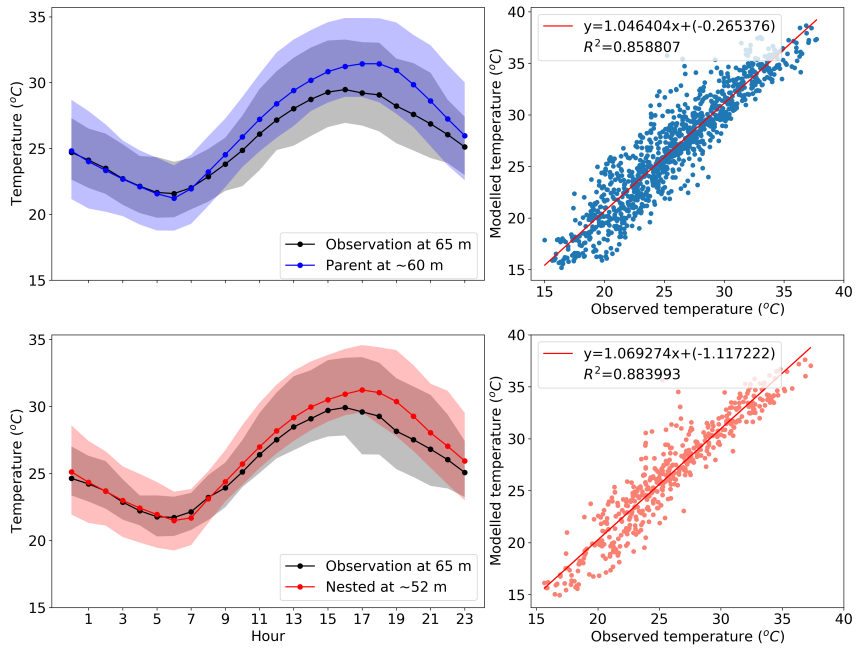

Figure B.1.2: Same as Fig.3.2.2, but for a different height (∼60 m).

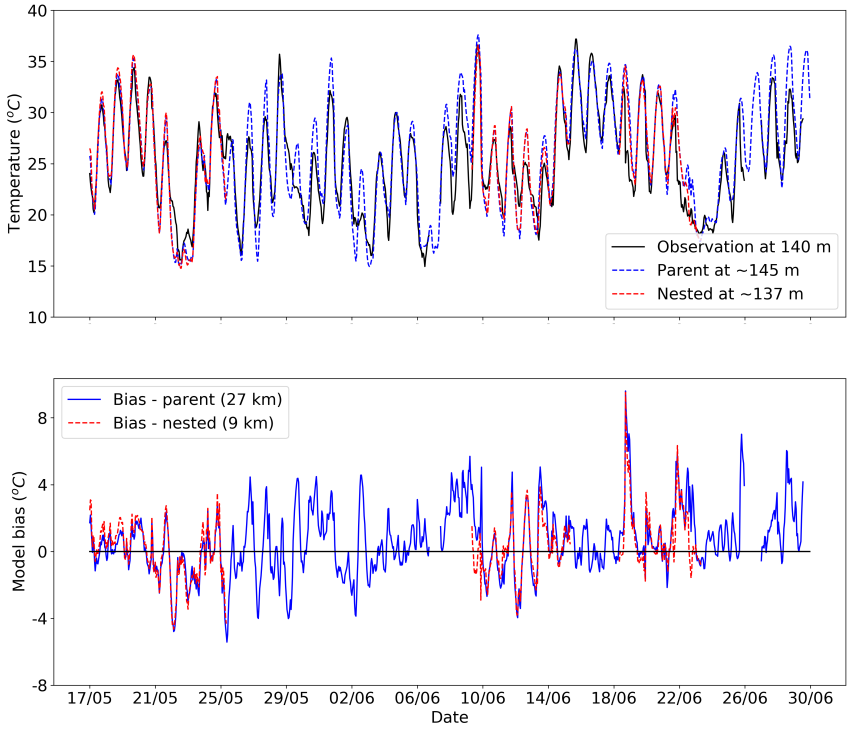

Figure B.1.3: Same as Fig.3.2.1, but for a different height (~145 m).

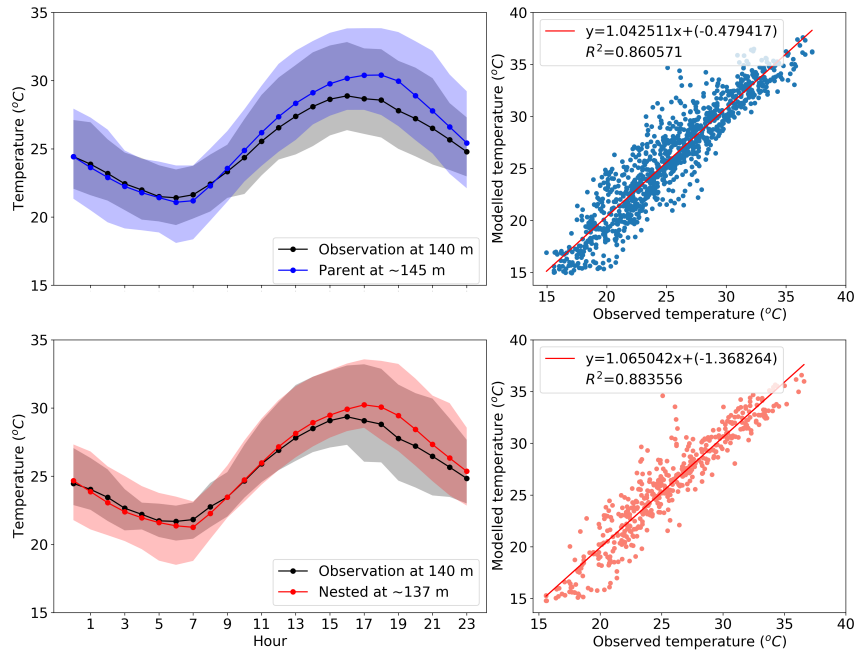

Figure B.1.4: Same as Fig.3.2.2, but for a different height (~145 m).

B.2 Relative humidity

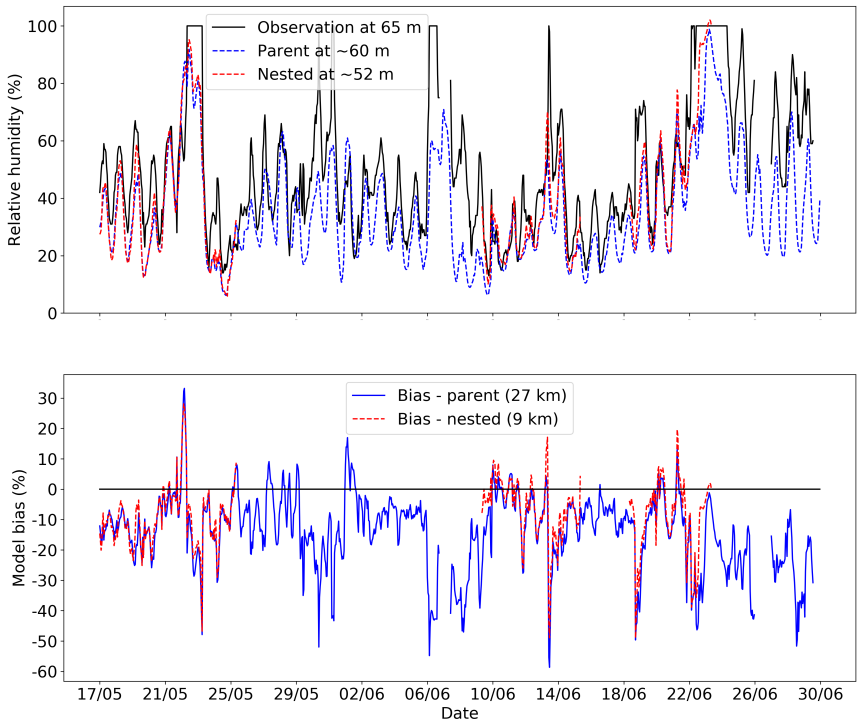

Figure B.2.1: Same as Fig.3.2.5, but for a different height (~60 m).

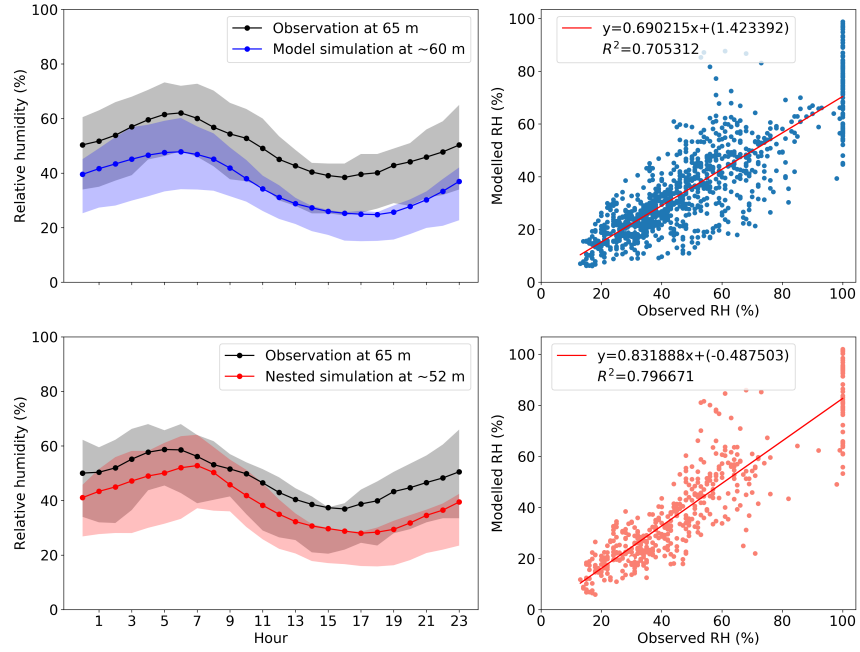

Figure B.2.2: Same as Fig.3.2.7, but for a different height (~60 m).

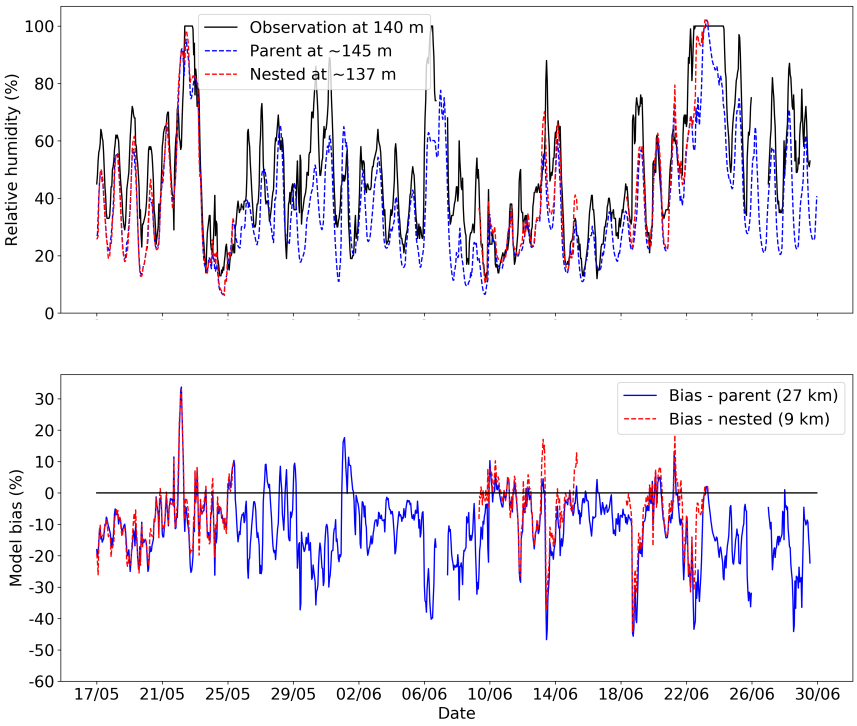

Figure B.2.3: Same as Fig.3.2.5, but for a different height (~145 m).

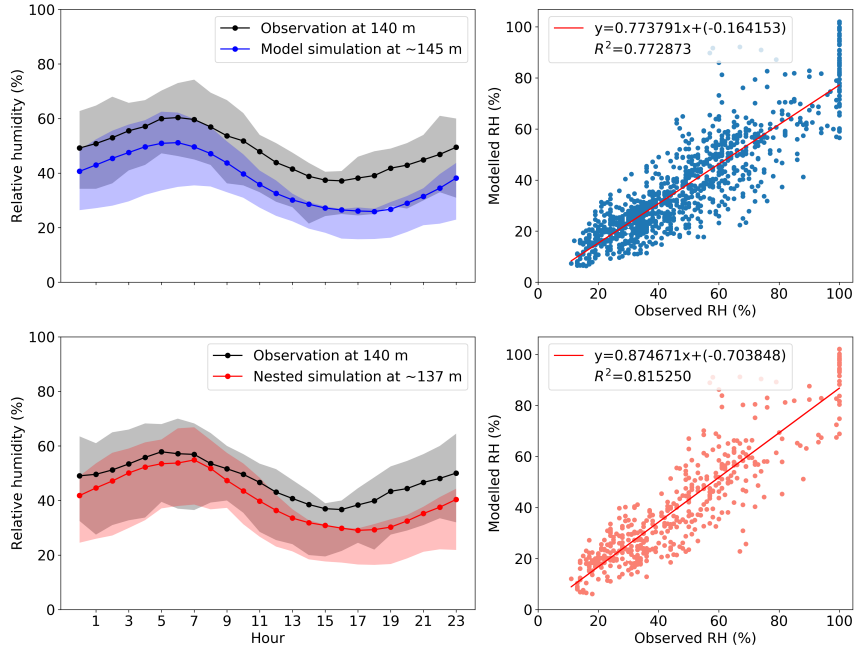

Figure B.2.4: Same as Fig.3.2.7, but for a different height (~145 m).

B.3 Wind speed and direction

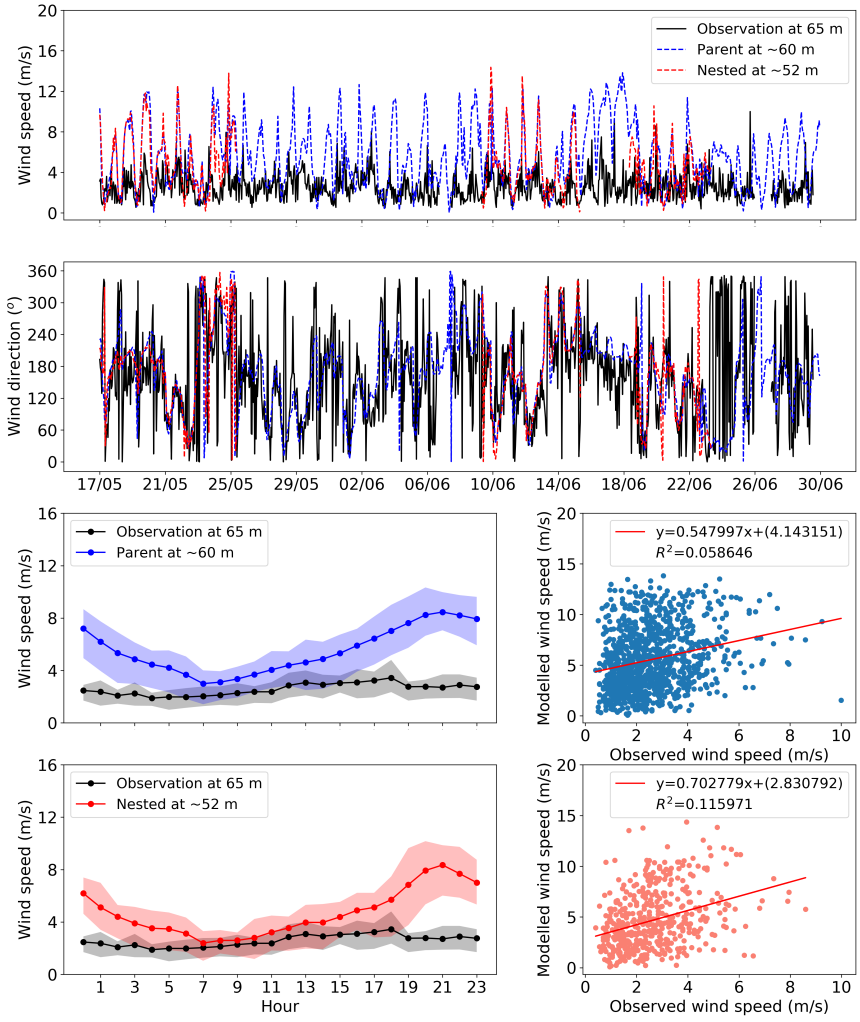

Figure B.3.1: Same as Fig.3.2.9, but for a different height (∼60 m).

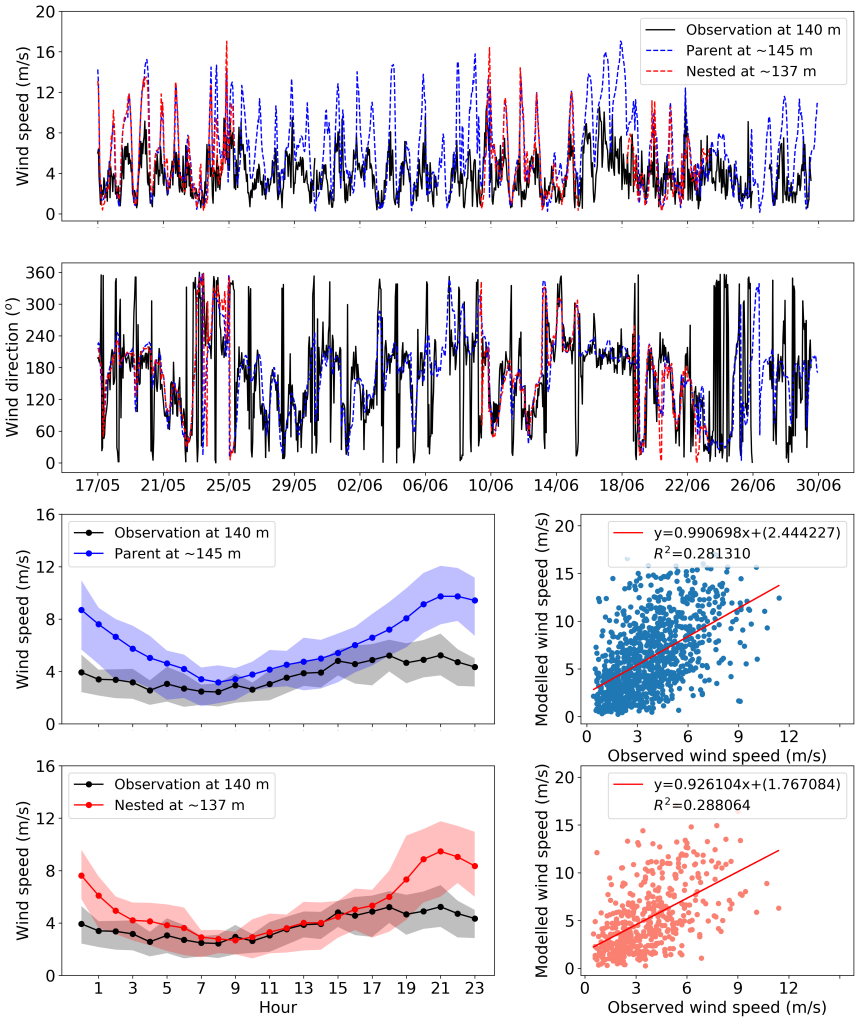

Figure B.3.2: Same as Fig.3.2.9, but for a different height (∼145 m).

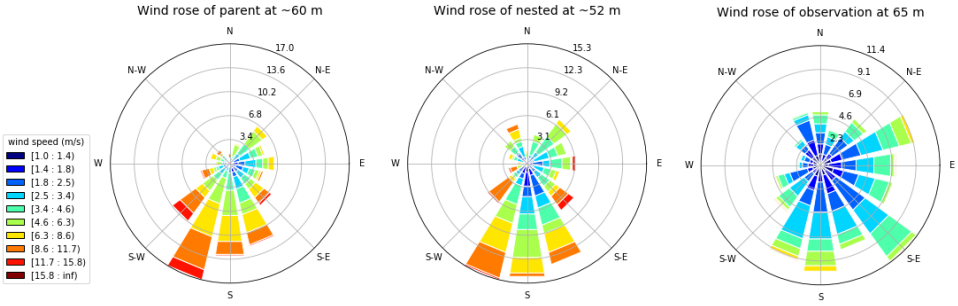

Figure B.3.3: Same as Fig. 3.2.11, but for a different height (∼65 m).

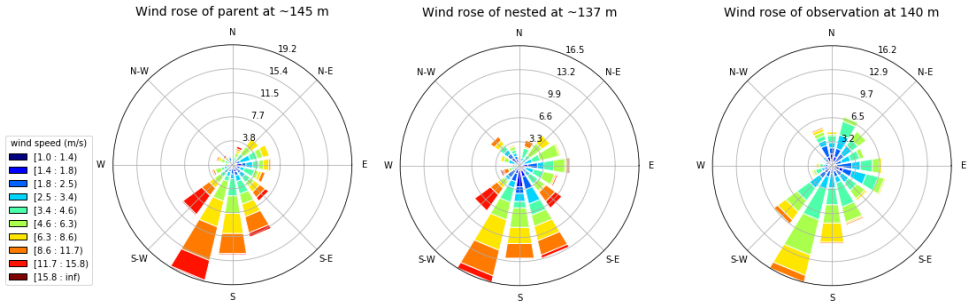

Figure B.3.4: Same as Fig. 3.2.11, but for a different height (∼140 m).